Spring 5-18-2012

Investigating the Electron Transport and Light Scattering Enhancement in Radial Core-Shell Metal-Metal Oxide Novel 3D Nanoarchitectures for Dye Sensitized Solar Cells

Gayatri Sahu
University of New Orleans, gsahu@my.uno.edu

Investigating the Electron Transport and Light Scattering Enhancement in Radial Core-Shell Metal-Metal Oxide Novel 3D Nanoarchitectures for Dye Sensitized Solar Cells

A Dissertation

Submitted to the Graduate Faculty of the
University of New Orleans
in partial fulfillment of the
requirements for the degree of

Doctor of Philosophy
in
Chemistry

By

Gayatri Sahu

B.S., Berhampur University, 2002
M.S., Berhampur University, 2005
M.S., University of New Orleans, 2011

May 2012

Dedicated to My Parents, Baba & Maa ….

Acknowledgements

I am delighted to express my pleasure to thank my research advisor Dr. Matthew A Tarr. He has really been an excellent advisor. I want to thank him for believing in me and also for giving me these interesting research projects which I enjoyed working on during last four years of PhD studies. He has shared his vast scientific knowledge, enthusiasm, and experience with me. He has encouraged me with his "pep talks" whenever he felt like I am disheartened and I need a confidence boost. He normally has a very busy schedule, but he would always find time to discuss my research progress. His ideas were so practical and innovative which increased my understanding of the concepts and helped me a lot to learn more about the science behind the subject. I can't thank him enough how much he has done for me. Working with him has given me an era of courage and self confidence to think of a chemistry problem by my own.

I want to thank my supervisory committee, Dr. John B Wiley, Dr. Weilie Zhou, Dr. Gabriel Caruntu, and Dr. David L Mobley, for their invaluable suggestions and clearing my doubts whenever I needed them.

The financial support by the Louisiana Board of Regents, LEQSF (2007-12)-ENH-PKSFI-PRS-04, college of sciences (COS) graduate student grant awards, students govt. (SGA) & COS travel grant awards are gratefully acknowledged.

My special thanks to Dr. Weilie Zhou and Dr. Heike B. Gabrisch who taught me electron microscopy. Thanks to Dr. Ray L Sweany whom I consider a true scientist and he helped me learning so much basic chemistry while I was a teaching assistant in 1028 lab under his instruction. Thanks to Mr. Harry Rees, the technician for his timely help. I acknowledge the generous help from Dr. Zhou's lab for allowing me to use his instruments for a few of my experiments. I appreciate the cordial help from Dr. John B Wiley and Jin-hee Lim for providing with the single channel potentiostat for the electrodeposition experimental work. I have been benefited from the instrument throughout my PhD studies.

It is a pleasure to thank Kai Wang for helping me with PLD experiments and also for constructive suggestions during the experiments. He is a very nice friend of mine and it was a pleasure working with him. He is one of the persons who inspired me to work hard to achieve my goals. Thanks to Scott Gordon for helping me with IPCE measurements and his helpful

suggestions for the EIS instrumental analysis. Heartiest thanks to Jiajun Chen and Haiqiao Su for teaching me e-beam nanolithography.

It was an exciting working experience with my current group members, Sarah King, Angela C. Ellender, Richard M. Prevost, Phoebe Zito Ray, Scott Gordon, Kristen Schexnayder, Ujwal Suresh Patil, Parisa Pirani, Donna V. Peralta, and Isabella J. Schmitt. Thank you all of you for all the fun, the loud laughs, the yummy B'day cakes, the true friendship and for showing me happy faces every morning in the lab. I also want to thank my past group members, Sourav Chakraborty, Curt Jarand, Ashley Quash, Venkata Kethineedi, Ariel Wicks, and Dr. David Bwambok for being so nice to me. It was a great opportunity working with them as well. I would also like to thank Dr. John B Wiley and his group members with whom I have shared good amount of fun time that left wonderful memories to be remembered for ever. They have always made my special days even more special by giving me tons of surprises and celebrating them whole heartedly.

I would like to thank all my teachers who have taught me during various stages of my educational career especially Dr. Ranjan Pradhan during my Bachelor's degree, and Dr. Rama Krushna Panda at Berhampur University during Master's degree. They are responsible for motivating me towards making Chemistry and Materials Science as major subjects in my career.

I would like to express my deep sense of gratitude to my parents Baba and Maa who are like God to me. Without their blessings not a single thing would have ever been possible in my life. I could be thru every hardship just by remembering their faces, which gives me moral support and willingness to fight to win. I am so glad and overwhelmed that I could be able to complete my Baba's dream to see his daughter receiving the PhD degree. I owe a very deep debt of gratitude to my father-in-law Bapa and mother-in-law Bou who love me always just like their daughter, prayed for me, stood by me in all adverse conditions.

It will be a little to acknowledge my family members, my sisters, Badanani, Bharatinani, Bhabaninani, Nandininani, and Sibanani for their moral support, their confidence in me and the unconditional love they have given me throughout my life. My special thanks to my bro-in-laws, my nieces, nephews, sister-in-law Mamun, and bro-in-law Sibun for their love, well wishes, and also for always making me feel very special in this world. Finally, it's an immense pleasure to thank my loving and caring husband Debasish with whom I have the joy and privilege of sharing all my successes, failures and fears of my life. He inspires me to chase my dreams. He is the person who is always there standing by me, surprises me by making my dreams come true. Without his sacrifices, understanding, and support nothing would have ever been possible.

Table of Contents

List of Tables

List of Figures

Abstract

Dye-sensitized solar cells (DSSCs) have attained considerable attention during the last decade because of the potential of becoming a low cost alternative to silicon based solar cells. Electron transport is one of the prominent processes in the cell and it is further a complex process because the transport medium is a mesoporous film. The gaps in the pores are completely filled by an electrolyte with high ionic strength, resulting in electron-ion interactions. Therefore, the electron transport in these so called state-of-the-art systems has a practical limit because of the low electron diffusion coefficient (D_n) in this mesoporous film photoanode. This work focuses on the influence of the advanced core-shell nanoarchitecture geometry on electron transport and also on the influence of electron-ion interactions. In order to achieve the proposed goals, DSSCs based on ordered, highly aligned, 3D radial core-shell Au-TiO_2 hybrid nanowire arrays were fabricated, using three different approaches. J-V, IPCE, and EIS characteristics were studied. The efficiency, light scattering and charge transport properties of the core-shell nanowire based devices were compared to TiO_2 nanotube as well as TiO_2 mesoporous film based DSSCs. The Au nanowires inside the crystalline TiO_2 anatase nanoshell provided a direct conduction path from the TiO_2 shell to the TCO substrate and improved transport of electrons between the TiO_2 and the TCO. The optical effects were studied by IPCE measurement which demonstrated that Au-TiO_2 nanowires showed an improved light harvesting efficiency, including at longer wavelengths where the sensitizer has weak absorption. The metal nanostructures could enhance the absorption in DSSCs by either scattering light enabling a longer optical path-length, localized surface plasmon resonance (LSPR) or by near-field coupling between the surface plasmon polariton (SPP) and the dye excited state. Rapid, radial electron collection is of practical significance because it should allow alternate redox shuttles that show relatively fast electron-interception dynamics to be utilized without significant sacrifice of photocurrent. A combination of improved electron transport and enhanced light harvesting capability make Au-TiO_2 core-shell nanowire arrays a promising photoanode nanoarchitecture for improving photovoltaic efficiency while minimizing costs by allowing thinner devices that use less material in their construction.

Keywords: TiO_2, Au-TiO_2, Ni-TiO_2, Nanotube, Core-shell nanowire, Electrodeposition, Template synthesis, E-beam nanolithography, Dye sensitized solar cells, Charge transport, Surface plasmons, Impedance, Recombination resistance.

Chapter 1

Introduction and Background

1.1. Renewable energy and energy sources

Of the many problems affecting the current human generation, increasing energy needs and concerns about global warming have led to greater focus on renewable energy sources. As fossil fuels become depleted, we will lean more towards renewable energy sources. The present annual energy consumption worldwide has reached a power consumption of 13 terawatts.[1] Earth's population is supposed to be 8-10 billion people by 2050.[2] So, even with excessive conservation and energy efficiency measures, rapid technology development and economic growth rate demand more than double the amount of energy (to 30 TW) by 2050, and more than triple the number (to 46 TW) by the end of the century.[2] The need for renewable energy is crucial at this point. At the beginning of February, 2007, the Intergovernmental Panel on Climate Change (*IPCC*) presented a report[3] concluding that global concentrations of carbon dioxide, methane and nitrous oxide have increased markedly as a result of human activities since 1750. The report states that the increase in carbon dioxide, the most important greenhouse gas, is primarily due to fossil fuel use. As for the increases in methane and nitrous oxide levels, however, the report states that these are primarily due to agriculture. The report further indicates that the increased concentrations of carbon dioxide, methane, and nitrous oxide have increased the average global temperature, a phenomenon known as "global warming." Averaged over time, the rate of temperature increase has doubled over the last 50 years (0.13 ºC per decade) compared to that of the last 100 years, and in total, the average global temperature has increased by 0.76 ºC since the beginning of the twentieth century. 2006's reported temperature rank amongst the warmest on record, the last 12 years accounting for the 11 warmest years in the instrumental record of global surface temperatures (since 1850). The report finally predicts that the average global temperature will increase between 0.6 and 4.0 ºC in the coming 100 years, depending on model parameters such as world population growth, primary energy source, and economic growth.[3] The consequences of global warming in the twentieth century include an increased melting of snow and ice in the Arctic and Antarctic regions, and average Arctic temperatures have increased almost twice the

global rate. Observations since 1961 also indicate that average ocean temperatures have increased to depths of at least 3000 m, causing the sea level to increase due to thermal expansion. The combined effects have increased the average sea level at a rate of 1.8 mm per year between 1961 and 2003, or 3.1 mm per year when calculated between 1993 and 2003.[3] So far, the consequences of global warming can be viewed as relatively mild, but given continuous world population and fossil fuel use, the average global temperature will most likely increase further. In the long-term, this can influence the climate zones and disturb well-established ecological systems. Eventually, if the temperature continues to increase, this will influence our everyday lives, since it changes the conditions of, for example, agriculture and fishing. Even though researchers have indicated that fossil fuel use is related to global warming,[4] the *IPCC* report is of particular importance since it directly targets policymakers and politicians.

Increasing energy needs and concerns about global warming have led to greater focus on renewable energy sources and specifically conversion of solar energy into electrical energy. The sun is the primary source for most energy forms found on the earth. It is clean, enormous, renewable, and provides approximately 100,000 terawatts of energy (10,000 times greater than the world's present consumption). It has been calculated that covering 0.1% of the earth's surface area with solar cells of 10% efficiency, corresponding to 1% of desert areas or 20% of the area of buildings and roads, the energy flux would provide for global electricity consumption.[5-6] If this hypothesis is made possible in reality, this will benefit our world by diversifying our energy supply, reducing our dependence on fuels, improving the quality of air we breathe and supporting our economy by recruiting jobs in the manufacture and installation of solar systems.

1.2. Solar cells

The science of solar cells began with the discovery of the photovoltaic effect by a French physicist, Edmund Becquerel, in 1839.[7] While carrying out an electrochemical experiment involving two metal plates in a dilute acidic solution, Becquerel observed that exposing the apparatus to sunlight increased the electrical energy it produced. The technology of photovoltaics began with the preparation of the first working solar cell by an American inventor, Charles Fritts, in 1883[8] which was made from selenium. Fritts made a 30 cm^2 device by melting selenium into a thin sheet onto an iron metal substrate. A gold-leaf film formed the top transparent contact.[8] This was a Schottky barrier device with an estimated efficiency of 0.5%. Although the photoelectric

effect was later explained by Einstein in 1905,[9] the era of the first solid state semiconductor p-n junction cell started in 1941 by Russel Ohl of Bell laboratories.[10-11] The research on silicon photovoltaics began with the pioneering work of a multidisciplinary research team at Bell Laboratories, of Pearson, Fuller and Chapin, in 1954.[12] They reported the creation of the first practical solar cell made of silicon. The solar cell consisted of an arsenic-doped silicon substrate with a boron-doped layer, a *p*-i-*n* device. This solar cell had an efficiency of 6% which was rapidly increased to 10%.[12] For many years, the main application of the technology was in space vehicle power supplies; the cost remained high, and the technology did not gain any significant public attention as an alternative energy source. Attention grew, however, in the 1980s and 1990s, alternative energy sources such as wind, water, biomass and solar became more or less synonymous with renewable energy sources, largely because of the concerns connected with pollution and global warming.

Today, solar energy is the main renewable energy source, largely because the potential of using the sun as a primary energy source is enormous. In the intervening 50 years, solar cell research and development has seen dramatic progress. Development of first generation photovoltaic (PV) devices was motivated principally by space applications of PV. These PV devices were based on crystalline semiconductors, such as Si and III-V compounds. First generation solar cells based on thin film technology, contributed to extra terrestrial needs such as light weight, stable long term performance in outer space, and having radiation resistance.[13] The impetus for second generation photovoltaics was the OPEC (Organization of Petroleum Exporting Countries) oil crisis and nuclear waste disposal problems. Second generation PV devices were based on thin film semiconductors, such as amorphous silicon (a-Si), cadmium telluride (CdTe), and copper indium diselenide (Cu (In,Ga) Se_2). In this approach, thin layers of the semiconductor material are deposited onto a supporting substrate, such as a large sheet of glass. Typically, less than a micron thickness of semiconductor material is required, 100–1000 times less than the thickness of a silicon wafer.[14] Reduced material use with associated reduced costs is a key advantage. Another advantage is that the unit of production, instead of being a relatively small silicon wafer, becomes much larger, as large, for example, as a conveniently handled sheet of glass might be. This reduces manufacturing costs. The main thin film modules are based on CdTe, amorphous silicon and Cu (In,Ga) Se_2 (CIGS). World record efficiencies for solar cells today are 24.7% for crystalline silicon, 24.5% for GaAs (thin film) and 19.2% for CIGS cells.[15] The materials used in these technologies, however include rare-earth elements, which could be a

restriction if PV were to be the main supplier for electricity generation. Both first and second generation solar cells rely on single junction devices. The theoretical thermodynamic efficiency limit in such single junction solar cells is 31%, assuming that each absorbed photon results in the formation of a single exciton (electron-hole pair) and that all photon energy in excess of the energy gap is lost as heat.[2,16] The maximum efficiency that can be reached with the conventional solar cell structure is given by the so-called single material or Schockley-Queisser limit.[17] This limit can be overcome by the use of various types of tandem cells, hot carrier cells, multiexciton generation multiband cells, polymer solar cells and third generation electrochemical cells.[18] This led to the recognition that alternative energy sources such as third generation PV ought to be developed to meet terrestrial electricity needs. Here, the objectives included improvement of conversion efficiency of thin film solar cells, search for low cost PV materials and economical technologies for cell production. The third generation of solar cell R&D is guided by long-term sustainability, environmental compatibility, and economically favorable factors. The third generation photovoltaics include hybrid and emerging technologies such as low temperature amorphous-crystalline silicon heterojunctions, thin film amorphous-nanocrystalline Si devices, dye sensitized solar cells, organic semiconductors and quantum dot sensitized solar cells. Third generation concepts are based on devices that can exceed the Schockley-Queisser limit. The physical limit is actually much higher. Considering the Sun as a black body at 5760 K and the solar cell (another black body) at 300 K, the Carnot efficiency limit is 95%.[19] This could only be realized if the electrons were not dethermalised before being extracted. These electrons are referred to as hot carriers and if they could be extracted, it would be possible to pass the 31% limitation. Multijunction cells are also a possibility, in which a range of bandgaps are combined in one cell. With new material developments, it is hoped that this limit can also be passed with lower cost nano-materials in third generation photovoltaics,[18] see Figure 1.1.

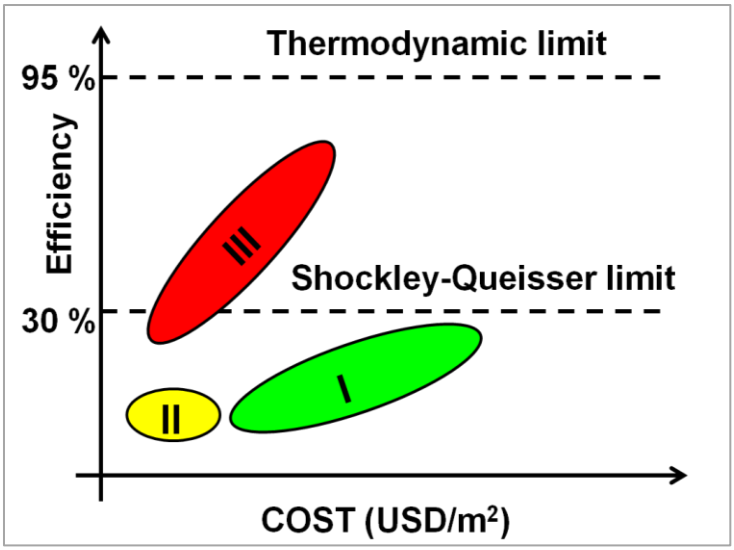

Fig.1.1 Efficiency and cost projections for first, second and third generation photovoltaic technology.

1.3. Photoelectrochemistry, an overview

This section contains an overview of the physics and chemistry of semiconductors and electrolytes, and of the junctions formed when they come into contact with each other. The basic ideas gained, have been applied to DSSC research.

1.3.1. The semiconductor

Solid materials can be categorized as conductors, insulators, or semiconductors, depending on their ability to transport electrical current.[20-21] As the name suggests, a conductor carries electrical current well, whereas an insulator cannot carry a current at all. Between these extremes is the semiconductor, the ability of which to transport an electrical current depends on doping and other conditions. When a solid material forms, several atomic orbitals combine to form molecular orbitals, with a spacing between the discrete energy levels that decreases with increasing number of atoms. When the number of atoms is large enough, the discrete energy levels are usually described in terms of continuous energy bands.[20,22] Some bands are filled, some are empty, and some are partly filled with electrons; depending on the overlap between individual bands,

different conducting properties and hence material types can be distinguished. A metal has either a partly filled band or two overlapping bands, one of which is filled and the other empty, so electrons can move relatively freely.[21] For semiconductors and insulators, however, there is a gap, *i.e.* a bandgap (E_g) between the energetically highest filled energy band, *i.e.*, the valence band (*VB*), and the energetically lowest empty energy band, *i.e.*, the conduction band (*CB*). If E_g is less than ~4.0 eV the material is a semiconductor, and if it is above ~4.0 eV, the material is an insulator.[20] TiO_2, usually the material of choice for *DSSCs*, has a bandgap of 3.0 or 3.2 eV, depending on the crystal structure, *i.e.*, rutile or anatase, respectively. Under normal circumstances, the *CB* is empty and the *VB* is filled, so a semiconductor cannot transport an electrical current. However, electrons can become excited from the *VB* to the *CB* by stimulating the semiconductor sample with light, provided the photon energy, E_{ph}, matches or exceeds E_g. The photon energy can be calculated from the photon frequency, ν, and the Planck constant, *h*, or alternately from the speed of light, *c*, and the wavelength, λ, as in *Eq*. 1.[20]

$$E_{ph} = h\upsilon = hc/\lambda \qquad (1.1)$$

The conductivity, σ, of a semiconductor is directly related to electrons in conduction band (e_{CB}^-) and holes in valence band (h_{VB}^+) via *Eq*. 1.2, where *q* is the elementary charge and μ*e* and μ*h* are the mobilities of electrons and holes, respectively.[20]

$$\sigma = q(\mu_e e_{CB}^- + \mu_h h_{VB}^+) \qquad (1.2)$$

From *Eq*. 1.2, it can be determined that the conductivity of a semiconductor is low due to a normally low e_{CB}^-. The conductivity can, however, be improved by introducing into the material atoms with fewer or more valence electrons. This process is known as doping, and a doping fraction of $1/10^6$ atoms can be sufficient to increase the conductivity significantly. In an undoped material, the Fermi level, E_f, is approximately in the middle of the bandgap, which means that the probability of finding an electron at that energy is half. By doping the material, the concentration of e_{CB}^- or h_{VB}^+ increases, shifting E_f upwards or downwards. If the introduced doping atoms have more valence electrons than do the atoms in the material, the excess electrons will be donated to the *CB* and the material is said to be n-doped. Conversely, if the doping atoms have fewer valence

electrons than do the atoms in the material, the material is p-doped. The energy diagrams of an undoped, n-doped, and p-doped semiconductor can be viewed in *Fig*. 2.[21]

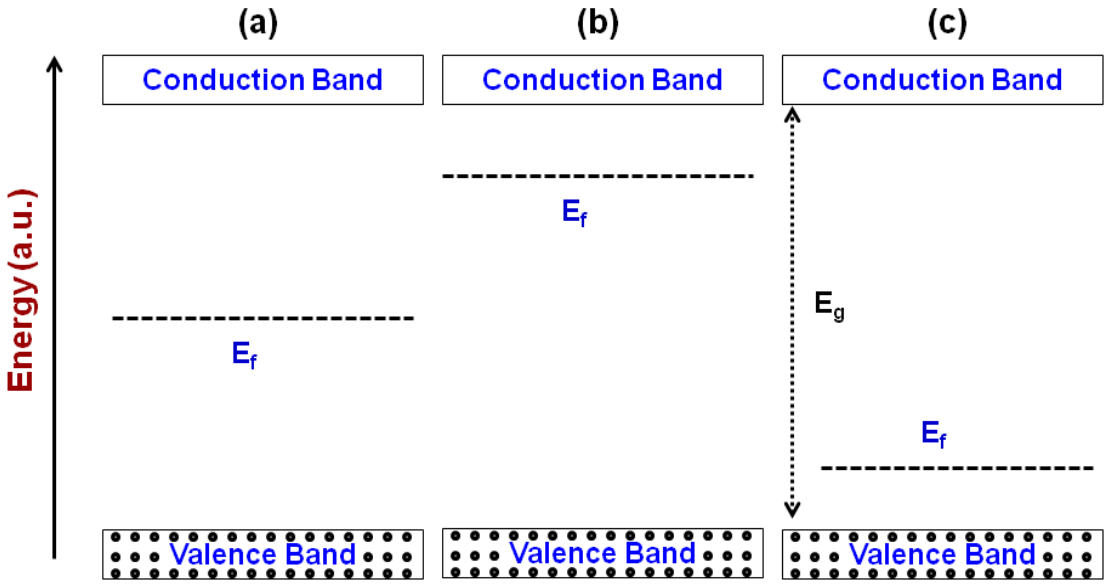

Fig.1.2 Approximate Fermi Levels, E_f for (a) an undoped semiconductor, (b) an n-doped semiconductor, and (c) a p-doped semiconductor. Also, the bandgap E_g is visualized approximately.

1.3.2. The semiconductor electrochemistry

In this section, the interface between a semiconductor and an electrolyte is presented, which is fundamentally important for understanding this thesis. Firstly, the concept of electrolyte is introduced and a presentation is made of how the structure of the semiconductor and electrolyte interface defines the relationship between charge and potential. Secondly, the possibility of transferring a charge over the interface is discussed.

An electrolyte is a solution that contains dissociated ions and behaves as a conducting medium. Unlike doped semiconductors, in which the electrical current is dominated by one type of carrier (electrons or holes), both types of positive and negative carriers are always present in equal concentrations in an electrolyte. If the ions themselves serve as a solute, the electrolyte is usually referred to as a molten salt or ionic liquid electrolyte.[23-24] The mobility of ions in an

electrolyte depends on the type and concentration of ions present, together with the properties of the electrolyte. If the relationship between mobility, μ, hydrodynamic radius, *r*, elementary charge, *q*, viscosity, η, and ionic charge, *n*, follows Stokes law (see *Eq*. 3), the conductivity of an electrolyte containing *i* species can be expressed by *Eq*. 4, where *F* is the Faraday constant and c_i, the concentration of each ion species.

$$\mu = \frac{|n|}{6\eta}\frac{q}{r} \qquad (1.3)$$

$$\sigma = F\sum_i |n_i|\mu_i c_i \qquad (1.4)$$

The conductivity of an electrolyte describes the transport of ions within an electrical field in the solution. In the absence of an electric field, or if the ions are completely screened by supporting electrolyte, the ions move due to diffusion. The diffusion coefficient, *D*, can be related to the mobility via the Einstein equation, *Eq*. 5, in which k_B is the Boltzmann constant and *T* is the absolute temperature.

$$D = \frac{k_B}{q}\, T\, \mu \qquad (1.5)$$

When a semiconductor is brought into contact with an electrolyte, electrons will flow through the junction until equilibrium is reached. If E_f is larger than potential of redox couple (U_{redox}), electrons will flow from the semiconductor to the electrolyte until $E_f = U_{redox}$. This transfer of electrons implies that the regions nearest the junction will have charge densities that differ from their individual bulk values. For the described situation, the region in which e_{CB}^- is lower than the bulk value, it is referred to as the depletion layer. Alternately, if U_{redox} is greater than E_f, electrons will flow from the electrolyte and electrons will be accumulated in the semiconductor, forming an accumulation layer. Both depletion and accumulation layers affect the band structures of the *CB* and the *VB*, but in different directions, a phenomenon known as band bending. A graphical presentation of band bending for an n-type semiconductor in contact with an electrolyte can be viewed in Fig. 1.3 below.

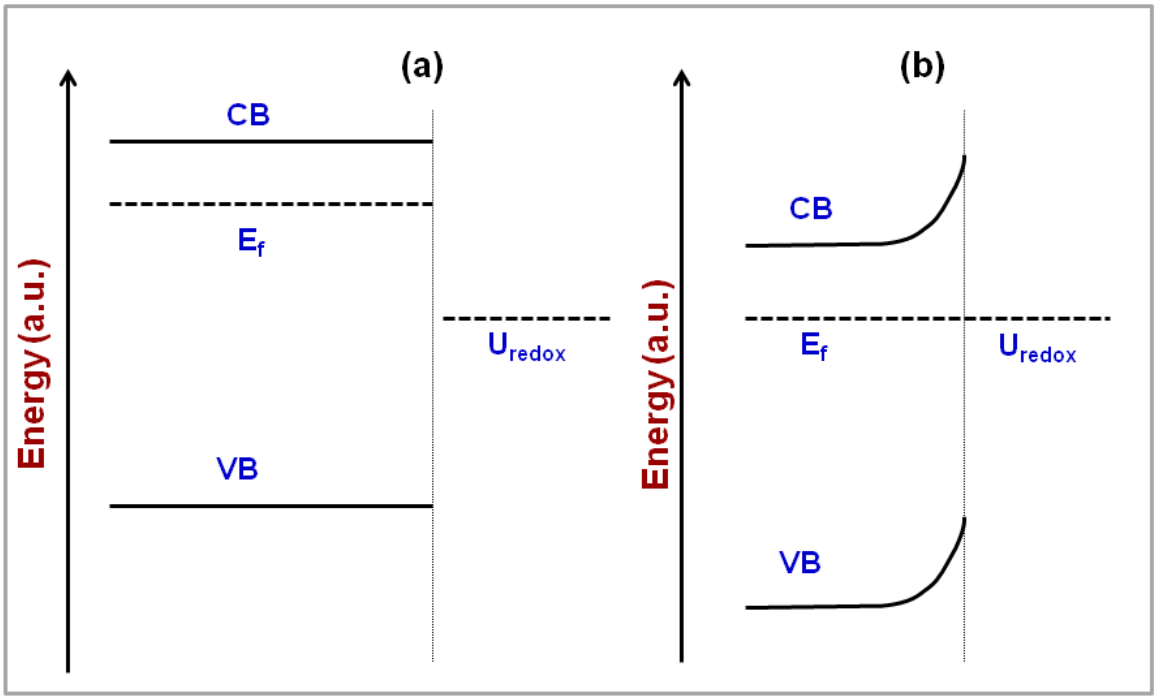

Fig.1.3 The band structures of an n-doped semiconductor before (a) and after (b) contact with an electrolyte

A negatively charged semiconductor surface will attract positive ions to the surface. We will now consider the case in which no electron or hole charge transfer reaction can take place at the interface. The separation of oppositely charged species gives rise to a potential difference between the semiconductor and the bulk electrolyte. This in turn gives rise to a Helmholtz layer, in which oppositely charged species are located at a distance, d, which depends on how closely the ions can reach the semiconductor surface. The separation of charges induces an electrical potential difference and an electrical field at the interface. The manner in which the variation of the separated charges, *dq*, depends on the potential difference across the interface, *dV*, is related by the capacitance, *C*.

$$dV = dq/\mathrm{C} \qquad (1.6)$$

Helmholtz capacitance, C, depends on the area, A, and the distance, d, of the separated charges according to equation 1.7 below,

$$C = A \varepsilon \varepsilon_o / d \qquad (1.7)$$

ε is the dielectric constant of the solution at the interface and ε_o is the permittivity of the free space. The distance, d, is related to how close to the surface the ions can reach, which is related to their size. Large ions therefore have a lower capacitance than smaller ions. At separation of one electron with a positive cation, a larger cation will give a larger potential difference at the interface.[20]

1.4. The dye sensitized solar cells (DSSCs)

1.4.1. Background

Sensitization of wide band gap semiconductors has already been seen in the past. Revealing the early days of photography in the 19th century Moser observed that photoelectric effect on silver plates was enhanced due to an erythrosine dye.[25] The breakthrough of dye sensitized devices as solar cell was based on some innovative points such as mesoporous semiconductors of high surface area which allowed high density of dye adsorption. Furthermore development of stable metal organic sensitizers bearing attachment groups which bind strongly with the semiconductors leads to enhanced charge injection efficiency. Based on these exciting facts, overall efficiencies of over 10% were obtained by O'Regan and Grätzel in 1991 for dye sensitized mesoporous TiO_2 electrodes in contact with an electrolyte containing an iodide/triiodide based redox system for dye regeneration.[26]

1.4.2. Design and working principle of dye sensitized solar cells

Regenerative photoelectrochemical solar cells based on photosensitization of nanocrystalline TiO_2 are regarded as a potential low-cost alternative to conventional solid-state devices.[26] A DSSC is in essence a photoelectrochemical system, in which a dye-sensitized n-type semiconducting oxide film deposited on a transparent conductive glass (TCO) substrate serves as working electrode i.e., the so-called photoanode. A platinum-coated glass substrate placed parallel to the working electrode with a face-to-face configuration acts as counter electrode (Fig. 4). The space between these two electrodes, which is approximately 40 µm in distance, is filled with a

liquid or solid electrolyte that plays a role of conducting media. The light irradiates from the working electrode side (front side illumination), passes through the transparent electrode, finally reaches the photoanode and gets absorbed by the dye molecules adsorbed on the oxide. In DSSCs, dye molecules adsorbed on the oxide play a role of ‘‘antenna’’ for photon capturing. Upon illumination, the exciton (electron-hole pairs) generated in the dye are immediately split, the photogenerated electrons then transfer from the dye molecules to the titania nanoparticle film and diffuse to the transparent conducting film of the collector electrode, which is connected to the external circuit. This optical absorption occurring in sensitizer dye molecules involves an electron transit process from the highest occupied molecular orbital (HOMO) to the lowest unoccupied molecular orbital (LUMO).[27] Within a cycle process, the oxidized dye molecules are reduced by the electrons in electrolyte and simultaneously, the oxidized triiodide molecules in the electrolyte are regenerated at the platinum coated counter electrode.[28] In this way the circuit is completed in order to generate an electric current. The unique feature of DSSCs is that the semiconductor is solely responsible for charge separation, and the photoelectrons are provided by the photosensitive dye working in concert with a third element of the cell, an electrolyte which is in contact with both the electrodes. This scheme effectively separates the two functions provided by silicon in a traditional p-n junction photovoltaic cell design. DSSCs offer advantages of being made from low cost materials and utilizing less complex equipment to manufacture. Besides this, low energy losses and lack of recombination make DSSCs workable under cloudy skies, unlike traditional designs which cease at some lower limit of illumination.[16]

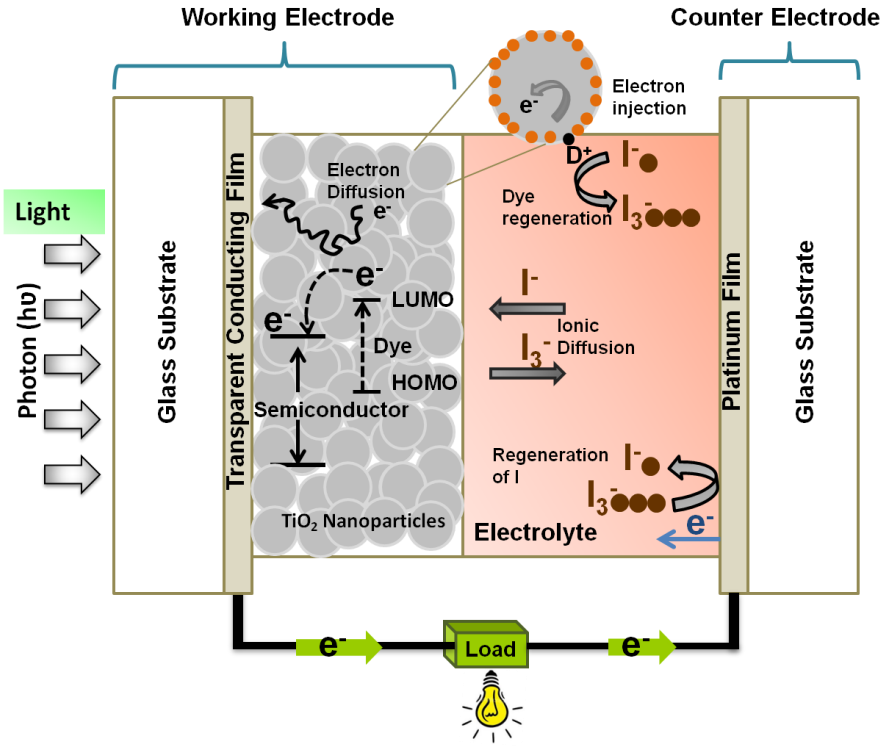

Photoinduced electronic processes:

1) $Dye + h\upsilon \rightarrow Dye^{+} + e^{-}$
2) $TiO_2 + e^{-} \rightarrow TiO_2^{-}$
3) $2Dye^{+} + 2I^{-} \rightarrow 2Dye + I_2$
4) $I_3^{-} + 2e^{-} \rightarrow 3I^{-}$

Fig. 1.4 Summary of the processes taking place during the regenerative cycle in the DSSC.

1.4.3. Advantages of dye sensitized solar cells

DSSC has great potential to become a successful third generation technology utilizing the nanoscale properties of the device. This technology will fulfill the expected prospective for solar energy conversion. This promising technology offers few interesting points such as:

- Low production and investment cost. Also, fabrication process is inexpensive[29]
- The manufacturing process is energy efficient resulting in shorter energy payback time (<1 year)[30]
- DSSCs perform relatively better than competitors in diffuse sunlight and under real outdoor conditions because when sensitized with a broad spectral dye like N3, the absorption spectrum of dye loaded TiO_2 overlaps with diffuse sunlight spectrum[26] Bifacial cells capture light from all angles[29]

- The performance of DSSCs is stable for a long period of time[26]. The N3 dye can show consistent performance over 10^7 to 10^8 cycles without getting decomposed[31] which will subject to a full lifetime of 10 to 20 years under full sunlight[32-33]
- Provides flexibility in materials of choices so better optimization of different components is possible. Opens up design opportunities, such as, transparency and multicolor options, building integration, consumer products, etc.[34]
- Novel nanoarchitectures like lightweight plastic and flexible fibers can be made to produce electricity from clothes, tents, awnings and window coverings[35-36]
- The materials used in DSSCs are non-toxic[30]

1.4.4. Dye (s) in dye sensitized solar cells

Accompanying with the development of DSSCs, organic dyes have been intensively studied with a focus on increasing the extinction coefficient and extending the optical absorption spectrum.[37-43]A variety of organic dyes used for DSCs can be found in literature, such as N3,[44] N719,[45] black dye,[46] K8,[43] K19,[47] CYC-B11,[48] and C101.[49] Some of them are already commercially available. Solar-to-electrical energy conversion efficiencies as high as 10-11% at AM 1.5 have been reported.[31,50-51] An ideal photo-sensitizer working under standard test conditions (STC), with corresponds to the air mass 1.5 (AM 1.5) spectrum with a total power of $1000W/m^2$, should act as a light-harvesting species. The sensitizer should absorb a wide range of the solar spectrum out to about 920 nm, show strong adsorption onto the semiconductor surface, and facilitate fast electron injection into the conduction band of the semiconductor also excited state energy level of the dye must be higher than the conduction band edge in order to allow electron injection. Furthermore, the dye LUMO should be energetically matched and strongly coupled to the semiconductor underneath.[52]

The theoretical value for a higher J_{sc} for a given dye and cell design can be determined by calculating the incident photon-to-current conversion efficiency (IPCE) which is given by:

$$IPCE(\lambda) = LHE(\lambda) \times \phi_{inj} \times \eta_e \qquad (1.8)$$

Where LHE is the light harvesting efficiency at a given wavelength, ϕ_{inj} is the electron injection efficiency and η_e is the absorbed photon to current conversion efficiency.[26]

$$\text{Quantitatively, IPCE } (\lambda) = \frac{\text{Jsc } (\lambda)}{\text{e } \phi\ (\lambda)} = 1240\ \frac{\text{Jsc } (\lambda)[\text{A cm}-2]}{\lambda\ [\text{nm}]\text{Pin } (\lambda)\ [\text{W cm}-2]} \qquad (1.9)$$

Where, *e* is the elementary charge. IPCE values provide practical information about the monochromatic quantum efficiencies of a solar cell.[53] More details about the IPCE phenomena will be provided in the later section of this chapter.

The best performance so far has been achieved by polypyridyl complexes of ruthenium and osmium referred to as (N3) having general structure ML_2X_2 where L stands for 2,2'-bipyridyl-4,4'-dicarboxylic acid ($dcbH_2$), M is Ru or Os and X represents a halide, cyanide or hiocyanate.[31,54] However, several dyes named as 'black dye' which is triisothiocyanato-(2,2':6',6"-terpyridyl-4,4',4"-tricarboxylato) ruthenium(II) tris(tetra-butylammonium),[46] organic dye named 2-cyanoacrylic acid-4-(bis-dimethyl fluoreneaniline) dithiophene (JK2)[55] have shown their best performances in DSSCs. Also multiple dye systems with different absorption maxima have been applied as sensitizer in order to achieve higher efficiency.[56]

1.4.5. Electrolyte (s) in dye sensitized solar cells

In DSSCs, the electrolytes are usually composed of I^-/I_3^- redox couple in organic solvents sealed between two electrodes. In order to be a perspective hole conductor, the electrolyte must have low optical absorption in the visible region of the solar spectrum, very good hole conductivity, low rate of evaporation and low rate of photo degradation. The liquid electrolyte in the cell was replaced by p-type semiconductor such as CuSCN immersed in ethanol electrolyte containing cyanine dye in order to avoid evaporation.[57] Several attempts have been made to improve the hole transport mechanism. For example, Matsumoto *et al.* have replaced liquid electrolytes with quasi-solidified polymer matrixes.[58] The quasi solid state polymer gel electrolytes have attracted much attention due to their high thermal stability, nonflammability, and negligible vapor pressure, good contact with both the electrodes and higher ionic conductivity.[59-60] However, the light to electricity conversion efficiency still remained lower than

that expected by using these gelators. This low efficiency is due to the high viscosity of the ionic liquids, which retards physical diffusion of I_3^- and I^-. This behavior is completely against the required criteria to have high light-to-electricity conversion efficiency in case of DSSCs. In order to overcome this difficulty, a new strategy for high rate of diffusion by giving a new path for the diffusion of the I_3^- and I^- was given by Yamanaka *et al.*[61] They used an ionic liquid crystal system (C_{12}MImI/I_2) with a smectic phase as an electrolyte for DSSCs that showed high short circuit current density and higher light to-electricity conversion efficiency. This result was due to the two dimensional electron conductive pathways given by the self assembled structure of the imidazolium polyiodide species among the redox mediators and increased the chances of exchange reactions occurring in the hole transporting mechanism.[61]

There are mainly two kinetic constraints for a successful redox shuttle. It must reduce the dye cation before the dye cation recombines with an electron in the photoanode, but should not allow the oxidized form of the shuttle to intercept an electron from the photoanode. The dual criteria of fast dye regeneration and slow interception place very challenging constraints on identifying effective redox shuttles. However, I_3^-/I^- has proven to be very effective in fulfilling the requirements of an effective redox shuttle to a great extent.[62] The uniquely good performance of I_3^-/I^- in DSSCs can be attributed to efficient dye regeneration combined with exceedingly slow electron transfer from TiO_2 to I_3^-. In addition, loss of electrons via interception by I_3^- is negligible (at short-circuit), allowing photo-injected electrons to be collected with near unity efficiency.[62]

Despite the excellent performance of I_3^-/I^- as a redox shuttle with N3 dye, the regeneration of dyes with I^- appears to be restricted to high driving-force reactions.[62] Furthermore, the mechanism of the reduction of dye cations by iodide is still unclear. Studies employing single crystal ZnO electrodes as a model system in contact with non-adsorbing, one-electron, outer-sphere redox couples such as, $[Co(t\text{-}Bu_2bpy)_3]^{3+/2+}$ were able to establish the dependence of the interfacial electron-transfer rate constant on driving force, reorganization energy, electrolyte composition and coupling.[63-66] Use of such non-adsorbing, one electron, outer-sphere redox shuttles in DSSCs, in conjunction with measurements with single crystal model systems, should allow for more complete understanding of interception and guide the design of future redox shuttles.

1.5. Titanium dioxide (TiO_2) in dye sensitized solar cells

Titanium dioxide TiO_2 is a wide band gap semiconductor implying a large gap between the valence band and conduction band, and with the Fermi level positioned in between this band gap. It is the most widely used material for the nanostructured semiconducting film in DSSCs because of its desirable optical and electronic properties. It is inexpensive, inert, non-toxic and available in abundance on earth.[67-68] The valence band of TiO_2 has predominantly O-2p character whereas the conduction band has predominantly Ti-3d character. TiO_2 occurs mainly in three crystalline forms: anatase, rutile, and brookite where the rutile phase is thermodynamically the most stable.[67] Both anatase and rutile have a tetragonal unit cell, whereas brookite has an orthorhombic unit cell.[69-70] The space groups of the three crystalline forms are: rutile-P42/mmm, anatase-I41/amd, and brookite-Pbca. The band gaps of both anatase and rutile are indirect, although there is also a direct forbidden transition near 3 eV in rutile. The band gap for TiO_2 in the anatase phase is 3.2 eV and in the rutile phase it is 3.0 eV.

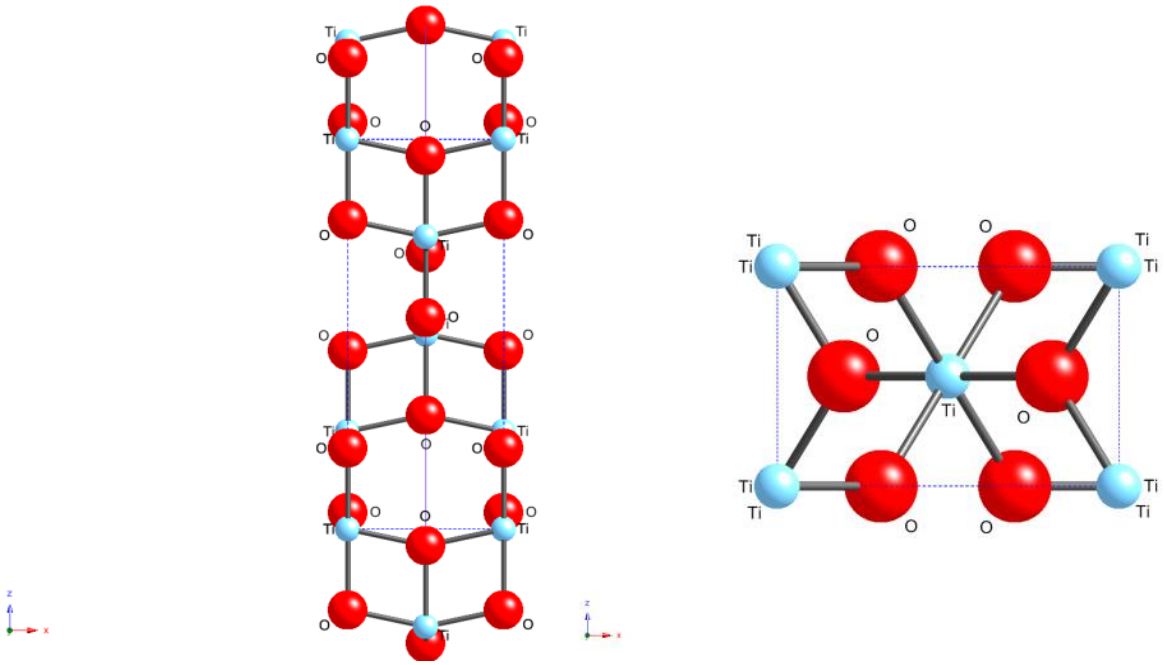

Fig.1.5 (a) TiO_2-anatase-b direction and (b) TiO_2-rutile-b direction

The nanostructured TiO_2 studied for DSSCs is dominated by the anatase phase, because of its large band gap and more negative conduction band potential result in higher photovoltage. The most common surfaces are the (101) followed by (100)/ (010) in approximately equal amount.[20,71] The position of the conduction band edge is dependent on the surface charge on the TiO_2. This property can be used to shift the position of the conduction band edge, and thereby the energy level matching and open circuit voltage.[20,72-74]Anatase TiO_2 does not absorb visible light.[75] Due to its smaller band gap, the rutile phase absorbs some blue light and it can absorb approximately 4% of the solar spectrum.[67,75] The anatase phase is photochemically more active than the rutile phase, probably due to its higher Fermi level energy and different arrangement of surface hydroxide groups. Therefore, the anatase phase is desirable for dye-sensitized solar cells.

1.6. Synthetic techniques

1.6.1. Sol-gel template synthesis

The sol-gel reaction mechanism involves first hydrolysis of a solution step where the metal cations are solvated by the water molecules to get a suspension of colloids (the sol) followed by a condensation step which is initiated by nucleophillic substitution (S_N) mechanism to polymerize the hydrolysis species to get the gel. The next step is to anneal the gel to obtain the desired material. The whole mechanism can be given by the equations (1.10-1.17) below:

$$\text{Hydrolysis: } Ti(OR)_4 + 4H_2O \xrightarrow{C_2H_5OH} Ti(OH)_4 + 4ROH, \text{ Where } R = C_3H_7 \quad (1.10)$$

The hydrolysis reaction has four possible steps:

$$(i)\ Ti(OR)_4 + H_2O \longrightarrow Ti(OR)_3(OH) + ROH \quad (1.11)$$

$$K_1 = [Ti(OR)_3(OH)][ROH]/[Ti(OR)_4][H_2O]$$

$$(ii)\ Ti(OR)_3(OH) + H_2O \longrightarrow Ti(OR)_2(OH)_2 + ROH \quad (1.12)$$

$$K_2 = [Ti(OR)_2(OH)_2][ROH]/[Ti(OR)_3(OH)][H_2O]$$

$$(iii)\ Ti(OR)_2(OH)_2 + H_2O \longrightarrow Ti(OR)(OH)_3 + ROH \quad (1.13)$$

$$K_3 = [Ti(OR)(OH)_3][ROH]/[Ti(OR)_2(OH)_2][H_2O]$$

$$(iv)\ Ti(OR)(OH)_3 + H_2O \longrightarrow Ti(OH)_4 + ROH \quad (1.14)$$

$$K_4 = [Ti(OH)_4][ROH] / [Ti(OR)(OH)_3][H_2O]$$

Where, K_1, K_2, K_3 and K_4 are equilibrium constants for the hydrolysis reaction.

Condensation: $Ti(OH)_4 \longrightarrow TiO_2(s) + 2H_2O$ (1.15)

The condensation reaction proceeds either through a water elimination reaction.

$Ti\text{-}OH + HO\text{-}Ti \longrightarrow Ti\text{-}O\text{-}Ti + H_2O$ (1.16)

or an alcohol elimination reaction.

$Ti\text{-}OR + HO\text{-}Ti \longrightarrow Ti\text{-}O\text{-}Ti + ROH$ (1.17)

A template approach using porous membranes often offers excellent size uniformity and flexibility in the diameter and length of the formed oxide nanotubes or fibrils on a nanometer scale as the templates contain cylindrical pores of uniform diameter. Furthermore, the approach allows varying the nanotube shell thickness by controlling the synthesis parameters. There are several types of membranes which have been used as templates for nanostructures synthesis. Most of the work has been done with the porous alumina (anodic aluminum oxide, AAO) membranes and 'track-etch' polymeric membranes made of polycarbonate (PC). Lakshmi *et al*. introduced sol–gel titania nanotubes using AAO membranes as sacrificial templates. In their experiments, the formation of oxide walls on the inner surfaces of pores was controlled by the exposure time of titanium isopropoxide precursors.[76-77] Michailowski *et al*. have synthesized highly arrayed TiO_2 nanotubes possessing a thin wall layer using a thermal decomposition process with titanium isopropoxide $Ti(OiPr)_4$.[78] In the solution- based processes, there undoubtedly exists a trade-off between the deposition of thin wall layers and the formation of continuous films, and this trade-off impedes precise control of the formation of wall layers. In addition to the monodispersity of oxide nanotubes, the ability to produce a thin as well as controllable wall layer of oxide nanotubes would allow for better applications using their electrical and optical properties. For instance, the optical properties of semiconductor oxide nanotubes could be sharply changed in one direction because of the quantum-size effect.[79-80] Furthermore, their electrical conductivity can be sensitively perturbed by accumulation or depletion of electrical carriers when additional molecules are adsorbed onto the surfaces of the thin oxide layers.[79]

1.6.2. Electrochemical processes

Electrochemical processes can be based upon charge (electron) transfer reactions between a solid metal and metal ions in the electrolyte. Electron reception by a metal ion (reduction) is deposition. On the other hand, electron release by a solid metal (oxidation) is etching. In most of electrochemical processes, vacuum conditions and high voltage bias are not necessary. Thus, the electrochemical process is advantageous in mass production and cost performance. Furthermore, electrochemical processes are capable of depositing and to etching various metal layers uniformly on large areas and also on surfaces of complicated structures. Electrochemical processing is classified into electrodeposition, electrochemical etching, electroless deposition and chemical etching. Electrodeposition has been applied to various fabrication processes for various micro/nano devices and systems. Here, we have explored the electrodeposition process in detail. Several representative electrodeposition processes are described in the literature. For instance, Au nanowire arrays using self-organized porous alumina templates,[81] Cu nanowire electrodeposition process is utilized to multi-level interconnection for ultra large scale integration (ULSI).[82] Electrodeposited magnetic films, such as NiFe, CoNiFe, are applied to thin film magnetic recording heads.[83] Furthermore, Ni electrodeposition is applied to the formation process of high aspect ratio structures.[84]

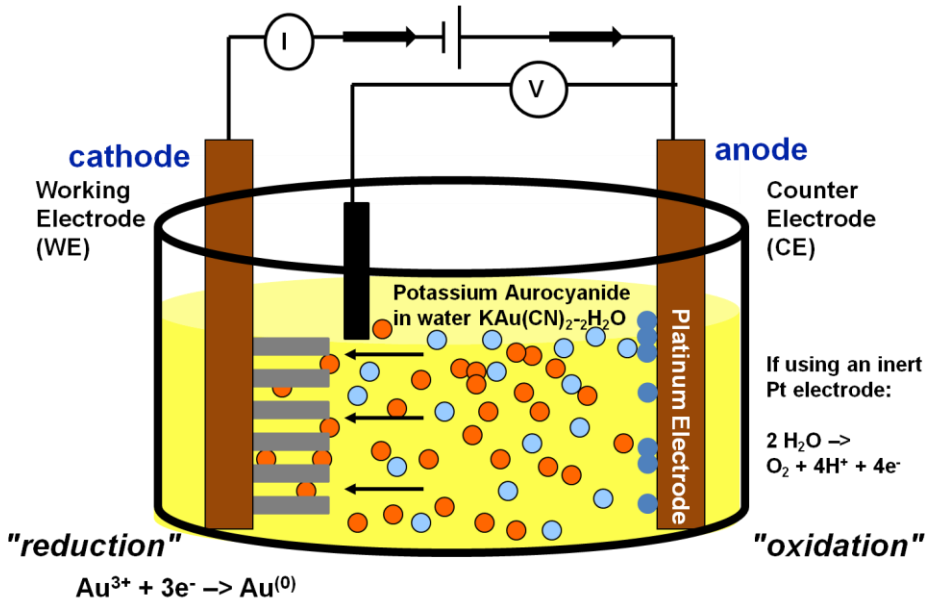

Fig.1.6 Schematic of electrodeposition bath

1.6.3. Fundamental theory of electrodeposition

The principle of electrodeposition is the reduction of a metal ion (M^{n+}) with electrons supplied from an external power source. The electron(s) are transferred to a metal ion through the metal electrode, where reduced metal atoms (M) deposit. When an electrode is immersed in an aqueous solution containing a metal ion, the electrode shows the equilibrium potential (E_e). Then, during the electrodeposition at current flow, the different potential (E_{dep}) is measured. The difference between E_e and E_{dep} is called overpotential (η).[85] The step flow of electrodeposition is basically consisting of diffusion of metal ion to the reaction site at working electrode and electron transfer from the counter electrode.

When the electron transfer step is slower than the diffusion step, electron transfer is the deposition-rate determining step, and the relationship between *(η)* and current density (*i*), which is corresponding to deposition-rate, is characterized by the Tafel equation as follows[86]

$$\eta = a + b \log |i| \qquad (1.18)$$

Where, *a* and *b* are constants. Therefore, in this case, electrodeposition rate is controllable by overpotential η.

On the other hand, when the diffusion step is the deposition-rate determining step, current density (*i*) is shown by the following equation:

$$i = nFD \frac{c}{\delta} \qquad (1.19)$$

where *n* is the number of electrons involved in the reaction, *F* is the Faraday constant, *D* is the diffusion coefficient, *c* is the bulk concentration of metal ion, and δ is the diffusion layer thickness.[87] In this case, electrodeposition rate is controllable by bulk concentration of metal ion and/or agitation, which will lead to reduce diffusion layer thickness. Furthermore, properties of the electrodeposited film, such as surface morphology, grain size, and crystalline state, are affected by various electrodeposition conditions, such as pretreatment (cleaning of the specimen), temperature, concentration of metal ion, agitation, kind of substrate, current density, additives into the electrolyte, etc.

1.6.4. Pulsed laser deposition (PLD)

Pulsed laser deposition (PLD) refers to the thin film deposition technique based on evaporation of material with a laser. Usually an excimer or Nd-YAG laser, producing an intense pulsed (repetition rate 0-100 Hz) laser beam in the UV range, is used. Typical wavelengths are 193 nm for ArF, 248 nm for KrF, 308 nm for XeCl excimer lasers, and 355 nm for Nd:YAG. Although for every material there exists a set of optimal parameters, in practice it is very hard to find this optimum since the parameters cannot be adjusted independently. For example, many parameters have been investigated for $YBa_2Cu_3O_7$ thin film deposition and the conclusions with respect to, among other things,[88] laser fluence,[89] spot size,[90] are expected to be applicable more generally.[88] It turns out that these characteristics of PLD greatly affect the growth of thin films.

1.6.4.1. Deposition conditions

Besides the deposition conditions, there are three important characteristics of PLD that distinguishes it from other thin film techniques: 1) the relative high energies of particles arriving at the substrate surface, 2) the relatively high deposition rates which can be achieved and 3) pulsed deposition. The species in the plasma plume can be divided into neutral and charged species, of which the latter have the highest kinetic energies (up to 250 eV). However, a very strong interaction of the ablated species with the ambient gas molecules has been observed.[91] Most of the energy is dispersed in a background gas through collisions with the cold gas molecules.

1.6.5. E-beam nanolithography (EBL)

Many light-based nanotechnology measurement and fabrication tools are limited by the wavelength of light. However, the smaller the wavelength of light, the higher the energy of the light, which can subsequently cause unwanted side effects. In addition, the resolution is limited by the wavelength, with smaller wavelengths giving better resolution. One way scientists get around these limitations is to use electrons instead of light. E-beam nanolithography (EBL) is such an approach. Basically, EBL technique consists of shooting a narrow, concentrated beam of electrons onto a resist coated substrate.[92] Electrons can induce the deposition of substances onto a

surface (additive), or etch away at the surface (subtractive). E-beam nanolithography is particularly important in micro and nano electronics, which require extremely precise placement of micro/nano sized circuit elements. E-beam nanolithography allows scientists to design and place elements at the smallest possible scale.[93] Also, electrons can be used to etch a "mask" whose patterns can be later transferred onto a substance using other techniques. However, with such precision, components can only be made very slowly and only one at a time, greatly increasing the time and cost and prohibiting mass commercial acceptance. Also, because electrons are charged particles, it is necessary to perform E-beam nanolithography inside a vacuum, further complicating the required equipment and processes.

Electron gun

The centerpiece behind EBL is the electron gun. The specifics of an electron gun could stretch pages, so it is sufficient to know that the electron gun is an apparatus that is able to "shoot" a beam of electrons in a specific direction. Two common E-beam emitters are lanthanum hexaboride crystal and a zirconium oxide coated tungsten needle. The emitter is first heated to produce and excite electrons on the surface. Then, when a high voltage is applied, the excited electrons accelerate towards a structure called the anode. By varying this voltage, the trajectory and the focus of the beam can be manipulated.

Electron optical column

The electron optical column is a system of lenses that, by a combination of electric and magnetic fields, has the ability to focus the electrons into a concentrated beam in a desired direction. Two parallel plates inside the column can be electrostatically charged to a precise degree; the resulting electric field is able to bend the beam in a desired direction.

Surface

After the beam is directed and concentrated by the optical column, it is ready to be focused on the surface. As with most lithography techniques, a substance called a photoresist covers the surface. However, E-beam photoresists are not as specific as other types. Technically, high energy electron bombardment will cause bond breakage in any polymer. When the beam hits the surface, either an additive or subtractive reaction takes place. An additive writing method uses the electrons to induce a deposition of a compound on the surface. Subtractive writing methods use

the E-beam to remove the sections of the resist and surface. This method is common in creating masks for other lithographic techniques such as UV lithography.

E-beam photoresists

Usually, the e-beam resists are high molecular-weight polymers dissolved in a liquid solvent. The polymer changes its structure when exposed to radiation, including electron radiation. Electron beam resists can be either positive or negative. After exposure to electrons, the positive resists are weakened by the scission of main- and side-chains and the exposed resists become more soluble in the developing solution. A solvent developer selectively washes away the weakened or lower molecular weight resist; thus, a positive tone pattern is formed in the resist film.[93] On the other hand, the negative resists are strengthened during exposure by a radiation-initiated cross-linking reaction and become less soluble in the developer. After the resists are developed, the pattern is transferred to the substrate through the lift-off process mentioned later.

Positive resists

Polymethyl methacrylate (PMMA) was one of the first resists developed for EBL and remains the most commonly used positive resist that has a moderate glass transition temperature of 114^{o}C. The PMMA comes in powder form and is dissolved in a solvent, such as anisole or chlorobenzene, of desired concentration. The resist liquid is dropped onto the substrate and then spun at high speed to form a thin coating. This is followed by soft bake processing at temperatures ranging from 130^{o}C to 170^{o}C with a hot plate or oven to bake out the casting solvent. The final resist thickness is determined by the PMMA concentration and by the spin speed. The typical developers used are 1:3 methyl isobutyl ketone: isopropanol (MIBK: IPA) for the highest contrast and 1:1 MIBK: IPA for the highest sensitivity.[94] The developed region is then removed by rinsing in pure IPA for 30 s. PMMA has extremely high resolution, and its ultimate resolution has been demonstrated to be less than 10 nm;[95] its major problems are its relatively poor sensitivity, poor dry etch resistance, and moderate thermal stability. Other important positive resists include PBS (polybutene-1-sulfone) and EBR-9 (a copolymer of trifluoroethyl a-chloroacrylate and tetrafluropropyl a-chloroacrylate) which have high sensitivity and ZEP (a copolymer of chloromethacrylate and methylstyrene) which has high-resolution. It is noted that the desired properties of a resist are high resolution and high sensitivity (high speed). Unfortunately, the resist that have higher sensitivity, including those mentioned here, usually have lower resolution, especially compared to PMMA.[96]

Negative resists

Negative resists tend to have less bias but they have problems with scum and swelling during development and bridging between features. Popular negative e-beam resists consist of the Shipley advanced lithography (SAL) product line, an epoxy copolymer of glycidyl methacrylate and ethylacrylate [P(GMA-EA)], also known as COP, and a partially chloromethylated polystyrene (CMS).[96]

Scanning methods

Raster scan

The e-beam is swept across the entire surface, pixel by pixel, with the beam being turned on and off according to the desired pattern. This method is easy to design and calibrate, however, because the beam is scanned across the entire surface, sparse patterns take the same amount of time to write as dense patterns, making this method inefficient for certain types of patterns.

Vector scan

The e-beam "jumps" from one patterned area to the next, skipping unwanted areas. This makes the vector scan much faster than the raster scan for sparse pattern writing. Adjustments to the beam can also be made relatively easily. However, it takes longer for the beam to settle, making it more difficult to maintain accurate placing for the beam.

Lift-off process

The lift-off process is a process of patterning a source material on the surface of a conducting substrate using a template such as photoresist. An inverse pattern is first created in the template, which is done by etching openings through the layer by using either electron beam lithography (EBL) or extreme ultraviolet lithography (EUVL) so that the target material can reach the surface of the substrate in those regions, where the final pattern is to be created. The target material is deposited over the whole area of the substrate, reaching the surface of the substrate in the etched regions as well as staying on top of the template in the regions where it was not previously etched. When the template is washed away with a lift-off solvent, the material on the top is also lifted-off and washed away together with the sacrificial layer below. For PMMA, acetone is the solvent typically used during lift-off. After the lift-off, the target material remains only in the regions where it had direct contact with the substrate. [92]

1.7. Characterization Techniques

Structural and phase characterization by electron microscopy

Electron microscopy is a very important tool for topographic and phase determination of various materials involving biology, medicine and material sciences. It has contributed greatly to the development of scientific theory. This wide spread use of electron microscopes is based on the fact that they permit the observation and characterization of materials on a nanometer (nm) to micrometer (μm) scale. This section presents the basic theory for electron microscopy (EMs), focusing on the two basic types of EMs; SEM, TEM.

1.7.1. Scanning electron microscopy (SEM)

The first Scanning Electron Microscope (SEM) debuted in 1942 with the first commercial instruments around 1965. Its late development was due to the electronics involved in "scanning" the beam of electrons across the sample.[92]

Operation

In SEM, a source of electrons is focused in vacuum into a fine probe that is raster scanned over the surface of the specimen. The electron beam passes through scan coils and objective lens that deflect horizontally and vertically so that the beam scans the surface of the sample (Figure 1.7). As the electrons penetrate the surface, a number of interactions occur that can result in the emission of electrons or photons from or through the surface. A reasonable fraction of the electrons emitted can be collected by appropriate detectors, and the output can be used to modulate the brightness of a cathode ray tube (CRT) whose x- and y- inputs are driven in synchronism with the x-y voltages rastering the electron beam. In this way an image is produced on the CRT; every point that the beam strikes on the sample is mapped directly onto a corresponding point on the screen[97]. As a result, the magnification system is simple and linear magnification is calculated by the equation:

$$M=L/l \quad (1) \qquad (1.20)$$

Where, L is the raster's length of the CRT monitor and l the raster's length on the surface of the sample.

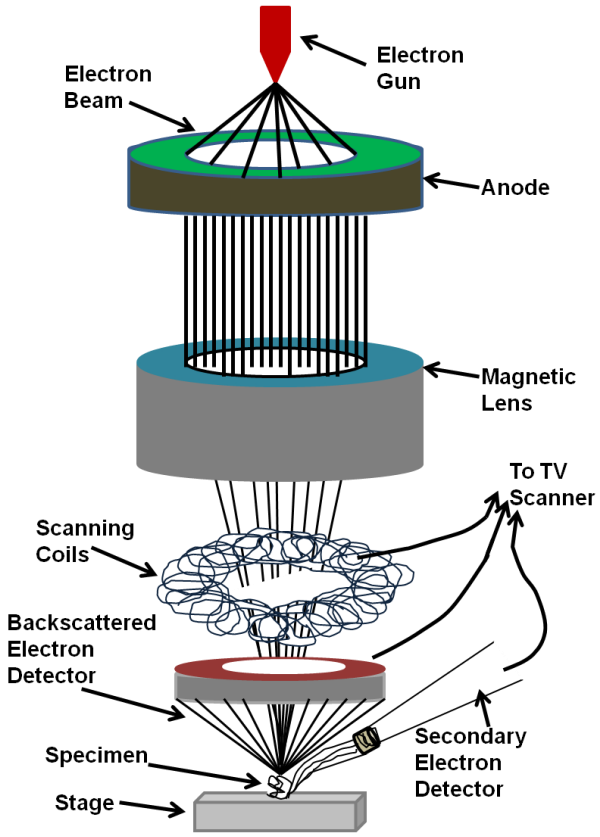

Fig.1.7 Ray Diagram for Working Principle of SEM

SEM works on a voltage between 2 to 50kV and its beam diameter that scans the specimen is 5nm-2µm. The principle images produced in SEM are of three types: secondary electron images, backscattered electron images and elemental X-ray maps. Secondary and backscattered electrons are conventionally separated according to their energies. When the energy of the emitted electron is less than about 50eV, it is referred as a secondary electron and backscattered electrons are considered to be the electrons that exit the specimen with an energy greater than 50eV.[98] Detectors of each type of electrons are placed in the microscope in proper positions to collect them.

Working principle of SEM

Secondary electrons

When a sample is bombarded with electrons, the strongest region of the electron energy spectrum is due to secondary electrons. The secondary electron yield depends on many factors, and is generally higher for high atomic number targets, and at higher angles of incidence. Secondary electrons are produced when an incident electron excites an electron in the sample and loses most of its energy in the process. The excited electron moves towards the surface of the sample undergoing elastic and inelastic collisions until it reaches the surface, where it can escape if it still has sufficient energy. Production of secondary electrons is very topography related. Due to their low energy (5eV) only secondaries that are very near the surface (<10 nm) can exit the sample and be examined. Any changes in topography in the sample that are larger than this sampling depth will change the yield of secondaries due to collection efficiencies. Collection of these electrons is aided by using a "collector" in conjunction with the secondary electron detector.

Backscattered electrons

Backscattered electrons consist of high-energy electrons originating in the electron beam, which are reflected or back-scattered out of the specimen interaction volume. The production of backscattered electrons varies directly with the specimen's atomic number. This differing production rates causes higher atomic number elements to appear brighter than lower atomic number elements. This interaction is utilized to differentiate parts of the specimen that have different average atomic number.

Advantages and disadvantages

Electrons in scanning electron microscopy penetrate into the sample within a small depth, so that it is suitable for surface topology, for every kind of samples (metals, ceramics, glass, dust, hair, teeth, bones, minerals, wood, paper, plastics, polymers, etc). It can also be used for chemical composition of the sample’s surface since the brightness of the image formed by backscattered electrons is increasing with the atomic number of the elements. This means that regions of the sample consisting of light elements (low atomic numbers) appear dark on the screen and heavy elements appear bright. Backscattered electrons are used to form diffraction images, called EBSD, that describe the crystallographic structure of the sample. In SEM, X-rays are collected to

contribute in energy dispersive X-ray analysis (EDX or EDS), which is used to determine the topography of the chemical composition of the sample. Consequently, SEM is only used for surface images and both resolution and crystallographic information are limited (because they're only referred to the surface). Other constraints are firstly that the samples must be conductive, so non-conductive materials are either Au, Ag or carbon-coated and secondly, that materials with atomic number smaller than carbon are not detected with SEM.[92]

1.7.2. Transmission electron microscopy (TEM)

Transmission Electron Microscopy (TEM) is a technique where an electron beam interacts and passes through a specimen. The electrons are emitted by a source and are focused and magnified by a system of magnetic lenses. The geometry of TEM is shown in Figure 1.8. The electron beam is confined by the two condenser lenses which also control the brightness of the beam, passes the condenser aperture and "hits" the sample surface. The electrons that are elastically scattered pass through the objective lens.[99] The objective lens forms the image display and the following apertures, the objective and selected area aperture are used to choose the elastically scattered electrons that will form the image of the microscope. Finally, the beam goes to the magnifying system that is consisted of three lenses, the first and second intermediate lenses which control the magnification of the image and the projector lens. The formed image is shown either on a fluorescent screen or in monitor or both and is printed on a photographic film.[99]

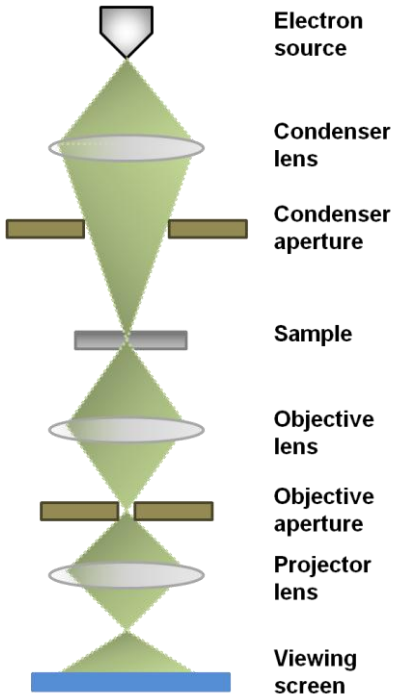

Fig.1.8 Ray Diagram for Working Principle of TEM

Operation

The operation of TEM requires an ultra high vacuum and a high voltage. Through a sequence of buttons and adjustments of focus and brightness of the beam, the settings of the microscope can be adjusted so that by shifting the sample holder the thin area of the sample can be located. Then by rotating the holder the sample begins to tilt. This is a way to observe as much areas as can be observed, so as to gather sufficient information on the specimen. Different types of images are obtained in TEM, using the proper apertures and the different types of electrons. As a result, diffraction patterns are shown because of the scattered electrons.[99] If the unscattered beam is selected, the bright field image is obtained. Dark field images are attained if diffracted beams are selected by the objective aperture. Also in TEM, analysis is done with EDX (energy dispersive X-ray), EELS (electron energy loss spectroscopy), EFTEM (energy filtered transmission electron microscopy), etc. Transmission microscopy allows actually seeing the specimen's structure and its atomic columns, thus compositional and crystallographic information is attained. However, TEM is a very expensive technique, expertise is needed and the sample preparation requires that very thin samples are achieved.

Important technological challenges

Transmission electron microscopes are capable of providing high resolution image and atomic structure of a crystal solving the problems in analyzing phase analysis, crystal structure of material. However, there are still some limitations which should be carefully evaluated and corrected before analyzing the structure. While collecting the image by TEM which is based on the ray optic theory, one can encounter with various lens defects such as astigmatism, chromatic aberration, and spherical aberration. These defects and aberrations may lead to wrong interpretation on the structure of the material. Astigmatism can be corrected by using stigmators, which are present in the form of auxiliary coil pairs and can be excited for astigmatism correction. Chromatic aberration can also be subsidized by suitable stabilization of high voltage by using ultra high vacuum. However, spherical aberration cannot be corrected easily. The spherical aberration always determines the resolution limit of a particular microscope. The spherical aberration is minimum for the microscope with high resolution limit. Today's transmission electron microscopes offer resolutions up to 0.1nm at 300kV and probe diameters as small as 0.34 nm. Thus, future trends include the use of ultrahigh vacuum TEM instruments for surface studies and computerized data acquisition for quantitative image analysis..[99]

1.7.3. Phase determination by powder X-ray diffraction (XRD)

The three-dimensional structure of non amorphous materials, such as minerals, is defined by regular, repeating planes of atoms that form a crystal lattice. When a focused X-ray beam interacts with these planes of atoms, part of the beam is transmitted, part is absorbed by the sample, part is refracted and scattered, and part is diffracted. Diffraction of an X-ray beam by a crystalline solid is analogous to diffraction of light by droplets of water, producing the familiar rainbow.[100] X-rays are diffracted by each mineral differently, depending on what atoms make up the crystal lattice and how these atoms are arranged. In powder X-ray diffractometry, X-rays are generated within a sealed tube that is under vacuum. A current is applied that heats a filament within the tube, the higher the current the greater the number of electrons emitted from the filament. This generation of electrons is analogous to the production of electrons in a television picture tube. A high voltage, typically 15-60 kilovolts, is applied within the tube. This high voltage accelerates the electrons, which then hit a target, commonly made of copper. When these

electrons hit the target, X-rays are produced. The wavelength of these X-rays is characteristic of that target. These X-rays are collimated and directed onto the sample, which has been ground to a fine powder (typically to produce particle sizes of less than 10 microns). A detector detects the X-ray signal; the signal is then processed either by a microprocessor or electronically, converting the signal to a count rate. Changing the angle between the X-ray source, the sample, and the detector at a controlled rate between preset limits is an X-ray scan.[100] When an X-ray beam hits a sample and is diffracted, we can measure the distances between the planes of the atoms that constitute the sample by applying Bragg's Law. i.e.

$$n\lambda = 2\,d \sin\theta \qquad (1.21)$$

where, the integer n is the order of the diffracted beam, λ is the wavelength of the incident X-ray beam, d is the distance between adjacent planes of atoms (the d-spacings), and θ is the angle of incidence of the X-ray beam. Since we know λ and we can measure θ, we can calculate the d-spacing. The geometry of an XRD unit is designed to accommodate this measurement. The characteristic set of d-spacings generated in a typical X-ray scan provides a unique "fingerprint" of the mineral or minerals present in the sample.[100] When properly interpreted, by comparison with standard reference patterns and measurements, this "fingerprint" allows for identification of the material.[100]

1.8. Photoelectrochemical techniques

1.8.1. Current-voltage measurements (I-V)

A current-voltage (I-V) curve shows the possible combinations of current and voltage output of a photovoltaic (PV) device.[101] A PV device, such as a solar module, produces its maximum current when there is no resistance in the circuit, i.e., when there is a short circuit between its positive and negative terminals. This maximum current is known as the short circuit current and is abbreviated I_{sc}. When the module is shorted, the voltage in the circuit is zero. Conversely, the maximum voltage occurs when there is a break in the circuit. This is called the open circuit voltage V_{oc}.[101] Under this condition the resistance is infinitely high and there is no current, since the circuit is incomplete.[13] These two extremes in load resistance, and the whole range of

conditions in between them, are depicted on the I-V curve. Current, expressed in amps, is on the (vertical) y-axis. Voltage/potential, in volts, is on the (horizontal) x-axis (Figure 1.9). The power available from a photovoltaic device at any point along the curve is just the product of current and voltage at that point and is expressed in watts. At the short circuit current point, the power output (P_{out}) is zero, since the voltage is zero. At the open circuit voltage point, the power output is also zero, but this time it is because the current is zero.[13]

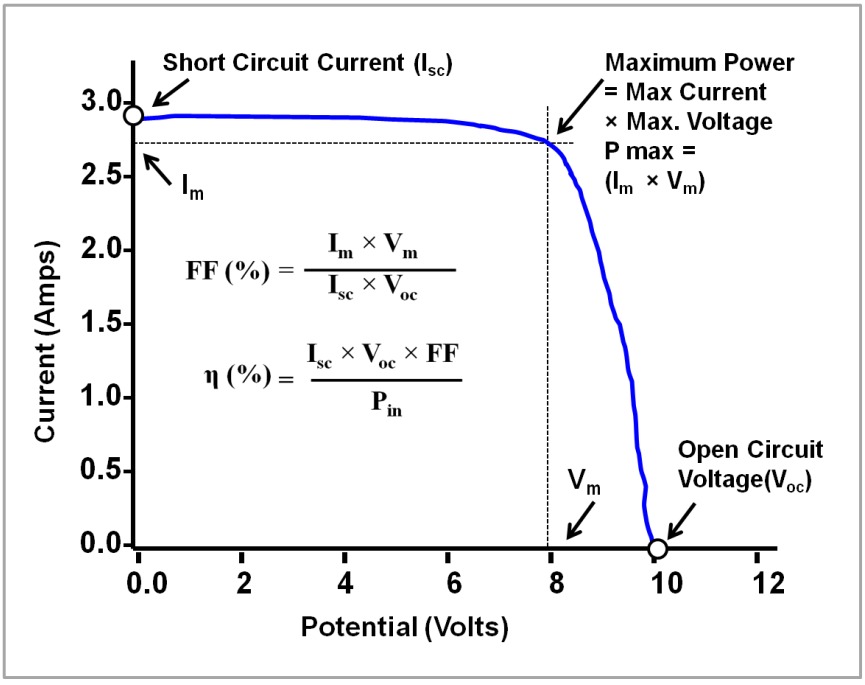

Fig.1.9 I-V Curve as function of light wavelength of solar cell tested under AM 1.5 conditions

Overall device photoconversion efficiency (η_{global}) is calculated from the I_{sc}, the V_{oc}, the fill factor (FF) and the intensity of the incident light i.e. input power (P_{in} = 100 mW/cm^2)

$$\eta = \frac{Pout}{Pin} = \frac{I_{sc} \times V_{OC} \times \mathrm{FF}}{Pin} \qquad (1.22)$$

The fill factor is calculated as

$$\mathrm{FF} = \frac{\mathrm{I_{max}} \times \mathrm{V_{max}}}{\mathrm{I_{sc}}\ \mathrm{V_{oc}}} \qquad (1.23)$$

Where, I_{max} and V_{max} are the coordinates of the power point curve maximum. The fill factor (FF) can be calculated by dividing the experimental power with theoretical power. The FF indicates the deviation of the I-V characteristic from a square like curve and is therefore dependent on series and shunt resistance. Figure 1.10 below illustrates the influence of increasing series resistance R_s and decreasing shunt resistance R_{sh} on the I-V curve characteristic. To obtain high fill factor, R_s has to be as small as possible, while R_{sh} needs to be as high as possible.[101]

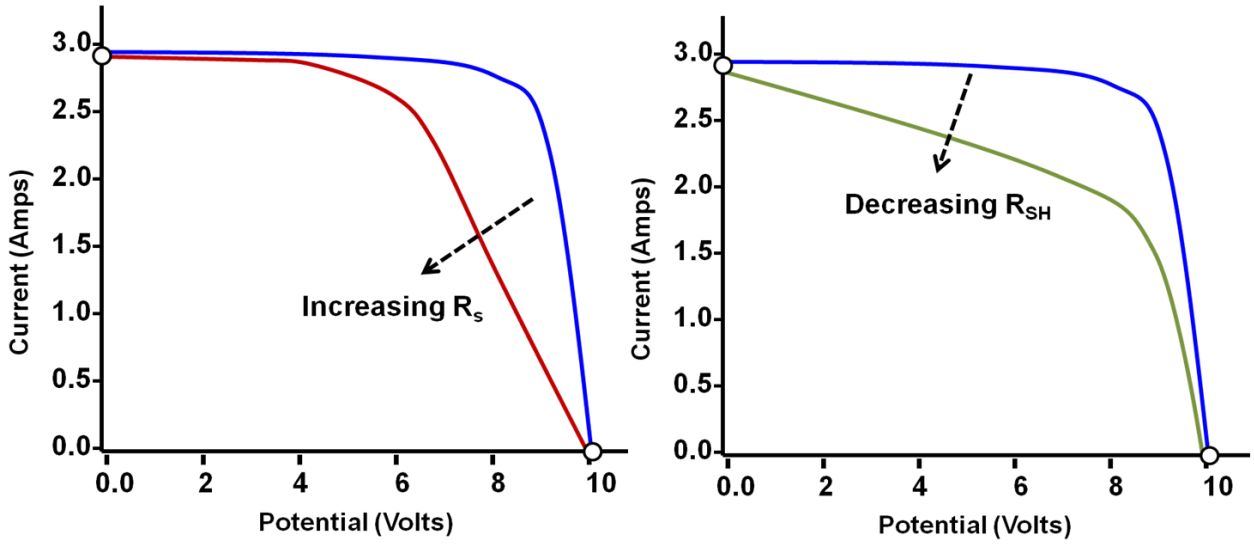

Fig 1.10 Effect of diverging R_s & R_{SH} from Ideality

J-V Characterization under standard condition

The power of the incident light, P_{in}, can be calculated from the emission spectrum of the light source. A standardized solar spectrum, *AM* 1.5, corresponding to an incident power of 1000 Wm^{-2} (=1.0 sun), is used to characterize solar cells. This spectrum corresponds approximately to a sunny mid-day in Stockholm, Sweden. "*AM*" is the abbreviation for air mass, so *AM* 1.5 implies that the light has to travel 1.5 times farther than direct incidence would before reaching ground level. The spectral distribution of the solar *AM* 1.5 emission spectrum has been given elsewhere.[20-21]

In the solar emission spectrum, it can be seen that a major fraction of the emitted photons have wavelengths greater than 400 nm, i.e. above the UV-region; therefore, as described earlier, using TiO_2 as a light absorbing material would yield low power conversion efficiencies. The sun does not always shine and on cloudy days, P_{in} can decrease to roughly 0.1 Sun outdoors, while indoors, using light sources such as lamps and diffuse light from windows, P_{in} can drop to only a few watts per square meter (~ 0.001 Sun). Considering that η, for a specific DSSC, is highly dependent on P_{in}, it is clear that efficient DSSCs must be designed with respect to these conditions. The short circuit current density J_{sc} of the cell is defined as I_{sc}/cm^2. The complete procedure for accurate determination of cell efficiencies according to standard reporting conditions (AM 1.5 Global, 1,000 W/m^2, 25°C) by J-V characterization is as follows[21]:

1) Determination of the spectral response of the test cell and the reference cell;
2) Calculation of the spectral mismatch factor, using spectral response, lamp spectrum and standard AM 1.5 global spectrum;
3) Adjustment of the lamp output to correct for spectral mismatch;
4) Measurement of the J-V characteristics; and
5) Calculation of the V_{oc}, J_{sc}, FF, and η.

1.8.2. Incident photon to current conversion efficiency (IPCE)

The IPCE measurement is performed in order to analyze the efficiency of a solar cell's conversion of light with a specific wavelength to photocurrent. This can be performed under

monochromatic light in which the photocurrent is measured for each wavelength. The measurement can also be performed under white bias illumination, with the monochromatic light being modulated. The latter will induce a modulation in the photocurrent, the amplitude of which can be detected by a lock-in amplifier. This is particularly important when the solar cell does not behave linearly with light intensity. The amplitude of the photocurrent signal is compared with the power of the monochromatic light in order to calculate the photocurrent conversion efficiency.[101-102] Generally, the IPCE can be expressed as the product of the absorption, η_{abs} , injection, η_{inj} , and collection efficiencies, η_{coll}.

$$IPCE = \eta_{abs}\, \eta_{inj}\, \eta_{coll} \qquad (1.24)$$

The incident photon to current conversion efficiency, IPCE, is defined by the ratio of the number of electrons generated in the solar cell to the number of photons incident on the photoactive surface of the device at a given wavelength. This key parameter can be expressed as,

$$IPCE\ (\lambda) = LHE\ (\lambda) \times \phi_{inj} \times \eta_{cell} \qquad (1.25)$$

Here, LHE(λ) is the light harvesting efficiency of photons of wavelength λ, ϕ_{inj} is the quantum yield for electron injection from the excited sensitizer into the conduction band of the semiconductor oxide, and η_{cell} the electron collection efficiency of the electrode. LHE (λ) is derived from the reciprocal absorption length α by,

$$LHE\ (\lambda) = 1 - 10^{\alpha d} \qquad (1.26)$$

Where, d is the thickness of the film and α is the absorption length which is given as,

$$\alpha = \sigma C \qquad (1.27)$$

Where, σ and C are the optical absorption cross-section and concentration of the sensitizer within the film, respectively. Values of σ for N3 and N719 dye are in the range of 1 to 2×10^7 cm^2/mol.

IPCE and photon flux measured in terms of current $I_p(\lambda)$ can be calculated by the following two simplified expressions :

$$I_p(\lambda) = \frac{I_S(\lambda) \times P_D(\lambda)}{P_L(\lambda)} \qquad (1.28)$$

$$\text{IPCE}(\%) = \frac{1240 \times I_S(\lambda)}{P_L(\lambda) \times \lambda \times 10} \qquad (1.29)$$

Where, $I_s(\lambda)$ is simple photocurrent in $\mu A/cm^2$, $P_D(\lambda)$ is direct AM 1.5 solar irradiance in $mW/cm^2/nm$, and $P_L(\lambda)$ the light intensity in mW/cm^2 (light from xenon lamp after passing through direct AM 1.5 filter) observed at wavelength λ. $I_p(\lambda)$ units are $\mu A/cm^2/nm$, with IPCE measured in percentage.[101]

1.8.3. Electrochemical impedance spectroscopy (EIS)

EIS stands for electrochemical impedance spectroscopy, and it has successfully been used to analyze processes in DSSC.[103-105] The details of this procedure and how it was utilized to study the kinetics of competition between various processes in DSSCs has been described in Chapter 5 of this dissertation. EIS involves the application of a potential sine waveform and recording the electrical current response. Upon the perturbation of the potential, charge carriers move in the material of the solar cell and charge transfer processes occur. When the frequency response from each process is separable, the effect from each process on the performance of the cell can be quantified. The model used to characterize the impedance data is normally described with equivalent circuits or differential equations. Impedance measurements on the DSC are performed in order to analyze the electrical properties, such as the charge transfer at the counter electrode with the redox electrolyte, the recombination reaction at the semiconductor-electrolyte interface, the transport of electrons through the semiconductor, the series resistance of the conducting glass substrate and the diffusion of redox species between the working and the counter electrodes. It is of great importance to quantify all of these processes in order to understand their impact on the solar cell conversion efficiency. The counter electrode, for example, can have an impact on the short circuit current that is due to poor regeneration.[106] The study of ionic liquids can reveal the impact on the J-V curve that is due to the slow ionic diffusion.[104] With impedance, it is possible to

study the band shift, transport and recombination processes of charge carriers in the semiconductor with different electrolytes.[103] Impedance can be compared for different semiconductors, such as ZnO.[107] The impedance measurement can be performed in the dark and in the light, with and without the presence of the dye. The working and counter electrodes of the solar cell can also be analyzed separately in a three-electrode setup.[108] The manner in which the method is used can provide a very flexible solution for the analysis of the solar cell. One drawback is that the time constants of the processes can coincide and so they cannot be separated. Because the time constants for the various processes change with applied potential and illumination, it is not possible to separate all the elements as a function of the applied potential and illumination intensity. There is a certain potential window within which each process can be seen for a given light intensity. Overall, it can be said that the total impedance of the system is directly correlated to the J-V measurement. If each process and its contribution to the total impedance can be separated, the effect that each component has on the J-V curve, and on DSSCs photovoltaic performance, can be clarified.

1.9. Scope of this research

1.9.1. Charge transport in conventional DSSCs

There are several processes that can affect and limit the performance of the DSSC. The absorption of light is the first step. In this, the dye layer is to absorb as many photons as possible from the solar spectrum, with a given absorption spectrum of the dye; this is related to the absorption efficiency. The absorption efficiency is defined by the extinction coefficient, the concentration of the dye and the thickness of the film. The second step is an efficient electron injection before the excited dye relaxes to its ground state or recombines with holes in the semiconductor or the redox couple. The injection efficiency is given by the driving force in free energy and the orbital overlap between the donor state of the dye and the acceptor state of the TiO_2 surface. The dye is oxidized after the electron injection and a charge separation is achieved. This results in a potential difference. In order for the dye to be able to absorb further photons and excite another electron, the initial reduced state of the dye molecule has to be regenerated. A limitation in the rate of regeneration, which would increase recombination reactions and therefore decrease the photocurrent, can be caused by several factors, such as the slow diffusion of redox

species, the kinetic processes at the Pt counter electrode and the regeneration kinetics from the redox species. After the injection of electrons into the semiconductor film, the electrons need to be collected efficiently at the conducting glass. In this process, there is a competition between the transport of the charge carriers to the TCO and the recombination of electrons to the electrolyte. The conduction band electrons are mobile and can be trapped in the semiconductor material due to defects or impurities. In the trapping model, there is an exchange of electrons between the conduction band level and the traps. The assumption is normally that trapped electrons cannot recombine with the electrolyte redox species and will therefore neither decrease nor increase the cell efficiency. The efficiency of collecting electrons at the TCO contact is called the charge-collection efficiency, which is related to the diffusion coefficient D and the electron lifetime τ_e. A poor charge collection efficiency limits the photocurrent from the DSSC. To summarize, there are processes in the DSSC with different time constants,[6] see figure 1.11. These processes compete and together have an impact on the overall efficiency of the cell. There are several processes occurring in the DSSC which are required for the solar cell to operate. These processes have a certain level of efficiency. The desired processes need an electrochemical potential difference in order to drive the photocurrent.

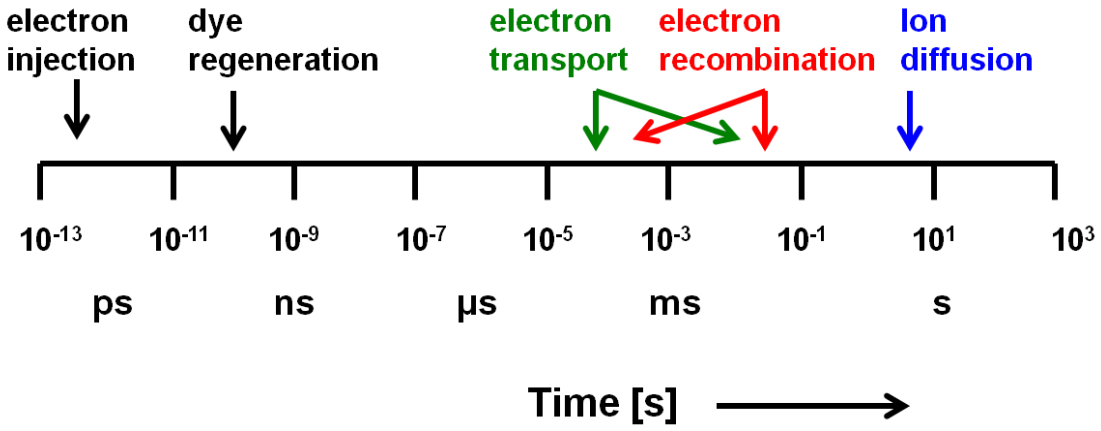

Fig. 1.11 The dynamics of the processes in DSSC. The only process that needs to slow down is the electron recombination in order to increase the performance of DSSC[6]

1.9.2. Electron transport processes in 1D nanostructure based DSSCs

The working electrodes in typical DSSCs consist of a 10 μm thick film comprised of a three-dimensional network of interconnected nanocrystalline semiconductor nanoparticles, typically 15 to 20 nm in diameter.[26] The large surface area associated with such films enables efficient light harvesting that in turn maximizes the amount of photogenerated charge. However, the structural disorder at the contact between two crystalline nanoparticles leads to enhanced scattering of free electrons, thus reducing electron mobility.[109] From the light intensity dependence of the electron diffusion coefficient in randomly packed TiO_2 nanoparticle films, it has been inferred that transport is limited by the residence time of electrons in traps[110-112] and the morphology associated with both the particle network[111,113-114] and the interparticle contact area.[115] Electron transport is a limiting factor in the performance of these nanoporous nanocrystalline electrodes, hindering the progress in achieving higher efficiencies.

The slow percolation of electrons through a random polycrystalline network and the poor absorption of low energy photons by available dyes are two of the major factors limiting the further improvement in the photoconversion efficiencies achievable using nanocrystalline DSSC.[116] A desirable film morphology would have the mesoporous channels aligned parallel to each other, vertically oriented with respect to the TCO glass current collector. The arrangement of the highly ordered TiO_2 nanotube arrays perpendicular to the surface permits direct charge transfer along the length of the nanotubes from the solution to the conductive substrate, thereby reducing the losses incurred by charge-hopping across nanoparticle grain boundaries.[117] Easier access to the nanotube-array surface, as well as better control of the interface makes this morphology desirable for DSSCs.[118-119] The enhancement in charge transport allows for improved light harvesting as thicker films can be used to increase the optical density, thus improving the absorption of low energy photons in the red and infrared regions without losing the additionally harvested charge carriers to recombination.[116]

1.9.3. Importance of 3D metal-metal oxide nanocomposites in advanced DSSCs

Many attempts have been made to improve the original DSSC design and circumvent its inherent limitations, with vertically aligned nanotube[120-123] or nanowire[116,124-125] arrays, which

provide the electrons with a direct, uninterrupted route to the anode. Even though this variation is expected to improve the performance, the efficiency of the modified DSSC typically remains in the 1–5% range. Many explanations have been proposed for why the above modifications have failed to improve the performance, including an insufficiently large surface area for dye adsorption compared to the nanoparticle film,[121,124] air trapped inside the nanotubes,[122] and large series resistance between the nanostructure and the electrodes[120-121]. A detailed analysis of the modified structures within the new designs is therefore desired, and critical analysis is inevitable in order to elucidate the failure mechanisms and quantify their effects.

As mentioned previously, in equation 1.22, in DSSCs the conversion efficiency is defined as the ratio of its electric power output to the incoming light intensity that strikes the cell.

Where, J_{sc} is the short-circuit current density, V_{oc} is the open circuit voltage, P_{in} is the incident solar intensity and FF is the fill factor.

According to Sodergren *et al.*,[126] the current density, J_{sc}, is given by the equation,

$$J_{sc} = qI_o(1- \eta_{inj} e^{-\alpha d}) - q D_o n_c^o d/L_n^2 (e^{qU/K_B T}-1) \qquad (1.30)$$

In equation (1.30) the first term represents the light generated current determined from the amount of light absorbed (I_o) and injection efficiency (η_{inj}), while the second term corresponds to dark current associated with transfer of electrons from TiO_2 to I_3^-. That means dark current needs to be small in order for J_{sc} to be high, eventually leading to high power conversion efficiency. L_n in the second term corresponds to diffusion length of electrons in TiO_2 and d corresponds to thickness of the film. L_n is thus given by the equation:

$$L_n = (D\zeta)^{1/2} \qquad (1.31)$$

Where, D is the diffusion coefficient and ζ is the lifetime of the electron. L_n relative to the thickness of the oxide film, d which should be

$$L_n/d >> 1 \text{ and } d > \alpha^{-1} \qquad (1.32)$$

Where, α is the wavelength absorption coefficient of the sensitized film.

Therefore, quantitative collection of photogenerated charge carriers (electrons) can be achieved when L_n is greater than the thickness of the film (d) from equation (1.32). The efficiency of the cell depends on several kinds of charge dynamics at the nanoscale level, such as the way the electrons move across the dye-photoanode interface, dye-anion interfaces and the way charges move through the dye. However, high conversion efficiencies are not easy to achieve, and the theoretical efficiency of 31%[2,16] is far more difficult.

In order to achieve this goal, we propose a novel method, which brings a modified DSSC in which the photoanode is made up of an interesting 3D nanoarchitecture of metal core and metal oxide shell. This novel nanostructure improved the device performance which was subjected to a series of systematic, controlled, and comparative studies in three different approaches. Core–shell nanowires of gold/nickel coated with anatase TiO_2 (Au/Ni-TiO_2) will be the subject of this study. The higher conductive metal core allows the electrons to be transported easily through it, instead of the lower-conducting TiO_2 shell, improving charge transport and decreasing recombination. Additionally, this structure offers an enhanced surface area for dye adsorption compared to traditional nanowires (NWs) due to the rough TiO_2 surface at the same time, taking care of recombination losses due to a thinner TiO_2 shell.

Another important point to consider behind this huge improvement in our Au-TiO_2 core-shell nanowire device performance is the interaction between light and metal nanowires that has attracted much attention in literature.[127-130] The metal nanowires are of considerable interest to nano electronics and future super large-scale integration circuits because of their potential use as interconnects, sensors, or integral device components. The electrical properties of metal nanowires, such as resistivity, failure current density, and Joule heating effect, are regarded as essential factors to evaluate metal nanowires for future applications. Scattering of surface plasmon polaritons (SPPs) on a nanostructured metal film has drawn particular attention since the early days.[131] The key issue for nanotechnology is how significantly this increased scattering affects the electrical properties of single nanowire. The metal gold, as a universal noble metal, is a suitable material to study surface plasmon resonances (SPR) properties which is the collective oscillation of the free conduction electrons at the surface driven by an external electromagnetic field of incident light. Gold has excellent electrical transport properties, because of its prominent confinement in the charge carriers and stabilization in physical and chemical properties. The effects have been proved through its application to nonlinear optics,[132] surface enhanced Raman scattering,[133] and plasmonics.[134] These nanowire systems strongly absorb incident light at specific

frequencies. Although the optical properties of metal spheres have already been described by Mie's theory in 1908,[135] the relationship between the nanowires' geometry and their nonlinear optical property has not been fully investigated.[136-138] A thorough knowledge and critical explanation of the above new nanoarchitectures is still required in order to address the mechanisms and their behavior as advanced 3D photoanode material in these third generation dye sensitized solar cells.

1.10. References

(1) Lewis, N. S. *Inorg. Chem.* **2005**, *44*, 6900.
(2) Lewis, N. S.; Nocera, D. G. *Proceedings of the National Academy of Sciences of the United States of America* **2006**, *103*, 15729.
(3) Alley, R. B., T.; Bindoff, N. L.; Chen, Z.; Chidthaisong,; A.; Friedlingstein, P. G., J.; Hegerl, G.; Heimann, M.;; Hewitson, B. H., B.; Joos, F.; Jouzel, J.; Kattsov, V.;; Lohmann, U. M., M.; Matsumo, T.; Molina, M.; Nicholls,; N.; Overpeck, J. Q., D.; Raga, G.; Ramaswamy, V.; Ren, J.;; Rusticucci, M. S., S.; Somerville, R.; Stocker, T. F.;; Stott, P. S., R. J.; Whetton, P.; Wood, R. A.; Wratt, D. **2007**.
(4) Oreskes, N. *Science* **2004**, *306*, 1686.
(5) Grätzel, M. *Nature* **2001**, *414*, 338.
(6) Grätzel, M. *Inorg. Chem.* **2005**, *44*, 6841.
(7) Becquerel, A. E. *Comptes Rendus des Séances Hebdomadaires* **1839**, *9*, 561.
(8) Fritts, C. E. *American J. of Science* **1883**, *26*, 465.
(9) Einstein, A. *Annalen der Physik* **1905**, *17*, 06.
(10) Ohl, R. S. *Bell, Ed. US* **1941**, *2402622*.
(11) Ohl, R. S. *Bell, Ed. US* **1941**, *2443542*.
(12) Chapin, D. M., C. S. Fuller, and G. L. Pearson, *Journal of Applied Physics* **1954**, *25*, 676.
(13) Moller H. Joachim *Artech House, INC.Norwood* **1993.**, 343 pages.
(14) Green, M. A. *Energy Policy* **2000**, *28*, 989.
(15) Martin A. Green, K. E. Y. H. W. W. *Progress in Photovoltaics: Research and Applications* **2008**, *16*, 435.
(16) Grätzel, M. *Philos. Trans. R. Soc. Lond. Ser. A Math. Phys. Eng. Sci. - Philosophical transactions of the Royal Society of London. Series A Mathematical, Physical and Engineering Sciences* **2007**, *365*, 1853.
(17) Shockley, W.; Queisser, H. J. *J. Appl. Phys.* **1961**, *32*, 510.
(18) Green, M. A. *Springer-Verlag: Berlin* **2003**, *Heidelberg*.
(19) Green, M. A. *Physica E* **2002**, *14*, 65.
(20) Memming, R. *Semiconductor Electrochemistry, Wiley-Vch*, **2001**.
(21) Sze, S. M. *Physics of Semiconductor Devices, John Wiley & Sons: New York* **1981**.
(22) Bard, A. J. F., Larry R. *Electrochemical Methods: Fundamentals and Applications, John Wiley & Sons, Inc.*, **1980**.
(23) Zistler, M.; Wachter, P.; Wasserscheid, P.; Gerhard, D.; Hinsch, A.; Sastrawan, R.; Gores, H. J. *Electrochimica Acta* **2006**, *52*, 161.

(24) Paulsson, H.; Berggrund, M.; Svantesson, E.; Hagfeldt, A.; Kloo, L. *Solar Energy Materials and Solar Cells* **2004**, *82*, 345.
(25) Moser, J. *Monatsch. Chem.* **1987**, *8*, 373.
(26) Oregan, B.; Grätzel, M. *Nature* **1991**, *353*, 737.
(27) Hagfeldt, A.; Grätzel, M. *Accounts of Chemical Research* **2000**, *33*, 269.
(28) A. Hauch; A. Georg *Electrochim. Acta* **2001**, *46*, 3457.
(29) *http://www.sony.net/Products/SC-HP/cx_news/vol56/sideview1.html*.
(30) McConnell, R. D. *Renewable and Sustainable Energy Reviews* **2002**, *6*, 273.
(31) Nazeeruddin, M. K.; Kay, A.; Rodicio, I.; Humphrybaker, R.; Muller, E.; Liska, P.; Vlachopoulos, N.; Gratzel, M. *J. Am. Chem. Soc.* **1993**, *115*, 6382.
(32) Grätzel, M. *Progress in Photovoltaics* **2000**, *8*, 171.
(33) Durrant, J. R.; Nelson, J.; Klug, D. R. *Materials Science and Technology* **2000**, *16*, 1345.
(34) Keis, K.; Bauer, C.; Boschloo, G.; Hagfeldt, A.; Westermark, K.; Rensmo, H.; Siegbahn, H. *Journal of Photochemistry and Photobiology a-Chemistry* **2002**, *148*, 57.
(35) Chittibabu., K.; Eckert., R.; Gaudiana., R.; Montello., L. L. A.; E Montello; and; P. Wormer *USA Patent No. WO2003065471*. **2000**.
(36) *Online resource: www. Konarka.com/products.*
(37) N. Robertson *Angew. Chem. Int. Edit* **2006**, *45*, 2338.
(38) L. Schmidt-Mende; U. Bach; R. Humphry-Baker; T. Horiuchi; H. Miura; S. Ito; S. Uchida; Grätzel, M. *Adv. Mater* **2005**, *17*, 813.
(39) D.B. Kuang; S. Ito; B. Wenger; C. Klein; J.E. Moser; R. Humphry-Baker; S.M. Zakeeruddin; M. Grätzel *JACS* **2006**, *128*, 4146.
(40) D. Hagberg; J. Yum; H. Lee; F. De Angelis; T. Marinado; K. Karlsson; R. Humphry-Baker; L. Sun; A. Hagfeldt; M. Grätzel *JACS* **2008**, *130*, 6259.
(41) M. Nazeeruddin; P. Pechy; T. Renouard; S. Zakeeruddin; R. Humphry-Baker; P. Comte; P. Liska; E. Costa; V. Shklover; L. Spiccia *J. Am. Chem. Soc* **2001**, *123*, 1613.
(42) C. Chen; S. Wu; C. Wu; J. Chen; K. Ho *Angew. Chem.* **2006**, *118*, 5954.
(43) C. Klein; M. Nazeeruddin; P. Liska; D. Di Censo; N. Hirata; E. Palomares; J. Durrant; M. Grätzel; . *Inorg. Chem* **2005**, *44*, 178—180.
(44) M.K. Nazeeruddin; A. Kay, I. R.; R. Humphrybaker; E.Muller; P. Liska; N. Vlachopoulos; M. Grätzel *JACS* **1993**, *115*, 6382—6390.
(45) M.K. Nazeeruddin; S.M. Zakeeruddin; R. Humphry-Baker; M. Jirousek; P. Liska; N. Vlachopoulos; V. Shklover; C.H. Fischer; M. Grätzel *Inorg. Chem* **1999**, *38*, 6298—6305.
(46) Nazeeruddin, M. K.; Pechy, P.; Gratzel, M. *Chemical Communications* **1997**, 1705.
(47) P. Wang; C. Klein; R. Humphry-Baker; S. Zakeeruddin; M. Grätzel *J. Am. Chem. Soc* **2005**, *127*, 808.
(48) C.Y. Chen; M.K.Wang; J.Y. Li; N. Pootrakulchote; L. Alibabaei; C.H. Ngoc-le; J.D. Decoppet; J.H. Tsai; C. Grätzel; C.G. Wu; S.M. Zakeeruddin; M. Grätzel *ACS Nano* **2009**, *3*, 3103.
(49) F. Gao; Y. Wang; D. Shi; J. Zhang; M.K. Wang; X.Y. Jing; R. Humphry-Baker; P. Wang; S.M. Zakeeruddin; M. Grätzel *JACS* **2008**, *130*, 10720.
(50) Barbe, C. J.; Arendse, F.; Comte, P.; Jirousek, M.; Lenzmann, F.; Shklover, V.; Grätzel, M. *Journal of the American Ceramic Society* **1997**, *80*, 3157.
(51) Green, M. A. E., K.; Bucher, K.; King, D. L.; Igari, S. *Prog. PhotoVolt. Res. Appl.* **1998**, *6*, 35.
(52) Grätzel, M. *Journal of Photochemistry and Photobiology C-Photochemistry Reviews* **2003**, *4*, 145.

(53) Hagfeldt, A.; Boschloo, G.; Sun, L. C.; Kloo, L.; Pettersson, H. *Chem. Rev.* **2010**, *110*, 6595.
(54) Amadelli, R.; Argazzi, R.; Bignozzi, C. A.; Scandola, F. *J. Am. Chem. Soc.* **1990**, *112*, 7099.
(55) Chen, P.; Yum, J. H.; De Angelis, F.; Mosconi, E.; Fantacci, S.; Moon, S. J.; Baker, R. H.; Ko, J.; Nazeeruddin, M. K.; Gratzel, M. *Nano Letters* **2009**, *9*, 2487.
(56) Chen, Y. S.; Zeng, Z. H.; Li, C.; Wang, W. B.; Wang, X. S.; Zhang, B. W. *New Journal of Chemistry* **2005**, *29*, 773.
(57) Oregan, B.; Schwartz, D. T. *Chemistry of Materials* **1995**, *7*, 1349.
(58) Matsumoto, M.; Wada, Y.; Kitamura, T.; Shigaki, K.; Inoue, T.; Ikeda, M.; Yanagida, S. *Bulletin of the Chemical Society of Japan* **2001**, *74*, 387.
(59) Kubo, W.; Murakoshi, K.; Kitamura, T.; Yoshida, S.; Haruki, M.; Hanabusa, K.; Shirai, H.; Wada, Y.; Yanagida, S. *Journal of Physical Chemistry B* **2001**, *105*, 12809.
(60) Priya, A. R. S.; Subramania, A.; Jung, Y. S.; Kim, K. J. *Langmuir* **2008**, *24*, 9816.
(61) Yamanaka, N.; Kawano, R.; Kubo, W.; Masaki, N.; Kitamura, T.; Wada, Y.; Watanabe, M.; Yanagida, S. *Journal of Physical Chemistry B* **2007**, *111*, 4763.
(62) Clifford, J. N.; Palomares, E.; Nazeeruddin, M. K.; Gratzel, M.; Durrant, J. R. *J. Phys. Chem. C* **2007**, *111*, 6561.
(63) Hamann, T. W.; Brunschwig, B. S.; Lewis, N. S. *Journal of Physical Chemistry B* **2006**, *110*, 25514.
(64) Hamann, T. W.; Gstrein, F.; Brunschwig, B. S.; Lewis, N. S. *J. Am. Chem. Soc.* **2005**, *127*, 13949.
(65) Hamann, T. W.; Gstrein, F.; Brunschwig, B. S.; Lewis, N. S. *J. Am. Chem. Soc.* **2005**, *127*, 7815.
(66) Hamann, T. W.; Gstrein, F.; Brunschwig, B. S.; Lewis, N. S. *Chem. Phys.* **2006**, *326*, 15.
(67) Kalyanasundaram, K.; Gratzel, M. *Coordination Chemistry Reviews* **1998**, *177*, 347.
(68) Gratzel, M. *Journal of Sol-Gel Science and Technology* **2001**, *22*, 7.
(69) Hu, Y.; Tsai, H. L.; Huang, C. L. *Journal of the European Ceramic Society* **2003**, *23*, 691.
(70) Mahshid, S.; Askari, M.; Ghamsari, M. S. *International Journal of Nanotechnology* **2009**, *6*, 961.
(71) Vittadini, A.; Selloni, A.; Rotzinger, F. P.; Gratzel, M. *Phys. Rev. Lett.* **1998**, *81*, 2954.
(72) Boschloo, G.; Haggman, L.; Hagfeldt, A. *Journal of Physical Chemistry B* **2006**, *110*, 13144.
(73) Furube, A.; Katoh, R.; Hara, K.; Sato, T.; Murata, S.; Arakawa, H.; Tachiya, M. *Journal of Physical Chemistry B* **2005**, *109*, 16406.
(74) Yu, S.; Ahmadi, S.; Sun, C. H.; Palmgren, P.; Hennies, F.; Zuleta, M.; Gothelid, M. *J. Phys. Chem. C* **2010**, *114*, 2315.
(75) Li, Y. X.; Hagen, J.; Schaffrath, W.; Otschik, P.; Haarer, D. *Solar Energy Materials and Solar Cells* **1999**, *56*, 167.
(76) Lakshmi, B. B.; Dorhout, P. K.; Martin, C. R. *Chemistry of Materials* **1997**, *9*, 857.
(77) Lakshmi, B. B.; Patrissi, C. J.; Martin, C. R. *Chemistry of Materials* **1997**, *9*, 2544.
(78) Michailowski, A.; AlMawlawi, D.; Cheng, G. S.; Moskovits, M. *Chemical Physics Letters* **2001**, *349*, 1.
(79) Sander, M. S.; Cote, M. J.; Gu, W.; Kile, B. M.; Tripp, C. P. *Advanced Materials* **2004**, *16*, 2052.
(80) Scholes, G. D.; Rumbles, G. *Nat. Mater.* **2006**, *5*, 683.
(81) Hulteen, J. C.; Martin, C. R. *Journal of Materials Chemistry* **1997**, *7*, 1075.
(82) P. C. Andricacos; C. Uzoh; J. O. Dukovic; J. Horkans; Deligianni, H. *IBM J. Res. Dev* **1998**, *42*, 567.

(83) Ragan, D. D.; Svedlindh, P.; Granqvist, C. G. *Solar Energy Materials and Solar Cells* **1998**, *54*, 247.
(84) Tao, F. F.; Guan, M. Y.; Jiang, Y.; Zhu, J. M.; Xu, Z.; Xue, Z. L. *Advanced Materials* **2006**, *18*, 2161.
(85) Caspari, W. A. *J. Phys. Chem.* **1899**, *30*, 89.
(86) J. Tafel *Z. Phys. Chem. A*, **1905**, *50*, 641.
(87) M. Paunovic, M. S. *The electrochemical society, INC.* **1998**.
(88) Chrisey, D. B.; Eds., G. K. H. *Pulsed laser deposition of thin films,* **1994**, *(John Wiley & Sons inc., New York,)*
(89) B. Dam; J.H. Rector; J. Johansson; Kars, S.; R. Griessen *Appl. Surf. Sci.* **1996**, *679*, 96.
(90) R.K. Singh *Mat. Sci. & Eng B* **1997**, *45*, 180.
(91) J. Gonzalo; C.N. Afonso; Perrière, J.; Roman, R. G. S. *Appl. Surf. Sci.* **1996**, *693*, 96.
(92) Zhou, W.; Wang, Z. L. *Scanning Microscopy for Nanotechnology: Techniques and Applications* **2006**, *Springer; 1 edition*, 536.
(93) Mitra, S. *Journal of the Electrochemical Society* **1980**, *127*, C374.
(94) G. H. Bernstein; D. A. Hill; W. Liu *J. Appl. Phys.* **1992**, *71*, 4066.
(95) Khoury, M.; Ferry, D. K. *J. Vac. Sci. Technol. B* **1996**, *14*, 75.
(96) Paula M. Mendes, S. J., Kevin Critchley, Jose Plaza, Yu Chen, Kirill Nikitin, Richard E. Palmer, Jon A. Preece, Stephen D. Evans, and Donald Fitzmaurice *Langmuir,* **2004**, *20*, 3766.
(97) William R. Herguth; President; Nadeau, G. *Applications of Scanning Electron Microscopy and Energy Dispersive Spectroscopy (SEM/EDS) To Practical Tribology Problems. Senior Technical Associate Herguth Laboratories, Inc.*
(98) C. Richard Brundle; Charles A. Evans Jr; Wilson, S. *Encyclopedia of materials characterization, Butterworth-Heinemann publications* **1992**.
(99) Williams, D. B.; Carter, C. B. *Transmission Electron Microscopy: A Textbook for Materials Science* **2004**, *Springer; 1st edition (August 31, 2004)* 703
(100) West, A. R. *Basic Solid State Chemistry* **1999**, *Wiley; 2 edition (August 11, 1999)* 496 pages
(101) Kalyanasundaram, K. *Dye-sensitized Solar Cells* **2010** *Publisher: EFPL Press; 1 edition (August 3, 2010)* 320 pages
(102) Guo, X. Z.; Luo, Y. H.; Zhang, Y. D.; Huang, X. C.; Li, D. M.; Meng, Q. B. *Rev. Sci. Instrum.* **2010**, *81*.
(103) Fabregat-Santiago, F.; Bisquert, J.; Garcia-Belmonte, G.; Boschloo, G.; Hagfeldt, A. *Solar Energy Materials and Solar Cells* **2005**, *87*, 117.
(104) Wang, Q. I., S.; Graetzel, M.; Fabregat-Santiago, F.; Mora-Sero, I.; Bisquert, J.; Bessho, T.; Imai, H. *J. Phys. Chem. B* **2006**, *110*, 25210.
(105) Fabregat-Santiago, F.; Bisquert, J.; Palomares, E.; Otero, L.; Kuang, D. B.; Zakeeruddin, S. M.; Grätzel, M. *J. Phys. Chem. C* **2007**, *111*, 6550.
(106) Fan, B. M., X.; Sun, K.; Ouyang *J. Applied Physics Letters* **2008**, *93*, 143103.
(107) Martinson, A. B. F.; Goes, M. S.; Fabregat-Santiago, F.; Bisquert, J.; Pellin, M. J.; Hupp, J. T. *Journal of Physical Chemistry A* **2009**, *113*, 4015.
(108) Ondersma, J. W.; Hamann, T. W. *J. Phys. Chem. C* **2010**, *114*, 638.
(109) Peng, T. Y.; Hasegawa, A.; Qiu, J. R.; Hirao, K. *Chemistry of Materials* **2003**, *15*, 2011.
(110) Cao, F.; Oskam, G.; Meyer, G. J.; Searson, P. C. *Journal of Physical Chemistry* **1996**, *100*, 17021.
(111) van de Lagemaat, J.; Frank, A. J. *Journal of Physical Chemistry B* **2001**, *105*, 11194.
(112) Nelson, J.; Haque, S. A.; Klug, D. R.; Durrant, J. R. *Physical Review B* **2001**, *63*.

(113) Benkstein, K. D.; Kopidakis, N.; van de Lagemaat, J.; Frank, A. J. *Journal of Physical Chemistry B* **2003**, *107*, 7759.
(114) Kopidakis, N.; Benkstein, K. D.; van de Lagemaat, J.; Frank, A. J.; Yuan, Q.; Schiff, E. A. *Physical Review B* **2006**, *73*.
(115) Cassiers, K.; Linssen, T.; Mathieu, M.; Bai, Y. Q.; Zhu, H. Y.; Cool, P.; Vansant, E. F. *Journal of Physical Chemistry B* **2004**, *108*, 3713.
(116) Law, M.; Greene, L. E.; Johnson, J. C.; Saykally, R.; Yang, P. D. *Nat. Mater.* **2005**, *4*, 455.
(117) Tenne, R.; Rao, C. N. R. *Philosophical Transactions of the Royal Society of London Series a-Mathematical Physical and Engineering Sciences* **2004**, *362*, 2099.
(118) Grätzel, M. *Journal of Photochemistry and Photobiology a-Chemistry* **2004**, *164*, 3.
(119) Adachi, M.; Murata, Y.; Okada, I.; Yoshikawa, S. *Journal of the Electrochemical Society* **2003**, *150*, G488.
(120) Zhu, K.; Neale, N. R.; Miedaner, A.; Frank, A. J. *Nano Letters* **2007**, *7*, 69.
(121) Mor, G. K.; Shankar, K.; Paulose, M.; Varghese, O. K.; Grimes, C. A. *Nano Letters* **2006**, *6*, 215.
(122) Paulose, M.; Shankar, K.; Varghese, O. K.; Mor, G. K.; Hardin, B.; Grimes, C. A. *Nanotechnology* **2006**, *17*, 1446.
(123) Chin-Jung Lin; Wen-Yueh Yu; Chien, S.-H. *Appl. Phys. Lett.* **2008**, *93*, 133107
(124) Baxter, J. B.; Aydil, E. S. *Applied Physics Letters* **2005**, *86*, 053114.
(125) Kongkanand, A.; Dominguez, R. M.; Kamat, P. V. *Nano Letters* **2007**, *7*, 676.
(126) Sodergren, S.; Hagfeldt, A.; Olsson, J.; Lindquist, S. E. *Journal of Physical Chemistry* **1994**, *98*, 5552.
(127) E. C. Walter, R. M. P., H. Liu, K. H. Ng, M. P. Zach, and F. Favier *Surf. Interface Anal.* **2002**, *34*, 409.
(128) R. MacKenzie, C. F., T. Sannomiya, V. Auzelyte, and J. Voros *Sensors* **2010**, *10*, 9808.
(129) X. P. Zhang, B. Q. S.; J. M. Hodgkiss; Friend, R. H. *Adv. Mater.* **2008**, *20*, 4455.
(130) J. Kong; N. R. Franklin; C. W. Zhou; M. G. Chapline; S. Peng; K. J. Cho; and H. J. Dai *Science* **2000**, *287*, 622.
(131) Bozhevolnyi, S. I. *Phys. Rev. B* **1996**, *54* 8177.
(132) T. Kitahara, A. S., H. Sano, and G. Mizutani *Appl. Surf. Sci.* **2003**, *219*, 271
(133) Z. Q. Tian; B. Ren; Wu, D. Y. *J. Phys. Chem. B* **2002**, *106*, 9463
(134) W. L. Barnes; A. Dereux; Ebbesen, T. W. *Nature* **2003**, *424*, 824
(135) Mie, G. *Ann. Phys.* **1908**, *25*, 377.
(136) D. Mo; J. Liu; H. J. Yao; J. L. Duan; M. D. Hou; Y. M. Sun; Y. F. Chen; Z. H. Xue; L. Zhang *J. Cryst. Growth* **2008**, *310*, 612
(137) J. L. Duan; J. Liu; H. J. Yao; D. Mo; M. D. Hou; Y. M. Sun; Y. F. Chen; L. Zhang *Mater. Sci. Eng., B* **2008**, *147*, 57.
(138) R. L. Zong; J. Zhou; B. Li; M. Fu; S. K. Shi; L. T. Li *J. Chem. Phys.* **2005**, *123*, 094710

Chapter 2

Synthesis and Application of Core-Shell Au/Ni-TiO_2 Nanowire Photoanode Materials for Dye Sensitized Solar Cells

Abstract

Dye sensitized solar cells (DSSCs) have been widely studied as alternatives for generation of electricity from sunlight due to their efficiency and cost effectiveness. Increasing the electron transport out of the metal oxide is important in achieving higher efficiency. Enhancing light absorption can also improve cell efficiency. The motive of this work was to synthesize and use Au/Ni-TiO_2 core-shell nanowires as anode materials in DSSC in order to increase cell efficiency by enhancing electron transport out of the oxide and/or increasing light collection efficiency. TiO_2 nanotubes were first grown in alumina templates using a sol-gel method. Gold/nickel nanowires were subsequently grown in the pores of these tubes by electrodeposition. Resulting nano-structured arrays were characterized using electron microscopy and diffraction techniques; the results show that the wires were highly aligned and well separated. The current density-voltage (J-V) behavior for the Au/Ni-TiO_2 core-shell nanowire based DSSCs was compared to the J-V data for TiO_2 nanotube based DSSCs, indicating substantial improvements upon incorporation of the Au/Ni core nanowires. $TiCl_4$ treatment of the Au/Ni-TiO_2 core-shell nanowire structures resulted in further efficiency improvements.

2.1. Introduction

Highly efficient and low cost conversion of solar energy to electricity remains a challenge even after many years of research. Dye sensitized solar cells (DSSCs) offer the potential for low cost cells, but efficiency has not improved beyond a maximum of 11% achieved around 1990.[1-2] The breakthrough of dye sensitized devices as solar cells was based on some innovative points, such as mesoporous semiconductors of high surface area which allowed high density of dye adsorption. Furthermore, development of stable organometallic sensitizers bearing attachment groups which bind strongly with the semiconductor led to enhanced charge injection efficiency. Based on these features, overall efficiencies of over 10% were obtained by O' Regan and Grätzel in 1991 for dye sensitized mesoporous TiO_2 electrodes in contact with an electrolyte containing an iodide/triiodide based redox couple for dye regeneration.[1-2] Even though the nanoparticle films provide high surface area for dye adsorption, the electron transport rate through the oxide is comparatively slow because of low electron diffusion in the polycrystalline oxide. The slow diffusion is caused by multiple trapping and de-trapping events occurring in the porous semiconductor grain boundaries of the TiO_2 nanoparticles.[3]

Electron transport in mesoscopic thin films is vulnerable to recombination losses at the particle-solution interface. Consequently, high interface recombination reaction rates limit the device efficiency. To resolve these problems, a DSSC based on an array of one-dimensional ZnO nanostructures was first introduced by Law *et al.* in 2005.[4] Unfortunately, the ZnO photoanodes consistently showed lower performance due to their instability in acidic dye media[5] and lower roughness factor (<200).[4] TiO_2, a more stable semiconductor material, was subsequently synthesized as nanorod arrays.[6-12] Fujihara *et al*. have achieved TiO_2 nanorod arrays on fluorine doped tin oxide glasses using a method called spray deposition.[6] The XRD pattern of the sintered TiO_2 nanorods revealed that the phase corresponded to anatase. Photovoltaic measurements were taken with these TiO_2 nanorod arrays as photoanodes under 1 sun (AM 1.5). power conversion efficiency (η) of 5.8%, a current density (J_{sc}) of ~13.7 mA/cm^2, an open circuit voltage (V_{oc}) of ~0.8 V, and a fill factor (FF) of ~51%. However the nanorods showed comparatively low surface area. To overcome the limitations of lower nanorod array surface area, TiO_2 nanotubes were prepared several methods and have been applied in DSSCs as photoanode materials.[13-18] The nanotube photoanodes were much more efficient at light harvesting due to the large nanocrystallite surface area available for dye adsorption. Also, the nanotubes provided an easier

pathway to capture photogenerated charges and transport them to the conducting electrode surface.[19] However, the need for decreasing the recombination of electrons and holes after band gap excitation was not fulfilled due to the bulk defects and grain boundaries which are major causes of limited photoconversion efficiency. There is a report which focuses on using nanoparticle decorated ZnO-TiO_2 core-shell nanorod arrays,[20] and the use of two different wide band gap semiconductors as anodes in DSSC has also been reported.[19,21-24] Three dimensional core-shell structures having TiO_2 as shell and various guest metal/metal oxide as core via electrodeposition have been reported.[25-30] Others have reported metal doped TiO_2 nanobelts[31] and have discussed the possibility of using the synthesized structures as photoanodes in photovoltaic devices but did not actually do so. The overall goal of the current research was to enhance the efficiency of DSSCs and practically achieve efficiency nearer to the theoretically expected value.[32-33] Since one of the major problems in achieving high efficiency is poor electron transport, we have synthesized Au-TiO_2 core-shell nanowires to overcome this barrier. There are reports which have synthesized various metal nanoparticles or nanorods embedded in TiO_2 nanotubes.[34-37] We have applied a novel technology to fabricate TiO_2 nanostructures with core Au nanorods, keeping a large TiO_2 surface area available for dye adsorption. We adopted a template based method for preparing these nanostructures because there are a number of useful features associated with this method. For example, it allows flexibility in tuning the length and diameter of the tubes. Furthermore, it allows varying the nanotube shell thickness by controlling the synthesis parameters. There are several types of membranes which have been used as templates for nanostructures synthesis. Most of the work has been done with porous alumina membranes (also known as anodic aluminum oxide, AAO) and track-etch polymeric membranes made of polycarbonate. We have used the AAO membranes to synthesize our photoanode materials. After synthesis, the desired nanoarchitectures were characterized using different probe techniques such as field emission scanning electron microscopy (FESEM), energy dispersive spectroscopy (EDS), transmission electron microscopy (TEM) and X-ray powder diffraction (XRD). Using the core-shell nanowire structures as photoanodes, DSSC devices were fabricated and the J-V characteristics were measured.

2.2. Experimental

2.2.1. Synthesis of TiO_2 nanotubes

In this study we used commercial AAO membranes supplied by the Whatman Corp. The average pore diameter and the thickness of the membranes used were 200 nm and 60 µm, respectively. In a typical synthetic process, the 200 nm pore size AAO membrane was masked on one side with transparent tape and then heated to 85° C for 15 minutes to remove any atmospheric water in the membrane. A sol-gel precursor solution was prepared by a modified method[14] utilizing titanium isopropoxide, $Ti(OC_3H_7)_4$, mixed with ethanol. The weight ratio of $Ti(OC_3H_7)_4$:C_2H_5OH was 3:1. The membrane was immersed in the precursor solution for 15-35 minutes. Tube length was related to immersion time, see Fig. 2.1 below for reference.

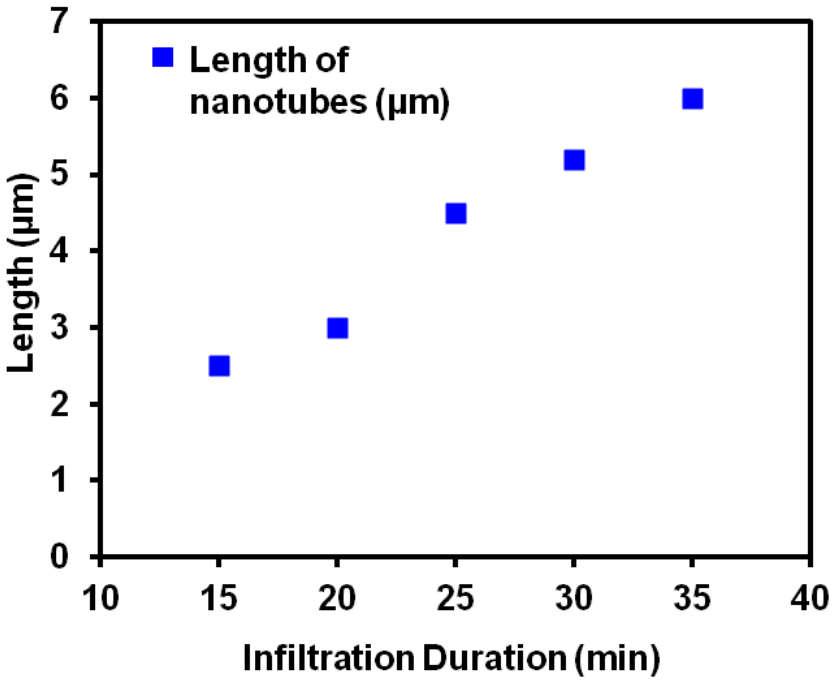

Fig 2.1 Effect of precursor infiltration duration on the length of TiO_2 nanotube arrays

Then excess liquid was wiped off from the exposed surface of the membrane. This wiping step was necessary in order to avoid an undesirable, thick film of TiO_2 on the surface of the AAO membrane which can clog the pores. The template was then left in a covered beaker for 12 hours which allowed for the solution to infiltrate the inner walls of the pores of AAO by capillary action, followed by evaporation of the ethanol and hydrolysis of the isopropoxide upon mixing

with water from ambient air. Next, the sample was annealed at 500 ^{o}C for 30 minutes in air. The difference in our method compared to the previously reported method[14] was that we have used a commercial AAO membrane with openings on both sides allowing us to prepare TiO_2 nanotubes open at both ends.

2.2.2. Synthesis of Au-TiO_2 core-shell nanowires

After the TiO_2 nanotubes were obtained with the desired morphology and crystalline anatase phase, bottom up constant current electrodeposition was carried out in order to grow Au-TiO_2 core-shell nanowires. In order to grow the Au nanowires inside the hollow channels of the TiO_2 nanotubes while still embedded in the AAO membranes, a silver film was first sputtered on the back of the template (the side containing the TiO_2 nanotubes). The Ag backed AAO template with TiO_2 nanotubes served as the working electrode (cathode), a Pt wire served as anode, and Ag/AgCl was used as the reference electrode. The gold plating solution (Orotemp 24) was purchased from Technic, Inc. The silver side of the template was attached to copper tape (3M), and the opposite side of the copper tape was covered with its original polymer backing as well as 3M Scotch tape so that electrodeposition could only occur through the open pores of the TiO_2 tubes within the AAO membrane. Electrodeposition was carried out at room temperature using constant current with a single channel potentiostat (EG&G Instruments Model 263A). Nanowires were grown into the TiO_2 nanotubes with a current of -0.9 mA for up to 80 minutes. This deposition allowed the wires to grow as far as to the top of the nanotubes, filling the entire channel with Au nanowires. The procedure is illustrated in Figure 2.2. After deposition, the sample was rinsed with distilled water, and the AAO containing nanostructure was etched slowly with 3 M NaOH for 30 minutes. The obtained core-shell nanowires were washed several times with distilled water resulting in well aligned nanowire arrays on a copper substrate. The nanowire arrays were later removed from the copper tape by washing with acetone.

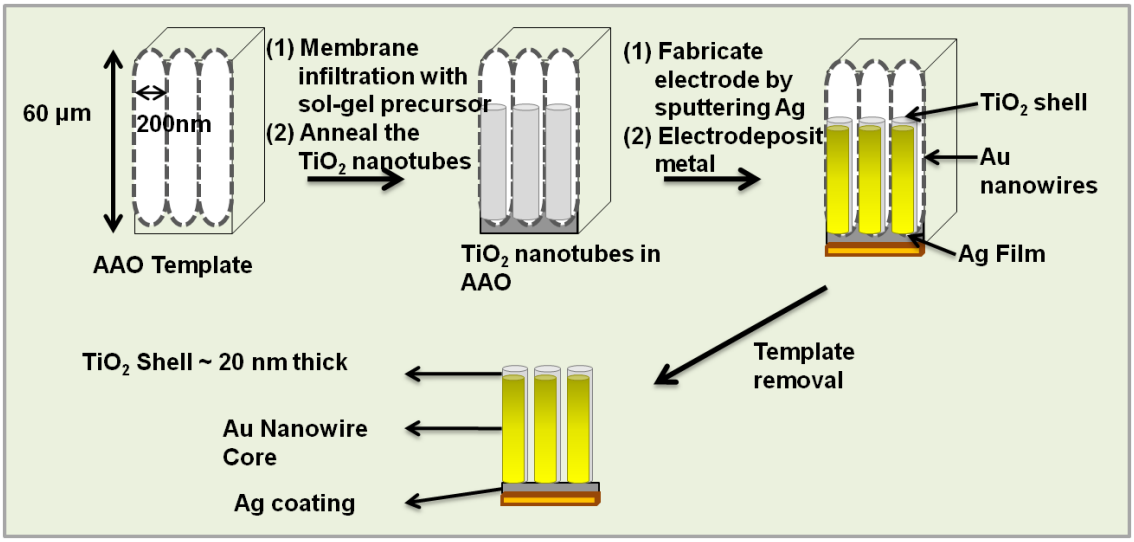

Fig. 2.2 Process for preparing templated Au–TiO_2 core-shell nanowires.

2.3. Characterization

The structures were characterized by a Carl Zeiss 1530 VP field emission scanning electron microscope (FESEM) and a JEOL 2010 conventional transmission electron microscope (TEM). The compositional analysis was conducted by energy dispersive X-ray spectroscopy (EDS). For FESEM observation, TiO_2 nanotube samples were attached to a glass substrate using epoxy glue. The AAO template was removed using aqueous 3 M NaOH for 45 minutes. The sample was observed by FESEM and XRD after drying overnight. The X-ray diffraction (XRD) patterns of samples were collected by a Philips X-pert PW 3040 MPD X-ray powder diffractometer operated at 40 kV and 40 mA current with Cu Kα radiation.

2.3.1. Solar cell fabrication and characterization

Photoanodes utilizing TiO_2 nanotubes and Au-TiO_2 nanowires were prepared by transferring the nanostructures onto a fluorine doped tin oxide (FTO) glass substrate obtained from Solaronix (TCO10-10, sheet resistance 10 Ω sq^{-1}) using a modified method.[14] First method involves depositing a thin layer (~2 µm) of nanocrystalline TiO_2 paste (Aldrich) onto the FTO conducting surface in order to promote adhesion of the nanostructures and also to prevent electrical shorting with the redox electrolyte coming into direct contact with the FTO layer. The AAO containing the TiO_2 nanotubes or Au-TiO_2 nanowires was attached to an adhesive transparent tape with the silver sputtered side of the AAO template (in case of Au-TiO_2 nanowires) attached to the adhesive

side of the tape. The AAO was dissolved away using 3 M NaOH for 45 minutes. This assembly, tape side up, was then applied to the TiO_2 coated FTO substrate, The tape was then peeled off and the remaining structure was heated to 450 ^oC for 30 minutes.[14] When the tape was removed, the thin layer of silver was peeled off along with the tape and was no longer visible after the tape was removed. See Fig. 2.3 below for reference.

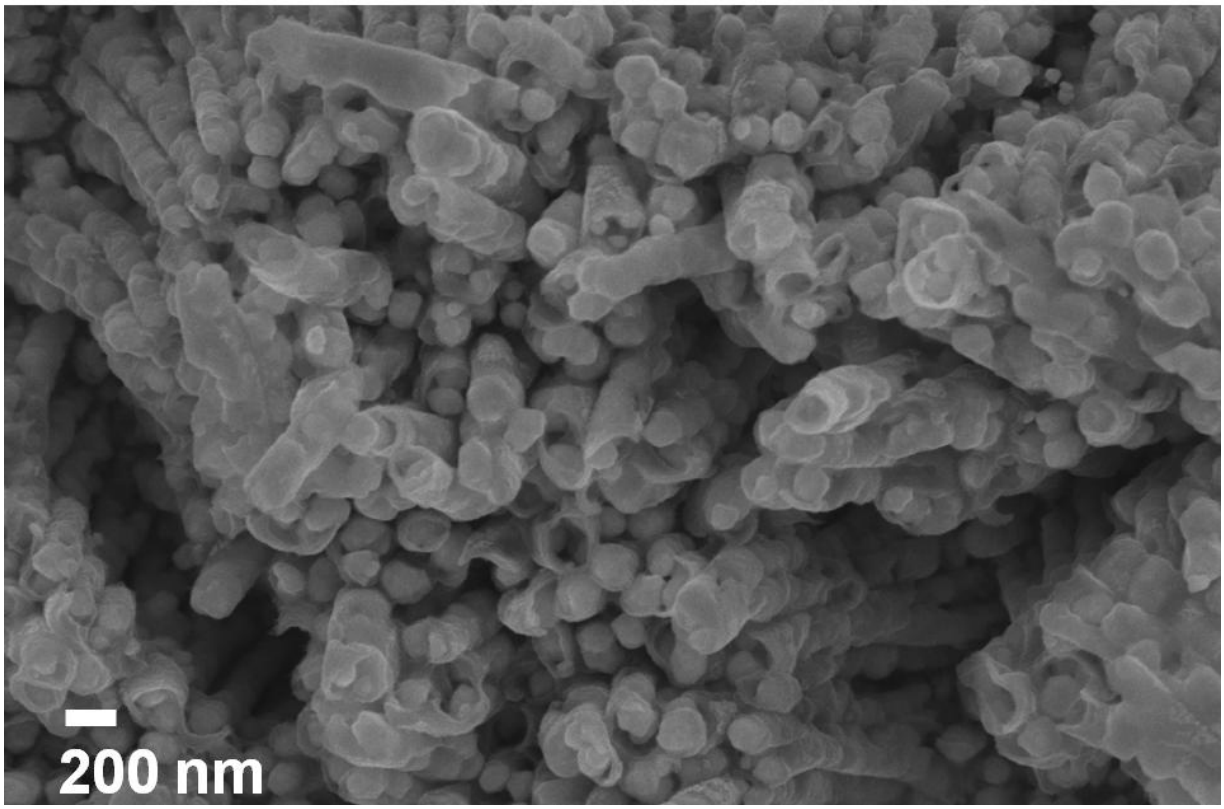

Fig. 2.3 FESEM image of the Au-TiO_2 core-shell nanostructure after the removal of Ag layer

In second method, the AAO containing TiO_2 nanotubes or Au-TiO_2 nanowires were dissolved in 3 M NaOH which resulted in free arrays of TiO_2 nanotubes or Au-TiO_2 core-shell nanowires in NaOH solution. The arrays of nanotubes or Au-TiO_2 nanowires were washed with DI H_2O four times in order to remove the residual NaOH. The nanostructures were then washed with ethanol to remove residual water. The freely suspended nanostructure arrays were then transferred and adhered onto a pre-cleaned FTO slide followed by annealing in air at 450^oC for 30 minutes. This second method was applied in order to assess the effect of the nanocrystalline TiO_2 paste on the performance of the device. The resulting TiO_2 nanotube or Au-TiO_2 core-shell nanowire film on

the FTO was sensitized for 24 hours by soaking in dye solution overnight. A ruthenium dye (N-535, Solaronix) was prepared by dissolving 25 mg of the solid in 1 mL of ethanol. A platinum coated FTO counter electrode was prepared by brushing with a thin layer of Platisol T (Solaronix). The I^-/I_3^- electrolyte was prepared using 0.6 M 1-methyl-3-propylimidazolium iodide, 0.05 M iodine, 0.05 M LiI and 0.5 M *tert*-butylpyridine in 25 mL acetonitrile:valeronitrile (1:1 volume ratio). Two small holes were drilled in the glass of the platinum electrode in order to later inject the electrolyte. The two electrodes were tightly sandwiched together by using Surlyn® sealant (Solaronix), and the sandwiched electrodes were sealed by heating for 5 minutes with a heat gun. The electrolyte was carefully introduced into the space between the two electrodes through one hole on the Pt electrode with a syringe. The drilled holes were then sealed. The details of the processes for transferring the nanostructures onto FTO using the first and second method and device fabrication has been given in Fig. 2.4 below. Photovoltaic data were measured using an ATLAS Suntest (CPS+) solar simulator set at 100 mW/cm^2 full spectrum power (equivalent to AM-1.5). J-V data were generated using a Keithley 2400 source meter. The light intensity of the xenon light source was adjusted by using an NREL calibrated silicon photodiode (Hamamatsu S1787-08 for visible to IR range). The incident photon to current efficiency (IPCE) was measured using a modified fluorescence spectrometer (PTI). In detail, a 75 watt xenon lamp was coupled to a monochromator with a computer controlled stepper motor (Superior Electric MO61-CS02). The intensity of incident light at each wavelength was measured by a calibrated silicon photodiode (Newport 818-UV-L) and the photoresponse of the test cell was subsequently measured under identical conditions.

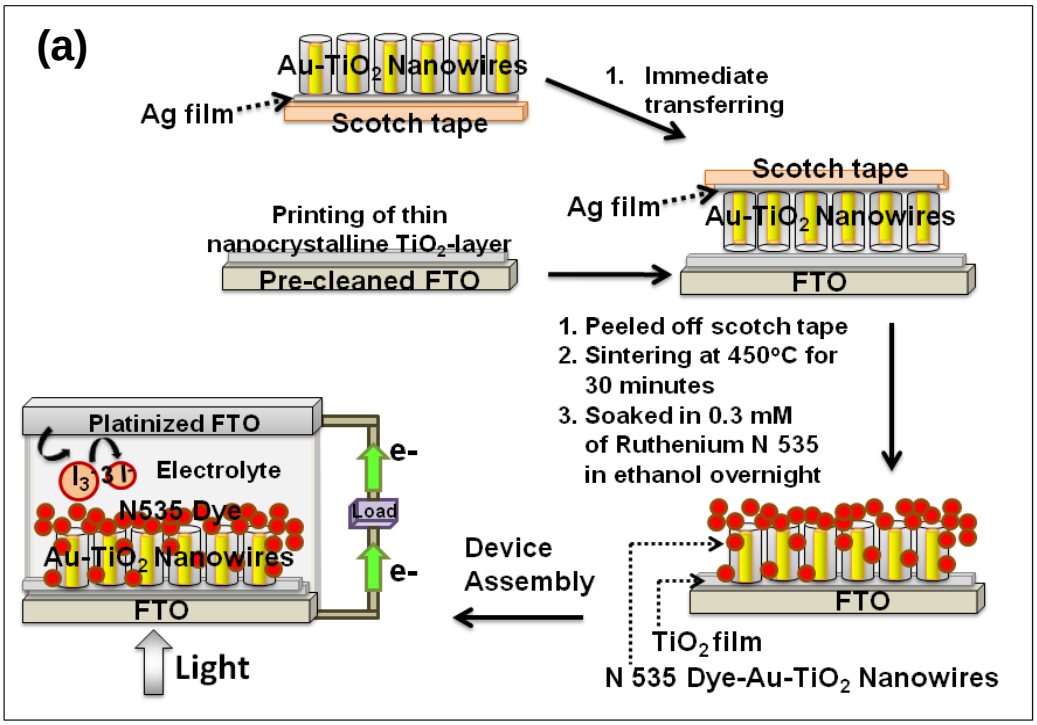

First Method: With Nanocrystalline TiO_2 paste

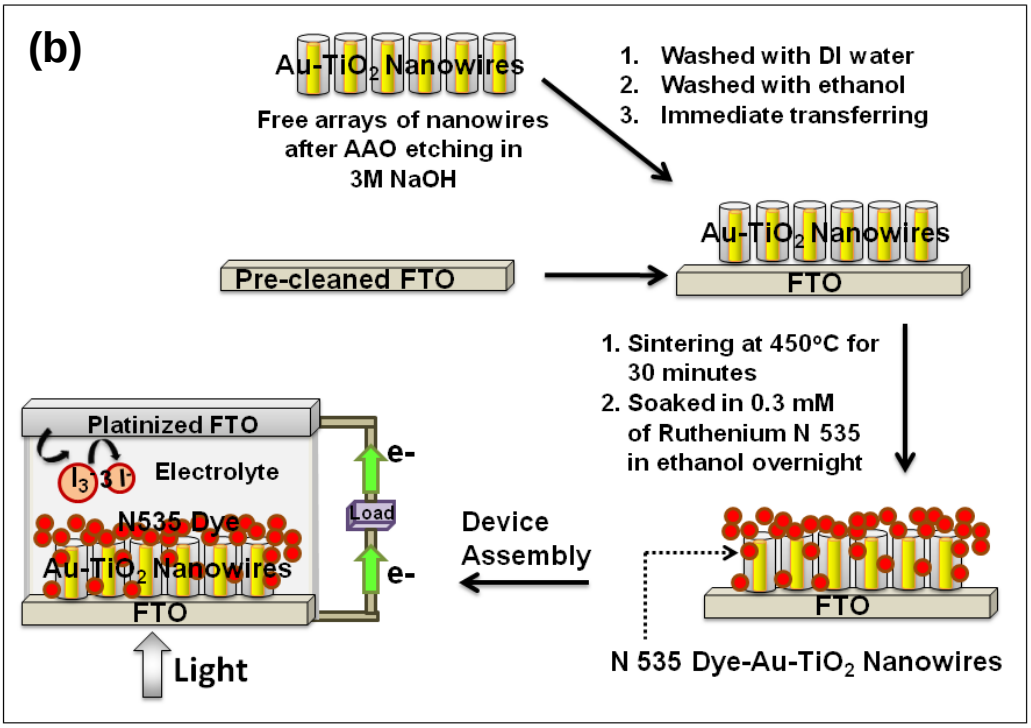

Second Method: Without Nanocrystalline TiO_2 paste

Fig. 2.4 Schematic of first (a) and second (b) methods of transferring the Au-TiO_2 core-shell nanowire onto FTO and fabrication of device

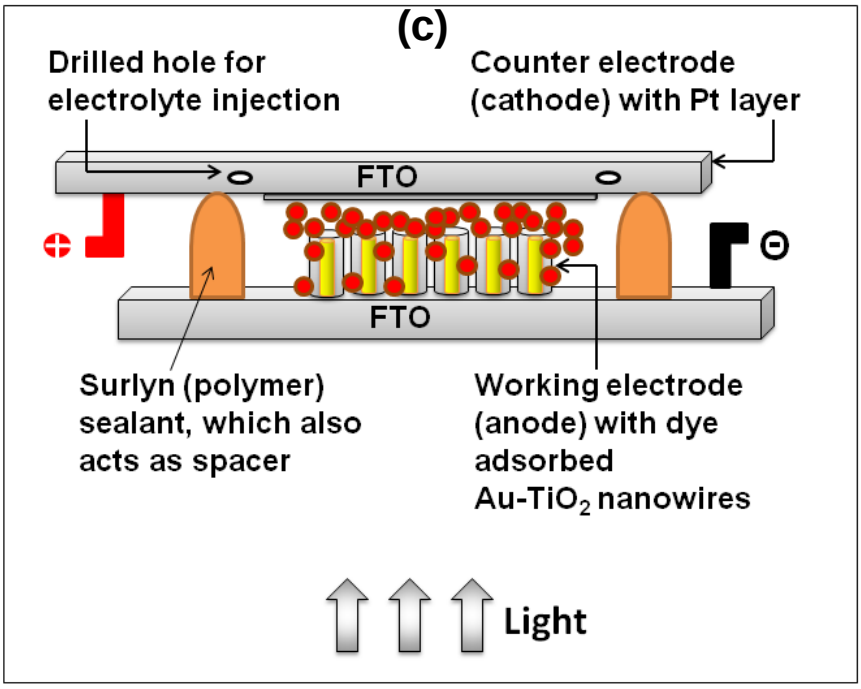

Fig. 2.4 (c) Schematic of side view of device assembly with Au-TiO_2 nanowire array as photoanode, not to scale.

2.3.2. $TiCl_4$ treatment

Surface treatment of the TiO_2 photoanodes with a TiO_2 precursor such as titanium tetrachloride $TiCl_4$[38-42] and titanium isopropoxide $Ti(OC_3H_7)_4$ [43] has already been proven to enhance solar cell device performance by increasing photocurrent, [44] enhancing surface area,[45] improving electron transport,[38] and improving anchoring of the dye[41]. In order to passivate gold exposed at the ends of our Au-TiO_2 nanowires, the Au-TiO_2 nanowire film on FTO was also subjected to 0.1 M $TiCl_4$ (Aldrich) aqueous solution in a closed chamber for 24 hours, then washed with distilled water. The electrode was annealed again at 450 ^oC for 30 minutes. The color of the electrode was off-white after the $TiCl_4$ treatment. FESEM images of TiO_2 nanotube arrays before and after $TiCl_4$ treatment without TiO_2 nanoparticle bottom layer has been given in figure 2.5 below. These anodes were treated with ruthenium dye and the DSSC devices were fabricated as described above for TiO_2 nanotube cells.

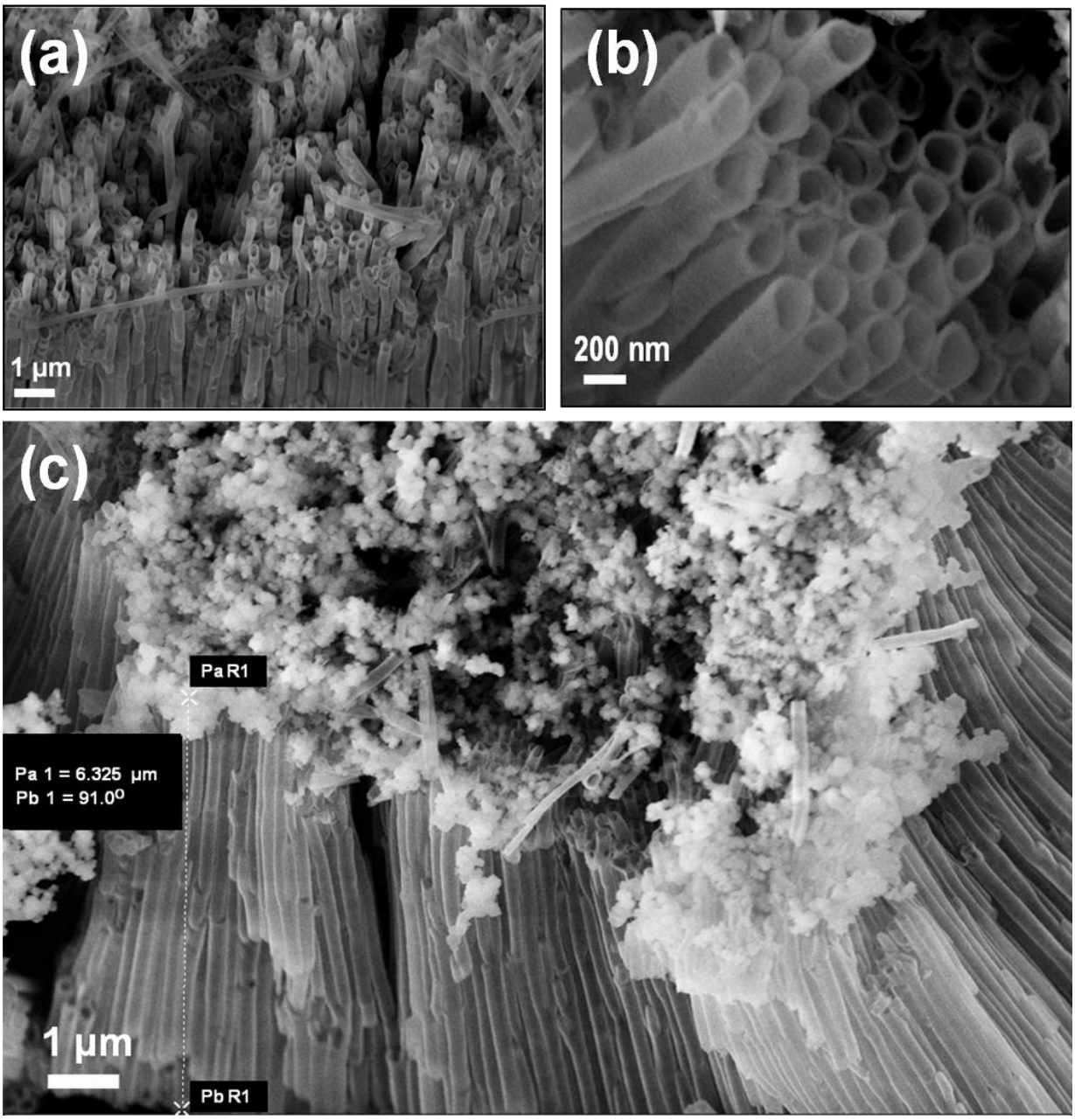

Fig. 2.5 FESEM images of 6.3 µm long TiO_2 nanotube arrays, (a), (b) before and (c) after $TiCl_4$ treatment without TiO_2 nanoparticle bottom layer

2.3.3. Dye desorption experiment

The amount of dye adsorbed on the nanostructures was measured by desorbing the dye with 0.2 M NaOH in ethanol The concentration of desorbed dye was determined by absorbance using a Cary 500 UV-Vis spectrophotometer.

2.4. Results and discussion

The mechanism for the synthesis of TiO_2 nanotubes by sol-gel reaction has been discussed elsewhere.[46] The AAO film containing TiO_2 nanotubes was heat-treated at 500^oC for 30 minutes, and the nanotubes obtained were found to be polycrystalline anatase. The XRD pattern in Fig 2.6 below showed that the TiO_2 nanotubes were highly crystalline anatase.

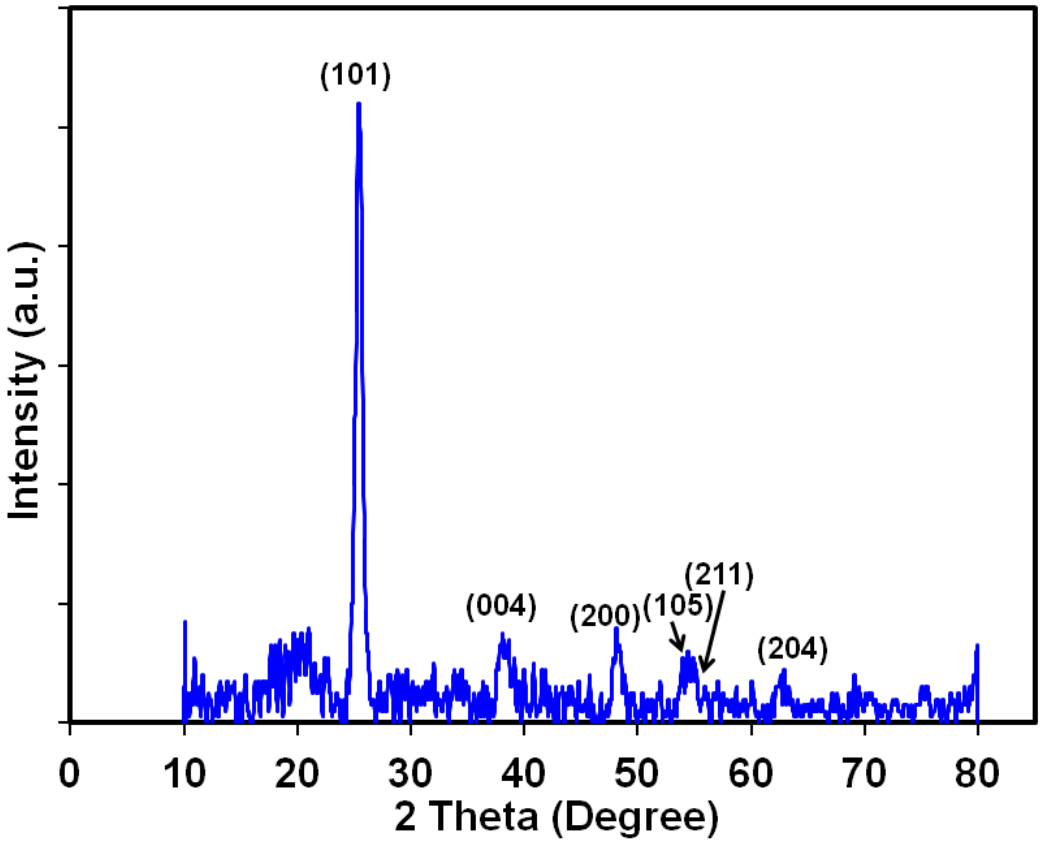

Fig. 2.6 XRD pattern of TiO_2 nanotube array on a glass substrate after removal of the AAO membrane Positions of anatase peaks are noted.

The XRD pattern above contains several peaks corresponding to anatase, and the absence of a peak at 27.45^o (rutile) suggests that the nanotubes consist predominantly of crystalline anatase

TiO_2 phase. The FESEM images and the EDS data of synthesized nanotubes are given in Figure 2.7 below, which shows that the synthesized structures were clearly composed of well aligned TiO_2 nanotube arrays. The TiO_2 nanotubes were around 2-3 μm in length with a ≈300 nm outer diameter. Based on these images, we approximate a tube density of 8 tubes per square micron. Nanotube wall thickness can be varied by varying the. immersion time of the AAO membrane into the precursor solution. For example, very thin walled nanotubes were obtained with a short immersion time of 2 minutes and thick walled nanotubes were obtained with a long immersion time of 10-15 minutes. The highly magnified thick walled anatase TiO_2 nanotubes are shown in Figure 2.7 (a) and low magnified side view has been given in Figure 2.7 (b). The nanotubes have a tendency to bundle tightly together due to the surface tension induced by solvent evaporation after the removal of the AAO template. This effect was apparent in all the FESEM images. However, open space is still visible between the tubes.

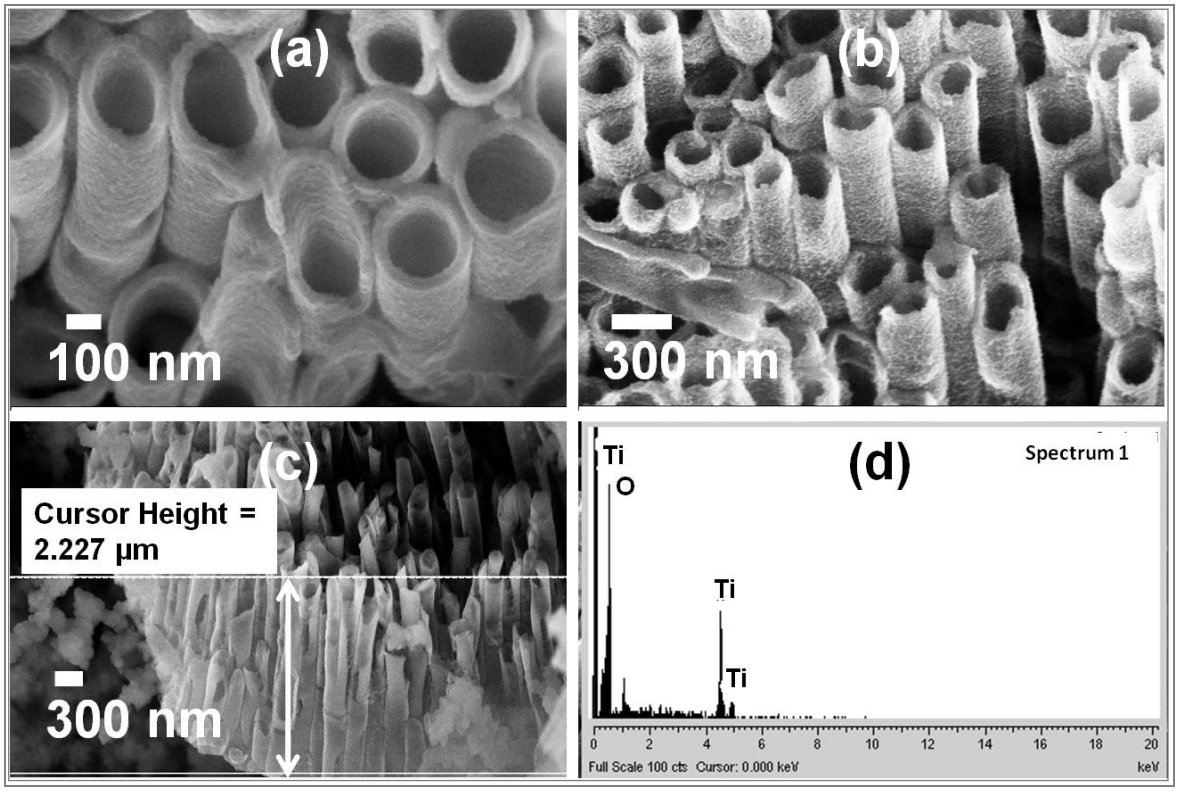

Fig. 2.7 Scanning electron micrographs of (a) top view and (b) side view of thick walled TiO_2 nanotubes; length of nanotubes shown in (c); EDS provided in (d)

To prepare TEM samples, after dissolving the nanotube containing AAO template with 3M NaOH for 30 minutes, TiO_2 nanotubes in the solvent were carefully removed with a syringe. The sample was then placed in a new glass vial, a few microliters of toluene were added, and the sample was sonicated for 5 min. This process dispersed the nanotubes without destroying the nanotube structure. TEM images of the TiO_2 nanotubes are given in Figure 2.8. These images confirm that the average nanotube shell thickness was ~5-15 nm and the tubes had a diameter of ~200 nm. The composition of the TiO_2 nanotubes was confirmed by EDS analysis, with data shown in Figure 2.8 (c).

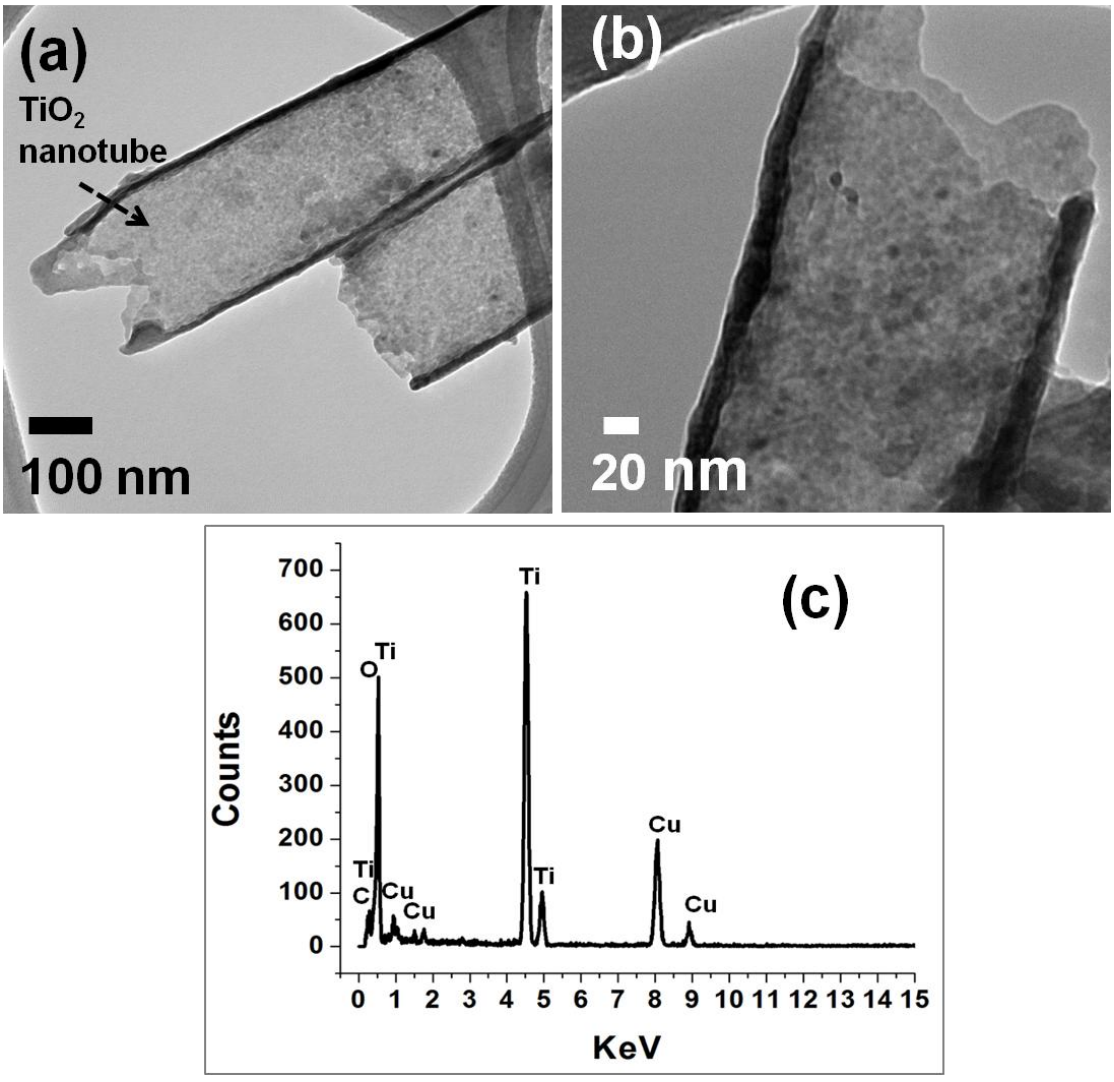

Fig. 2.8 TEM images of sol–gel synthesized TiO_2 nanotubes (a, b) and corresponding EDS data (c).

Figure 2.9 shows FESEM images of both morphological and compositional data of Au-TiO_2 core-shell nanowire arrays on a Cu substrate. Figures 2.9 (a)-(c) show the top views of the Au filled TiO_2 nanotubes taken at various magnifications. The images prove the successful growth of the Au-TiO_2 core-shell nanoarchitectures. Figure 2.9 (d) presents the EDS data for the Au-TiO_2 core-shell nanowires, which clearly indicate the presence of Au, Ti, and O.

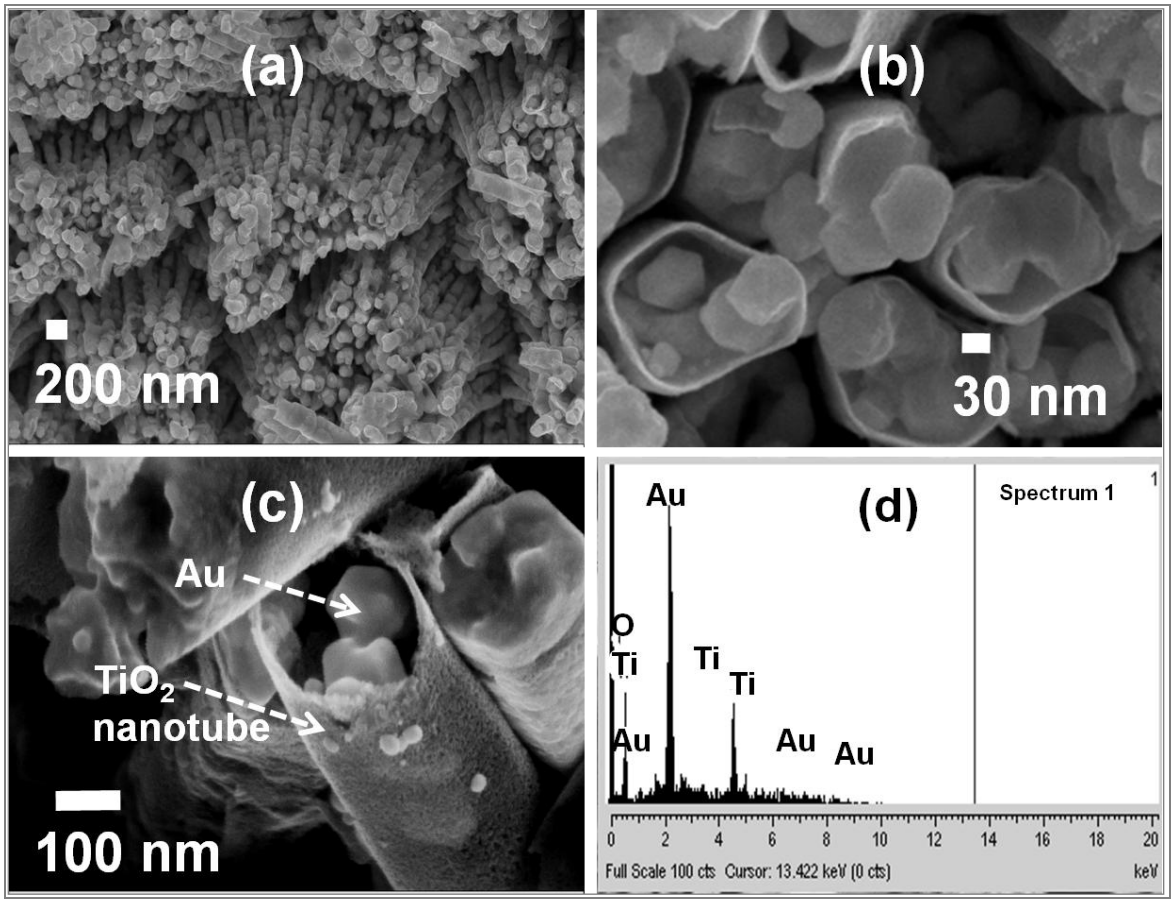

Fig. 2.9 FESEM images of Au–TiO_2 core-shell nanowires (a)–(c) and corresponding EDS data (d).

Figure 2.10 shows the representative TEM images of the as prepared Au-TiO_2 core-shell nanowires. The Au filled TiO_2 nanotubes were about 200 nm in diameter. The dark portion inside the shell corresponds to gold, and the gray, polycrystalline regions are the TiO_2 shell. It can be clearly seen that the hollow channel of the TiO_2 nanotube was entirely filled with gold up to near the tip of the tube. One limitation of this gold filling method is that the metal was polycrystalline in nature, possibly causing poor contact between the oxide and the metal and through the metal

core. However, slower electrodeposition might create single crystalline nanowires of gold that would be expected to perform even better for photovoltaic charge transport. We have chosen gold as the material for the metallic core due to its excellent conductivity, inertness, and thermal and chemical stability. Also, metallic nanowires provide enhancement of light absorbance through scattering effects.[47]

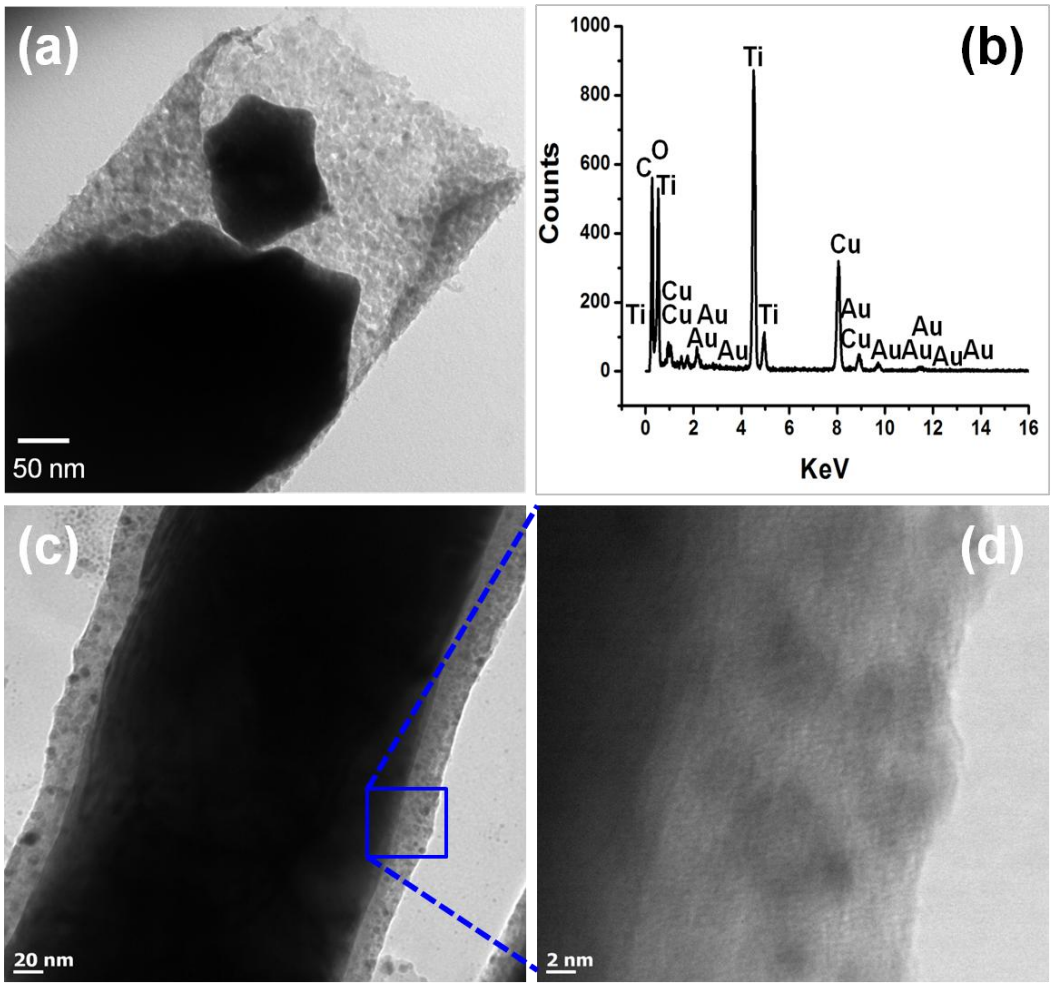

Fig. 2.10 Representative TEM images of the (a) tip of one Au-TiO_2 core-shell nanowire and (b) EDS spectrum of the Au–TiO_2 nanowires showing the presence of both Au and Ti. (c) Side of one Au-TiO_2 core-shell nanowire and (d) HRTEM image of the area shown in a block in (c)

Complete filling of the hollow tube was possible because of the bottom-up electrodeposition method used to fill the TiO_2 tubes. The mechanism for the metal growth might be described as follows: The pore bottoms have been made highly conductive by sputtering a thin layer of Ag (< 20 nm), whereas the wall of TiO_2 tube has substantial resistance.

This arrangement allows for uniform pore filling of gold by electrodeposition from pore bottom to the top, resulting in a homogeneous and continuous core-shell nanostructure. The composition of the core-shell nanowire depicted in Figure 2.10 (a), was verified by EDS Figure 2.10 (b). Figure 2.10 (c) shows the side of one Au-TiO_2 nanowire which varifies that the TiO_2 shell is ~20 nm. Figure 2.10 (d) is the HRTEM image that was taken from the area shown in a block in Figure 2.10 (c). The EDS spectrum indicates that the nanostructure is composed of Au, Ti, and O. The Cu peak comes from the grid. Au-TiO_2 core-shell nanowire arrays were also used as photoanode by attaching them to an FTO substrate using the same method described above. Good contact between the gold and the FTO is an important factor in achieving efficient electron transport. Based on FESEM and TEM images, the gold cores come close to the tip of the TiO_2 nanotubes and are consequently in close proximity to the TiO_2 paste. The synthesized structures served as the photoanode in dye sensitized solar cell devices. Ruthenium dye (N-535) was the sensitizer and I^-/I_3^- served as the redox couple. The J-V characteristics were measured under 100 mW/cm^2 simulated sunlight (AM 1.5). We compare the current-voltage characteristics of TiO_2 nanotube solar cells with that of Au-TiO_2 core-shell nanowires and surface passivated Au-TiO_2 core-shell nanowire solar cells. The active area of the anodes for each cell was in the range of 0.12 to 1.04 cm^2. A schematic of the core-shell nanowire device is given in Figure 2.11 (a) below. A digital picture of one of the handmade devices made from Au-TiO_2 core-shell nanowire arrays of active surface area 0.28 cm^2 is shown in Figure 2.11 (b). The J-V curves obtained are given in Figure 2.12 below.

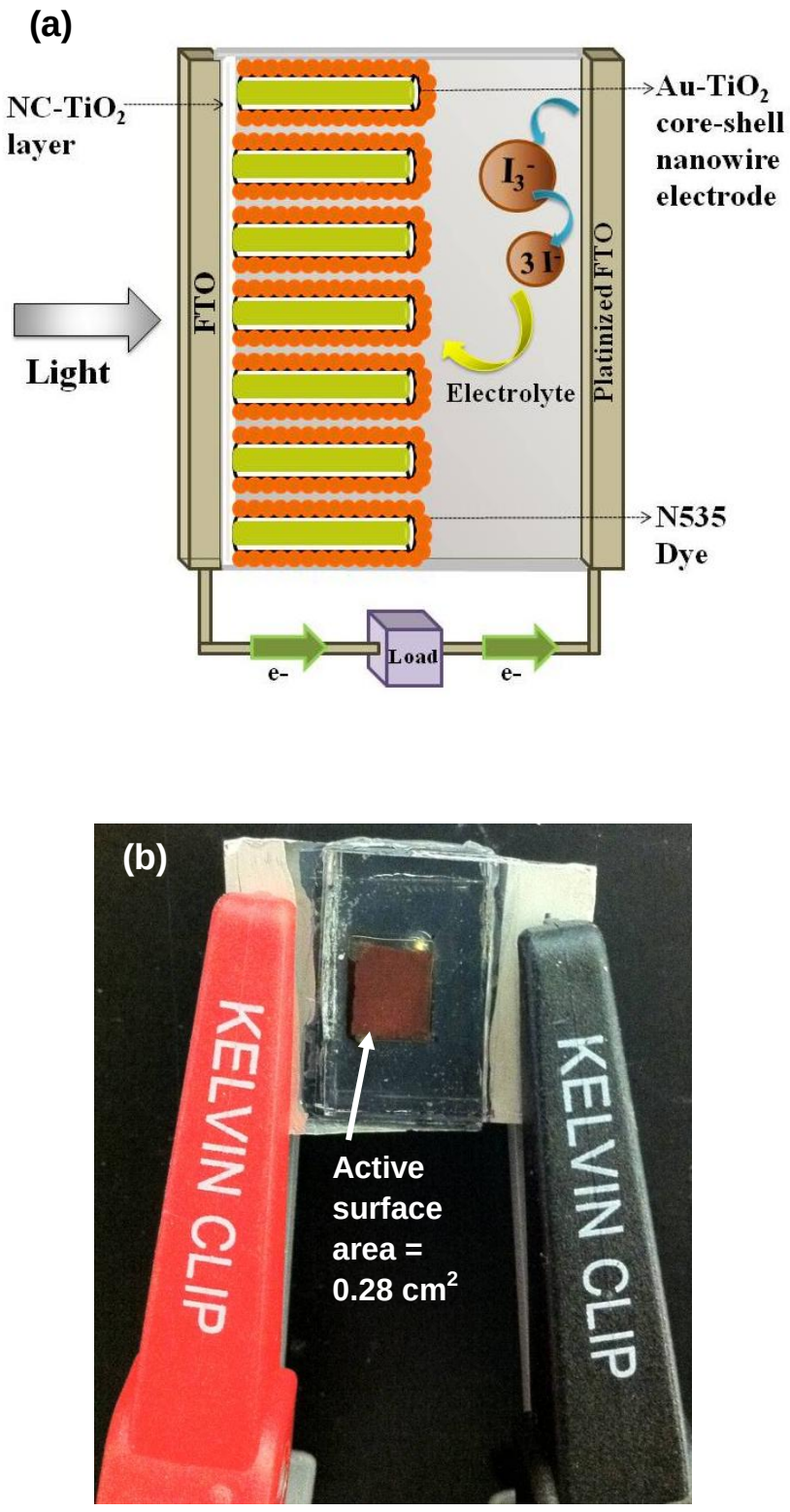

Fig. 2.11 (a) Schematic of assembled TiO_2 nanotube DSSC or Au–TiO_2 core-shell DSSC (NC = nanocrystalline). Not to scale; tube lengths exaggerated to better illustrate structure. (b) A digital picture of one of the handmade devices with active surface area 0.28 cm^2.

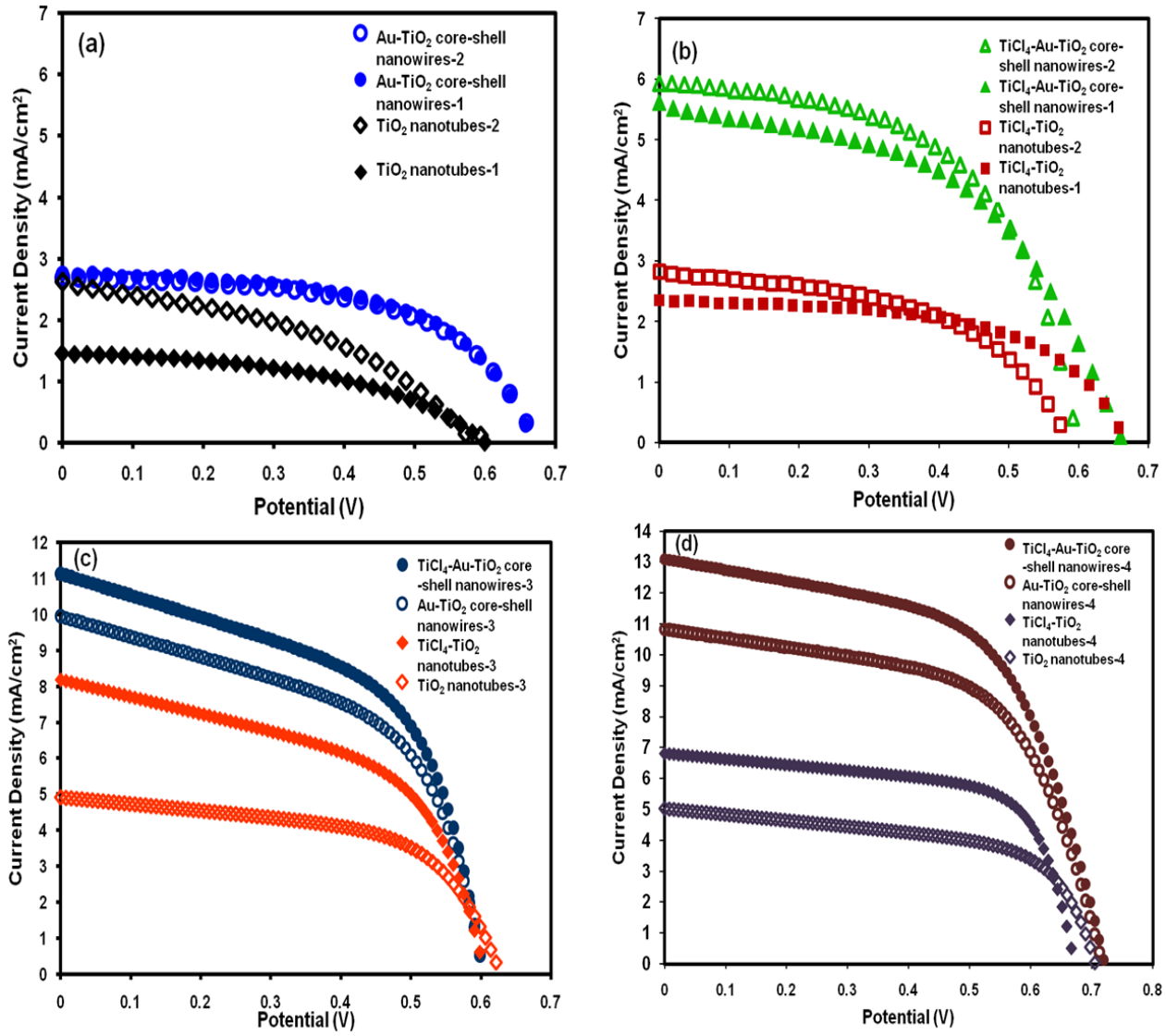

Fig. 2.12 J–V curves for DSSC employing various nanotubes. Panel (a) presents first and second cells made from TiO_2 nanotubes (open and closed black diamonds) and first and second cells made from Au–TiO_2 core-shell nanowires (open and closed blue circles). Panel (b) presents first and second cells made from $TiCl_4$ treated TiO_2 nanotubes (open and closed red squares) and $TiCl_4$ treated Au–TiO_2 core-shell nanowires (open and closed green triangles). Panel (c) presents data for cells made from nanostructures without a TiO_2 nanoparticle adhesion layer: TiO_2 nanotubes (open orange diamonds), $TiCl_4$–TiO_2 nanotubes (closed orange diamonds), Au–TiO_2 core-shell nanowires (open dark blue circles), and $TiCl_4$–Au–TiO_2 core-shell nanowires (closed dark blue circles). Panel (d) presents another set of data for cells made from long (~6 µm) nanostructures without a TiO_2 nanoparticle adhesion layer: TiO_2 nanotubes (open purple diamonds), $TiCl_4$–TiO_2 nanotubes (closed purple diamonds), Au–TiO_2 core-shell nanowires (open brown circles), and $TiCl_4$–Au–TiO_2 core-shell nanowires (closed brown circles). Cell efficiencies and other parameters listed in Table 1.

Table 2.1 J-V characteristics of dye-sensitized TiO_2 nanotube, Au-TiO_2 core-shell nanowire, $TiCl_4$ treated TiO_2 nanotube and $TiCl_4$ treated Au-TiO_2 core-shell nanowire DSSCs under 1 sun.

Photoanode Film Type	Approx. Length (μm)	TiO_2 nanoparticle adhesion layer	J_{sc} (mA/cm^2)	V_{oc} (V)	FF (%)	η (%)
TiO_2 Nanotube-1	3	Yes	1.45	0.60	46.8	0.41
TiO_2 Nanotube-2	2.5	Yes	2.62	0.59	40.8	0.63
$TiCl_4$ treated Nanotube-1	2.5	Yes	2.35	0.68	55.6	0.89
$TiCl_4$ treated Nanotube-2	2.5	Yes	2.82	0.59	49.7	0.83
Au-TiO_2 core-shell-1	3	Yes	2.76	0.67	56.0	1.02
Au-TiO_2 core-shell-2	3	Yes	2.69	0.69	55.0	1.04
$TiCl_4$ treated Au-TiO_2 core-shell-1	3	Yes	5.62	0.68	48.0	1.83
$TiCl_4$ treated Au-TiO_2 core-shell-2	2.5	Yes	5.93	0.61	54.5	1.97
TiO_2 Nanotube-3	3	No	4.92	0.62	57.6	1.78
$TiCl_4$-TiO_2 Nanotube-3	3	No	8.18	0.60	52.2	2.59
Au-TiO_2 core-shell-3	3	No	9.95	0.60	52.7	3.16
$TiCl_4$-Au-TiO_2 core-shell-3	3	No	11.13	0.60	53.4	3.58
TiO_2 Nanotube-4	6	No	5.02	0.70	58.8	2.08
$TiCl_4$-TiO_2 Nanotube-4	6	No	6.8	0.67	65.0	2.98
Au-TiO_2 core-shell-4	6	No	10.83	0.71	58.4	4.53
$TiCl_4$-Au-TiO_2 core-shell-4	6	No	13.10	0.71	57.1	5.40

The TiO_2 nanotubes had ~5-15 nm wall thickness, 300 nm outer diameter and 2-3 μm length. The J-V data obtained upon illumination is given in Table 2.1 above. The average efficiency and fill factor of two TiO_2 nanotube based devices was found to be (0.5 ± 0.2) % and (44 ± 4) % respectively. When the TiO_2 underlayer used for adhesion of the nanowire arrays was tested alone

as a DSSC, its efficiency was only 0.35%, indicating that the underlayer did not contribute substantially to the performance of the nanowire devices. See figure 2.13 below for the information.

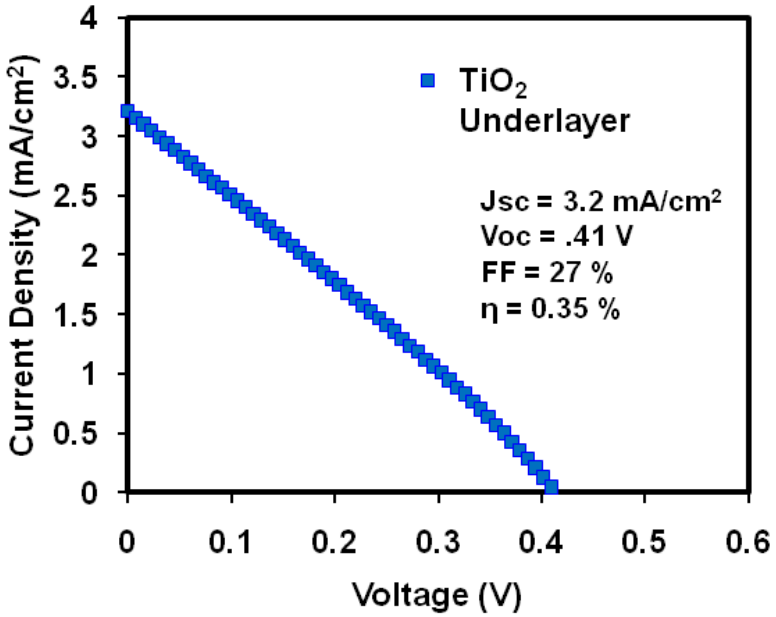

Fig. 2.13 J-V curve and J-V curve parameters of underlayer TiO_2 nanoparticles film

The Au-TiO_2 core-shell nanowire samples had a nanowire outer diameter of ~200 nm and a lengthh of 2-3 µm. Upon illumination the J-V data obtained were compared to the hollow TiO_2 nanotube DSSC data. The Au-TiO_2 core-shell nanowire based DSSC device showed an efficiency of (1.03 ± 0.01) % and fill factor of (56 ± 1) % on average for two devices. The short-circuit current density, open-circuit voltage, fill factor, and efficiency were found to be increased for the gold-filled tubes. Overall, the cell efficiency using Au-TiO_2 core-shell nanowires as anode was found to be more than double that obtained for TiO_2 only nanotubes. This doubling in efficiency occurred despite the fact that filling the TiO_2 tubes with gold reduced the available surface area by roughly a factor of two. Consequently, the ability of the gold core to enhance photovoltaic current is estimated to account for a four fold enhancement in efficiency per unit area of TiO_2 surface. However, the J_{sc} was still lower than desireded. To make further improvements, we covered the Au-TiO_2 core-shell nanowire surface with a thin layer of TiO_2 by treatment with $TiCl_4$, and then fabricated DSSC devices using the surface treated core-shell

nanowires as photoanode. The J-V data obtained are given in Figure 2.12 and are listed in Table 2.1. When these data were compared to the original Au-TiO_2 core-shell nanowire device, the J_{sc} was increased substantially compared to that obtained for the untreated Au-TiO_2 core-shell device. This improvement of approximately 84% is in line with previous reports for $TiCl_4$ treatment of nanocrystalline TiO_2 DSSC.[41-42,48] The earlier work suggested that increased surface area and improved dye adsorption were responsible for improvements, but preventing charge recombination has also been proposed as a mechanism.[49] For comparison, we treated the TiO_2 nanotube DSSC device with $TiCl_4$ as well. The J-V curve is given in Figure 2.12, and cell parameters are given in Table 2.1. The average efficiency was improved up to 65% for the two $TiCl_4$ treated TiO_2 nanotube devices.

Although $TiCl_4$ treatment of the hollow TiO_2 nanotubes resulted in improved efficiency, the gold-TiO_2 core-shell structures still showed substantially greater efficiency compared to the hollow tubes. The trend in fill factor was 44 ± 4 for the two TiO_2 nanotube devices tested, 55.5 ± 0.1 for the two Au-TiO_2 core-shell nanowire DSSC devices tested, and 51 ± 5 for the two $TiCl_4$ treated Au-TiO_2 core-shell nanowire DSSC devices tested. These results indicate that the fill factor was improved upon addition of the Au core. Subsequent $TiCl_4$ treatment of the Au-TiO_2 core-shell structure did not produce a further improvement in fill factor.

In order to compare the cell parameters of the TiO_2 nanotube and Au-TiO_2 core-shell nanowire based DSSCs with and without the bottom mesoporous TiO_2 nanoparticle layer, we fabricated one batch of devices without the nanoparticle layer and measured the J-V properties under simulated AM 1.5 light. The J-V curves are given in figure 2.12 (c), and the cell parameters are summarized in Table 2.1. Without the TiO_2 adhesion layer, the J_{sc} was increased from 2.62 mA/cm^2 to 4.92 mA/cm^2 and η was increased from 0.63% to 1.78% for TiO_2 nanotubes. Similarly, the $TiCl_4$-TiO_2 nanotube cell performance was substantially increased without the TiO_2 nanoparticle layer at the bottom of the nanostructure. The same was the case with Au-TiO_2 core-shell nanowire and $TiCl_4$-Au-TiO_2 core-shell nanowire based DSSCs when the devices were made without the TiO_2 nanoparticle adhesion layer. The current density was increased from 2.76 to 9.95 mA/cm^2 whereas the efficiency was increased from 1.02% to 3.16% in case of the Au-TiO_2 core-shell nanowire DSSCs. Also, the current density was increased from 5.93 to 11.13 mA/cm^2 and the efficiency was increased from 1.97% to 3.58% for the $TiCl_4$-Au-TiO_2 core-shell nanowire DSSCs. Using the same method when the next set of devices were fabricated with ~6 µm long TiO_2 nanotubes and Au-TiO_2 core-shell nanowires (XRD data for Au-TiO_2 nanaowire

arrays are given in Fig. 2.14 below), the efficiency of the $TiCl_4$-Au-TiO_2 core-shell device was 5.40%. The fill factor and open-circuit voltage did not differ substantially between cells with and without the TiO_2 adhesion layer, while the short-circuit current density and efficiencies significantly increased by eliminating the TiO_2 adhesion layer.

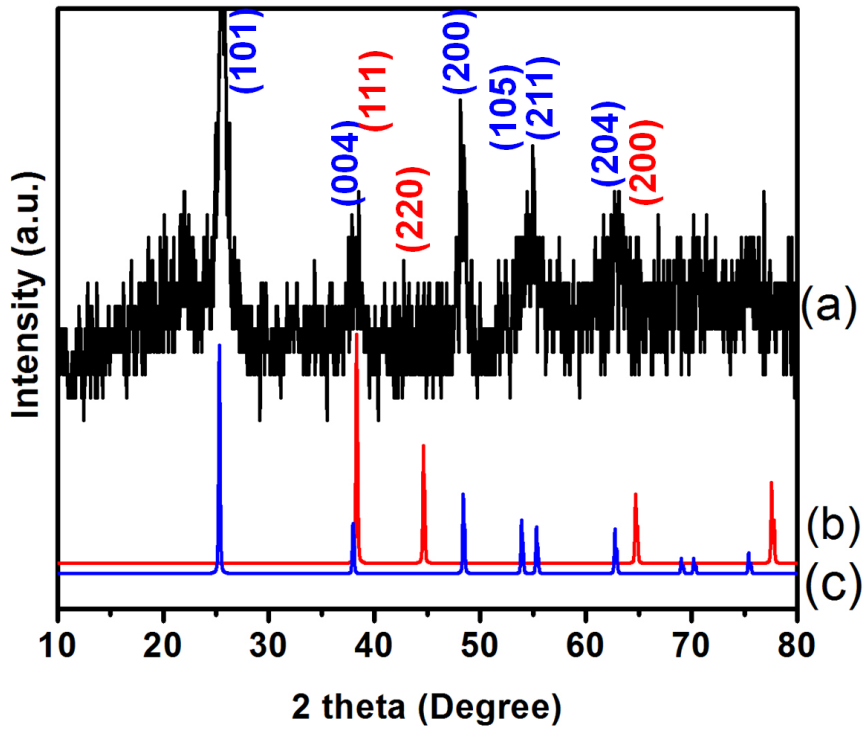

Fig. 2.14 (a) XRD pattern of 6 µm long Au-TiO_2 nanowire array and the calculated pattern of (b) Au (pdf # 00-001-1172, red) and (c) anatase TiO_2 (pdf #00-001-0562, blue).

One possible explanation for this increased trend in J_{sc} and η could be the absence of a partially insulating TiO_2 nanoparticle layer between the nanostructures and the FTO, resulting in better electron transport from the TiO_2 nanostructured array into the FTO. By utilizing the approach of others to attach the TiO_2 nanotubes on the FTO by a thin layer of TiO_2 nanocrystalline paste,[14,50-51] which has shown to provide good adhesion to TiO_2 nanostructures, we generated the first set of data. To further investigate the effect of this adhesive layer on the device performance, we applied a new method to transfer the nanostructures onto the FTO without the use of the adhesion layer. The new transfer process likely resulted in lower resistance between the anode and the FTO back contact.

To further investigate the reasons for higher photocurrent for the solar cells based on Au-TiO_2 core-shell nanowires, we measured the IPCE of ~3 µm long TiO_2 nanotube and Au-TiO_2 core-shell nanowire based solar cells. The data is shown in Figure 2.15 below.

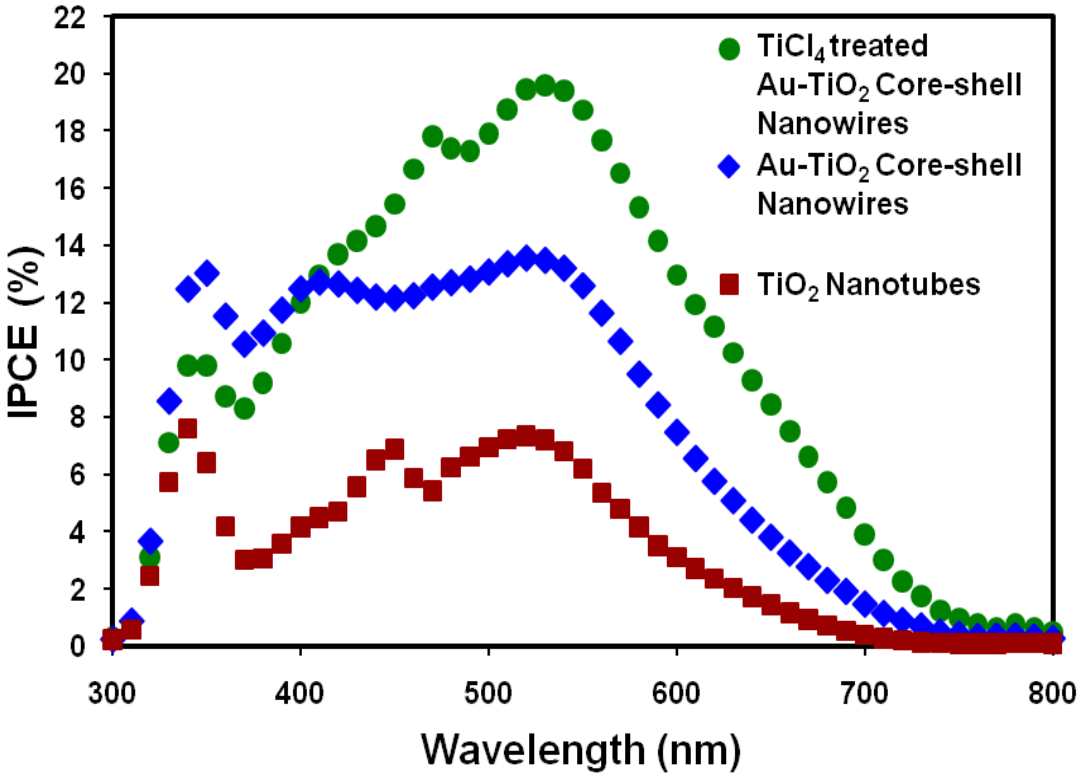

Fig. 2.15 IPCE spectra of DSSCs based on ~3 µm long TiO_2 nanotubes, Au-TiO_2 core-shell nanowires, and $TiCl_4$ treated Au-TiO_2 core-shell nanowires.

The IPCE for $TiCl_4$ treated Au-TiO_2 core-shell nanowire based device exhibited a peak of about 19.5% IPCE at 530 nm as well as a small shoulder at 400 nm. These peaks are in close agreement with the absorption spectrum for the N3 dye, which has local maxima at 400 and 533 nm, both corresponding to a metal-to-ligand charge transfer transitions. The IPCE for the Au-TiO_2 core-shell nanowire based device exhibited a peak of about 13.5% at 520 nm as well as small shoulder at 400 nm. Notably, the IPCE profile of the $TiCl_4$ treated Au-TiO_2 core-shell nanowire based device was broadened and red shifted with respect to the untreated Au-TiO_2 cell. Normalized versions of these spectra are provided in Fig. 2.16 below.

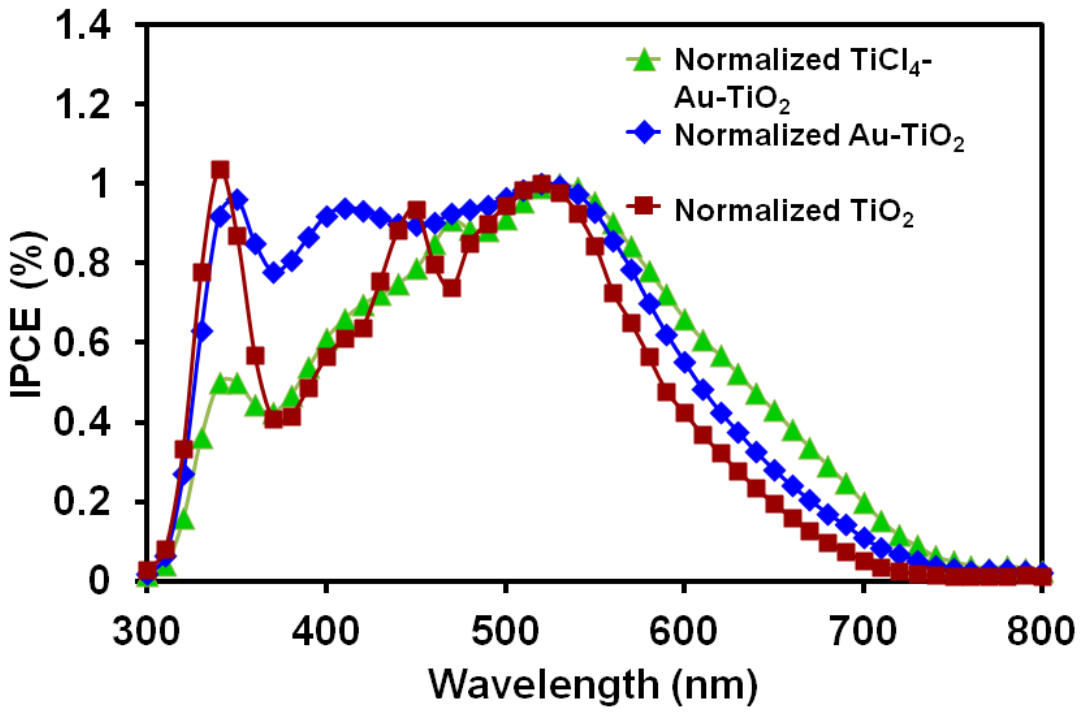

Fig. 2.16 The normalized IPCE spectra of $TiCl_4$-Au-TiO_2 nanowire, Au-TiO_2 nanowire and TiO_2 nanotube

The most likely reason for this broadened spectrum is the light scattering effect due to the TiO_2 layer on top of the Au-TiO_2 nanowire array surface. In addition, the Au-TiO_2 core-shell nanowire cell showed a red shift compared to the pure TiO_2 tubes, facilitating the utilization of sunlight in the full spectrum range. We propose that the cause of this observed red shift was due to scattering effects of the Au nanowire array.[52-53] The maxima of IPCE values measured at approximately 520 nm were 7.3% and 13.5% for TiO_2 nanotube and Au-TiO_2 core-shell nanowire cells, respectively. The difference in these IPCE spectra for both normalized and non-normalized has been given in Figure 2.17 below. The curves did not have a flat profile, indicating that there were wavelength dependent shifts in the IPCE spectrum after incorporation of gold in the TiO_2 nanotubes.[52]

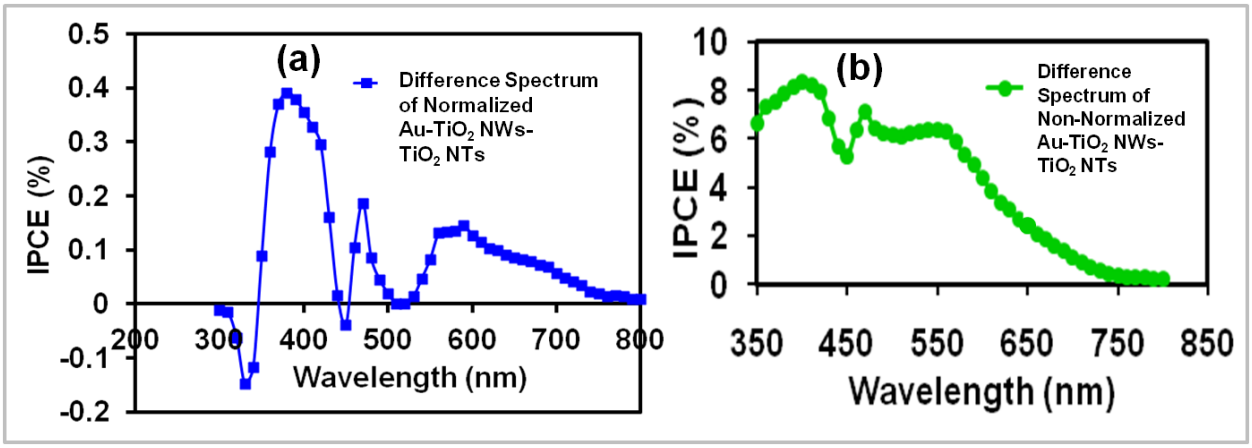

Fig. 2.17 The difference IPCE spectra of (a) normalized Au-TiO_2 nanowire and the TiO_2 nanotube DSSC, and (b) non-normalized Au-TiO_2 nanowire and the TiO_2 nanotube DSSC.

Furthermore in order to study the number of collected charge carriers to the number of photons incident on DSSCs made of longer nanostructures, we measured the IPCE of ~6 µm long nanostructure based devices. The data is presented in Fig. 2.18 below.

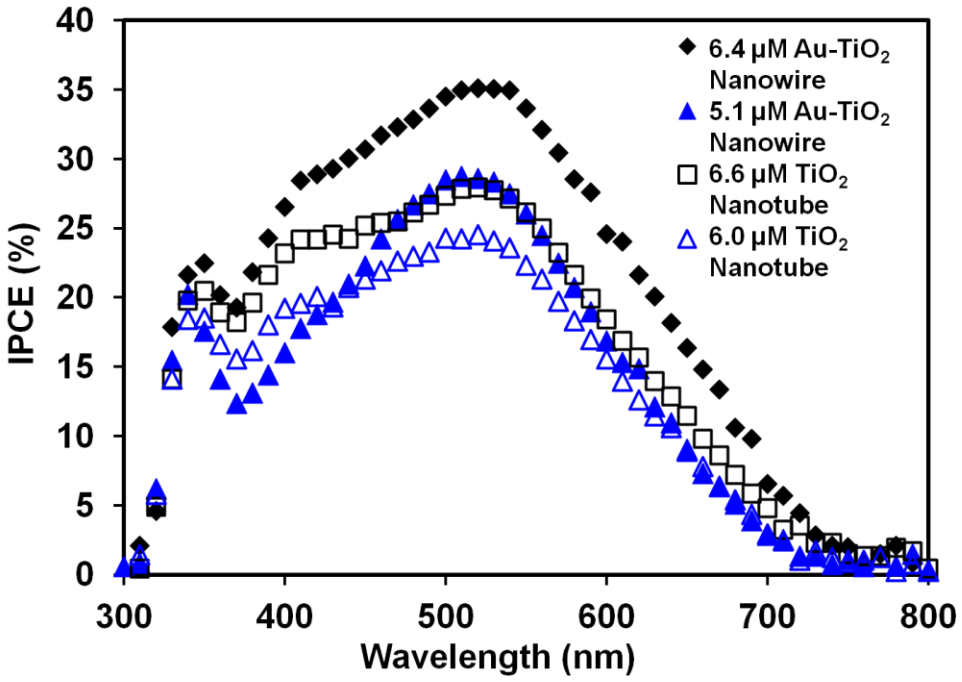

Fig. 2.18 The IPCE spectra of ~6 µm long TiO_2 nanotube DSSC and Au-TiO_2 nanowire DSSC.

The IPCE for a 6.4 μm Au-TiO_2 core-shell nanowire based device exhibited a peak of about 35% IPCE at 530 nm as well as a small shoulder at 620 nm. Overall, the IPCE spectra was enhanced with longer nanostructures as compared to the shorter (3μm) nanostructures (Fig.2.15). The obvious reason for this enhancement is improved light harvesting efficiency as well as more available dye to absorb more solar light in case of longer structures.

To evaluate the influence of gold insertion and $TiCl_4$ treatment on the dye adsorption on the photoanodes, the amount of chemisorbed dye was evaluated by desorption followed by quantitation with UV-Vis absorbance spectroscopy (Table 2). The amount of dye on each of the nanotube and nanowire structures was not substantially different even with $TiCl_4$ treatment. However, the mesoporous TiO_2 nanoparticle film alone demonstrated at least a 15% higher dye loading even though it was only half as thick as the anodes with both the mesoporous film and a nanotube or nanowire array combined. This result suggests that the adhesion layer was not effectively coated with dye when it was underneath a nanotube or nanowire array. Since overall dye loading was similar for all devices, other factors must have contributed to enhanced photocurrent for the Au-TiO_2 and $TiCl_4$ treated arrays. Most likely causes include increased light absorbance due to scattering and increased electron transport due to conducting pathways added by the gold nanowires. The former is related to light scattering due to the metallic gold in the Au-TiO_2 nanowires or TiO_2 particles deposited by $TiCl_4$ treatment. This explanation is consistent with other findings.[54-55] While IPCE data suggest enahncements due to scattering, additional studies are needed to fully assess the role of both light enhancement effects and electron tranport effects. Ongoing invetigations aim to elucidate details of the mechanisms that resulted in higher efficiencies for the Au-TiO_2 core-shell devices.

Table 2.2 Dye loading on various electrode types.
*Thickness of nanotube or nanowires array only; 2 μm nanoparticle film was underneath this layer.

Sample	Thickness (μm)	Adsorbed Dye Concentration ($\times 10^{-7}$ mol cm^{-2})
TiO_2 Nanoparticles	2.1	7.1
TiO_2 Nanotubes	2.5*	5.9
Au-TiO_2 Nanowires	2.3*	6.0
$TiCl_4$-Au-TiO_2 Nanowires	2.3*	6.1

2.5. Application of Ni-TiO_2 core-shell nanowire photoanodes in dye sensitized solar cells

The 3D core-shell Au-TiO_2 nanowire arrays showed improved photovoltaic performance, because of the greatly increased interface area, efficient charge separation, light scattering and transport properties. However, gold is a relatively expensive metal to be solely considered for applying in these advanced 3D core-shell devices. The above study was conducted as a proof of concept and gold was the choice of metal due to its inertness as well as excellent chemical and physical stability. Herein, the versatile method is carried out to fill the nanotubes with other less expensive metals such as Ni. Interestingly, high-yield Ni-TiO_2 core-shell nanowire arrays are observed arising from the conductive Ag layer on the back of the AAO. Subsequently, the reductively filled Ni-TiO_2 core-shell nanoarchitectures were applied as photoanode in advanced dye-sensitized solar cells (DSSCs).

2.5.1. Synthesis of Ni-TiO_2 core-shell nanowire arrays

After the TiO_2 nanotubes were obtained with the desired anatase phase and morphology, bottom up constant current electrodeposition was carried out in order to grow Ni-TiO_2 core-shell nanowire arrays. The same procedure was followed as described previously for synthesizing Au-TiO_2 nanowire arrays. The nickel plating solution (Nickel Sulfamate RTU) was purchased from Technic, Inc. Electrodeposition was carried out at room temperature using constant current with a single channel potentiostat (EG & G Instruments Model 263A). Nanowire arrays were grown into the TiO_2 nanotubes with a current of -0.9 mA for up to 30 minutes. This deposition allowed the wires to grow as far as to the top of the nanotubes, filling the entire channel with Ni nanowires. After deposition, the sample was rinsed with distilled water, and the AAO containing nanostructure was etched slowly with 3 M NaOH for 30 minutes. The obtained core-shell nanowire arrays were washed several times with distilled water resulting in well aligned nanowire arrays on a copper substrate. The nanowire arrays were later removed from the copper tape by washing with acetone.

2.5.2. Structural characterization of Ni-TiO_2 core-shell nanowire arrays

After the nanowire array generation, the structures were characterized both morphologically and compositionally, as imaged in Figure 2.19. It shows FESEM images of Ni-TiO_2 core-shell nanowire arrays on a Cu substrate. Figures 2.19 (a)-(c) represent the cross section and top views

of the Ni filled TiO_2 nanotubes taken at various magnifications. The images prove the successful growth of the Ni-TiO_2 core-shell nanoarchitectures and the inter-nanowire distance is ~10 nm. Figure 2.19 (d) presents the EDS data for the Ni-TiO_2 core-shell nanowire arrays, which clearly indicate the presence of Ni, Ti, and O core-shell nanowire cells. The active area of the anodes for each cell was in the range of 0.12 to 0.24 cm^2.

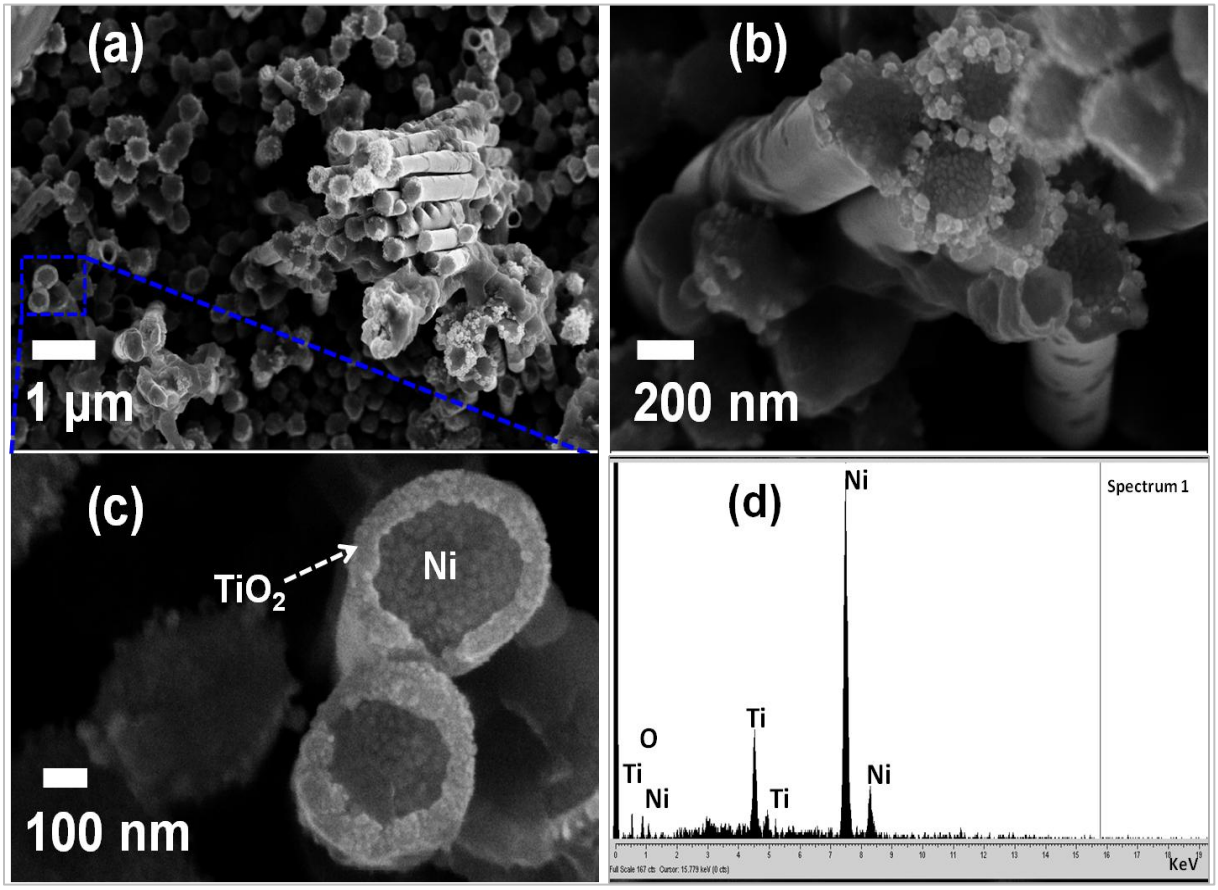

Fig. 2.19 FESEM images of Ni–TiO_2 core-shell nanowire arrays (a)–(c) and corresponding EDS data (d).

2.5.3. Solar Cell Fabrication and Electrochemical Characterization

Photoanodes utilizing TiO_2 nanotube and Ni-TiO_2 nanowire arrays were prepared by transferring the nanostructures onto a fluorine doped tin oxide (FTO) glass substrate obtained from Solaronix (TCO10-10, sheet resistance 10 Ω sq^{-1}) using the second method as described in

figure 2.4 (b). The resulting TiO_2 nanotube or Ni-TiO_2 core-shell nanowire film on the FTO was sensitized with dye (N-535, Solaronix) solution overnight. The same procedure was used for the fabrication of devices as was done for the Au-TiO_2 core-shell nanowire cells described above. The J-V characteristics were measured under 100 mW/cm^2 simulated sunlight (AM 1.5). The current-voltage characteristics of TiO_2 nanotube solar cells were compared with that of Ni-TiO_2

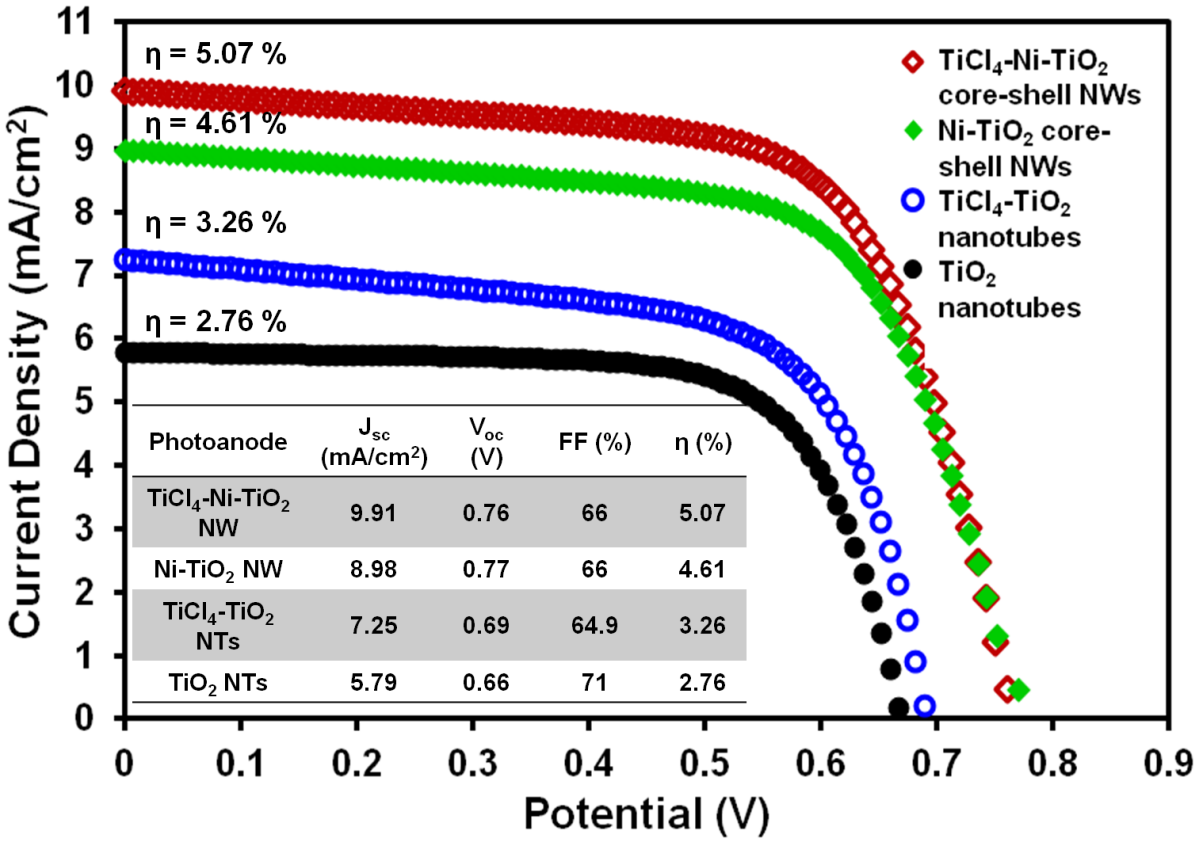

Photoanode	J_{sc} (mA/cm^2)	V_{oc} (V)	FF (%)	η (%)
$TiCl_4$-Ni-TiO_2 NW	9.91	0.76	66	5.07
Ni-TiO_2 NW	8.98	0.77	66	4.61
$TiCl_4$-TiO_2 NTs	7.25	0.69	64.9	3.26
TiO_2 NTs	5.79	0.66	71	2.76

Fig. 2.20 J–V curves for DSSC employing various photoanodes. Data presents TiO_2 nanotube (closed black circles), $TiCl_4$–TiO_2 nanotube (open blue circles), Ni–TiO_2 core-shell nanowire (closed dark red diamonds), and $TiCl_4$–Ni–TiO_2 core-shell nanowire (open green diamonds). Corresponding cell efficiencies and other parameters listed on each curve.

The comparative J-V characteristic studies of DSSCs with and without $TiCl_4$ treatment are plotted in Figure 2.20. Without $TiCl_4$ treatment, the TiO_2 based DSSCs yield an overall power conversion efficiency (η) of 2.76%. Whereas, the power conversion efficiency was increased to 3.26% with a short-circuit current density (J_{sc}) of 7.25 mA/cm^2, open circuit voltage (V_{oc}) of 0.69

V, and fill factor (FF) of 64.9% after the surface treatment with $TiCl_4$. By employing the reductively electrodeposited Ni-TiO_2 core-shell nanowire, the DSSC shows enhanced photo conversion efficiency (η = 4.61 %) with increased V_{oc}, J_{sc} and FF values (0.77 V, 8.98 mA/cm^2 and 66% respectively). Furthermore, the $TiCl_4$ treated Ni-TiO_2 core-shell nanowire DSSC showed even higher performance in terms of conversion efficiency and current generation up to η = 5.07 % and 9.91 mA/cm^2 respectively). However, the fill factor remains the same and open-circuit voltage is almost equal V_{oc}=0.77 V and 0.76 V for bare Ni-TiO_2 nanowire and $TiCl_4$-Ni-TiO_2 nanowire devices respectively. The FF results suggest that the series resistance in both types of devices was almost identical. Also, V_{oc} given by the energy level difference between the Fermi level of TiO_2 and the redox potential of the electrolyte did not change noticeably. This fact suggests that the enhanced efficiency observed in case of $TiCl_4$-Ni-TiO_2 nanowire cell was a combined effect of 1) the increased conductivity of nanotubes due to Ni filling that provides ease of electron transport in the DSSCs, leading to enhanced performance. 2) The conductive Ni nanowire inside the TiO_2 nanotube provides easy, uninterrupted, and fast charge conduction which separates the charge generation and collection functions by two separate entities improving charge transport and decreasing recombination 3) $TiCl_4$ treatment of this structure offers efficient anchoring of dye compared to bare Ni-TiO_2 nanowire arrays due to the rough TiO_2 surface present on top of these core-shell nanowire arrays.

Overall, with improved short-circuit current density (J_{sc}), and fill factor (FF) of the surface treated Ni-TiO_2 core-shell nanowire device demonstrated improved performance in solar conversion efficiency. The J-V curve data also suggests that not only gold, but also less expensive nickel can also be applied as the inner core metal in order to perform its job as a current collector and safely transport the electrons out of the oxide for better solar conversion efficiency.

2.6. Exploring the potential use of one-electron transfer ferrocene/ferrocenium hexafluorophosphate (Fc/Fc^+) redox couple in 3D Au-TiO_2 core-shell nanowire based DSSCs

Light harvesting in dye-sensitized solar cells (DSSCs) is achieved by a monolayer of sensitizer dye molecules located at the interface of a wide-bandgap oxide semiconductor electrode and a redox electrolyte[2]. The electrolyte does two major functions. First, a redox mediator is present that effectively regenerates the dye followed by a photoinduced charge injection from the dye into the semiconductor electrode. Second, it facilitates charge transport to the adjacent Pt counter-electrode, which is accomplished through an ion diffusion mechanism. The iodide/triiodide (I^-/I_3^-) couple is the most common redox couple used in DSSC electrolytes to date, that affords excellent energy conversion efficiencies of up to 10.3 % and 11.0% for metal-free organic sensitizers and ruthenium-based sensitizers respectively.[56-58]

Advantages of I^-/I_3^- redox shuttle:

- Efficient dye regeneration (reducing the oxidized dye formed from charge injection)
- Slow e^- transfer from TiO_2^- to I_3^- to allow for good charge collection allowing photo-injected electrons to be collected with near unity efficiency
- Good solubility to facilitate ion diffusion
- Fast electron-transfer kinetics with minimal over-potential at the counter electrode

Despite its superior performance, I^-/I_3^- couple does have some limitations that derive from its corrosive nature and complex redox chemistry[59] Overcoming these constraints could lead to further improvements in DSSC performance and ease of fabrication. The following equations summarize the electron transfer reactions involved in photocurrent generation in a DSSC based on the two-electron I^-/I_3^- redox system:

$$Dye + h\upsilon \rightarrow Dye^* \quad (2.1)$$

$$Dye^* \rightarrow e^-(TiO_2^-) + Dye^+ \quad (2.2)$$

$$Dye^+ + I^- \rightarrow (Dye - I) \quad (2.3)$$

$$(Dye - I) + I^- \rightarrow Dye + I_2^{-\cdot} \quad (2.4)$$

$$2I_2^{-\cdot} \rightarrow I_3^- + I^- \quad (2.5)$$

Dye regeneration involves the formation of the intermediate radical species $I_2^{\cdot-}$, which exhibits a more negative redox potential than the corresponding standard redox potential of I^-/I_3^- thus representing an additional energy activation barrier for the dye regeneration process.[59] Because the photovoltage of a DSSC is determined by the difference between the quasi-Fermi level of the TiO_2 and the Nernst potential of the redox couple, the energy mismatch between its redox potential and the HOMO level of the sensitizer lowers the open circuit voltage and thereby the conversion efficiency of the DSSC. The redox potential of the iodide/triiodide redox shuttle is about 0.34 V versus NHE, and the HOMO level of the standard sensitizer N3 is about 1.1 V versus NHE[60] (see Figure 2.21). Thus, there is a driving force needed for dye regeneration of about 0.8 V, which is the main loss in the DSSC. The achievable photocurrent is also limited by the I^-/I_3^- redox shuttle due to its inability to regenerate far-red absorbing dyes[61] and due to competitive absorption of the light by triiodide.[62]

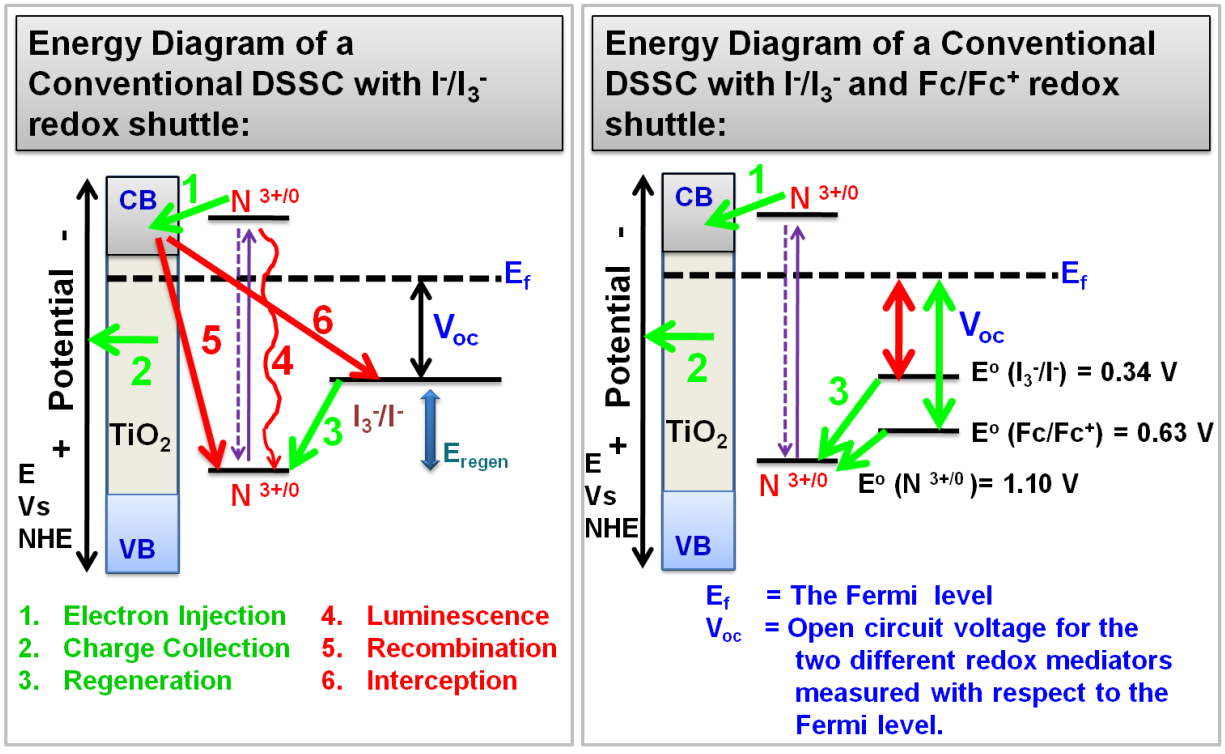

Fig. 2.21 Schematic energy diagram for a nanostructured TiO_2 electrode sensitized with N3 dye with iodide/triiodide, and ferrocene/ferrocenium redox couple versus normal hydrogen electrode (NHE).

Therefore, it is essential to find an alternative redox couple in order to achieve higher efficiency for DSSCs. One-electron outer-sphere redox couples, such as ferrocene/ferrocenium (Fc/Fc^+), are a promising alternative to the I^-/I_3^- redox couple because they should reduce the driving force needed to regenerate the dye (Figure 2.21).

Advantages of the Ferrocene/Ferrocenium (Fc/Fc^+) redox shuttle:

- Non-corrosive mediator exhibits well-defined electrochemistry (it is an IUPAC-recommended reference redox couple)
- Commercially available on a large scale
- It has a more favorable redox potential than the I^-/I_3^- redox couple (0.63 V vs. NHE), which should result in a higher open-circuit voltage (V_{oc})
- Dye regeneration by ferrocene is a simple one-electron transfer reaction that does not involve the cleavage or reformation of chemical bonds or the formation of high-energy intermediate radical species (unlike I^-/I_3^-)

Unfortunately, the use of kinetically fast one-electron outer sphere redox couples leads to a low photovoltage and photocurrent in DSSCs due to enhanced recombination with electrons in the TiO_2 conduction band.[62] We have tested the use of core-shell nanostructures to determine if they will facilitate the use of the ferrocene system as a redox couple.

2.6.1. Experimental

Ferrocene/Ferrocenium (Fc/Fc^+) Electrolyte Preparation

The electrolyte consisted of 0.13 M ferrocene (Aldrich), 0.013 M ferrocenium hexafluorophosphate (Aldrich), 0.2 M tetrabutylammonium hexafluorophosphate (Aldrich) in anhydrous propylene carbonate (Sigma-Aldrich).[63] Fresh solutions of the electrolyte were prepared each time due to stability problems of the ferrocenium ion in air. For comparison, some solar cells were prepared using 0.5 M 1-methyl-3-propylimidazolium iodide and 0.05 M iodine in propylene carbonate. The solar cell fabrication method was the same as described in section 2.3.1.

2.6.2. Electrochemical Characterization

Figure 2.22 shows the J-V characteristics under 1 sun illumination for a series of DSSCs sensitized with N535 dye using the ferrocene/ferrocenium and/or iodide/triiodide redox couple.

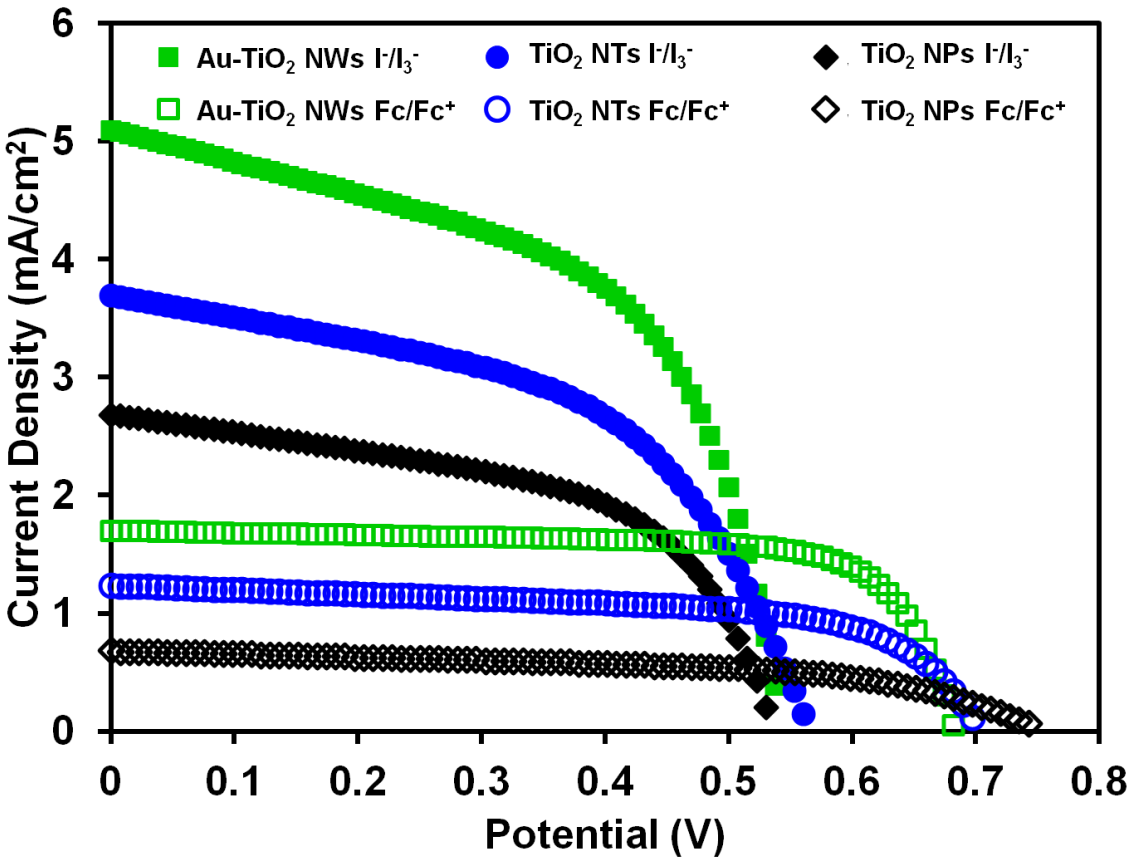

Fig. 2.22 J–V curves for DSSCs employing various redox shuttles. Data presents TiO_2 nanoparticle (NPs) cell with Fc/Fc^+ (open black diamonds) and I^-/I_3^- (closed black diamonds). TiO_2 nanotube (NTs) Fc/Fc^+ (open blue circles) and I^-/I_3^- (closed blue circles). Au-TiO_2 core-shell nanowire (NWs) Fc/Fc^+ (open green squares), and I^-/I_3^- (closed green squares). Corresponding cell efficiencies and other parameters are listed in table 2.2

Table 2.3 J-V characteristics of N535 dye-sensitized TiO_2 nanoparticle (NPs), TiO_2 nanotube (NTs), and Au-TiO_2 core-shell nanowire (NWs) DSSCs with I^-/I_3^- and Fc/Fc^+ redox shuttles under 1 sun.

Redox Shuttles	Photoanode Film Type	J_{sc} (mA/cm^2)	V_{oc} (V)	FF (%)	η (%)
Iodide/Tri-iodide I^-/I_3^-	Au-TiO_2 NWs	5.1	0.54	54 %	1.51 %
Iodide/Tri-iodide I^-/I_3^-	TiO_2 NTs	3.7	0.56	51 %	1.07 %
Iodide/Tri-iodide I^-/I_3^-	TiO_2 NPs	2.7	0.53	54 %	0.77 %
Ferrocene/ Ferrocenium Fc/Fc^+	Au-TiO_2 NWs	1.7	0.68	73 %	0.85 %
Ferrocene/ Ferrocenium Fc/Fc^+	TiO_2 NTs	1.2	0.70	62 %	0.54 %
Ferrocene/ Ferrocenium Fc/Fc^+	TiO_2 NPs	0.69	0.75	54 %	0.28 %

In the experiment, an efficiency of 0.85% was observed with Au-TiO_2 core-shell nanowire photoanode when the ferrocene/ferrocenium electrolyte was used in DSSCs in conjunction with the N535 ruthenium dye. In comparison, Au-TiO_2 core-shell nanowire with I^-/I_3^- redox shuttle showed an efficiency of 1.51%. However, the ferrocene/ferrocenium electrolyte showed an increase in V_{oc} and FF, with substantial decrease in J_{sc}, which left the overall efficiency under 1%. These outer sphere redox shuttles suffer from fast recombination via the substrate (shunting). This detrimental effect can be readily overcome by using appropriate blocking layer. As expected the Fc/Fc^+ DSSC clearly outperformed the classical DSSC in terms of V_{oc} increase. High photovoltage of 0.68 V was achieved for the Fc/Fc^+ DSSC, which exceeds the V_{oc} of I^-/I_3^- DSSC by 140 mV. This finding has great potential for future research and improvement of this one

electron transfer outer sphere redox shuttle provided the fast charge recombination at the TiO_2 conduction band is prevented.

2.7. Summary

We synthesized novel Au/Ni-TiO_2 core-shell nanoarchitectures and used them in dye sensitized solar cells. Adding gold cores to TiO_2 nanotubes resulted in a two-fold improvement in efficiency compared to hollow TiO_2 nanotubes. This improvement is likely the result of a combination of 1) improved pathways for electron transport out of the anode after photoinduced charge injection and 2) light focusing effects caused by the metal nanostructures. Furthermore, removing the partially insulating nanocrystalline TiO_2 nanoparticle layer form the bottom of the nanostructures resulted in significant improvements, suggesting that direct contact of the nanowire arrays with the conducting substrate is an important condition for good efficiency. For core-shell structures with an oxide thickness of less than 20 nm and a core conductor that spans the entire length of the tubes, electrons injected into the oxide only have to travel around 20 nm before reaching a conductor. As a consequence, the use of fast redox couples like ferrocene was possible with dye cells based on these core-shell structures. Further treatment of the core-shell structures with $TiCl_4$ resulted in an additional improvement in the efficiency. This improvement is likely caused by additional light scattering effects. The dye cells with core-shell photoanodes increased the current generation substantially, thereby increasing the solar conversion efficiencies. Au-TiO_2 core-shell structures treated with $TiCl_4$ exhibited a fourfold enhancement in cell efficiency compared to untreated TiO_2 nanotubes, suggesting that the new structures may lead to improved methods for producing more efficient DSSCs. Although this proof of concept study utilized gold core as the main conducting media, use of less expensive metal Ni was also feasible to produce the faster electron transport, affording significant improvements in DSSCs efficiency. This approach proved that Ni can also be used as the core material that will decrease the cost for these core-shell nanowire photovoltaic nanoarchitectures. Future studies may aim to develop further improved methods by increasing the length and surface area of TiO_2 as well as utilizing alternate redox couples with appropriate blocking layer which will prevent shunting paths and lead to higher efficiencies.

2.8. References

(1) O'Regan, B.; Moser, J.; Anderson, M.; Grätzel, M. *J. Phys. Chem.* **1990**, *94*, 8720.
(2) O'Regan, B.; Grätzel, M. *Nature* **1991**, *353*, 737.
(3) Kopidakis, N.; Schiff, E. A.; Park, N. G.; van de Lagemaat, J.; Frank, A. J. *J. Phys. Chem. B* **2000**, *104*, 3930.
(4) Law, M.; Greene, L. E.; Johnson, J. C.; Saykally, R.; Yang, P. D. *Nature Materials* **2005**, *4*, 455.
(5) Keis, K.; Magnusson, E.; Lindstrom, H.; Lindquist, S. E.; Hagfeldt, A. *Sol. Energy Mater. Sol. Cells* **2002**, *73*, 51.
(6) Fujihara, K.; Kumar, A.; Jose, R.; Ramakrishna, S.; Uchida, S. *Nanotechnology* **2007**, *18*.
(7) Beppu, T.; Yamaguchi, S.; Hayase, S. *Japanese Journal of Applied Physics Part 1-Regular Papers Brief Communications & Review Papers* **2007**, *46*, 4307.
(8) Enache-Pommer, E.; Boercker, J. E.; Aydil, E. S. *Applied Physics Letters* **2007**, *91*.
(9) Boercker, J. E.; Enache-Pommer, E.; Aydil, E. S. *Nanotechnology* **2008**, *19*.
(10) Feng, X. J.; Shankar, K.; Varghese, O. K.; Paulose, M.; Latempa, T. J.; Grimes, C. A. *Nano Letters* **2008**, *8*, 3781.
(11) Wang, W. L.; Lin, H.; Li, J. B.; Wang, N. *Journal of the American Ceramic Society* **2008**, *91*, 628.
(12) Jose, R.; Thavasi, V.; Ramakrishna, S. *Journal of the American Ceramic Society* **2009**, *92*, 289.
(13) Paulose, M.; Shankar, K.; Varghese, O. K.; Mor, G. K.; Hardin, B.; Grimes, C. A. *Nanotechnology* **2006**, *17*, 1446.
(14) Kang, T. S.; Smith, A. P.; Taylor, B. E.; Durstock, M. F. *Nano Letters* **2009**, *9*, 601.
(15) Mor, G. K.; Shankar, K.; Paulose, M.; Varghese, O. K.; Grimes, C. A. *Nano Letters* **2006**, *6*, 215.
(16) Macak, J. M.; Tsuchiya, H.; Ghicov, A.; Yasuda, K.; Hahn, R.; Bauer, S.; Schmuki, P. *Current Opinion in Solid State & Materials Science* **2007**, *11*, 3.
(17) Berger, S.; Tsuchiya, H.; Schmuki, P. *Chemistry of Materials* **2008**, *20*, 3245.
(18) Liu, S. M.; Gan, L. M.; Liu, L. H.; Zhang, W. D.; Zeng, H. C. *Chem. Mater.* **2002**, *14*, 1391.
(19) Kamat, P. V. *J. Phys. Chem. C* **2007**, *111*, 2834.
(20) Wang, M. L.; Huang, C. G.; Cao, Y. G.; Yu, Q. J.; Deng, Z. H.; Liu, Y.; Huang, Z.; Huang, J. Q.; Huang, Q. F.; Guo, W.; Liang, J. K. *J. Phys. D-Appl. Phys.* **2009**, *42*, 155104.
(21) Law, M.; Greene, L. E.; Radenovic, A.; Kuykendall, T.; Liphardt, J.; Yang, P. D. *J. Phys. Chem. B* **2006**, *110*, 22652.
(22) Chappel, S.; Chen, S. G.; Zaban, A. *Langmuir* **2002**, *18*, 3336.
(23) Arakawa, H. *Nippon Kagakkai Koen Yokoshu* **2001**, *86*, 16.
(24) Martinson, A. B. F.; Elam, J. W.; Liu, J.; Pellin, M. J.; Marks, T. J.; Hupp, J. T. *Nano Letters* **2008**, *8*, 2862.
(25) Xie, Y.; Zhou, L.; Huang, C.; Huang, H.; Lu, J. *Electrochimica Acta* **2008**, *53*, 3643.

(26) Banerjee, S.; Mohapatra, S. K.; Das, P. P.; Misra, M. *Chemistry of Materials* **2008**, *20*, 6784.
(27) Wang, Q.; Zhu, K.; Neale, N. R.; Frank, A. J. *Nano Letters* **2009**, *9*, 806.
(28) Mohapatra, S. K.; Kondamudi, N.; Banerjee, S.; Misra, M. *Langmuir* **2008**, *24*, 11276.
(29) Chen, S. G.; Paulose, M.; Ruan, C.; Mor, G. K.; Varghese, O. K.; Kouzoudis, D.; Grimes, C. A. *J. Photochem. Photobiol. A-Chem.* **2006**, *177*, 177.
(30) Fang, D.; Huang, K. L.; Liu, S. Q.; Qin, D. Y. *Electrochemistry Communications* **2009**, *11*, 901.
(31) Zhang, H. Y.; Ji, T. H.; Liu, Y. F.; Cai, J. W. *J. Phys. Chem. C* **2008**, *112*, 8604.
(32) Grätzel, M. *Philos. Trans. R. Soc. A-Math. Phys. Eng. Sci.* **2007**, *365*, 993.
(33) Lewis, N. S.; Nocera, D. G. *Proc. Natl. Acad. Sci. U. S. A.* **2006**, *103*, 15729.
(34) Zhu, W.; Wang, G. Z.; Hong, X.; Shen, X. S.; Li, D. P.; Xie, X. *Electrochimica Acta* **2009**, *55*, 480.
(35) Zhu, W.; Wang, G. Z.; Hong, X.; Shen, X. S. *J. Phys. Chem. C* **2009**, *113*, 5450.
(36) An, H. Q.; Li, J. X.; Zhou, J.; Li, K. R.; Zhu, B. L.; Huang, W. P. *Journal of Materials Chemistry* **2010**, *20*, 603.
(37) Mohapatra, S. K.; Banerjee, S.; Misra, M. *Nanotechnology* **2008**, *19*.
(38) Barbe, C. J.; Arendse, F.; Comte, P.; Jirousek, M.; Lenzmann, F.; Shklover, V.; Grätzel, M. *Journal of the American Ceramic Society* **1997**, *80*, 3157.
(39) Park, N. G.; Schlichthorl, G.; van de Lagemaat, J.; Cheong, H. M.; Mascarenhas, A.; Frank, A. J. *J. Phys. Chem. B* **1999**, *103*, 3308.
(40) Nazeeruddin, M. K.; Kay, A.; Rodicio, I.; Humphrybaker, R.; Muller, E.; Liska, P.; Vlachopoulos, N.; Grätzel, M. *J. Am. Chem. Soc.* **1993**, *115*, 6382.
(41) Zeng, L. Y.; Dai, S. Y.; Wang, K. J.; Pan, X.; Shi, C. W.; Guo, L. *Chin. Phys. Lett.* **2004**, *21*, 1835.
(42) Charoensirithavorn, P.; Ogomi, Y.; Sagawa, T.; Hayase, S.; Yoshikawaa, S. *J. Electrochem. Soc.* **2010**, *157*, B354.
(43) D. Menzies, R. C., Y. B. Cheng, G. Simon, L. Spiccia *Journal of the Australasian Ceramic Society* **2003**, *39*, 108.
(44) O'Regan, B. C.; Durrant, J. R.; Sommeling, P. M.; Bakker, N. J. *J. Phys. Chem. C* **2007**, *111*, 14001.
(45) Yip, C. T.; Mak, C. S. K.; Djurisic, A. B.; Hsu, Y. F.; Chan, W. K. *Appl. Phys. A-Mater. Sci. Process.* **2008**, *92*, 589.
(46) Barringer, E. A.; Bowen, H. K. *Langmuir* **1985**, *1*, 414.
(47) Siegel, A.; Goncalves, M. R.; Ameling, R.; Marti, O. *J. Opt. A-Pure Appl. Opt.* **2007**, *9*, S443.
(48) Sommeling, P. M.; O'Regan, B. C.; Haswell, R. R.; Smit, H. J. P.; Bakker, N. J.; Smits, J. J. T.; Kroon, J. M.; van Roosmalen, J. A. M. *J. Phys. Chem. B* **2006**, *110*, 19191.
(49) Ito, S.; Murakami, T. N.; Comte, P.; Liska, P.; Grätzel, C.; Nazeeruddin, M. K.; Grätzel, M. *Thin Solid Films* **2008**, *516*, 4613.
(50) Lin, C. J.; Yu, W. Y.; Chien, S. H. *Journal of Materials Chemistry* **2010**, *20*, 1073.
(51) Chen, Q. W.; Xu, D. S. *J. Phys. Chem. C* **2009**, *113*, 6310.
(52) Ferry, V. E.; Munday, J. N.; Atwater, H. A. *Advanced Materials* **2010**, *22*, 4794.
(53) Atwater, H. A.; Polman, A. *Nature Materials* **2010**, *9*, 205.
(54) Wang, Z. S.; Kawauchi, H.; Kashima, T.; Arakawa, H. *Coordination Chemistry Reviews* **2004**, *248*, 1381.

(55) Hu, L. H.; Dai, S. Y.; Weng, J.; Xiao, S. F.; Sui, Y. F.; Huang, Y.; Chen, S. H.; Kong, F. T.; Pan, X.; Liang, L. Y.; Wang, K. J. *J. Phys. Chem. B* **2007**, *111*, 358.
(56) Chen, C. Y.; Wang, M. K.; Li, J. Y.; Pootrakulchote, N.; Alibabaei, L.; Ngoc-le, C. H.; Decoppet, J. D.; Tsai, J. H.; Grätzel, C.; Wu, C. G.; Zakeeruddin, S. M.; Grätzel, M. *Acs Nano* **2009**, *3*, 3103.
(57) Zeng, W. D.; Cao, Y. M.; Bai, Y.; Wang, Y. H.; Shi, Y. S.; Zhang, M.; Wang, F. F.; Pan, C. Y.; Wang, P. *Chemistry of Materials* **2010**, *22*, 1915.
(58) Yu, Q. J.; Wang, Y. H.; Yi, Z. H.; Zu, N. N.; Zhang, J.; Zhang, M.; Wang, P. *Acs Nano* **2010**, *4*, 6032.
(59) Boschloo, G.; Hagfeldt, A. *Accounts of Chemical Research* **2009**, *42*, 1819.
(60) Zhang, Z.; Chen, P.; Murakami, T. N.; Zakeeruddin, S. M.; Grätzel, M. *Advanced Functional Materials* **2008**, *18*, 341.
(61) Schlichthorl, G.; Huang, S. Y.; Sprague, J.; Frank, A. J. *J. Phys. Chem. B* **1997**, *101*, 8141.
(62) Gregg, B. A.; Pichot, F.; Ferrere, S.; Fields, C. L. *J. Phys. Chem. B* **2001**, *105*, 1422.
(63) Feldt, S. M.; Cappel, U. B.; Johansson, E. M. J.; Boschloo, G.; Hagfeldt, A. *J. Phys. Chem. C* **2010**, *114*, 10551.

Chapter 3

Radial Core-Shell Au–TiO_2 Nanoarchitectures Formed by Pulsed Laser Deposition for Enhanced Efficiency in Dye Sensitized Solar Cells

Abstract

Vertically aligned Au-TiO_2 core-shell nanowire arrays were synthesized by using a two step method. Au nanowires were first synthesized using a galvanostatic constant current electrodeposition technique. A shell of anatase TiO_2 was subsequently grown on the Au nanowires using pulsed laser deposition. The core-shell nanostructures were then characterized using electron microscopy, electron diffraction, and X-ray diffraction techniques. The results showed that the wires were highly aligned and well separated. Dye sensitized solar cells were then fabricated using the core-shell nanowire arrays as photoanode, N535 dye as the sensitizer and I_3^-/I^- as the redox electrolyte. The Au nanowires inside the highly crystalline TiO_2 anatase nanoshell provided a direct conduction path and improved transport for electrons between the TiO_2 and the conducting substrate. This efficient electron conduction out of the oxide semiconductor enhanced the current generation as well as the power conversion efficiency of the cell. The influence of the $TiCl_4$ post-treatment on Au-TiO_2 core-shell nanowire electrodes was investigated and compared to nontreated films. Cell efficiencies were improved due to higher photocurrents as a result of this post-treatment. Optical effects of the metal nanowire may have also contributed to improved performance.

3.1. Introduction

Limited energy resources present an important problem for society in the 21st century. Solar energy, as a clean and renewable energy source, is expected to replace fossil fuels. Dye sensitized solar cells (DSSCs) have been studied as attractive alternatives for electricity generation from solar light due to their high efficiency and cost effectiveness.[1] In a DSSC, a dye adsorbed onto the mesoporous TiO_2 electrode absorbs a photon from solar light and forms an excited state dye which can be thought of as an electron-hole pair exciton. The excited dye transfers an electron to the semiconducting TiO_2 and the electron is then transferred to the conducting substrate electrode. This process separates the electron-hole pair, leaving the hole on the dye. The hole is filled by an electron from the iodide ion supplied by the (I_3^-/I^-) redox couple. Even though nanoparticle films provide high surface area for dye adsorption, the electron transport rate in the TiO_2 is comparatively slow because of low electron diffusion coefficients. The slow diffusion is caused by TiO_2 nanoparticles having multiple trapping and de-trapping events occurring in the porous semiconductor grain boundaries.[2] Previous results clearly show that the electron transport process in disoriented polycrystalline mesoscopic thin films is vulnerable to trap limited electron diffusion and recombination losses at the particle interface since the electrons travel by a random walk through the network of interconnected oxide nanoparticles.[3-4] This effect is likely a main cause of the high interface recombination reaction rates and limits the device efficiency. Thus, to resolve these problems, many attempts have been put forth to improve the state-of the-art DSSC design. A DSSC based on an array of one-dimensional (1D) ZnO nanostructures was first introduced by Law *et al.* in 2005,[5] and there are reports of synthesizing nanoparticles/nanowire composites[6] and nanoparticles/nanotube composites[7] of TiO_2 anatase phase with an aim of achieving enhanced efficiency with a good conducting media. Particularly, DSSCs made of TiO_2 ordered structures as photoanode can produce improved solar cell devices due to the prolonged stability of the anatase phase, faster electron transport, and slower charge recombination. However, despite all these positive aspects of TiO_2 nanoarchitectures as photoanodes in DSSCs, the wide band gap (3.2 eV) permits only use of ultraviolet light without a dye sensitizer. The need of decreasing the recombination of electrons and holes generated by band gap excitation persists, and TiO_2 solar cell efficiency is limited due to the bulk defects and grain boundaries which are important causes of limited photoconversion efficiency. Three dimensional core-shell structures having TiO_2 as

shell and various guest metal/metal oxide as core via electrodeposition have been reported.[8-13] Zhu *et al.* reported metal nanoparticle chains and rods inside TiO_2 nanotubes using an alumina membrane as template.[14-15] There are also reports of metal doped TiO_2 nanobelts,[16] metal coated TiO_2 nanotubes[17] and metal oxide TiO_2 nanorod-nanotube arrays[18] with suggested application as photoanode materials in photovoltaics. There are a few reports on using nanoparticle decorated ZnO-TiO_2 core-shell nanorod arrays[19] and of two different wide band gap semiconductors as anodes in DSSCs.[20-23] Additional work applied carbon nanofiber (CNF)-TiO_2 core-shell photoanode materials in DSSCs[24-28] which provided easy, uninterrupted transport of electrons from the semiconductor to the collecting anode. The efficiency remained in the 1-5% range. Various explanations have been proposed for why the above approaches failed to enhance the performance of DSSCs, including lower surface area at the semiconductor surface for dye loading[29] and high series resistance between the nanostructure and the electrodes.[30] A thorough knowledge and critical explanation of the above new architectures is still required in order to address the mechanisms and behavior.

One possible way to boost DSSC power conversion efficiency is to increase the diffusion length, L_n of electrons within the oxide layer relative to the thickness of the oxide film, d, so that, $L_n/d >> 1$ and $d > \alpha^{-1}$, where α is the wavelength dependent absorption coefficient of the dye film.[20] Current can be increased by making $L_n >> d$. The best TiO_2 cells have $L_n/d \leq 2$.[31] A higher L_n/d ratio of the nanocrystalline film can be achieved by decreasing d while maintaining $d > \alpha^{-1}$ by using high molar absorption coefficient dyes [32] or TiO_2 semiconductors with very high surface area[33].

Since one of the major problems in achieving high efficiency is poor electron transport, we have synthesized Au-TiO_2 core-shell nanowire arrays to overcome this barrier. The motivation of this study was to create a semiconductor morphology that can provide both high surface area for maximum dye adsorption and efficient electron transport that delivers the electrons to the back contact with minimal recombination. The core-shell nanowires provided an easy pathway for electron conduction from the TiO_2 layer through the Au core while maintaining the thickness of the TiO_2 layer much smaller than the mean electron diffusion length which is reportedly in the range of 10-20 μm for mesoporous films.[34] Au nanowires were fully coated with a 30-50 nm layer of anatase with a large TiO_2 surface area available for dye adsorption. There are very few reports

on the fabrication of core-shell structures and their use as electrodes in DSSC. Chou *et al.* first reported a nanostructure for DSSC based on indium tin oxide (ITO) coated with a TiO_2 layer.[35] Joanni *et al.* reported the synthesis of ITO-TiO_2 core-shell nanowires and their application as photoanodes in DSSCs[36] followed by Ye *et al.* who have achieved template based synthesis of nanowire-nanotube hybrid arrays[37] and Wang *et al.* who used electrophoretic deposition to achieve ITO-TiO_2 nanowires.[38] We have previously prepared core-shell Au-TiO_2 nanostructures for photovoltaics using a sol-gel approach.[39] In this approach, we adopted a template based method for preparing these nanostructures because there are a number of useful features associated with this method. For example, it allows flexibility in tuning the length and diameter of the nanowires. We have used porous alumina membranes (also known as anodic aluminum oxide, AAO) to synthesize our photoanode materials.

3.2. Experimental methods

3.2.1. Preparation of Au-TiO_2 core-shell nanowire arrays

Au nanowires were synthesized by a previously reported method.[40] We have used porous alumina membranes as templates to grow Au nanowires using galvanostatic constant current electrodeposition. AAO membranes (Whatman Corp.) were 25 mm in diamter, had an average pore diameter of 200 nm, and had a thickness of 60 µm. Electrochemical deposition was accomplished by converting the AAO into a working electrode (cathode) by sputtering one side with Ag (~20 nm thick). The Ag film side was attached to one side of a piece of two sided copper tape (3M) with the polymer coating intact on the opposite side to avoid undesired metal deposition on the Ag film or copper during electroplating. The AAO was fixed with an alligator clip and was immersed in the plating solution with the open pores exposed to the electroplating solution. The other side of the alligator clip was connected to the potentiostat. A platinum wire was used as the counter electrode and Ag/AgCl (Accumet) was used as the reference electrode. The Au plating solution (Orotemp 24) was purchased from Technic, Inc. Electrodeposition was carried out at room temperature using galvanostatic constant current of -0.9 mA with a single channel potentiostat/galvanostat (Model 263A, EG&G Instruments) to grow Au nanowires in the nanopores of the AAO membrane. It took 60 minutes to grow 3-4 µm long Au nanowires. The sample was washed with DI water several times. The AAO membrane was dissolved using 3 M NaOH and washed with DI water to remove the NaOH residue. Finally, the sample was dried in

air to achieve the arrays of Au nanowires standing vertically on the Cu tape. The Au-TiO_2 core-shell nanowire arrays were fabricated by pulsed laser deposition (PLD) of a TiO_2 shell on the gold nanowire array. The overall schematic of the synthesis is given in Figure 3.1 below.

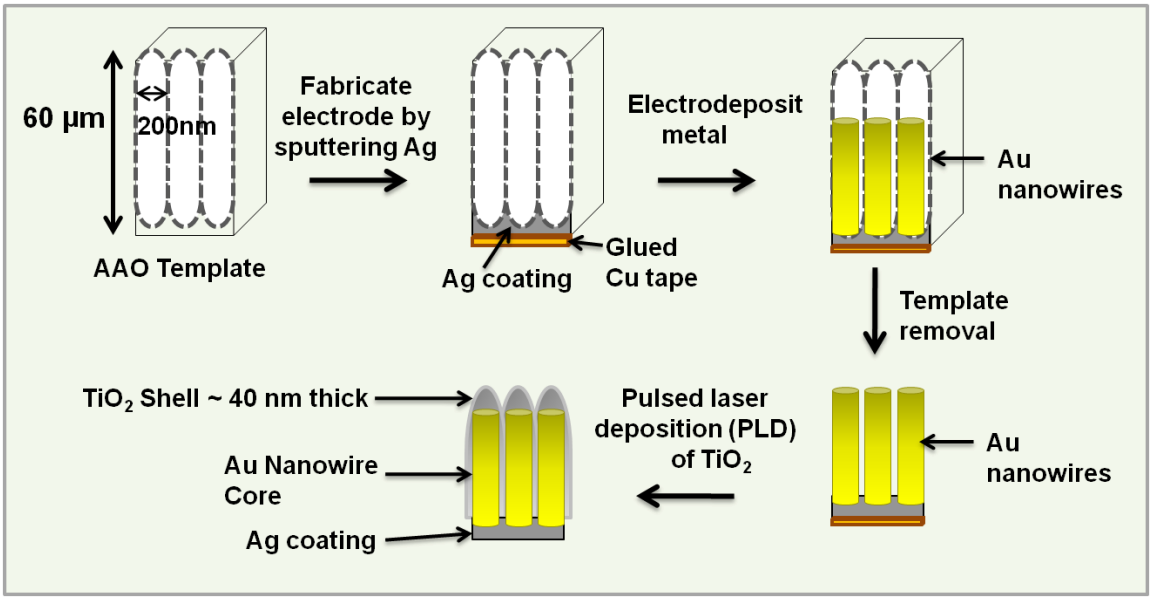

Fig. 3.1 Schematic for synthesizing metal-oxide core-shell nanowires

PLD is a very unique technique that uses laser pulses to ablate the specified target to produce the depositing flux. The flux is subsequently deposited on the substrate facing the target to create the desired crystals. The depositing species arrive in short bursts in the order of 10-100 µs. The kinetic energy of the depositing ions is of the order of 10-100 eV. There is a report in which the authors have used this PLD to synthesize transparent semiconducting CuI thin films and applied them as photoanode material in DSSCs.[41] Others have synthesized nanocrystalline TiO_2 thin films on conducting ITO substrates using PLD and later used them as anodes in DSSCs.[42-44] In our case, the Au nanowire arrays were employed as the substrate and the target was a TiO_2 anatase pellet. A 12 mm diameter TiO_2 pellet was prepared by pressing anatase TiO_2 nanopowder of 30-40 nm in diameter (Aldrich) with a Carver manual pellet press and then sintering at 500 ^oC for 12 hours. A neodymium-doped yttrium aluminum garnet (Nd:YAG) laser was used to ablate the TiO_2 disc target. The laser wavelength, energy density, deposition time and repetition were 266 nm, 650 mJ/cm^2, ~30 min and 5 Hz, respectively. The distance from the target to the substrate

was 3 cm. During the deposition, the pressure in the system was pumped to ~10^{-3} torr and the temperature was kept at 500 ^{o}C in order to preserve the anatase phase and stoichiometry of TiO_2. The Au-TiO_2 nanostructures came off of the Cu tape due to the melting of the glue at the elevated temperature during the PLD process. However, the nanostructures were supported by the ~20 nm Ag film that was sputtered onto the AAO membrane prior to electrodeposition. The core-shell nanostructures were pasted onto a fluorine doped tin oxide (FTO) glass substrate obtained from Solaronix (TCO10-10, sheet resistance 10 Ω sq^{-1}) by means of conducting Ag paint (Ted Pella) in order to make the back side (Pt) illuminated DSSCs. The details concerning transfer of nanostructures onto FTO for both back side and front side illuminated DSSCs will be discussed later.

3.2.2. Preparation of platinized counter electrode and electrolyte

A platinum coated FTO counter electrode was prepared bybrushing with a thin layer of Platisol T (Solaronix). The I^-/I_3^- electrolyte was prepared using 0.6 M 1-methyl-3-propylimidazolium iodide, 0.05 M iodine, 0.05 M LiI and 0.5 M *tert*-butylpyridine in 25 mL acetonitrile:valeronitrile (1:1 volume ratio). Two small holes were drilled in the glass of the platinum electrode in order to later inject the electrolyte.

3.2.3. Preparation of mesoporous TiO_2 nanoparticles film on FTO

The mesoporous anatase TiO_2 film used as photoanode for comparison with the core-shell photoanodes was prepared as reported.[45] The prepared TiO_2 paste was spread on a FTO substrate by doctor-blade technique to give a uniform flat and smooth surface using an adhesive tape spacer. The thickness of the nanoparticles film was measured using a profilometer (SLOAN Dektak II).

3.2.4. Surface passivation of the Au-TiO_2 core-shell nanowires

In some cases, the Au-TiO_2 nanowire film on FTO was also subjected to 0.1 M $TiCl_4$ (Aldrich) aqueous solution in a closed chamber for 24 hours, then washed with distilled water. The electrode was annealed again at 450 ^{o}C for 30 minutes. The color of the electrode was off-white after the $TiCl_4$ treatment. These anodes were treated with ruthenium dye and the DSSC devices were fabricated

3.3. Characterization & fabrication

3.3.1. Structural characterization

After synthesis, the desired Au- TiO_2 core-shell nanoarchitectures were characterized using different probe techniques such as field emission scanning electron microscopy (FESEM), energy dispersive spectroscopy (EDS), transmission electron microscopy (TEM) and X-ray powder diffraction (XRD).

3.3.2. Solar cell fabrication

To make front side (core-shell nanowire) illuminated DSSCs, the Ag film was etched away first by conc. HNO_3 and the resulting Au-TiO_2 core-shell nanowire array was pasted onto a FTO substrate (See Fig. 3.2 and 3.3 below) for details concerning transfer of nanostructures onto FTO for both back side and front side illuminated DSSCs. The resulting Au-TiO_2 nano structures on the FTO were sensitized for 24 hours by soaking in dye solution. A ruthenium dye solution (N-535, Solaronix) was prepared by mixing 25 mg of the solid in 1 mL of ethanol. The two electrodes were sandwiched together by using Surlyn® sealant (Solaronix), and the sandwiched electrodes were sealed by heating for 5 minutes with a heat gun. The electrolyte was carefully introduced into the space between the two electrodes through one hole on the Pt electrode with a syringe. The drilled holes were then sealed in order to prevent electrolyte evaporation.

3.3.3. Device characterization

Photovoltaic data were measured using a Newport® 50-500W 67005 solar simulator set at 100 mW/cm^2 full spectrum power. Current density-voltage (J-V) curves were generated using a Keithley 2400 source meter. The light intensity of the xenon light source was calibrated by using an NREL calibrated silicon photodiode (Hamamatsu S1787-08 for visible to IR range).

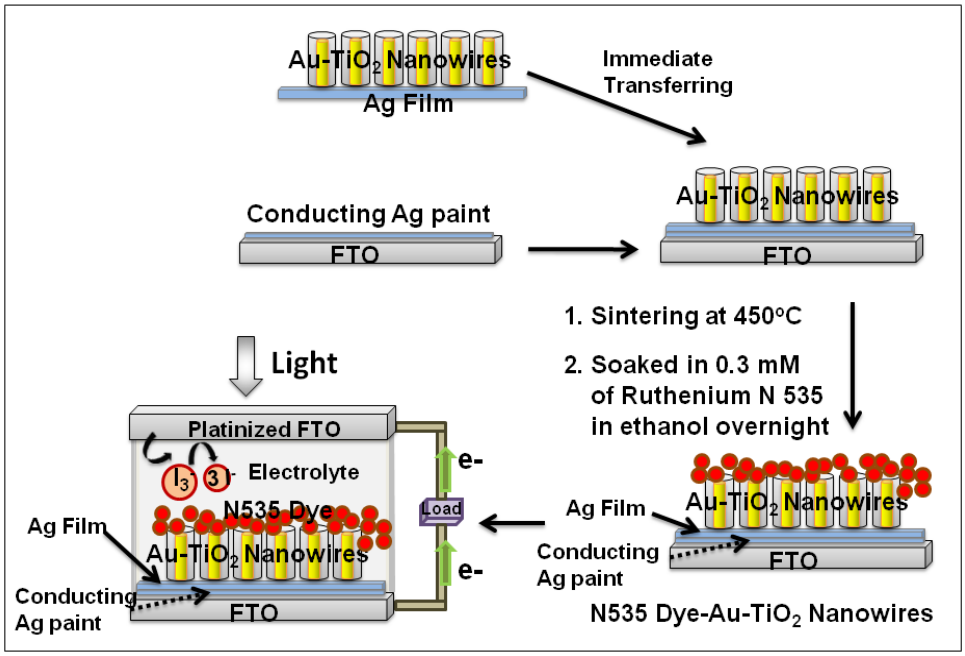

Fig. 3.2 Schematic of backside illuminated DSSCs

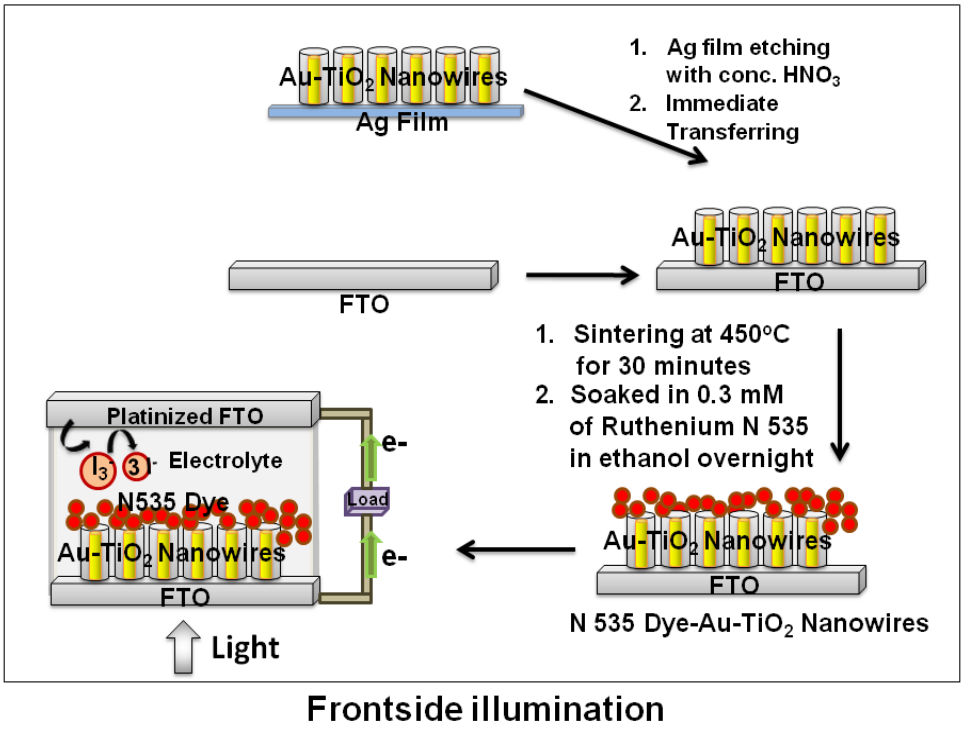

Fig. 3.3 Schematic of frontside illuminated DSSCs

3.3.4. Actual surface area calculations and dye loading

The approximate surface area of the nanowires was calculated by referring to a FESEM image of one array of Au-TiO_2 nanowires. Four different areas of 4 μm^2 each were randomly selected. The numbers of nanowires in each area were manually counted and averaged to be 23. The length (l) and radius (r) of one nanowire was 4.5 µm and 0.15 µm respectively as determined from the FESEM image. Calculating and adding the surface area formula for a cylinder (i.e $2\pi rl$) and for a circle (i.e. πr^2), the surface area of one nanowire was calculated to be 4.31 μm^2. The actual surface area of 23 nanowires was calculated by multiplying 23 by 4.31 μm^2 which was equal to 99.2 μm^2. Therefore the actual surface area was approximately 25 times greater than the flat surface area, not taking into account additional area due to surface roughness. For the 0.24 cm^2 device, the approximate total surface area of the wires was calculated to be 5.96 cm^2. The amount of dye adsorbed on the nanostructures was measured by desorbing the dye with 0.2 M NaOH in ethanol. The concentration of desorbed dye was determined by absorbance using a Cary 500 UV-Vis spectrophotometer.

3.4. Results and discussion

3.4.1. Au nanowire arrays

Figure 3.4 shows the low (a) and high (b) magnification FESEM images of electrochemically synthesized Au nanowire arrays. Fig.3.4 (a) illustrates a typical area (50 × 50 µm) of the nanostructures imaged by FESEM. The inter-wire distance was about 100-400 nm as is evident in Fig. 3.4 (b). Fig 3.4 (c) shows that the average length of the Au nanowires was ~3-5 µm and the diameter was ~200 nm. The EDS spectrum in Fig. 3.4 (d) shows the elemental analysis of the nanowires which gives peaks for Au. The peak for carbon was generated from the carbon tape used in the sample holder during FESEM imaging. Fig. 3.5 (a) shows a representative TEM micrograph of a Au nanowire from the array. This image confirms the nanowire diameter of ~200 nm. Fig.3.5 (b) shows the EDS data for the nanowire showing peaks for Au. The Cu peak is from the Cu grid. To examine the overall crystallinity of the nanowire arrays, the XRD pattern was collected and is shown in Figure 3.6 The XRD data also confirm the face centered cubic structure of metallic gold.

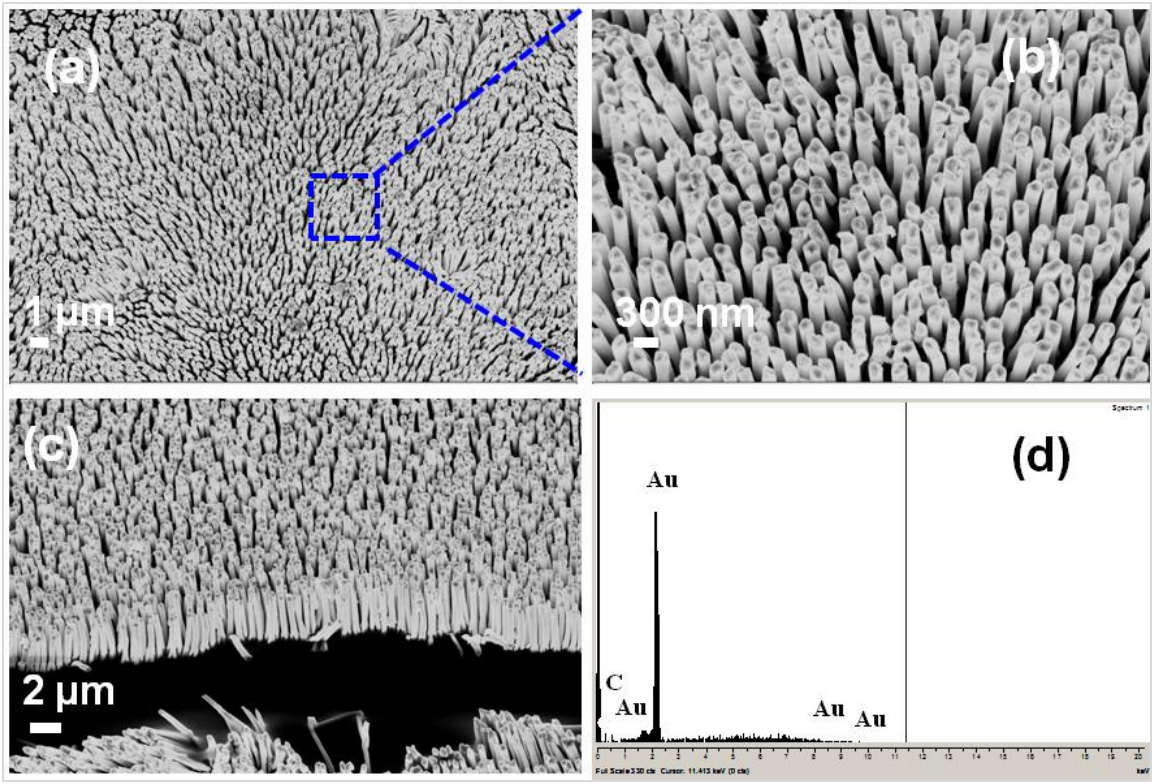

Fig. 3.4 (a), (b) and (c) FESEM images of Au Nanowires. Fig. 3.4 (d) EDS data for the nanowire array.

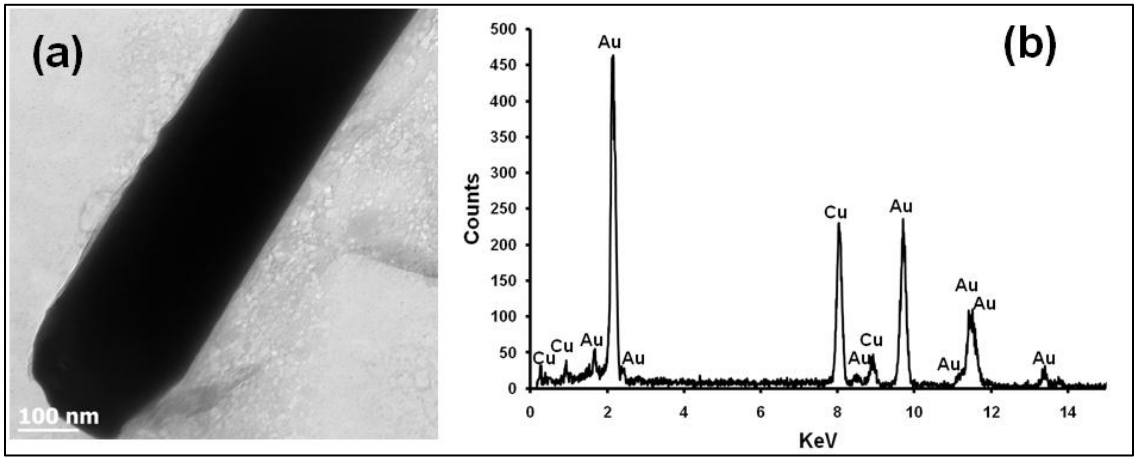

Fig. 3.5 TEM image of Au Nanowire. Fig. (b) EDS of Au nanowire generated from the nanowire shown in Fig. 3.5 (a).

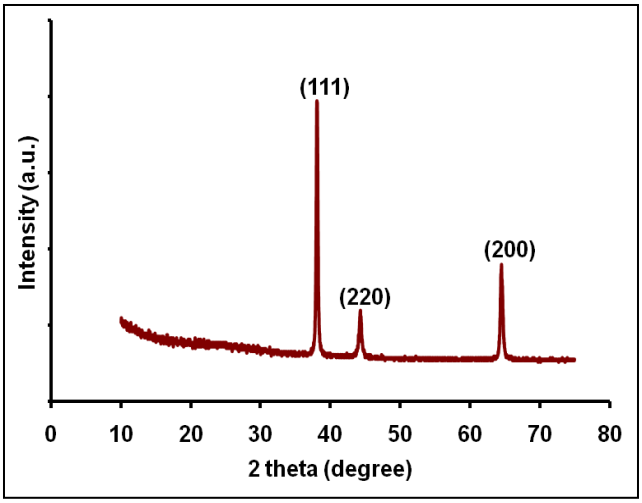

Fig. 3.6 XRD pattern of prepared Au nanowires.

3.4.2. Au-TiO_2 core-shell nanowire arrays

The Au-TiO_2 core-shell nanowire arrays were fabricated by electrodeposition followed by pulsed laser deposition. The morphology and the composition of the synthesized Au-TiO_2 core-shell nanowires were examined by FESEM and EDS. The images clearly illustrate the high alignment of the core-shell nanowire arrays on the substrate and that they are composed of Au and TiO_2. Figure 3.7 represents the FESEM images of Au-TiO_2 core-shell nanowire arrays. Fig. 3.7 (b) reveals the high surface area available on the rough oxide surface, which will allow for more dye adsorption. Fig. 3.7 (c) shows a large area of the Au nanowire sample that is completely covered with TiO_2 with the nanostructures standing vertically on the Ag film. This image is representative of the entire sample. The EDS data in Fig. 3.7 (d) show that the structure is made of Au, Ti and O without any detectable impurities.

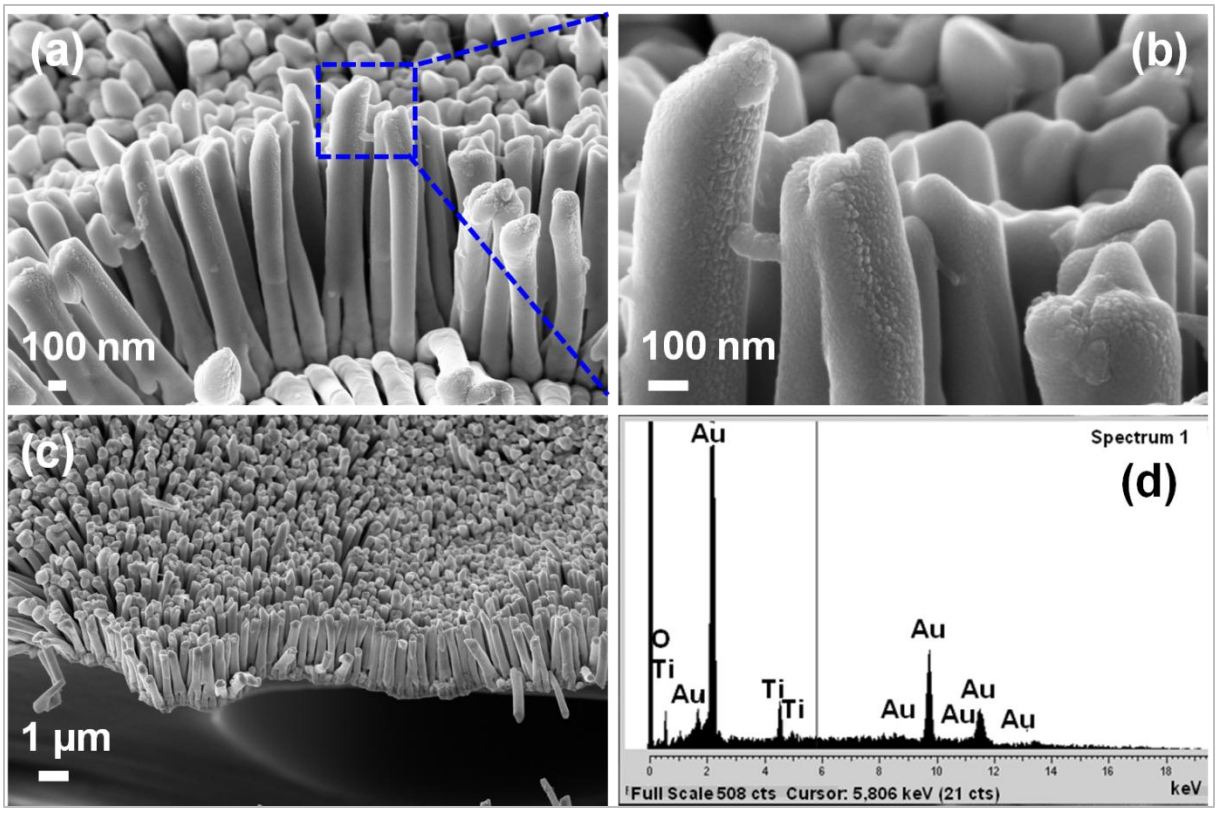

Fig. 3.7 (a), (b) and (c). FESEM images of Au-TiO_2 core-shell nanowires. Fig. 3.7 (d) EDS elemental analysis data of the as grown Au-TiO_2 core-shell nanowire arrays giving peaks for Au, Ti and O.

Figure 3.8 (a) represents FESEM images from the top view of a Au-TiO_2 core-shell nanowire array along with the corresponding EDS spectrum in Fig.3.8 (b) taken from the bottom of one nanowire. These data show that the PLD technique is capable of coating even the bottom of the Au nanowires with the desired oxide material. This achievement was not possible with sputtering where only the tip of the wires was coated with Ti layers (images not shown). Figure 3.8 (c) represents the uniform silver coating on the back of the Au-TiO_2 nanowire array. The PLD approach was able to completely coat all exposed metal and result in a structure in which only TiO_2 was exposed to the electrolyte solution of the DSSC. It has been reported for PLD that variation of the laser fluence, background gas pressure, deposition temperature or time has high impact on the thickness of the semiconductor layer.[46-48] In our case, deposition time was ~30 minutes.

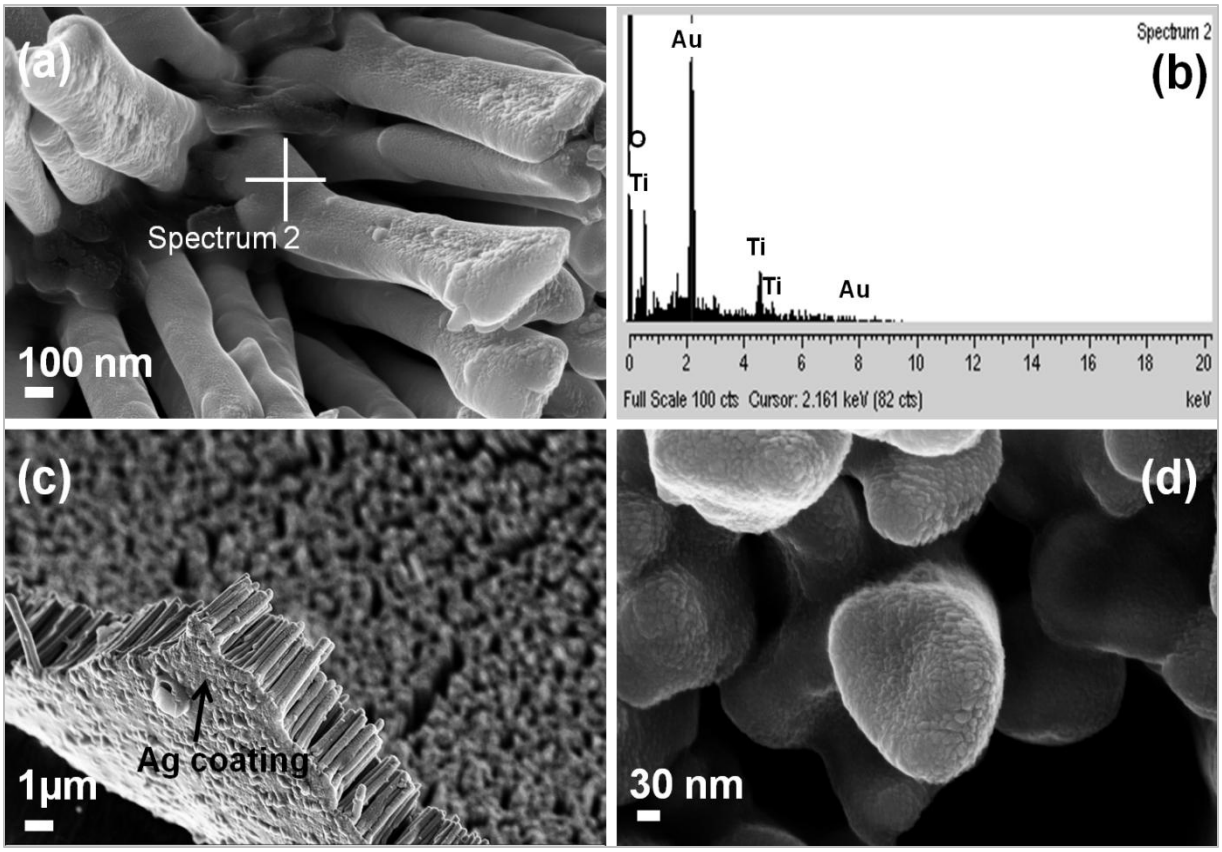

Fig. 3.8 FESEM images of Au-TiO_2 core-shell nanowire arrays; (a) top view of array of nanowires, (b) EDS elementary analysis data of the as grown Au-TiO_2 core-shell nanowire arrays giving peaks for Au, Ti and O), (c) array of Au-TiO_2 core-shell nanowires showing the Ag film on which they are supported, (d) highly magnified top view of the Au-TiO_2 core-shell nanowires.

TEM imaging was used to examine the structure and the thickness of the TiO_2 shell of core-shell nanowires after deposition of TiO_2 using PLD. The results are shown in Figure 3.9. Compared with the TEM image of bare Au nanowires given in Fig. 3.5 (a), the TiO_2 coated nanowire surface was very rough as shown in Fig. 3.9. A continuous shell of TiO_2 is evident on all parts of the wire surface, with a thickness of ~40 nm on the sides of the wires and slightly thicker at the tip. EDS analysis confirmed the presence of both gold and Ti.

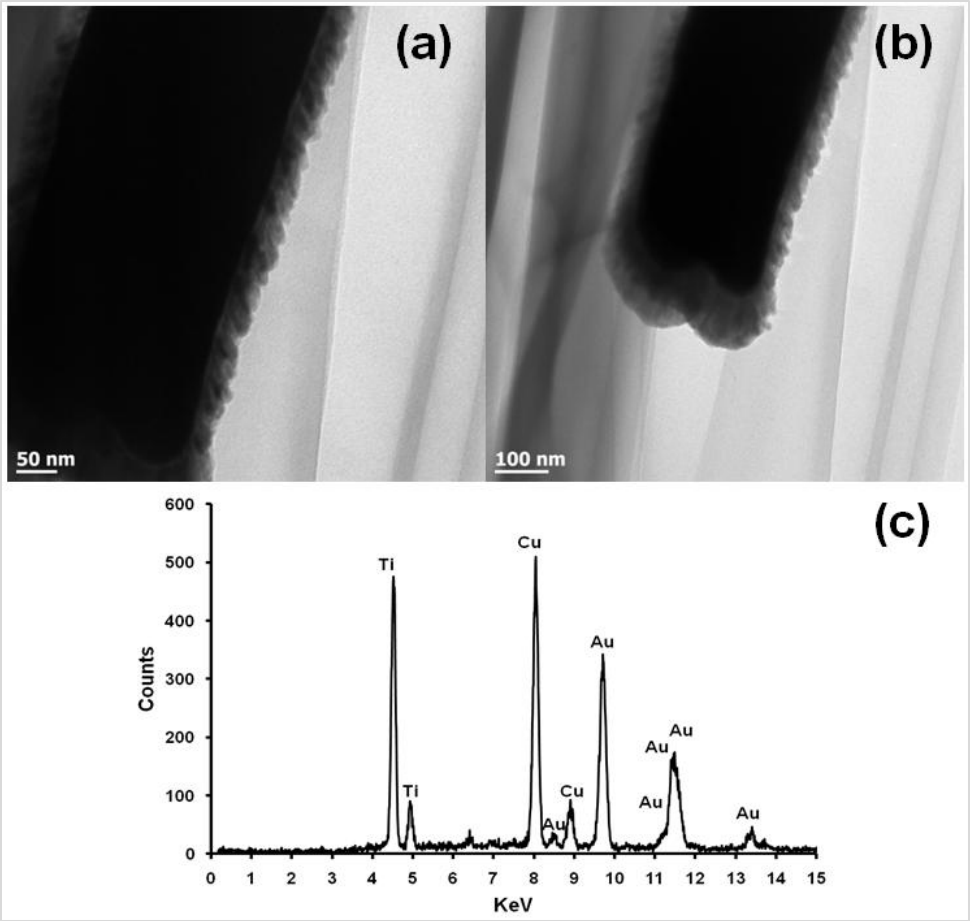

Fig. 3.9 (a) and (b) TEM images of Au-TiO_2 core-shell nanowires, (c) EDS spectrum showing peaks for Au and Ti (copper is from the TEM support). PLD treatment was conducted for 30 min.

The HRTEM image in Figure 3.10 (a) shows the edge of the core-shell nanowire where the TiO_2 coating was ~40 nm. The distance between two consecutive lattice fringes was calculated to be 3.52 Å which corresponds to the (101) plane of tetragonal anatase TiO_2. The results are shown in the lattice resolved HRTEM image in Fig. 3.10 (b). The Au core is dark in color due to the higher density of the gold. The selected area electron diffraction (SAED) pattern in Fig. 3.10 (c) represents the concentric rings generated from the Au-TiO_2 core-shell nanowires. The innermost rings are labeled with gold (right) and TiO_2 anatase (left) indices. The concentric rings in the SAED pattern reveal the polycrystalline nature of the Au-TiO_2 core-shell nanowire architectures. The synthesized structures served as the photoanode in dye sensitized solar cell devices. Ruthenium dye (N-535) was the sensitizer, and I^-/I_3^- served as the redox couple.

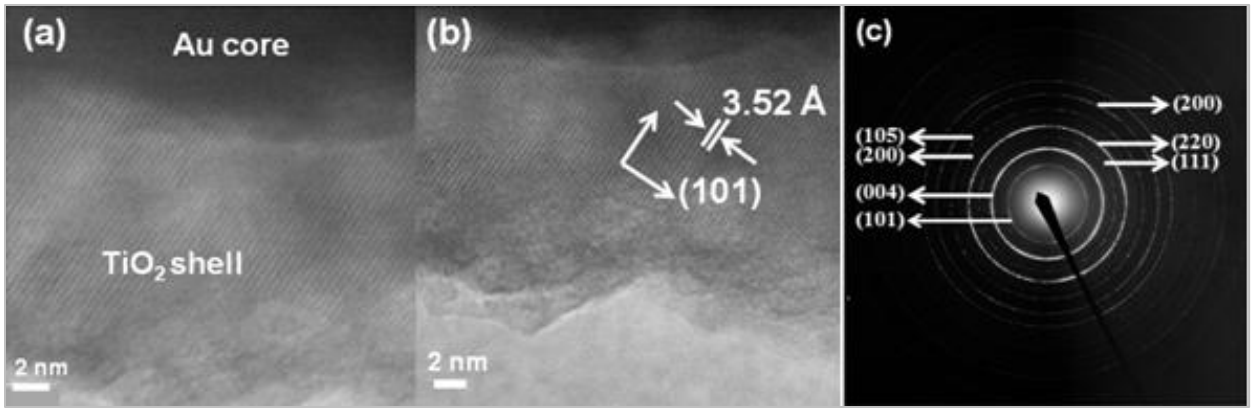

Fig. 3.10 (a) and (b) HRTEM images of the Au-TiO_2 core-shell nanowire, (c) SAED pattern of the Au-TiO_2 nanowires, with innermost rings labeled, left side indices for anatase TiO_2 and right side indices for fcc Au.

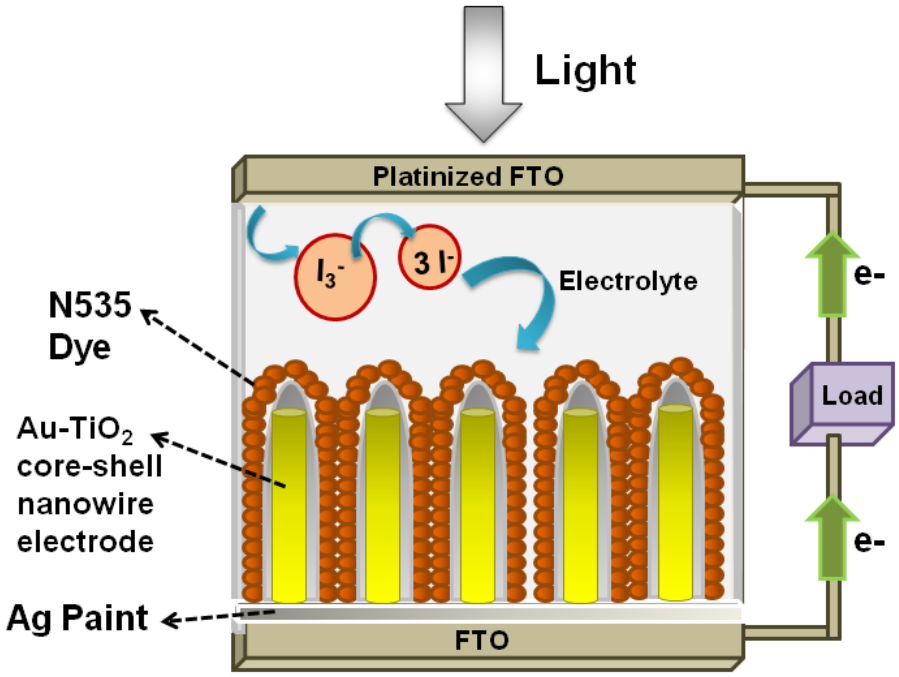

Fig. 3.11 Schematic of assembled backside illuminated Au-TiO_2 nanowire DSSC or $TiCl_4$ treated Au-TiO_2 core-shell DSSC.

A schematic of the core-shell nanowire device is given in Figure 3.11. The J-V characteristics were measured under 100 mW/cm^2 simulated sunlight. We compared the current-voltage characteristics of Au-TiO_2 nanowire solar cells with that of the TiO_2 nanoparticle based DSSCs

and $TiCl_4$ surface passivated Au-TiO_2 core-shell nanowire DSSCs. Treatment with 0.1 M $TiCl_4$ (aq) was used in order to improve the surface area of the Au-TiO_2 core-shell nanowire arrays. Surface treatment of the TiO_2 photoanodes with a TiO_2 precursor such as titanium tetrachloride $TiCl_4$ [49-53] and titanium isopropoxide $Ti(OC_3H_7)_4$ [54] has already been proven to enhance solar cell device performance by increasing photocurrent,[55] enhancing surface area,[56] improving electron transport,[49] and improving anchoring of the dye.[52] The morphology of the Au-TiO_2 nanowires before and after the $TiCl_4$ treatment was observed by FESEM imaging for checking any visual change in before and after $TiCl_4$ treatment. The data is given in Fig. 3.12 and 3.13 respectively. The J-V curves and data obtained upon illumination are given in Figure 3.14 and Table 1 respectively. At first the devices were illuminated through the backside (Pt electrode) due to the presence of the opaque silver film and paint on the photoanode side. Although necessary for these devices with Ag film, backside illumination is detrimental because the redox couple can absorb some of the incident light before it reaches the photoanode.

In order to study the effect of a metal core inside the TiO_2 shell on the photovoltaic performance of DSSCs, we compared the J-V data of several devices (Table 1). The 3 µm long Au-TiO_2 core-shell nanowire device showed a J_{sc} and η of 4.6 mA/cm^2 and 2.3% respectively, while the corresponding values for a 3 µm thick TiO_2 mesoporous DSSC were 2.8 mA/cm^2 and 1.06%. A higher V_{oc} of the DSSC with Au-TiO_2 core-shell device compared to that of the cell with TiO_2 nanoparticles is in accordance with their J_{sc} values. A higher J_{sc} implies a faster electron transfer in the device, which favors an increased V_{oc} for the Au-TiO_2 core-shell device. The best efficiency and best fill factor (FF) of the 3.5 µm Au-TiO_2 core-shell nanowire based devices were found to be 3.7% and 66.0% respectively. The results were obtained by applying only a ~40 nm TiO_2 layer which coated the entire core metal from top to bottom. The ability of the gold core to transport electrons quickly out of the oxide and light scattering effects due to the gold metal core are both potential reasons for the improved efficiency in the core-shell DSSC devices. Additional devices were prepared and treated with $TiCl_4$ prior to obtaining J-V curves.

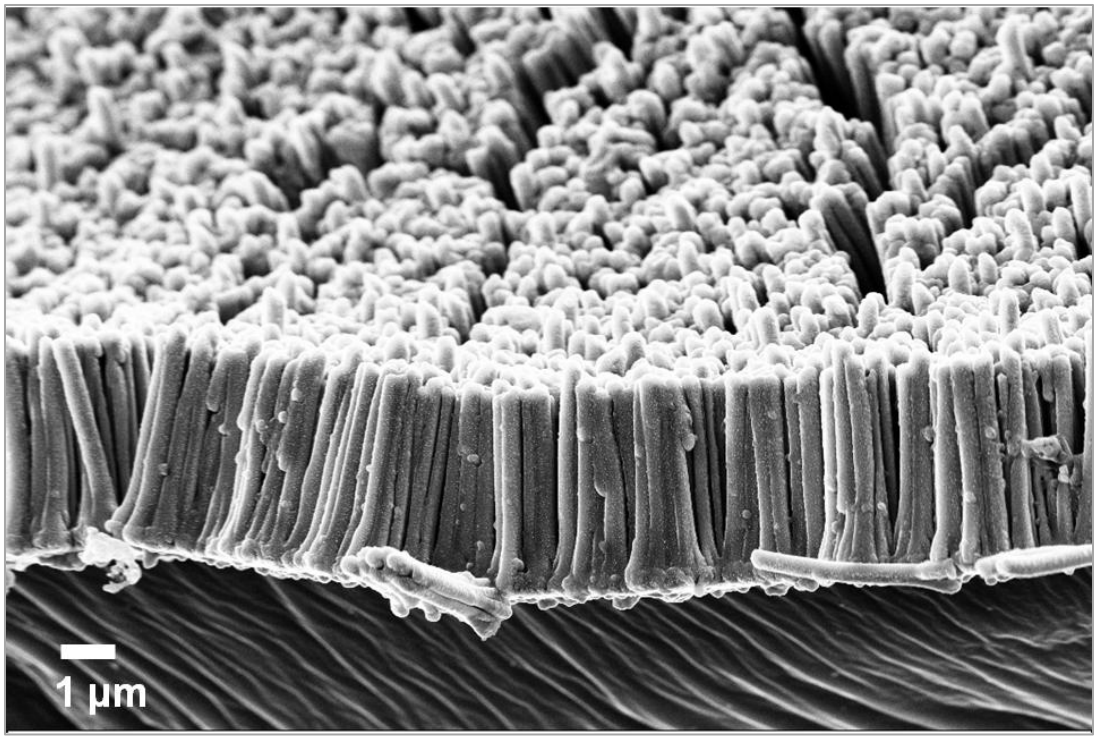

Fig. 3.12 4.5 µm long Au-TiO_2 core-shell nanostructures before $TiCl_4$ treatment

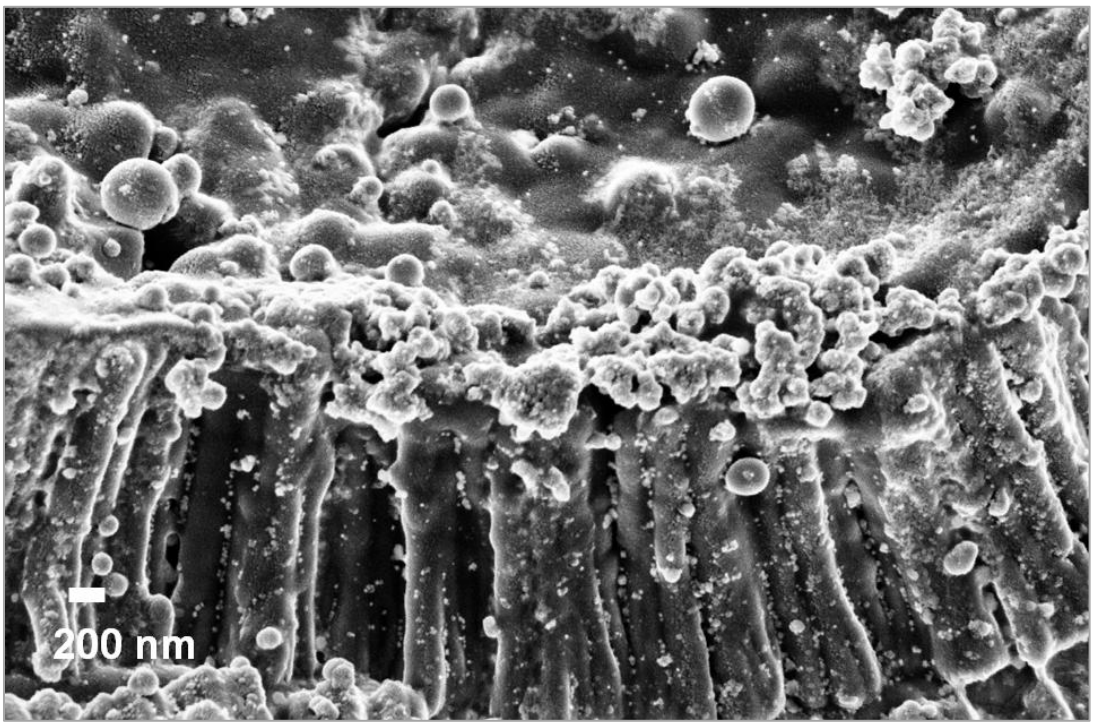

Fig. 3.13 4.5 µm long Au-TiO_2 core-shell nanostructures after $TiCl_4$ treatment

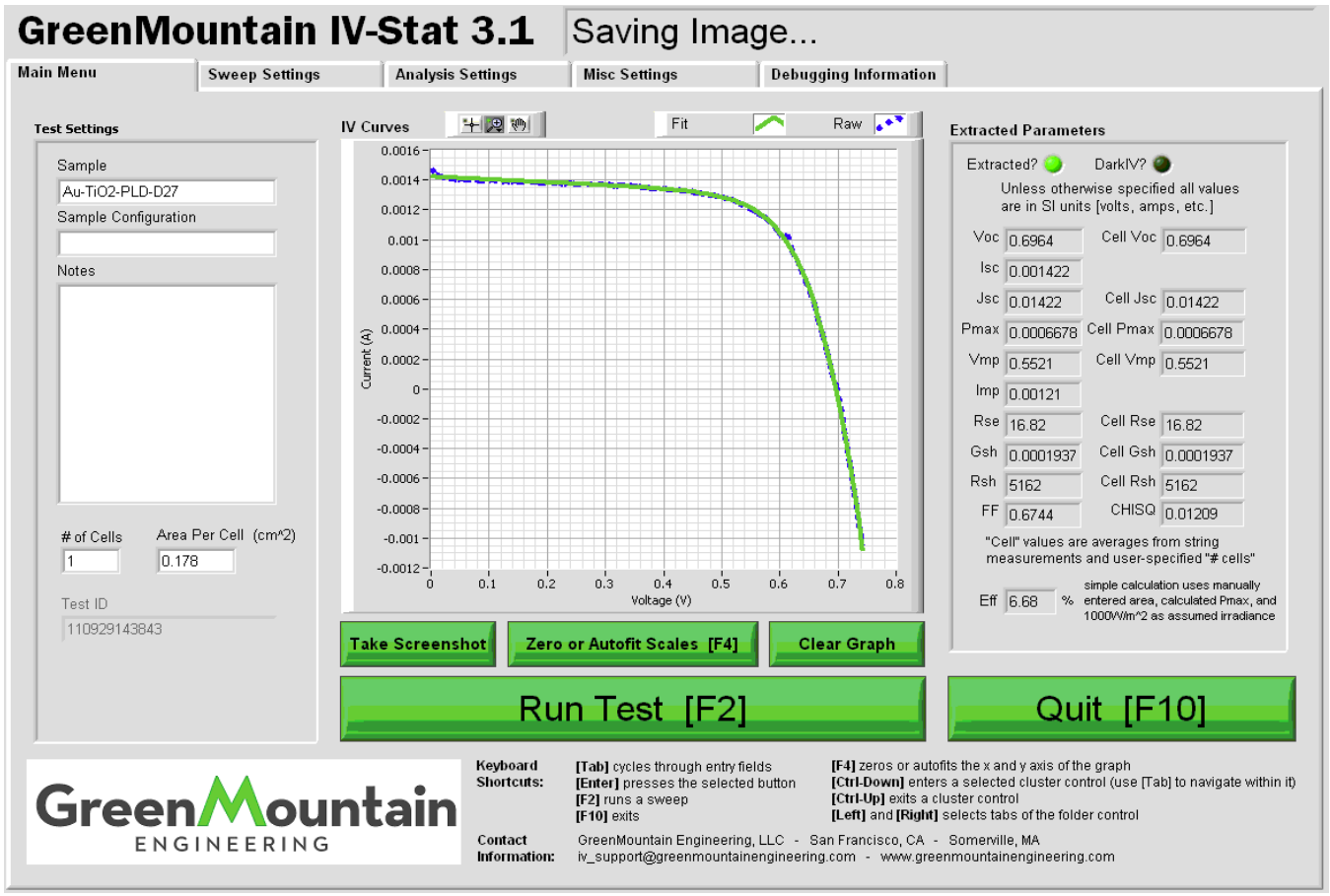

Fig. 3.14 (i) An example of I-V curve generated from one of the nanowire based devices

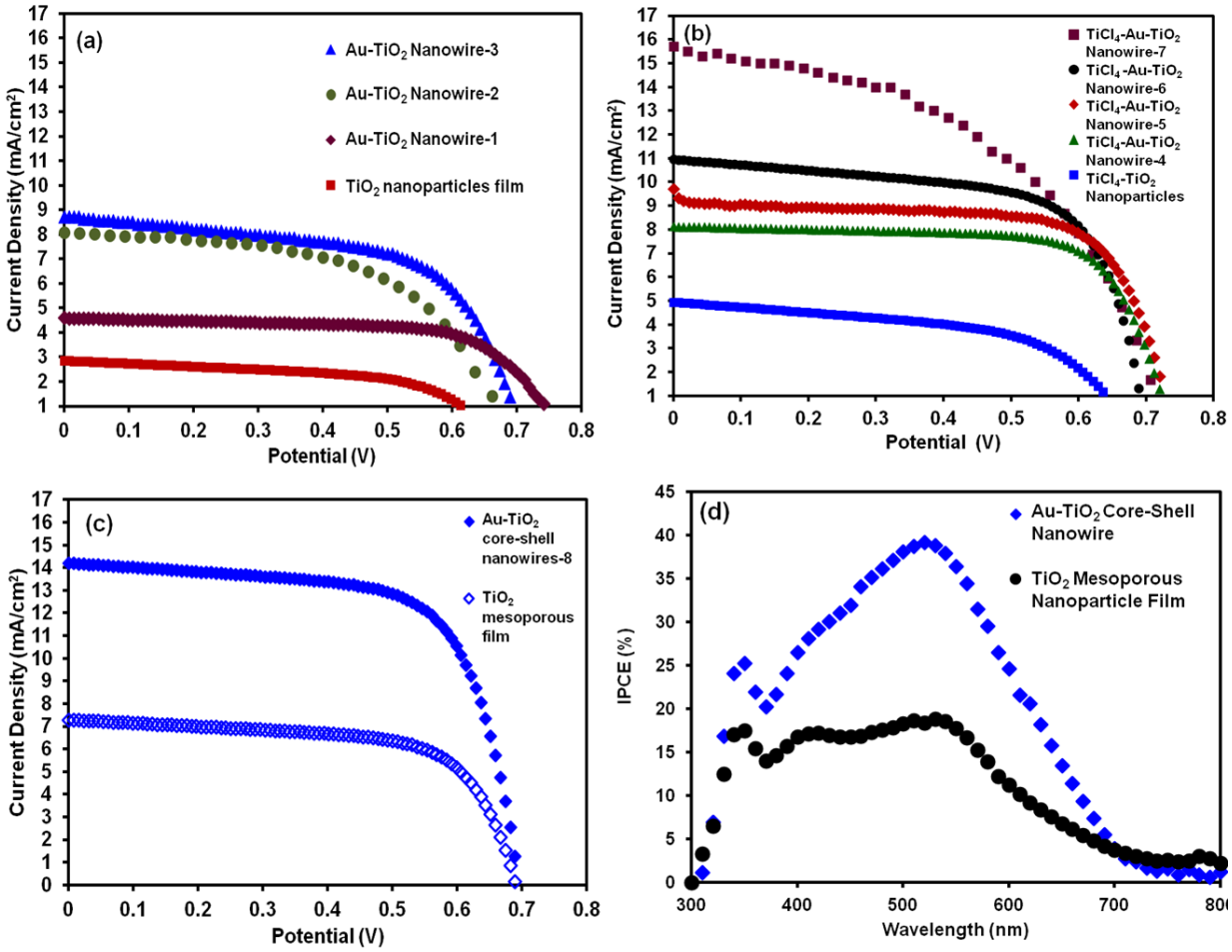

Fig. 3.14 (ii) (a) J-V curves of DSSCs fabricated with backside illuminated bare Au-TiO_2 core-shell nanowire and TiO_2 mesoporous nanoparticle film (b) J-V curves of backside illuminated $TiCl_4$ treated Au-TiO_2 core-shell nanowire and $TiCl_4$ treated TiO_2 mesoporous nanoparticle film DSSCs. Devices 2 and 7 were measured using a different solar simulator which had some light fluctuations that contributed to the low fill factor. (c) J-V curves of frontside illuminated Au-TiO_2 core-shell nanowire and TiO_2 mesoporous nanoparticle film DSSCs and, (d) IPCE spectra of DSSCs based on Au-TiO_2 core-shell nanowire and TiO_2 mesoporous nanoparticle film.

Table 3.1 J-V Characteristics of dye-sensitized Au-TiO_2 core-shell nanowires, and $TiCl_4$ treated Au-TiO_2 core-shell nanowires DSSCs under 1 Sun (AM 1.5)

Photoanode Film Type	Type of Illumination	Approx.Film Thickness (μm)	J_{sc} (mA/cm^2)	V_{oc} (V)	FF (%)	η (%)
Au-TiO_2 core-shell nanowires-1	Backside	3.0	4.6	0.78	66	2.3
Au-TiO_2 core-shell nanowires-2	Backside	3.5	8.0	0.68	55	3.0
Au-TiO_2 core-shell nanowires-3	Backside	3.5	8.7	0.71	59	3.7
$TiCl_4$ treated Au-TiO_2 core-shell nanowires-4	Backside	4.0	8.1	0.73	71	4.3
$TiCl_4$ treated Au-TiO_2 core-shell nanowires-5	Backside	4.5	9.7	0.74	69	4.7
$TiCl_4$ treated Au-TiO_2 core-shell nanowires-6	Backside	4.9	11.0	0.69	65	5.0
$TiCl_4$ treated Au-TiO_2 core-shell nanowires-7	Backside	4.9	15.7	0.73	49	5.6
Au-TiO_2 core-shell nanowires-8	Frontside	4.2	14.2	0.69	67	6.7
TiO_2 mesoporous nanoparticles film	Frontside	4.0	7.3	0.69	65	3.3
TiO_2 mesoporous nanoparticles film	Backside	3.0	2.8	0.66	55	1.0
$TiCl_4$ treated TiO_2 mesoporous nanoparticles film	Backside	4.0	4.9	0.67	53	1.7

Efficiency for these devices ranged from 4.3-5.6%, with a trend of increasing efficiency with increasing length of the core-shell nanowires. Direct comparison of a 4 µm $TiCl_4$ treated core-shell nanowire device and a 4 µm $TiCl_4$ treated mesoporous nanoparticle device showed a 2.4 fold higher efficiency for the core-shell device.

In order to check the effect of frontside illumination on device efficiency, we measured the J-V curves and their parameters by fabricating devices using a facile process involving dissolving the Ag film off the Au-TiO_2 core-shell nanowire array and strongly adhering it onto FTO glass followed by sintering at high temperature. The fabrication process of the transparent photoanode is provided in Fig. 3.3 and an FESEM image of the Au-TiO_2 core-shell nanostructure after the Ag layer removal is provided in Fig. 3.15 below. The obtained solar conversion efficiency of 6.7% for the frontside illuminated DSSC is much higher than those of the backside illuminated DSSCs obtained in this study (5.6%). This difference is most likely due to better light transport through the frontside (FTO only) vs the backside (platinized FTO and electrolyte). Dye desorption experiments showed similar dye loading among all devices tested (Table 2).

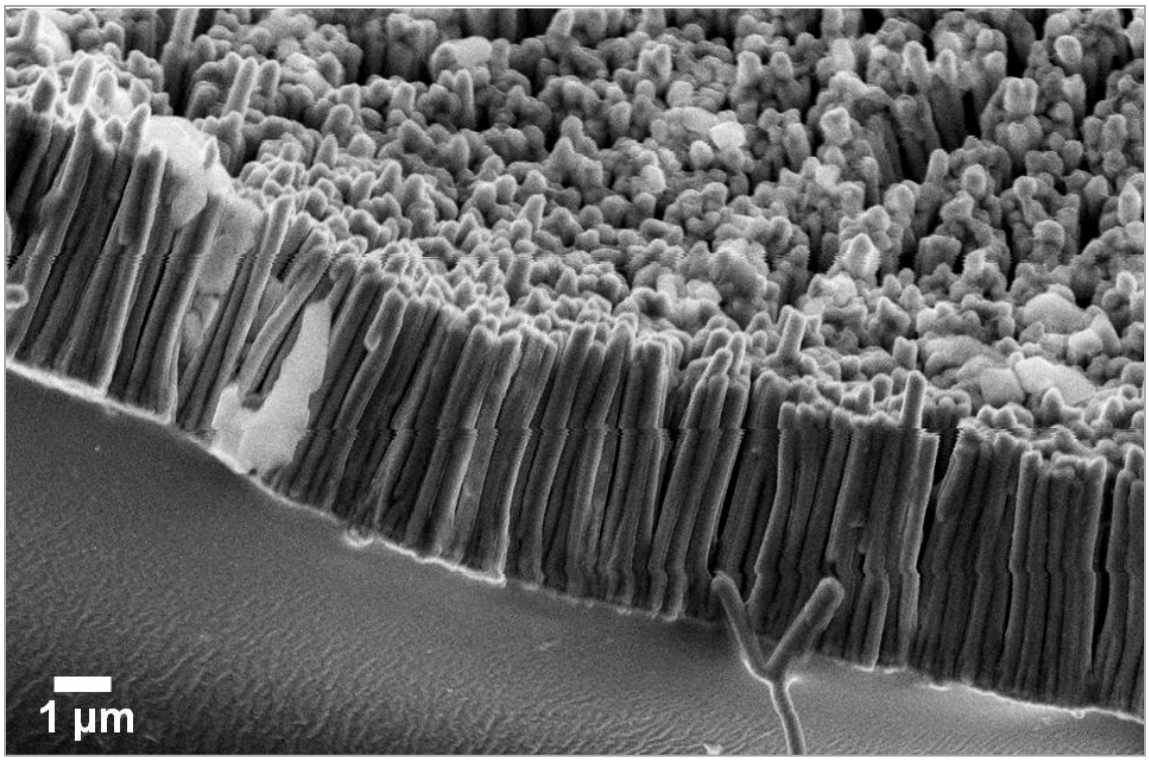

Fig. 3.15 FESEM image of the 4.5 µm long Au-TiO_2 core-shell nanowire array on FTO after the removal of the Ag layer.

Table3.2 Dye loading on photoanode films. After dye desorption with 0.1 M NaOH in ethanol, dye concentration was determined by absorbance at 310 nm followed by conversion to mol/cm^2.

Photoanode Type	**Dye Loading (mol/cm^2)**
TiO_2 nanoparticle film (4.4 µm)	3.9×10^{-6}
Au-TiO_2 core-shell nanowires (4.5 µm)	3.1×10^{-6}
$TiCl_4$-treated core-shell nanowires (4.5 µm)	3.3×10^{-6}

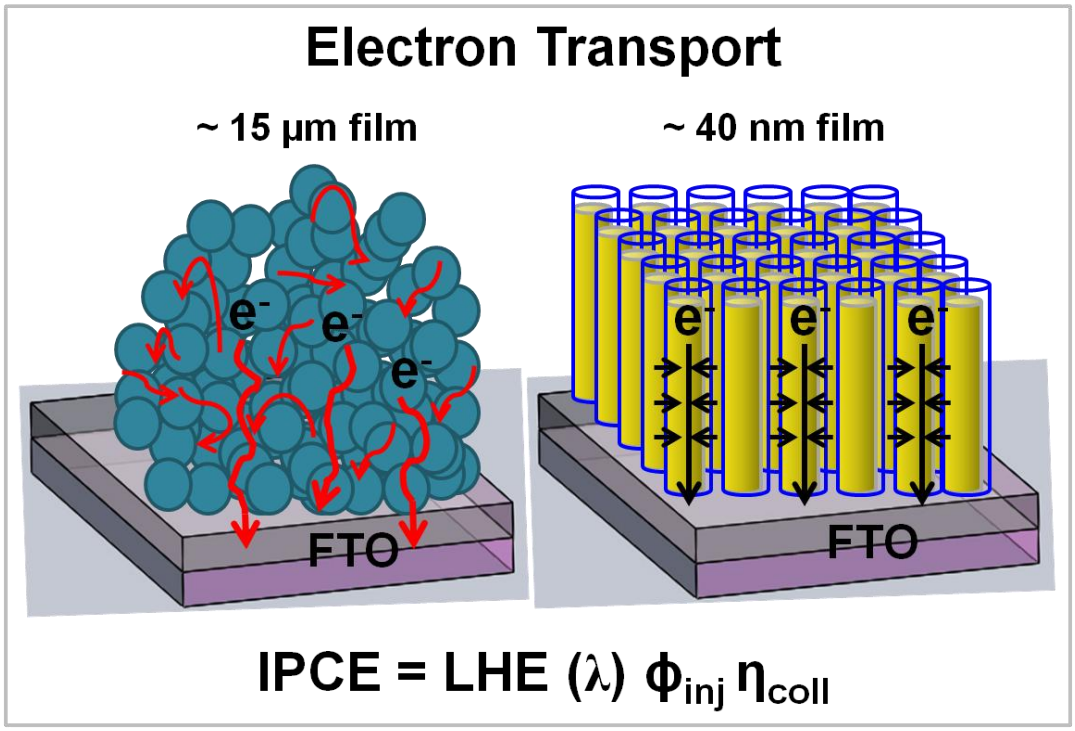

Fig. 3.16 Schematic showing the electron transport mechanism in TiO_2 nanoparticle network and Au-TiO_2 core-shell nanowire arrays. Not to scale.

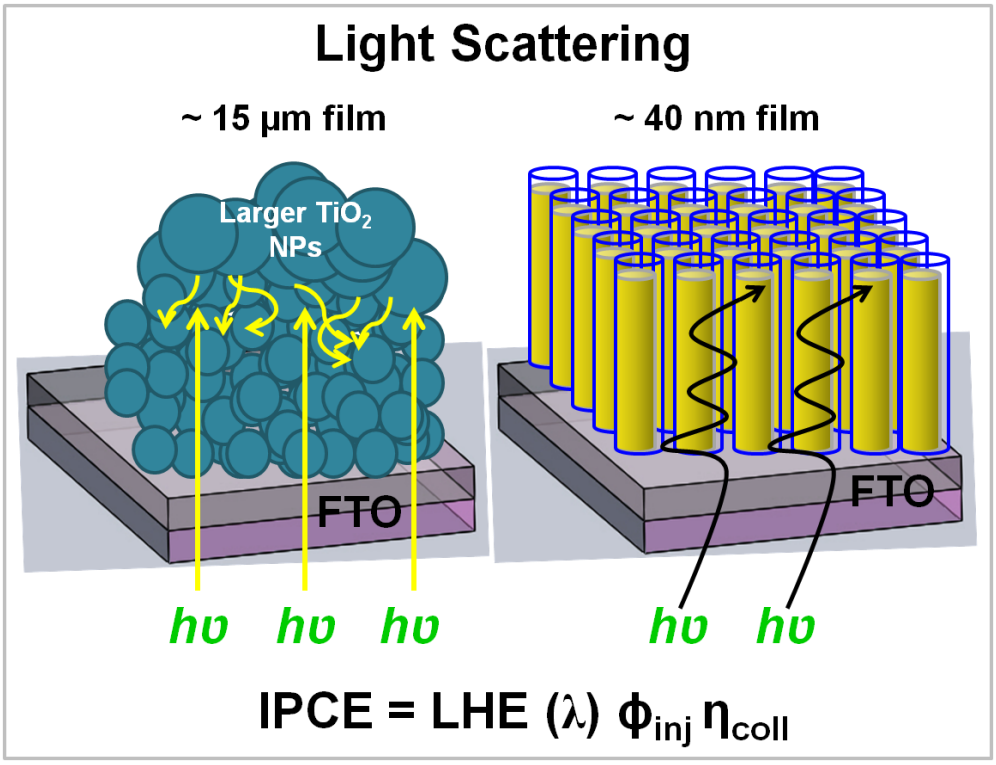

Fig. 3.17 Schematic showing the light scattering mechanism in TiO_2 nanoparticle network and Au-TiO_2 core-shell nanowire arrays. Not to scale.

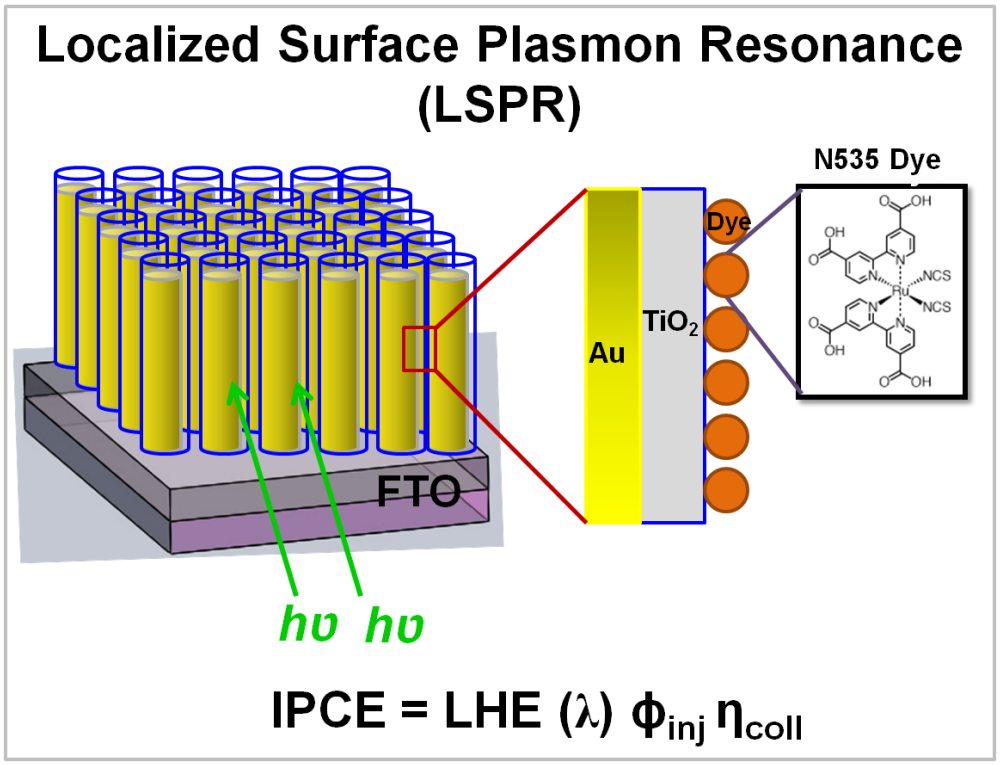

Fig. 3.18 Schematic showing the exploitation of LSPR in Dye-TiO_2-Au system. Not to scale.

Consequently, changes in dye loading cannot account for the enhanced efficiency for the core-shell device. Likely explanations include 1) improved electron transport due to the presence of the conducting metal core within the ~ 40 nm TiO_2 film unlike the ~15 µm thick mesoporous TiO_2 nanoparticle film where electrons need to transfer from particle to particle to reach the transparent conductive oxide (TCO) (e^- transport mechanism is given in a schemiatic in Fig. 3.16), 2) increased path length of the generated photons due to scattering from the metal nanowire arrays which is also seen in case of larger TiO_2 nanoparticle layer in mesoporous film (light scattering phenomena has been well picturized in a schematic in Fig. 3.17), and 3) enhanced absorbance caused by optical effects of the metal nanowire array such as enhanced localized surface plasmon resonance (LSPR). Upon excitation the free electrons in gold cause large near-field amplitude and a resonantly enhanced scattering cross section known as near field scattering. If the large near field in the vicinity of the gold nanostructure would be overlapped by the extinction of the light absorbing material such as dye of the solar cell, the overall absorption will be increased. This is because the conduction electrons of the gold nanowire core resonate with the electric field of incident light giving rise to surface plasmon resonance (SPR). As a result, the plasmon-enhanced extinction of the dye increases due to the increased electromagnetic field. The localized fields excite the dye more efficiently than the incident light so the gold nanowire arrays function as light harvesting antennas for the dye molecules as long as the dye molecules are near the metal's effective electromagnetic field. (LSPR phenomena have been illustrated in Fig. 3.18).

Comparing mesoporous and core-shell devices, we observed a shift to higher V_{oc} for the core-shell devices with one exception in the frontside illuminated devices (Fig. 3.14 c). This could be due to reduced dark current in the frontside illuminated device which increases the V_{oc} of the device. This result indicates better electron transport most likely caused by the thin oxide film.[57] The core-shell devices also exhibited higher FF than the mesoporous film devices. A 3 µm core-shell device had a FF of 66% while the 3 µm mesoporous device had a FF of 56% (Table 1). Similarly, a 4 µm $TiCl_4$ treated core-shell device had a FF of 71% while the 4 µm $TiCl_4$ treated mesoporous film device had a FF of 53%. The core-shell nanowires had a dye loading of 3.1×10^{-6} mol/cm^2 when only the flat geometrical surface area (i.e. 0.24 cm^2) was taken into consideration (Table 2). The $TiCl_4$ treated Au-TiO_2 core-shell nanowires had a dye loading of 3.3×10^{-6} mol/cm^2. The amount of dye loading on the 4.5 µm long Au-TiO_2 core-shell nanowire array and on the 4.5 µm $TiCl_4$ treated Au-TiO_2 core-shell nanowires was compared with a 4.4 µM thick film of mesoporous anatase. The mesoporous TiO_2 film had a dye loading of 3.9×10^{-6} mol/cm^2. The

dye loading on the nanowire array was comparable to that on the mesoporous film. Previously reported dye loading values for DSSC range from 7.3×10^{-8} mol/cm^2 to 4.8×10^{-5} mol/cm^2.[58-60] Our values fall within this broad range. However, the most important observation from our results is the relative loading of dye on the different structures. The nanowire arrays that we prepared had similar dye loading to a mesoporous film of comparable thickness, but the core-shell nanowire array devices had much greater photoconversion efficiency. Consequently, the enhanced efficiency of the core-shell nanowire devices is caused by a factor other than increased dye loading.

To further investigate the reasons for higher photocurrent for the solar cells based on Au-TiO_2 core-shell nanowires, we measured the incident photon to current efficiency (IPCE) of mesoporous TiO_2 nanoparticle and Au-TiO_2 core-shell nanowire based solar cells. As shown in Figure 3.14 (d), the IPCE for Au-TiO_2 core-shell nanowire based device exhibited a peak of about 39.1% IPCE at 520 nm as well as a small shoulder at 400 nm. These peaks are in close agreement with the absorption spectrum for the N535 dye, which has local maxima at 400 and 533 nm, both corresponding to metal-to-ligand charge transfer transitions. The IPCE for the TiO_2 nanoparticle based device exhibited a peak of about 18.3% at 520 nm as well as small shoulder at 400 nm. Notably, the IPCE profile of the Au-TiO_2 core-shell nanowire based device was broadened and red shifted with respect to the TiO_2 nanoparticle cell. The most likely reason for this broadened spectrum is light scattering by the Au nanowire array, resulting in enhanced light path length in the oxide/dye layer.[61-63] The observed red shift for the Au-TiO_2 core-shell nanowire cell will facilitate utilization of sunlight in the full spectrum range. The difference between these IPCE spectra (Figure 3.19 below) did not have a flat profile, indicating that there were wavelength dependent shifts in the IPCE spectrum due to the presence of gold in the Au-TiO_2 nanowires. The maximum in the difference spectrum is near 520 nm, very close to the absorbance maximum of the dye. These results suggest possible coupling of the near field radiation with the absorbance dipole of the dye,[64] which is no more than 30 nm from the metal surface. Resonance enhancement in absorbance cross sections near metal surfaces have been previously reported.[65-68] In addition to the red shift, there is a small but reproducible peak near 620 nm for the structures with a gold core (see Fig. 3.14 d and 3.19). Complete explanation of these optical features requires further in depth characterization of the optical properties of the core-shell nanowire arrays, a task that is currently underway.

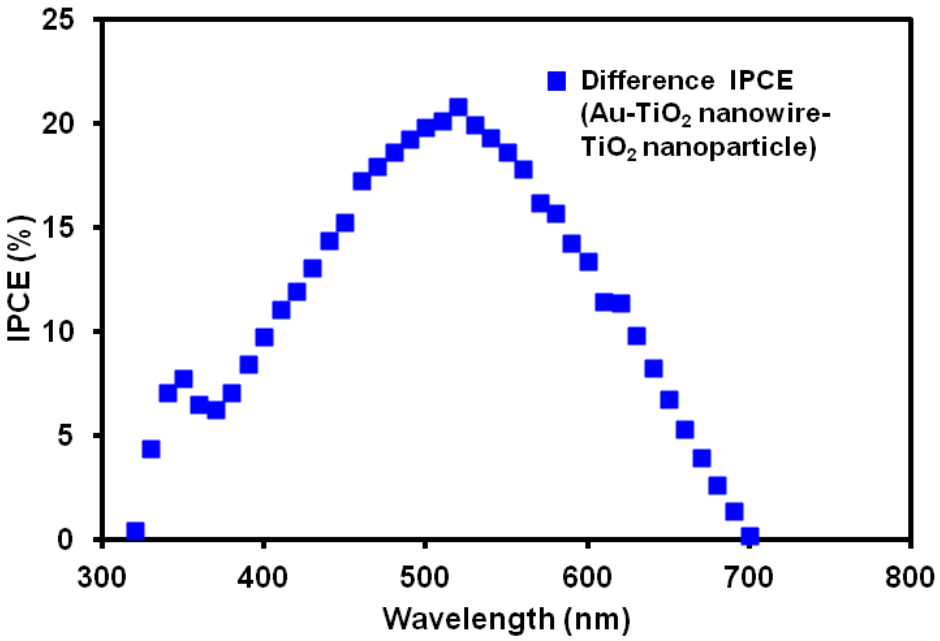

Fig. 3.19 The difference in IPCE spectrum of the Au-TiO_2 core-shell DSSC and TiO_2 nanoparticle DSSC.

Further improvements in the current densities and efficiencies could be obtained by growing longer nanowires with smaller diameter which would offer higher surface area and greater light harvesting. Nanowire aspect ratio is a huge factor to consider when it comes to providing control over the electron transport out of the anode. Growing longer wires with smaller diameter will enhance surface area and thus provide better light harvesting, which will substantially improve the current densities and efficiencies of cells made from nanowires[58,69] A decrease in dark current causes the open circuit voltage to increase based on the relationship

$$V_{oc} = (k_B T/q) \ln(I_{photo}/I_{dark} + 1) \qquad (3.1)$$

Where k_B is the Boltzmann constant, T is temperature in Kelvin, q is the charge, and I_{dark} and I_{photo} are the dark and photocurrents, respectively.[70] A decrease in semiconductor layer thickness will decrease the recombination rate which will subsequently decrease the dark current in the cell. A decrease in dark current will cause the V_{oc} to increase and therefore the overall consequence will result in an increase in the device efficiency. Reducing the semiconductor layer thickness will

also allow for use of polycrystalline semiconductor materials with low minority carrier diffusion lengths. Thinner films will reduce the cost of devices due to reduced material, crystallinity and purity demands and will open up room for using potentially inexpensive semiconductors with impurities and defects, for example CuO. The metal-metal oxide core-shell nanowire approach used in this study allowed the use of a thin (~40 nm) semiconductor layer.

A promising new DSSC photoanode design was introduced where electrons created at the ~40 nm thick semiconductor layer radially diffuse to a metal core and are efficiently collected at the back contact. We have chosen gold as the material for the metallic core for proof of concept studies due to its high conductivity, thermal and chemical stability, and light focusing properties. Additional development of the preparation techniques will potentially lead to devices made from lower cost conductors such as copper or aluminum. The currently observed power conversion efficiency of 4.3% for a 4.0 μm $TiCl_4$-Au-TiO_2 core-shell nanowire cell was higher than the 2.38% efficiency observed for a 3.0 μm untreated Au-TiO_2 core-shell nanowire DSSC. Furthermore, the efficiencies were only 1.8% and 1.1% for a 4 μm $TiCl_4$-TiO_2 mesoporous nanoparticle film DSSC and 3 μm untreated TiO_2 mesoporous nanoparticle film DSSC, respectively. This evaluation confirms that our PLD grown Au-TiO_2 core-shell nanowire based devices showed 2.2 to 2.4 times higher efficiency than the TiO_2 mesoporous nanoparticle film DSSC of the same thickness. Recently reported data by Grätzel's group for TiO_2 deposited by pulsed laser deposition directly onto an ITO substrate with no metal nanowires showed efficiencies of 3.1% (2 μm film), 4.9% (7 μm film) and 3.7 % (13 μm film).[42] The 2 μm PLD grown TiO_2 film showed a 2.3 times lower efficiency as compared to their corresponding TiO_2 mesoporous film DSSC of the same thickness. An important reason for the highly efficient mesoporous film DSSCs is their expertise in fabrication of high quality devices. In contrast, our work showed a 2.2 to 2.4 fold increase in the core-shell devices compared to the mesoporous devices. This difference underscores the importance of the metal core in improving the performance of devices based on PLD deposited TiO_2. Our cell efficiency was limited by residual series resistance, most likely caused by imperfect contacts in our cell. Resolving these deficiencies should improve our efficiency well above the 6.7% we have already achieved. Furthermore, we utilized the N535 dye, which has a narrower absorbance spectrum compared to the C101 dye used by Grätzel's group. Another improvement we can make is increasing the length of our structures. Using 7 μm long PLD grown TiO_2 structures on ITO, Grätzel's group achieved their maximum efficiency of 4.9%, indicating that efficiency improves as the thickness

of the TiO_2 increases as long as a maximum thickness is not exceeded. We can expect improvements by increasing the length of our structures and utilizing dyes that will have better coverage of the solar spectrum. The core-shell nanowire approach has considerable potential for making dramatic improvements in DSSC efficiency. Treatment of our devices with $TiCl_4$ resulted in important improvements in efficiency (Table 1). Although previous reports have attributed such improvements to increased surface area and increased dye loading,[56] our dye desorption data (Table 2) did not show an increase in dye loading after $TiCl_4$ treatmenmt. Furthermore, comparing J-V data for devices with and without $TiCl_4$ treatment, no noticeable change in shunt current was observed. Samples without $TiCl_4$ treatment exhibited minimal shunt current as evidenced by the flatness of the J-V curve extending close to V_{oc}, This behavior suggests that little if any gold is directly exposed to the electrolyte. Based on these observations, the $TiCl_4$ generated efficiency improvements recorded in this study are most likely due to improved light scattering.[50]

3.5. Summary

We synthesized novel Au-TiO_2 core-shell nanoarchitectures and used them in dye sensitized solar cells. These core-shell structures showed very good performance in solar energy conversion. This improvement is likely the result of 1) photon confinement in nanowires due to light scattering or focusing effects and 2) improved pathways for electron transport out of the anode after photoinduced charge injection caused by the metal nanowire array. With an oxide thickness of 40 nm and a core conductor that spans the entire length of the core-shell structure, electrons injected into the oxide only have to travel around 40 nm before reaching a conductor. As a consequence, the use of fast redox couples like ferrocene may become feasible with dye cells constructed from these core-shell nanostructures. The dye cells with core-shell photoanodes increased the current generation substantially as compared to the mesoporous nanoparticle film based DSSCs, thereby increasing the solar conversion efficiencies. Future studies aim to develop further improvements by increasing the length and surface area of TiO_2, utilizing lower cost core materials, using dyes with broader spectral coverage and utilizing alternate redox couples.

3.6. References

(1) Oregan, B.; Grätzel, M. *Nature* **1991**, *353*, 737.
(2) Kopidakis, N.; Schiff, E. A.; Park, N. G.; van de Lagemaat, J.; Frank, A. J. *J. Phys. Chem. B* **2000**, *104*, 3930.
(3) Peter, L. M. *Phys. Chem. Chem. Phys.* **2007**, *9*, 2630.
(4) Nelson, J.; Chandler, R. E. *Coord. Chem. Rev.* **2004**, *248*, 1181.
(5) Law, M.; Greene, L. E.; Johnson, J. C.; Saykally, R.; Yang, P. D. *Nature Materials* **2005**, *4*, 455.
(6) Tan, B.; Wu, Y. Y. *J. Phys. Chem. B* **2006**, *110*, 15932.
(7) Chen, J. G.; Chen, C. Y.; Wu, C. G.; Lin, C. Y.; Lai, Y. H.; Wang, C. C.; Chen, H. W.; Vittal, R.; Ho, K. C. *J. Mater. Chem.* **2010**, *20*, 7201.
(8) Xie, Y.; Zhou, L.; Huang, C.; Huang, H.; Lu, J. *Electrochimica Acta* **2008**, *53*, 3643.
(9) Banerjee, S.; Mohapatra, S. K.; Das, P. P.; Misra, M. *Chemistry of Materials* **2008**, *20*, 6784.
(10) Wang, Q.; Zhu, K.; Neale, N. R.; Frank, A. J. *Nano Letters* **2009**, *9*, 806.
(11) Mohapatra, S. K.; Kondamudi, N.; Banerjee, S.; Misra, M. *Langmuir* **2008**, *24*, 11276.
(12) Chen, S. G.; Paulose, M.; Ruan, C.; Mor, G. K.; Varghese, O. K.; Kouzoudis, D.; Grimes, C. A. *J. Photochem. Photobiol. A-Chem.* **2006**, *177*, 177.
(13) Fang, D.; Huang, K. L.; Liu, S. Q.; Qin, D. Y. *Electrochemistry Communications* **2009**, *11*, 901.
(14) Zhu, W.; Wang, G. Z.; Hong, X.; Shen, X. S.; Li, D. P.; Xie, X. *Electrochimica Acta* **2009**, *55*, 480.
(15) Zhu, W.; Wang, G. Z.; Hong, X.; Shen, X. S. *Journal of Physical Chemistry C* **2009**, *113*, 5450.
(16) Zhang, H. Y.; Ji, T. H.; Liu, Y. F.; Cai, J. W. *Journal of Physical Chemistry C* **2008**, *112*, 8604.
(17) An, H. Q.; Li, J. X.; Zhou, J.; Li, K. R.; Zhu, B. L.; Huang, W. P. *J. Mater. Chem.* **2010**, *20*, 603.
(18) Mohapatra, S. K.; Banerjee, S.; Misra, M. *Nanotechnology* **2008**, *19*.
(19) Wang, M. L.; Huang, C. G.; Cao, Y. G.; Yu, Q. J.; Deng, Z. H.; Liu, Y.; Huang, Z.; Huang, J. Q.; Huang, Q. F.; Guo, W.; Liang, J. K. *J. Phys. D-Appl. Phys.* **2009**, *42*.
(20) Law, M.; Greene, L. E.; Radenovic, A.; Kuykendall, T.; Liphardt, J.; Yang, P. D. *J. Phys. Chem. B* **2006**, *110*, 22652.
(21) Kamat, P. V. *Journal of Physical Chemistry C* **2007**, *111*, 2834.
(22) Chappel, S.; Chen, S. G.; Zaban, A. *Langmuir* **2002**, *18*, 3336.
(23) Martinson, A. B. F.; Elam, J. W.; Liu, J.; Pellin, M. J.; Marks, T. J.; Hupp, J. T. *Nano Letters* **2008**, *8*, 2862.
(24) Li, Z. Z.; Rochford, C.; Baca, F. J.; Liu, J. W.; Li, J.; Wu, J. *Nanoscale Res. Lett.* **2010**, *5*, 1480.
(25) Lee, K. M.; Hu, C. W.; Chen, H. W.; Ho, K. C. *Solar Energy Materials and Solar Cells* **2008**, *92*, 1628.
(26) Kongkanand, A.; Dominguez, R. M.; Kamat, P. V. *Nano Letters* **2007**, *7*, 676.
(27) Liu, J. W.; Kuo, Y. T.; Klabunde, K. J.; Rochford, C.; Wu, J.; Li, J. *Acs Applied Materials & Interfaces* **2009**, *1*, 1645.
(28) Liu, J. W.; Li, J.; Sedhain, A.; Lin, J. Y.; Jiang, H. X. *Journal of Physical Chemistry C* **2008**, *112*, 17127.

(29) Mor, G. K.; Shankar, K.; Paulose, M.; Varghese, O. K.; Grimes, C. A. *Nano Letters* **2006**, *6*, 215.
(30) Zhu, K.; Vinzant, T. B.; Neale, N. R.; Frank, A. J. *Nano Letters* **2007**, *7*, 3739.
(31) Grätzel, M. *J. Photochem. Photobiol. A-Chem.* **2004**, *164*, 3.
(32) Kuang, D. B.; Ito, S.; Wenger, B.; Klein, C.; Moser, J. E.; Humphry-Baker, R.; Zakeeruddin, S. M.; Grätzel, M. *Journal of the American Chemical Society* **2006**, *128*, 4146.
(33) Zukalova, M.; Zukal, A.; Kavan, L.; Nazeeruddin, M. K.; Liska, P.; Grätzel, M. *Nano Letters* **2005**, *5*, 1789.
(34) Grätzel, M. *Chem. Lett.* **2005**, *34*, 8.
(35) Tammy P. Chou, S. J. L., and Guozhong Cao *Proceedings of SPIE-the international society for optical engineering* **2003**, *5224*, 5224.
(36) Joanni, E.; Savu, R.; Goes, M. D.; Bueno, P. R.; de Freitas, J. N.; Nogueira, A. F.; Longo, E.; Varela, J. A. *Scripta Materialia* **2007**, *57*, 277.
(37) Ye, Z. X.; Liu, H. D.; Schultz, I.; Wu, W. H.; Naugle, D. G.; Lyuksyutov, I. *Nanotechnology* **2008**, *19*.
(38) Wang, H. W.; Ting, C. F.; Hung, M. K.; Chiou, C. H.; Liu, Y. L.; Liu, Z. W.; Ratinac, K. R.; Ringer, S. P. *Nanotechnology* **2009**, *20*.
(39) Sahu, G.; Gordon, S. W.; Tarr, M. A. *RSC Advances* **2012**, *2*, 573.
(40) Bok, H. M.; Kim, S.; Yoo, S. H.; Kim, S. K.; Park, S. *Langmuir* **2008**, *24*, 4168.
(41) Rusop, M.; Shirata, T.; Sirimanne, P. M.; Soga, T.; Jimbo, T. *Jpn. J. Appl. Phys. Part 1 - Regul. Pap. Short Notes Rev. Pap.* **2003**, *42*, 4966.
(42) Sauvage, F.; Di Fonzo, F.; Bassi, A. L.; Casari, C. S.; Russo, V.; Divitini, G.; Ducati, C.; Bottani, C. E.; Comte, P.; Graetzel, M. *Nano Letters* **2010**, *10*, 2562.
(43) Wang, G. B.; Fu, M. G.; Lu, B.; Du, G. P.; Li, L.; Qin, X. M.; Shi, W. Z. *Applied Physics a-Materials Science & Processing* **2010**, *100*, 1169.
(44) Noh, J. H.; Lee, S.; Kim, J. Y.; Lee, J. K.; Han, H. S.; Cho, C. M.; Cho, I. S.; Jung, H. S.; Hong, K. S. *Journal of Physical Chemistry C* **2009**, *113*, 1083.
(45) Lee, B.; Hwang, D. K.; Guo, P. J.; Ho, S. T.; Buchholtz, D. B.; Wang, C. Y.; Chang, R. P. H. *J. Phys. Chem. B* **2010**, *114*, 14582.
(46) Bailini, A.; Di Fonzo, F.; Fusi, M.; Casari, C. S.; Bassi, A. L.; Russo, V.; Baserga, A.; Bottani, C. E. *Applied Surface Science* **2007**, *253*, 8130.
(47) Infortuna, A.; Harvey, A. S.; Gauckler, L. J. *Adv. Funct. Mater.* **2008**, *18*, 127.
(48) Di Fonzo, F.; Casari, C. S.; Russo, V.; Brunella, M. F.; Bassi, A. L.; Bottani, C. E. *Nanotechnology* **2009**, *20*.
(49) Barbe, C. J.; Arendse, F.; Comte, P.; Jirousek, M.; Lenzmann, F.; Shklover, V.; Grätzel, M. *Journal of the American Ceramic Society* **1997**, *80*, 3157.
(50) Park, N. G.; Schlichthorl, G.; van de Lagemaat, J.; Cheong, H. M.; Mascarenhas, A.; Frank, A. J. *J. Phys. Chem. B* **1999**, *103*, 3308.
(51) Nazeeruddin, M. K.; Kay, A.; Rodicio, I.; Humphrybaker, R.; Muller, E.; Liska, P.; Vlachopoulos, N.; Grätzel, M. *Journal of the American Chemical Society* **1993**, *115*, 6382.
(52) Zeng, L. Y.; Dai, S. Y.; Wang, K. J.; Pan, X.; Shi, C. W.; Guo, L. *Chin. Phys. Lett.* **2004**, *21*, 1835.
(53) Charoensirithavorn, P.; Ogomi, Y.; Sagawa, T.; Hayase, S.; Yoshikawaa, S. *J. Electrochem. Soc.* **2010**, *157*, B354.
(54) D. Menzies, R. C., Y. B. Cheng, G. Simon, L. Spiccia *Journal of the Australasian Ceramic Society* **2003**, *39*, 108.
(55) O'Regan, B. C.; Durrant, J. R.; Sommeling, P. M.; Bakker, N. J. *Journal of Physical*

Chemistry C **2007**, *111*, 14001.
(56) Yip, C. T.; Mak, C. S. K.; Djurisic, A. B.; Hsu, Y. F.; Chan, W. K. *Applied Physics a-Materials Science & Processing* **2008**, *92*, 589.
(57) Ferry, V. E.; Verschuuren, M. A.; Li, H. B. T.; Verhagen, E.; Walters, R. J.; Schropp, R. E. I.; Atwater, H. A.; Polman, A. *Optics Express* **2010**, *18*, A237.
(58) Baxter, J. B.; Aydil, E. S. *Applied Physics Letters* **2005**, *86*, 053114.
(59) Hafez, H.; Wu, J. H.; Lan, Z.; Li, Q. H.; Xie, G. X.; Lin, J. M.; Huang, M. L.; Huang, Y. F.; Abdel-Mottaleb, M. S. *Nanotechnology* **2010**, *21*.
(60) Keis, K.; Magnusson, E.; Lindstrom, H.; Lindquist, S. E.; Hagfeldt, A. *Solar Energy Materials and Solar Cells* **2002**, *73*, 51.
(61) Ferry, V. E.; Munday, J. N.; Atwater, H. A. *Advanced Materials* **2010**, *22*, 4794.
(62) Atwater, H. A.; Polman, A. *Nature Materials* **2010**, *9*, 205.
(63) Rockstuhl, C.; Fahr, S.; Lederer, F. *Journal of Applied Physics* **2008**, *104*.
(64) Bardhan, R.; Grady, N. K.; Cole, J. R.; Joshi, A.; Halas, N. J. *Acs Nano* **2009**, *3*, 744.
(65) Chen, H. A.; Long, J. L.; Lin, Y. H.; Weng, C. J.; Lin, H. N. *Journal of Applied Physics* **2011**, *110*.
(66) Qian, L. H.; Das, B.; Li, Y.; Yang, Z. L. *J. Mater. Chem.* **2010**, *20*, 6891.
(67) Penninck, L.; Mladenowski, S.; Neyts, K. *Journal of Optics* **2010**, *12*.
(68) Shafran, E.; Mangum, B. D.; Gerton, J. M. *Physical Review Letters* **2011**, *107*.
(69) Zhang, Q. F.; Cao, G. Z. *Nano Today* **2011**, *6*, 91.
(70) Moller, H. J. *Semiconductors for Solar Cells* **1993**.

Chapter 4

Efficient Dye Sensitized Solar Cells by Plasmonic Au-TiO_2 Core-Shell Nanopillars

Abstract

An investigation into incorporating core-shell Au-TiO_2 nanopillars in dye-sensitized solar cells has been reported. The plasmon-enhanced light absorption, photocurrent, and power conversion efficiency for iodide/triiodide electrolyte based dye-sensitized solar cells has been demonstrated. Our spectroscopic data indicates that the corrosion-protected gold nanopillar as plasmonic optical elements of the photoelectrode help in plasmon-enhanced photocarrier generation which in turn increases photocurrents of Au-TiO_2 nanopillars system. The efficiency obtained with only TiO_2 nanopillar and plasmon enhanced Au-TiO_2 core-shell nanopillar based dye-sensitized solar cells has been systematically studied using J-V curve parameters. Over the range of only TiO_2 nanopillar cells and the Au-TiO_2 nanopillar cells examined, there was a clear enhancement of the dye extinction when plasmonic gold nanopillars were present. The results indicate that substantially larger optical enhancements are achievable with even larger active surface area of the photoanodes, suggesting that even greater photocurrent and efficiency enhancements may be achievable.

4.1. Introduction

Dye sensitized solar cells are considered to be one of the most promising third generation excitonic solar cells.[1-3] However, there are two primary challenges in optimizing DSSCs for real applications: 1) providing fast electron transport out of the semiconductor to enhance the charge transfer and 2) maximizing the light harvesting efficiency.[3] DSSCs with ordered nano TiO_2 structures as photoanode have produced improved solar cell devices due to the prolonged stability of the anatase phase, faster electron transport, enhanced ability to accept electrons into the conduction band, and slower charge recombination.[4] However, despite these positive aspects of using TiO_2 nanoarchitectures as photoanodes, the wide band gap (3.2 eV) permits only the use of ultraviolet radiation without a dye sensitizer. There are several approaches which focus on using various core-shell nanostructures as anodes in DSSCs[5,6-11] and carbon nanofiber (CNF)-TiO_2 core-shell structures as photoanode materials in DSSCs[12-16] in order to provide easy, uninterrupted transport of electrons from the semiconductor to the collecting anode. The heterogeneous systems provided ideal conditions for energy generation. However, the efficiency remained in the 1-7 % range. If the electron transport out of the semiconductor layer could be increased while maintaining high surface area available for enough dye adsorption, this arrangement would provide a new approach for improved efficiency in this new class of electrochemical cells.

Another efficient way to boost DSSC efficiency would be improving the photon capture cross section in the active semiconductor layer. The current as well as voltage can be increased by a greater number of electron-hole (e-h) pair generations in spectral regions where light absorption is insufficient. These increases will be useful because the charge transport in DSSCs puts severe constraints on the semiconductor layer thickness.[17] Nanometer sized metallic nanoparticles are efficient candidates in the energy technologies due to their tunable optical cross sections associated with their localized surface plasmon resonances (LSPRs).[18] Surface plasmons (SPs) are the charge density oscillations of conduction electrons at the interface between two media with opposite dielectric constants, for example a metal and an insulator. Careful design and architectural efficiency are needed to cause these metallic structures to trap light and concentrate it into a thin semiconductor layer. The field of surface plasmon photonics can benefit nanoscale thin-film solar cells. Surface plasmon photonics is very well explored due to its inherent property of having high concentrations of free electron oscillations available for collective trapping and concentrating light into the semiconductor layer.[19-23] However, the detailed study of plasmonic

effects on DSSCs has not yet been thoroughly investigated.[24] There are a few reports on the effect of LSPRs on the DSSCs performances that have studied the distance dependence of the plasmon enhanced extinction of the dye with incorporation of Ag nanoparticles into the thin amorphous layer of TiO_2,[25] the effect of embedded Au nanoparticles in the TiO_2 nanoparticle layer on the photocurrents of DSSCs,[26] incorporation of Au-SiO_2 core-shell nanoparticles into the TiO_2 layer in DSSCs,[27] enhanced light absorption and scattering by suspending SiO_2 core-Ag shell particles into the mesoporous TiO_2 nanoparticles composite layer,[28] and by increasing the dye's absorption coefficient by decreasing the photoanode thickness through suspension of Ag-TiO_2 core-shell nanoparticles into the TiO_2 nanoparticle layer.[29] Here we report a different approach toward plasmon enhanced DSSCs by fabricating Au-TiO_2 core-shell nanopillars directly on an FTO substrate. Our approach has several advantages. First, a TiO_2 shell covering the Au nanopillars is utilized in order to prevent recombination reactions as well as protecting the metal nanopillars from corrosion by I^-/I_3^- electrolyte. Second, electron transport out of the TiO_2 layer is expected to be very fast due to the thin (15-20 nm) active layer of TiO_2. Third, in order to maximize the effect of LSPs we use a very small Au core of 200 nm in diameter and 200 nm in height coated with a 15-20 nm shell of TiO_2. By utilizing Au-TiO_2 core-shell nanopillars, we have demonstrated enhanced optical absorption of the nanostructures in the thin film, which is due to the strong localized electric field generated by LSPs. In principle, metal nanostructures could enhance the absorption in DSSCs by either scattering light enabling a longer optical path-length, by a dipole-dipole interaction and resonant energy transfer or by near-field coupling between the surface plasmon polariton (SPP) and the dye excited state.

4.2. Experimental

4.2.1. Nanopillar fabrication

We have utilized e-beam nanolithography (EBL) and sputtering to achieve plasmonic core-shell nanopillar arrays. The detailed schematic of the fabrication process is given in Figure 4.1 below. Initially, a 1 wt% solution of negative polymer resist (poly methyl methacrylate Micro Chem 950, PMMA A8) in chlorobenzene was spin coated on a fluorine doped conductive transparent SnO_2 substrate (FTO, Solaronix, TCO10-10, sheet resistance 10 Ω sq^{-1}) to give $\approx$ 400

nm layer template. The PMMA has a very small interaction volume which allows very small patterns to be formed. The e-beam writing created patterned holes in the PMMA template. This patterning was done by using nanopattern generation (NPG) software attached to the Carl Zeiss 1530 VP field emission scanning electron microscope FESEM instrument. The exposed resist was removed with methyl isobutyl ketone (MIBK) and isopropyl alcohol (IPA). MIBK:IPA solvent ratio was (1:3). A 200 nm Au metal layer was then deposited by sputter coating. The remaining PMMA layer, along with the Au deposited on it, was removed in a subsequent lift off step by dissolving in acetone to leave Au pillar arrays on the FTO. The lift-off technique is based on patterning target materials on conductive substrates using sacrificial templates for example, photoresist. The detailed process involves, creating an inverse pattern on the template layer which is done by etching openings through the layer by using either electron beam lithography or extreme ultraviolet lithography (EUVL) so that the target material can reach the surface of the substrate in those regions where the final pattern is to be created. The target material is deposited over the whole area of the wafer, reaching the surface of the substrate in the etched regions and staying on top of the sacrificial layer in the regions where it was not previously etched. When the sacrificial layer is washed away with a lift-off solvent, the material on the top is lifted-off and washed away together with the sacrificial layer below. For PMMA, acetone is the solvent typically used during lift-off. After the lift-off, the target material remains only in the regions where it had direct contact with the substrate.

The gold nanopillar patterning step was done to check the improvements and corrections needed in the experiments. This particular step of removal of the resist to make gold pillars on the FTO was not the final step. It was an additional step required to check the consistency of the whole process before making the final Au-TiO_2 core-shell nanopillars.

In another attempt the core-shell Au-TiO_2 nanopillars were created by following the same method as described above for Au nanopillars, except sputter coating with gold was followed by sputter coating with Ti. The thickness of titanium was kept to 15-20 nm using the thickness monitoring system attached to the sputtering system (Cressington 308R). The patterns were then developed to remove exposed resist followed by lift off to obtain Au-Ti core-shell nanopillar arrays on the FTO substrate. Later, the nanostructures were annealed in air to convert Ti into TiO_2 and finally Au-TiO_2 nanopillar arrays (Au-TiO_2 NPLs) were obtained on FTO. Again in another

attempt, only TiO_2 nanopillars were patterned on FTO following the same procedure without the gold deposition step. Annealing of these structures yielded TiO_2 nanopillars (TiO_2 NPLs) on FTO. The well ordered TiO_2 and Au-TiO_2 core-shell nanopillar arrays were subjected to a comparative study in order to gain more insight into the role of plasmonic structures for improving DSSC performance.

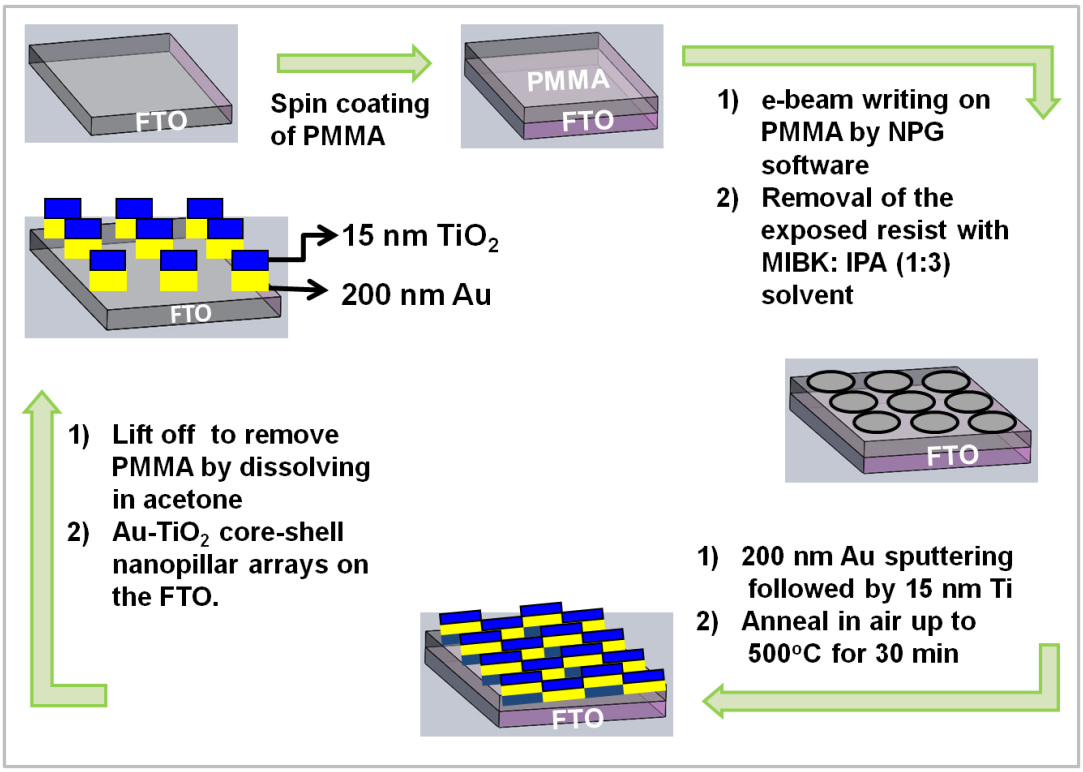

Fig. 4.1 Schematic of core-shell metal-metal oxide nano-structure preparation

4.3. Characterization

The structures were characterized by a Carl Zeiss 1530 VP field emission scanning electron microscope (FESEM). The compositional analysis was conducted by energy dispersive X-ray spectroscopy (EDS).

4.4. Absorbance measurement

The absorption spectra of the nanostructures were recorded in the reflectance mode after each process by using a Cary 500 UV-Vis spectrophotometer. For comparisons and to check the consistency in properties, we measured the absorbance of two TiO_2 nanopillar arrays and two Au-TiO_2 nanopillar arrays with each pair patterned with similar conditions and having similar morphology.

4.5. DSSC fabrication

Photoanodes utilizing TiO_2 nanopillar and Au-TiO_2 nanopillar arrays on FTO were used for DSSC fabrication. First, the structure was heated in air to 450 ^oC for 30 minutes. The resulting TiO_2 nanopillar or Au-TiO_2 core-shell nanopillar film on the FTO was sensitized for 24 hours by soaking in a dye solution overnight. A ruthenium dye (N-535, Solaronix) was prepared by dissolving 25 mg of the solid in 1 mL of ethanol. A platinum coated FTO counter electrode was prepared by brushing with a thin layer of Platisol T (Solaronix). The I^-/I_3^- electrolyte was prepared using 0.6 M 1-methyl-3-propylimidazolium iodide, 0.05 M iodine, 0.05 M LiI and 0.5 M *tert*-butylpyridine in 25 mL acetonitrile:valeronitrile (1:1 volume ratio). Two small holes were drilled in the glass of the platinum electrode in order to later inject the electrolyte. The two electrodes were tightly sandwiched together by using Surlyn® sealant (Solaronix), and the sandwiched electrodes were sealed by heating for 2 minutes with a heat gun. The electrolyte was carefully introduced into the space between the two electrodes through one hole on the Pt electrode with a syringe. The drilled holes were then sealed. Photovoltaic data were measured using an Oriel Newport 500 watt solar simulator set at 100 mW/cm^2 full spectrum power (equivalent to AM-1.5). J-V data were generated using a Keithley 2400 source meter. The light intensity of the xenon light source was adjusted by using an NREL calibrated silicon photodiode (Hamamatsu S1787-08 for visible to IR range).

4.6. Results and discussion

We have employed EBL patterned Au-TiO_2 core-shell nanopillars to improve DSSC efficiency. EBL is versatile technique and plays an important role in the fabrication of functional devices based on nanoscale structures of the noble metals.[30-31] We extended the method further by patterning metal-metal oxide core-shell nanopillar arrays on FTO. The EBL technique allowed particle shape and interparticle distance control in the arrays. Also, it allowed creating the nanopillars directly on the FTO substrates, which is an important factor in maximizing the performance of DSSCs. Figure 4.2 shows FESEM images of nanostructures obtained in this study. Fig. 4.2 (a) shows that nanoholes were successfully created on PMMA resist with an average hole diameter 200 nm and a center to center interhole distance of 200 nm. Fig. 4.2 (b) shows a 30º angle tilted view with respect to the sample normal of the Au nanopillars which shows that the Au nanopillars were 200 nm in height and 200 nm in diameter. Fig. 4.2 (c) and (d) are the top view images (low and high magnification) of Au-TiO_2 core-shell nanopillars patterned on an FTO substrate. Fig 4.2 (e) represents the EDS spectrum from the structure in 4.2 (c) showing peaks for Au, Ti and O. Fig. 4.3 (a) shows the TiO_2 nanopillars (without gold) that were successfully patterned directly on the FTO substrate. The EDS spectrum illustrates the presence of Ti and O Fig. 4.3 (b). Also apparent from the EDS spectrum is the absence of gold in this sample.

The optical absorbance spectra of the four different photoanodes are presented in Fig. 4.4. The absorbance was red-shifted with the incorporation of Au nano-pillars inside the TiO_2 nano-pillars. In detail, Fig. 4.4 illustrates the optical absorbance of the plasmonic nanostructures before the dye is attached. As expected, the absorbance intensifies and red shifts from shorter to longer wavelength with the use of Au-TiO_2 core-shell nanopillar photoanodes due to the higher dielectric constant surrounding the Au nanopillars inside the Au-TiO_2 core-shell nanopillars. In order to check the consistency, two photoanodes were patterned with same conditions and parameters. Then absorbance was measured for each of them separately. The red shift was visible in both the core-shell nanopillar architectures which were compared to the two TiO_2 only nanopillar patterns. The absorbance spectrum of N535 adsorbed onto a flat FTO substrate is included in the data set for comparison. The optical absorption data given here clearly demonstrates that the LSPRs play

an important role in shifting the absorbance peak of the nanostructures from a short wavelength to a longer wavelength with incorporation of plasmonic Au nanostructures.

After optical measurements were recorded, cells were fabricated and photovoltaic J-V data were obtained. Solar cells data are given in Fig. 4.5 along with the detailed list of the other parameters obtained are given in Table 4.1.

The most common state of the art plasmon enhanced DSSCs to date employ metallic nanoparticle scatterers deposited on top of an already fabricated solar cell device. These cells have the advantage that the device fabrication process is simple and the procedure does not have to be modified substantially in order to incorporate the plasmonic nanoparticles. However, since the bare metal nanoparticles are vulnerable to the corrosive I^-/I_3^- and metal surfaces provide a site for recombination of injected electrons with the redox couple, there is motivation to find alternate methods to fabricate the plasmonic devices.

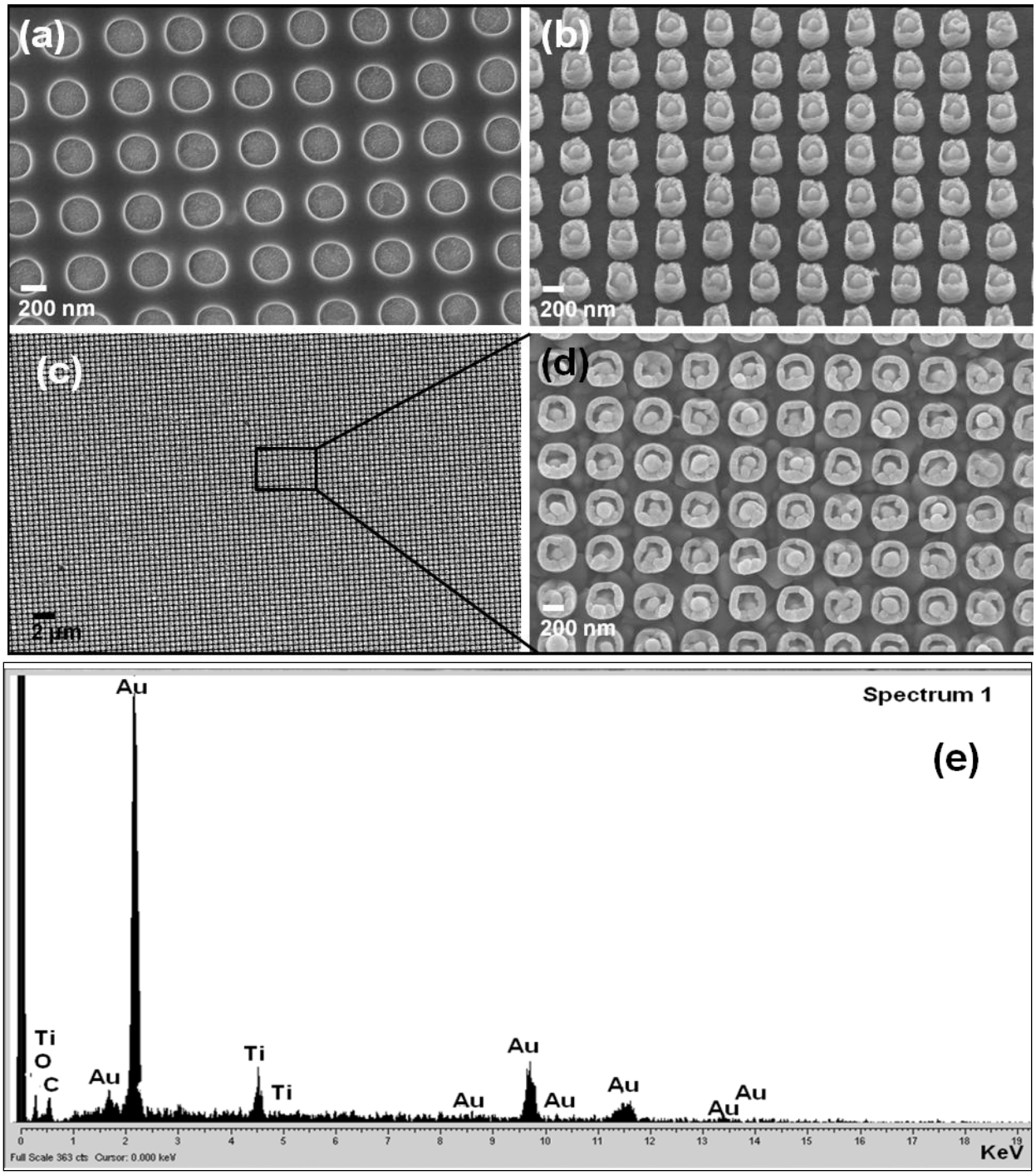

Fig. 4.2 (a) FESEM image of nano-holes in PMMA resist on FTO substrate after e-beam writing and removal of the exposed resist. Fig. 4.2(b) Au nanopillars on FTO. Fig. 4.2(c) and 4.2(d) low and high magnification FESEM images of the e-beam nanolithographically patterned Au-TiO_2 core-shell nanopillars on FTO. Fig. 4. 2 (e) EDS peaks for Au, Ti and O from array in 4.2 (c).

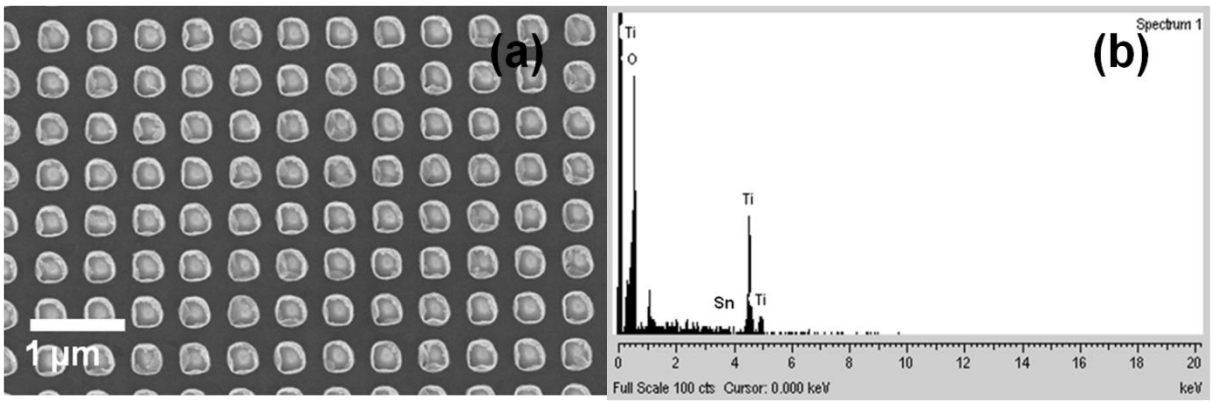

Fig. 4.3 (a) FESEM image of the e-beam nanolithographically patterned TiO_2 nanopillars on FTO substrate. Fig. 4.3 (b) EDS peaks for Ti and O. (Sn peak originates from the FTO substrate)

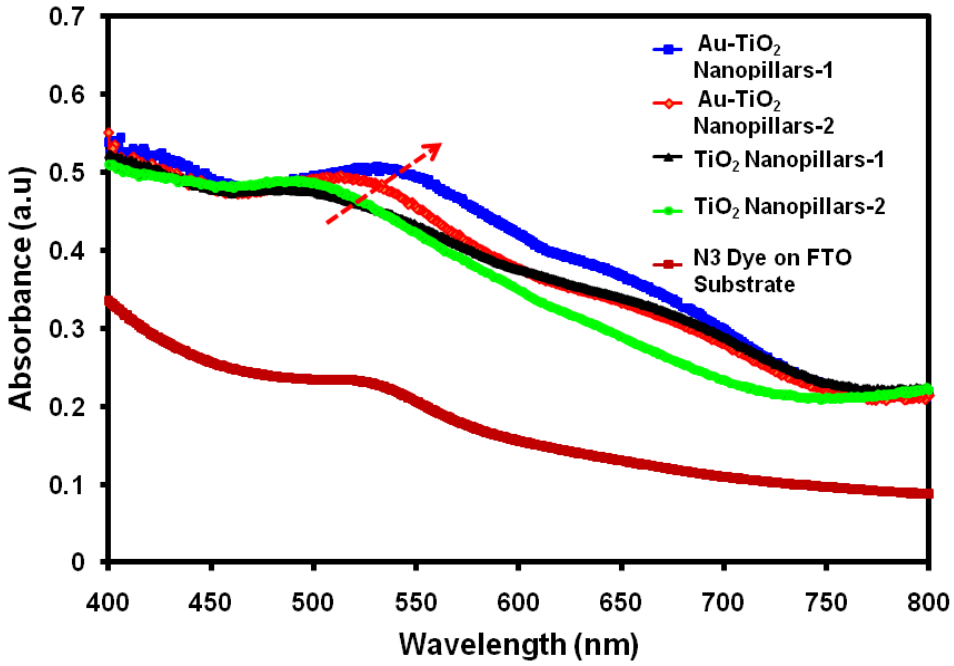

Fig. 4.4 Optical properties of the photoanodes before the dye is attached

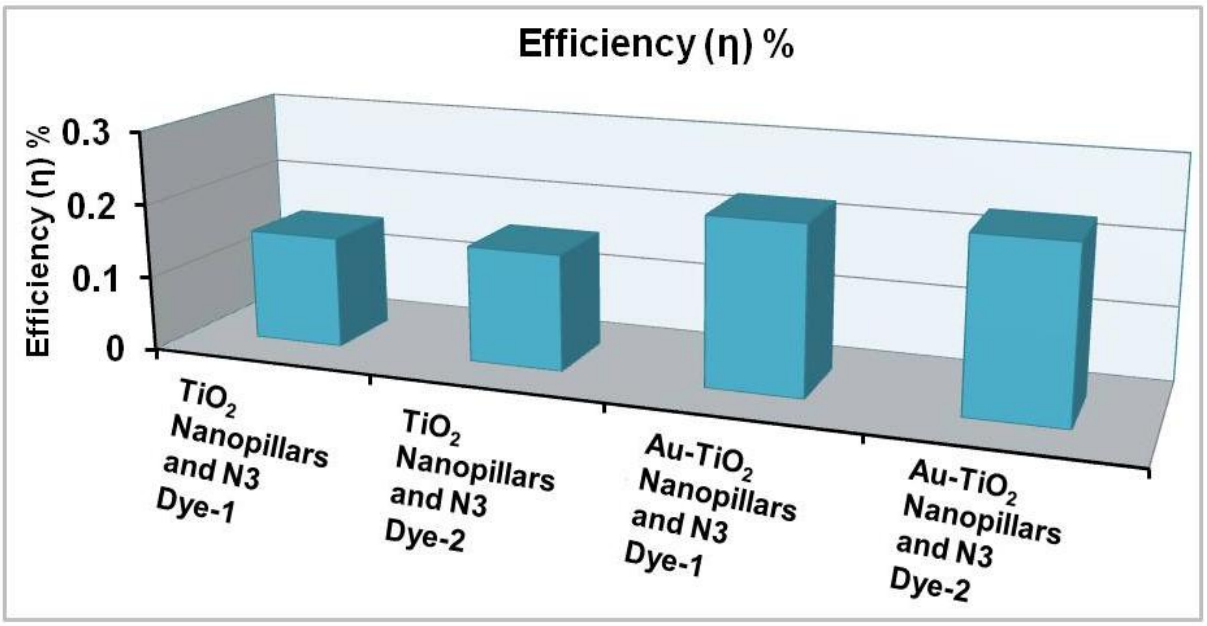

Fig. 4.5 Power conversion efficiencies for DSSCs employing various nanopillar arrays as photoanodes. Data shows TiO_2 nanopillars 1 and/or 2 for first and second cells made with N3 dye as sensitizer. Au-TiO_2 core-shell nanopillars 1 and/or 2 for first and second cells made from Au-TiO_2 nanopillars with N3 dye. Other J-V curve parameters are listed in Table 4.1.

Table 4.1 J-V characteristics of dye-sensitized TiO_2 nanopillar and Au-TiO_2 core-shell nanopillar DSSCs under 1 sun

Photoanode film type	**V_{oc} (V)**	**J_{sc} (mA/cm^2)**	**FF (%)**	**(η) %**
TiO_2 NPLs-1	0.594	6.86E-04	37.1	0.151
TiO_2 NPLs-2	0.674	7.11E-04	32.8	0.157
Au-TiO_2 NPLs-1	0.473	1.57E-03	30.5	0.226
Au-TiO_2 NPLs-2	0.476	1.61E-03	30.2	0.231

The Au-TiO_2 NPLs are patterned in such a way that the gold nanopillars are embedded inside a 15 nm thin layer of TiO_2. This TiO_2 shell covering gold nanopillars is utilized to prevent recombination and back reaction, protecting metal NPLs during device fabrication, as well as preventing metal NPLs from corrosion by redox species in the electrolyte.

Cell efficiencies are presented in Figure 4.5. Cells with only TiO_2 NPLs had a power conversion efficiency η of $0.15 \pm (4.45 \times 10^{-3})$ %. Cells with Au-TiO_2 NPLs were considerably more efficient than either of the reference cells. The best cell (15 nm of TiO_2 coated Au NPLs) had an efficiency of $0.23 \pm (3.00 \times 10^{-3})$ % which is increased by 53%. Notably, this further confirms that for very thin (15 nm) TiO_2 layers, the transport properties of TiO_2 are sufficient for photo energy conversion in DSSCs. Open circuit voltages (V_{oc}) of up to 670 mV were recorded for the TiO_2 NPL cells (see Table 1). The TiO_2 NPL only DSSC showed a current density of $0.69 \pm (1.79 \times 10^{-5})$ mA/cm^2 whereas the plasmon-enhanced DSSCs with Au-TiO_2 NPLs exhibited a current density of $1.59 \pm (2.49 \times 10^{-5})$ mA/cm^2. Compared with the TiO_2 NPL only DSSC, the fill factor (FF) and open-circuit voltage of the plasmon-enhanced Au-TiO_2 NPL DSSC were close, while J_{sc} significantly increased by 130%. Since $\eta = J_{sc}V_{oc}FF/P_{in}$, where P_{in} is the intensity of incident light (constant), the improvement in efficiency for the plasmon-enhanced DSSC is mainly due to the increased photocurrent corresponding to light scattering and enhanced dye absorption by LSPRs. The incorporation of plasmonic Au-TiO_2 nanopillars in the DSSC provides scattering of the long wavelength in sunlight and consequently increased light absorption.

4.7. Summary

The optical absorbance spectra of the four different photoanodes showed that the absorbance was red-shifted with the incorporation of Au-TiO_2 core-shell nanopillars in DSSCs as opposed to TiO_2 only nanopillars as anodes. J-V curves were generated by fabricating DSSCs out of these photoanodes and efficiencies were obtained. The efficiency was increased by 53% for the Au-TiO_2 nanopillars based devices as compared to the cells made out of TiO_2 only nanopillars. The results suggest that larger gains in plasmon–enhanced photocurrent are possible with device optimization.

4.8. References

(1) Ardo, S.; Meyer, G. J. *Chemical Society Reviews* **2009**, *38*, 115.
(2) O'Regan, B.; Grätzel, M. *Nature* **1991**, *353*, 737.
(3) Martinson, A. B. F.; Hamann, T. W.; Pellin, M. J.; Hupp, J. T. *Chemistry-a European Journal* **2008**, *14*, 4458.
(4) Hart, J. N.; Cheng, Y. B.; Simon, G. P.; Spiccia, L. *Journal of Nanoscience and Nanotechnology* **2008**, *8*, 2230.
(5) Wang, M. L.; Huang, C. G.; Cao, Y. G.; Yu, Q. J.; Deng, Z. H.; Liu, Y.; Huang, Z.; Huang, J. Q.; Huang, Q. F.; Guo, W.; Liang, J. K. *Journal of Physics D-Applied Physics* **2009**, *42*.
(6) Law, M.; Greene, L. E.; Radenovic, A.; Kuykendall, T.; Liphardt, J.; Yang, P. D. *Journal of Physical Chemistry B* **2006**, *110*, 22652.
(7) Kamat, P. V. *Journal of Physical Chemistry C* **2007**, *111*, 2834.
(8) Chappel, S.; Chen, S. G.; Zaban, A. *Langmuir* **2002**, *18*, 3336.
(9) Martinson, A. B. F.; Elam, J. W.; Liu, J.; Pellin, M. J.; Marks, T. J.; Hupp, J. T. *Nano Letters* **2008**, *8*, 2862.
(10) Sahu, G.; Gordon, S. W.; Tarr, M. A. *RSC Advances* **2012**, *2*, 573.
(11) Sahu, G.; Wang Kai; Gordon, S. W.; Zhou, W.; Tarr, M. A. *RSC Advances* **2012**, *Advance article, DOI: 10.1039/C2RA01030E*.
(12) Li, Z. Z.; Rochford, C.; Baca, F. J.; Liu, J. W.; Li, J.; Wu, J. *Nanoscale Research Letters* **2010**, *5*, 1480.
(13) Lee, K. M.; Hu, C. W.; Chen, H. W.; Ho, K. C. *Solar Energy Materials and Solar Cells* **2008**, *92*, 1628.
(14) Kongkanand, A.; Dominguez, R. M.; Kamat, P. V. *Nano Letters* **2007**, *7*, 676.
(15) Liu, J. W.; Kuo, Y. T.; Klabunde, K. J.; Rochford, C.; Wu, J.; Li, J. *Acs Applied Materials & Interfaces* **2009**, *1*, 1645.
(16) Liu, J. W.; Li, J.; Sedhain, A.; Lin, J. Y.; Jiang, H. X. *Journal of Physical Chemistry C* **2008**, *112*, 17127.
(17) Huynh, W. U.; Dittmer, J. J.; Alivisatos, A. P. *Science* **2002**, *295*, 2425.
(18) Kreibig, U.; Vollmer, M. *Springer Series New York* **1995**, p. 546.
(19) Haug, F. J.; Soderstrom, T.; Cubero, O.; Terrazzoni-Daudrix, V.; Ballif, C. *Journal of Applied Physics* **2008**, *104*.
(20) Tvingstedt, K.; Persson, N. K.; Inganas, O.; Rahachou, A.; Zozoulenko, I. V. *Applied Physics Letters* **2007**, *91*.
(21) Franken, R. H.; Stolk, R. L.; Li, H.; van der Werf, C. H. M.; Rath, J. K.; Schropp, R. E. I. *Journal of Applied Physics* **2007**, *102*.
(22) Schropp, R. E. I.; Li, H.; Franken, R. H.; Rath, J. K.; van der Werf, C. H. M.; Schuttauf, M. A.; Stolk, R. L. *Thin Solid Films* **2008**, *516*, 6818.
(23) Rockstuhl, C.; Fahr, S.; Lederer, F. *Journal of Applied Physics* **2008**, *104*.
(24) Hagglund, C.; Zach, M.; Kasemo, B. *Applied Physics Letters* **2008**, *92*.
(25) Standridge, S. D.; Schatz, G. C.; Hupp, J. T. *Journal of the American Chemical Society* **2009**, *131*, 8407.
(26) Kawawaki, T.; Takahashi, Y.; Tatsuma, T. *Nanoscale* **2011**, *3*, 2865.
(27) Brown, M. D.; Suteewong, T.; Kumar, R. S. S.; D'Innocenzo, V.; Petrozza, A.; Lee, M. M.; Wiesner, U.; Snaith, H. J. *Nano Letters* **2011**, *11*, 438.
(28) Ding, B.; Lee, B. J.; Yang, M. J.; Jung, H. S.; Lee, J. K. *Advanced Energy Materials* **2011**, *1*, 415.

(29) Jifa, Q. X., Dang; Paula, T. Hammond; and Angela, M. Belcher *Acs Nano* **2011**, *ASAP*.
(30) Gotschy, W.; Vonmetz, K.; Leitner, A.; Aussenegg, F. R. *Applied Physics B-Lasers and Optics* **1996**, *63*, 381.
(31) Lamprecht, B.; G. Schider *Phys. Rev. Lett* **2000**, *84*, 4721.

Chapter 5

Impedance Investigation of Dye Sensitized Solar Cells Based on Radial Core-Shell Au-TiO_2 Nanowire Photoanodes

Abstract

Electronic charging and conducting properties of vertically oriented Au-TiO_2 core-shell nanowire arrays were analyzed using impedance spectroscopy and compared with TiO_2 nanotube and TiO_2 nanoparticle cells. In dye-sensitized solar cells, there is a competition between transport of electrons through the porous semiconductor electrode toward the conducting substrate and back reaction of electrons to recombine with I_3^- ions in the semiconductor-electrolyte interface. This competition determines the charge collection efficiency. This mechanism is strongly influenced by the electronic distribution and geometrical nano-architecture of the semiconductor. Herein, we systematically analyze the electrochemical parameters of Au-TiO_2 nanowire, TiO_2 nanotube and TiO_2 nanoparticle-based electrodes by electrochemical impedance spectroscopy (EIS). The results show that the intrinsic three-dimensional crystalline structure of Au-TiO_2 nanowires can promote the efficient charge transport through the metal-semiconductor network, which effectively blocks the recombination of electrons with I_3^- ions in the semiconductor-electrolyte interface, resulting in an increase of electron lifetime and a higher conductivity. Furthermore, the radial vertically oriented Au-TiO_2 nanowire provides efficient channels for electron transport and therefore increases electron diffusion length. These data provide a basic understanding of the role of Au-TiO_2 geometrical structure in solar energy conversion. The novel 3D Au-TiO_2 nanowire based electrode can further improve energy conversion efficiency in DSSCs.

5.1. Introduction

The J-V curve is the most fundamental measurement in which the performance of a photovoltaic device is revealed. The J-V curve answers the question of how good the device works or what is the efficiency of the cell, but it gives very limited information about the limiting factors and resistances of individual components that hinder device performance. Electrochemical impedance spectroscopy (EIS) is an advanced technique that can be used to study the charge transfer resistance and interfacial capacitance that are present in DSSCs. Time constants can be measured by using the EIS equivalent circuit parameters in order to determine the mechanism of electron transport through the semiconductor.

5.1.1. Definition of impedance

Electrical resistance can be defined as the ability of a circuit element to resist the flow of electrical current. Ohm's law (Equation 5.1) defines resistance in terms of the ratio between voltage, V, and current, I.

$$R = \frac{V}{I} \qquad (5.1)$$

However, the well known Ohm's law has its limit. It can only be used to systems with only one circuit element, i.e. the ideal resistor. An ideal resistor has several properties such as:

- Obeys Ohm's law at all current and voltage levels.
- Shows resistance that is independent of frequency.
- AC current and voltage signals though resistors are always in phase with each other.

In the real world, the circuit elements show much more complex behavior which means we have to rely on 'impedance', a more complex circuit parameter. Like resistance, impedance is a measure of the ability of a circuit to resist the flow of electrical current, but it is not limited by the simplifying properties listed above. Electrochemical impedance is usually measured by applying an AC potential to an electrochemical cell and then measuring the current through the cell. If we apply a sinusoidal potential excitation, the response to this potential is an AC current signal. This

current signal can be analyzed as a sum of sinusoidal functions. Electrochemical impedance is normally measured using a small excitation signal in order to maintain the cell's response as pseudo-linear. The characteristic of a pseudo-linear system is that the sine wave current response to a sine wave applied potential will be a sine function observed at the same frequency but will be shifted in phase. One instance is given in Figure 5.1 below.

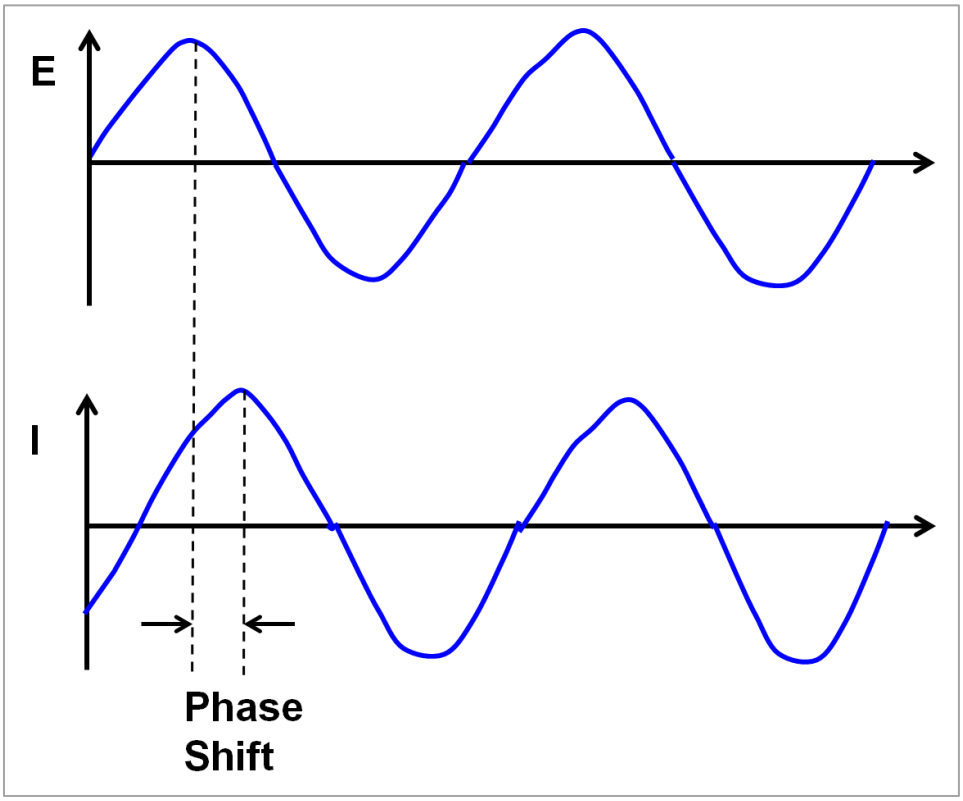

Fig 5.1 Sine wave current response in a pseudo-linear system

An expression for impedance (Z) of the system can be derived similar to Ohm's law with potential and current functions as:

$$Z = E_t/I_t = E_o \text{ Sin } (\omega t)/ I_o \text{ Sin } (\omega t + \phi) = Z_o \text{ Sin } (\omega t)/ \text{ Sin } (\omega t + \phi) \quad (5.2)$$

The mathematical derivation steps of the above expression has been given elsewhere.[1] The impedance can be expressed in terms of a magnitude, Z_o, and a phase shift, ϕ. If the impedance is represented as a complex function, the potential is described as,

$$E_t = E_o \exp (j\omega t) \quad (5.3)$$

And the current response as,

$$I_t = I_o \exp (j\omega t\text{-}\phi) \quad (5.4)$$

The impedance (Z) is represented as a complex number,[1]

$$Z(\omega) = E/I = Z_o \exp (j\phi) = Z_o (\cos \phi + j \sin \phi) \quad (5.5)$$

5.1.2. Data generation

In the impedance measurement the system is normally kept at a steady state followed by applying an AC potential and measuring the AC current through the cell. The universally accepted method allows for complex impedance and the phase shift measurements at a particular frequency. In the actual measurement, a range of frequencies are scanned through, typically 100 kHz to 10 mHz. Using model equivalent circuits, impedance parameters can be assigned for components internal to the cell. In addition to the scanning frequencies, the EIS parameters are also obtained at various conditions of steady state i.e. different bias voltages or illumination intensities, in order to generate a thorough knowledge on the trend of behavior of the various elements.

5.2. Data interpretation

5.2.1. Nyquist plot

The expression for Z (ω) in eq. 5.5 has a real and an imaginary part. If the real part is plotted on the X-axis and the imaginary part on the Y-axis of a chart, we get a Nyquist plot. See figure 5.2 below for reference. The Y-axis is negative and that each point on the Nyquist plot is the impedance at one frequency. The curve has been annotated to show that low frequencies are on the right side of the plot and higher frequencies are on the left. On the Nyquist plot the impedance can be represented as a vector (arrow) of length $|Z|$. The angle between this vector and the X-axis, commonly called the phase angle, φ [=argument(arg Z)]. Arg is a function that gives the angle between the position vector and positive real axis in a complex plot. The semicircle on a Nyquist plot is characteristic of a single time constant. Electrochemical impedance plots often contain several semicircles. Often only a portion of a semicircle is seen. Nyquist plots have one major limitation: They do not give the complete information on the exact frequency that was used to record one point.

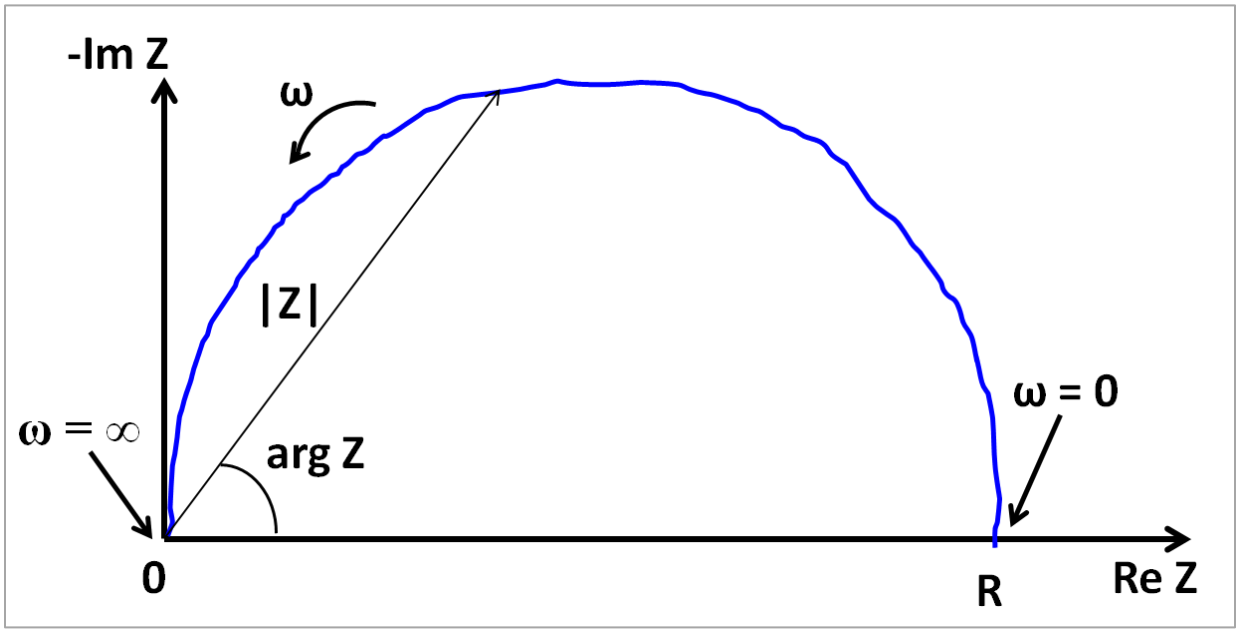

Fig 5.2 Nyquist plot with impedance vector

5.2.2. Bode plot

Another important representation of the EIS measurement is the Bode phase plot. The impedance is plotted with log frequency on the X-axis and both the absolute values of the impedance ($|Z|=Z_o$) and the phase-shift on the Y-axis. Unlike the Nyquist plot, the Bode plot gives the complete frequency information.

5.2.3. EIS, applied to DSSC

Recently, electrochemical impedance spectroscopy has been widely used to analyze internal resistances in DSSCs.[2-5] There are four frequencies those are particularly important for the DSSC impedance spectra, which are given by the characteristic frequencies and time constants for each process. The time $1/\omega_{CE}$ for the counter electrode is related to the time constant of charge transfer at the electrolyte and Pt counter electrode interface where, ω_{CE} is the angular frequency of the counter electrode. The transit time for the charge carrier transport in the semiconductor is $1/\omega_{tr}$. The lifetime of the electrons, which is related to the recombination process, has a time constant $1/\omega_{rec}$. The characteristic time for ion diffusion is ω_d.[6] When these frequencies are well separated, $\omega_{CE} < \omega_{tr} < \omega_{rec} < \omega_d$, it is possible to characterize each element, to calculate its corresponding DC-resistance and thereby the contribution from each element to the J-V curve. Figure 5.3 below represents the Nyquist plot of a core-shell nanowire DSSC showing the individual resistances and four characteristic angular frequencies.

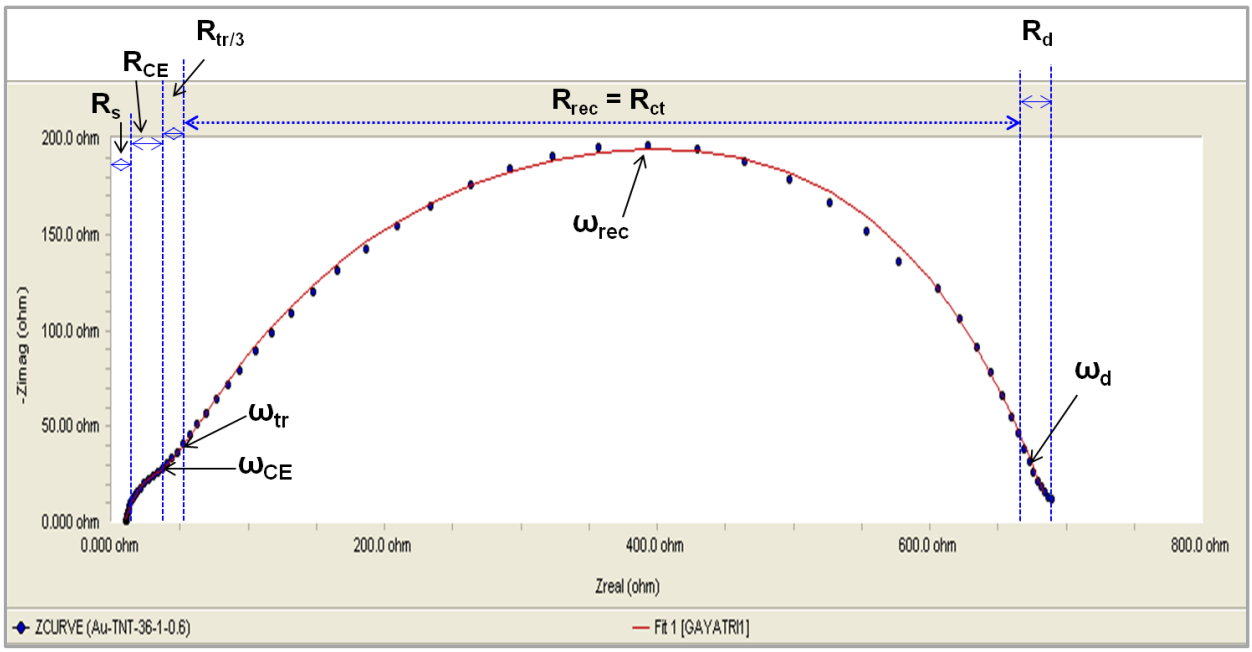

Fig 5.3 The Nyquist plot of the transmission line model of the Au-TiO_2 core-shell nanowire DSSC with 0.6 V bias voltage. The following parameters are displayed: Series resistance, R_s, resistance at the counter electrode, R_{CE}=R_{pt}, charge transport resistance, R_{tr}, recombination resistance R_{rec} = R_{ct}, and diffusion resistance, R_d. Four corresponding characteristic angular frequencies are given by ω_{CE}, ω_{tr}, ω_{rec} and ω_d.

There are two main features apparent in this impedance spectrum. The first arc seen in the high frequency region, which is essentially constant with respect to applied potential, results from the charge transfer resistance, R_{CE}=R_{Pt}, and double-layer capacitance, C_{Pt}, at the platinized counter electrode.[6-7] The second arc observed at lower frequencies, which depends strongly on applied potential, results from the charge transfer resistance of the recombination process, R_{ct}, and the chemical capacitance, C_μ, of the TiO_2 film.[6-7] The electron transport resistance is manifested as a linear feature in the high frequency region, and can thus be obscured by the impedance of charge transfer at the platinum electrode.[6]

The selected illumination level and potential determine the response of the elements of the solar cell. At open-circuit potential and illumination, it is possible in most cases to identify the counter electrode recombination resistance and diffusion resistance. However, performing the impedance measurement in the dark is the easiest way to extract the transport properties of the

cell.[8] The recombination in this case is minimal without the presence of light, and transport and recombination can be well separated with respect to their time constants.[8]

5.3. Experimental

All EIS experiments were performed in the dark using a Gamry Reference 600 potentiostat equipped with a frequency response analyzer. The impedance spectra were recorded at direct applied potentials from 0.2 to 0.8 V. The AC potential applied was 10 mV. The range of frequency used was from 100 kilohertz (kHz)-50 millihertz (mHz). (The range is universally represented in a decreasing order due to higher frequency region starting from zero on real axis on the Nyquist plot)

The photoanodes were synthesized and the respective devices were fabricated, following the same method as explained in chapter 2, sections 2.2 and 2.3 of this dissertation.

5.4. Results and discussion

Impedance spectroscopy was used to investigate the electron dynamics in DSSCs employing three types of photoanodes such as 3D Au-TiO_2 core-shell nanowire, 1D TiO_2 nanotube and 0D TiO_2 nanoparticle network. A typical Nyquist plot of a core-shell nanowire DSSC is shown in Figure 5.3 above.

The electronic processes in the DSSC are very well described by a transmission line model developed by Bisquert and coworkers,[5-6,9-10]. Upon forward bias, electrons are injected from the FTO substrate into the semiconductor oxide and the film is charged by electron propagation through the TiO_2 network. Meanwhile, a fraction of the injected conduction band electrons are lost by reaction with the I_3^- ions in the electrolyte.[11].

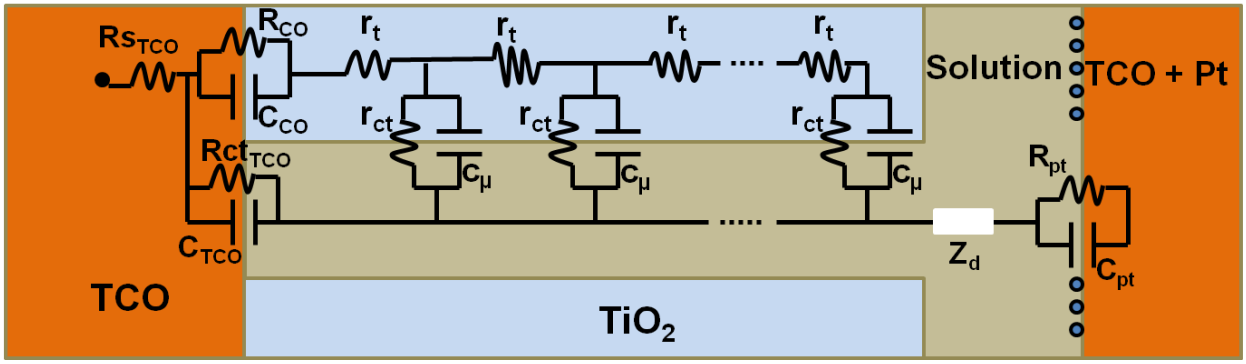

Fig 5.4 General equivalent circuit model used to fit EIS data of the DSSCs.

Table 5.1 Equivalent-circuit parameters of DSSC measured and derived from EIS

Measured Parameters	Derived Values	
Recombination Resistance, R_{ct} (Ω μm)	Mean Electron Lifetime (ms)	$\tau_n = 1/2\pi f_{max}$
Capacitance, C_μ (μF)	Mean Electron Transit time (ms)	$\tau_d = (r_t/r_{ct})L^2 \tau_n$
Transport Resistance, R_{tr} (Ω μm^{-1})	Diffusion Coefficient	$D_n = L^2/\tau_d$
Electron Collection Efficiency, η_{cc} (%)	Diffusion Length (μm)	$L_n = \sqrt{D_n \tau_n}$
Frequency, f (Hz)	Electron Conductivity ($\Omega^{-1}cm^{-1}$)	$\sigma_n = (L/B)R_{tr}^{-1}$

Where, L= length of nanostructures and B = projected active surface area

By fitting impedance data with the transmission line, provided in figure 5.4 above,[4-5] we can obtain characteristic elements that describe the effect of electrode architecture on the electronic process occurring in the cell. The main features that have been analyzed are given in table 5.1. Those are charge-recombination resistance (R_{ct}) on the semiconductor-electrolyte interface between the electron and the I_3^- in the electrolyte, chemical capacitance (C_μ), electron lifetime (τ_n), electron conductivity (σ_n) and electron diffusion length (L_n). The obtained data give a good explanation on the improved performance of 3D Au-TiO_2 nanostructures versus the 1D TiO_2 nanotube and 0D TiO_2 nanoparticle electrode which is summarized below.

5.5. Importance of characteristic impedance parameters

5.5.1. Recombination resistance (R_{ct})

The recombination process in a DSSC is mainly the interfacial charge transfer of electrons in the semiconductor, to oxidized ions in the electrolyte. Monitoring this recombination at the semiconductor/electrolyte interface is perhaps the most critical and challenging issue when striving to improve the DSSC performance. One possible way to analyzing recombination process in a DSSC is to study the recombination resistance (R_{ct}) using EIS. Charge recombination resistance, R_{ct} needs to be much larger than the charge transport resistance a feature that is necessary for good performance of a DSSC.[12]

5.5.2. Chemical capacitance (Cμ)

The chemical capacitance (Cμ) is another important parameter to study from EIS which is associated with delocalized, transport states. Upon illumination, electrons are injected from the photoexcited dye into the semiconductor and move towards the FTO substrate, while the electrolyte reduces the oxidized dye and transports the holes to the Pt electrode. Due to the presence of bandgap states, it increases additional possibilities for loading the semiconductor with charges. According to photovoltaic principles,[13] dye injection under illumination increases the number of electron density, n, which raises the quasi-Fermi level, E_f, that produces the photovoltage. An equation, $dE_f = -qdV$, where q is the elementary charge, gives rise to the relationship of voltage to carrier density in EIS. This relationship can be stated in a term called chemical capacitance Cμ which has the general form,

$$C\mu = \frac{dn}{dV} \qquad (5.6)$$

This means the chemical capacitance increases with forward bias, signifying greater carrier accumulation and higher probability of surface trap states below the conduction band edge.[13]

5.5.3. Time constants : e^- lifetime (τ_n) & e^- diffusion coefficient (D_n)

With the parameters obtained from impedance spectra, R_{ct}, C_μ, and R_t, we can calculate the basic electron transport and recombination parameters such as: D_n, τ_n and L_n. This set of parameters is frequently used in studying the electronic processes in DSSC, due to several reasons. The chemical diffusion coefficient, D_n, can be further related to the basic models for transport in disordered nanostructural materials.[14-16] The main time constants of DSSC i.e. the transit time, $\tau_d = L^2/D_n$, and the electron lifetime, $\tau_n = 1/2\pi\, f_{max}$, are very useful tools in collecting and validating the comparative analysis of the various electronic processes along with the collection efficiency of the nanostructure based DSSC.[17]

According to the quasi-static theory developed by Bisquert and Vikhrenko,[17] the mean electron lifetime, τ_n, is related to the conduction band electron lifetime, τ_o, by the expression,

$$\tau_n = \left(\frac{\partial nt}{\partial nc} \right) \tau_o \qquad (5.7)$$

Where n_t is the trapped electron density, n_c is the conduction band electron density, and τ_o is the inverse of the pseudo-first order rate for back-transfer of electrons from the conduction band. The relationship set up between the occupancy of these traps and the electron density in the conduction band is disturbed when variables such as the illumination intensity or the voltage are changed. Simply, the electron lifetime is defined as the total time an electron will remain in the oxide before it recombines with the redox species in the electrolyte. The longer the electron stays in the oxide, the better chance it has of being collected at the FTO and producing current. The electron lifetime is a consequence of trapping or de-trapping of electrons at states located in the band gap of the oxide. Therefore, the electron lifetime is strongly influenced by the voltage of the cells.

5.5.4. e^- conductivity (σ_n)

Another important parameter studied from the fit of EIS data is the electron conductivity, σ_n, which can be derived[18] according to,

$$\sigma_n = \left(\frac{L}{B}\right) R_{tr}^{-1} \qquad (5.8)$$

Where R_{tr} is the transport resistance, L is the length of the nanostructures, and B is the projected active surface area of the photoanode. The electron conductivity needs to be as high as possible in order to provide fast band conduction of electrons in the semiconductor.

5.5.5. Electron diffusion length (L_n)

The last factor studied from EIS measurement governing charge collection efficiency is the effective diffusion length, L_n, which is defined in terms of the recombination resistance and transport resistance by which the injected electrons are efficiently collected at the conducting substrate. The L_n may be calculated from,[9] see equation 5.9.

$$L_n = \sqrt{D_n \tau_n} = d\sqrt{\tau_n/\tau_d} = d\sqrt{R_{ct}/R_{tr}} \qquad (5.9)$$

Theoretically, diffusion length is a measure of the distance an electron will travel in the photoanode before it recombines with the oxidized species in the redox couple. To achieve a high charge-carrier collection efficiency, the diffusion length needs to be larger than the film thickness, $L_n > d$.

5.6. Various nanoarchitecture based EIS data interpretation

5.6.1. Recombination resistance (R_{ct}) data

Figure 5.5 presents R_{ct} values for the three electrodes Au-TiO_2 core-shell nanowire (black squares), TiO_2 nanotube (blue triangles), and TiO_2 nanoparticle (red diamonds) based cells at the bias voltage range of (0.5-0.7) V. It is clear that the R_{ct} value of Au-TiO_2 nanowire cell is much larger than that of TiO_2 nanotube and TiO_2 nanoparticle cell, indicating that the Au-TiO_2 nanoarchitectures can effectively prevent the electrons from recombination with the oxidized-state species, like I_3^- in the electrolyte. The recombination process always competes with the collection of electrons. Due to the relatively slow transport through the TiO_2 electrode, recombination of electrons with I_3^- ions in the electrolyte cannot be ignored. However, advanced 3D nanoarchitectures based photoanodes can decrease the rate of recombination which was seen in case of the Au-TiO_2 core-shell nanowire cells.

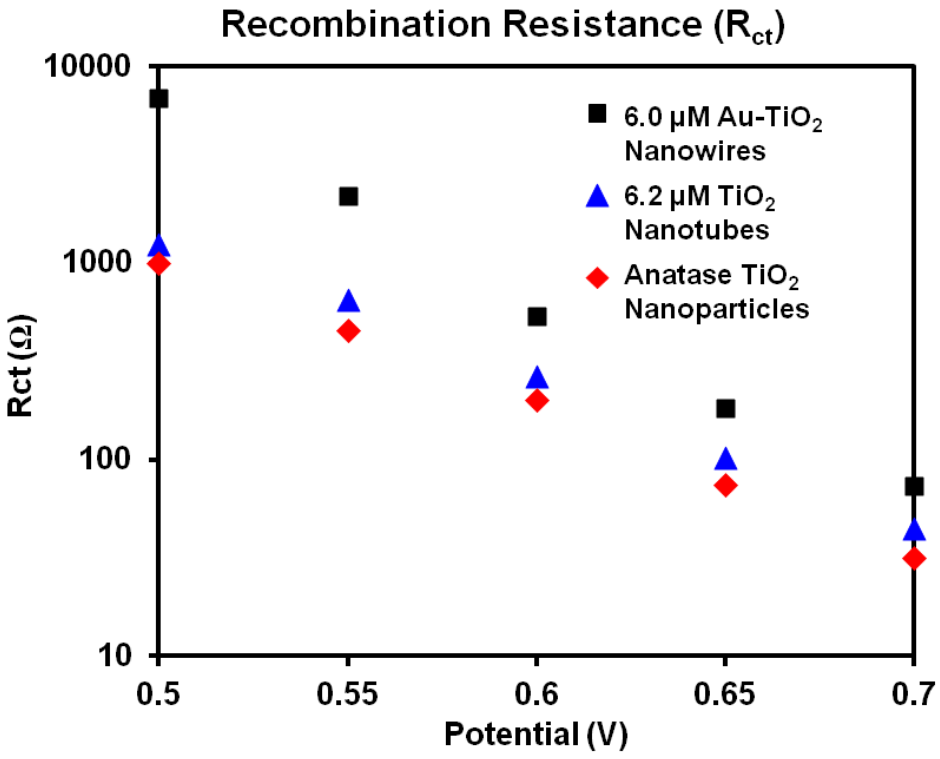

Fig 5.5 Charge recombination resistance (R_{ct}) extracted from EIS measurements for DSSCs with Au-TiO_2 core-shell nanowire (black squares), TiO_2 nanotube (blue triangles), and TiO_2 nanoparticle (red diamonds) photoanodes.

5.6.2. Chemical capacitance (Cμ) data

As described in the previous section, the chemical capacitance is a measure of the total density of free electrons in the conduction band and the localized electrons in the trap states.[2,19] Figure 5.6 below shows the chemical capacitance of cells with various electrodes. It is clearly shown that the TiO_2 nanostructures in the electrodes significantly influence the value of capacitance. Across the measured range, the capacitance of TiO_2 nanoparticle is larger than that of Au-TiO_2 nanowire and TiO_2 nanotube cell, indicating the density of trap sites below the conduction band edge is much higher in the TiO_2 nanoparticle cell. The capacitance data also shows that the Au-TiO_2 core-shell anode does have slightly more trap sites than the nanotube photoanode, but it has significantly less traps than the mesoporous film.

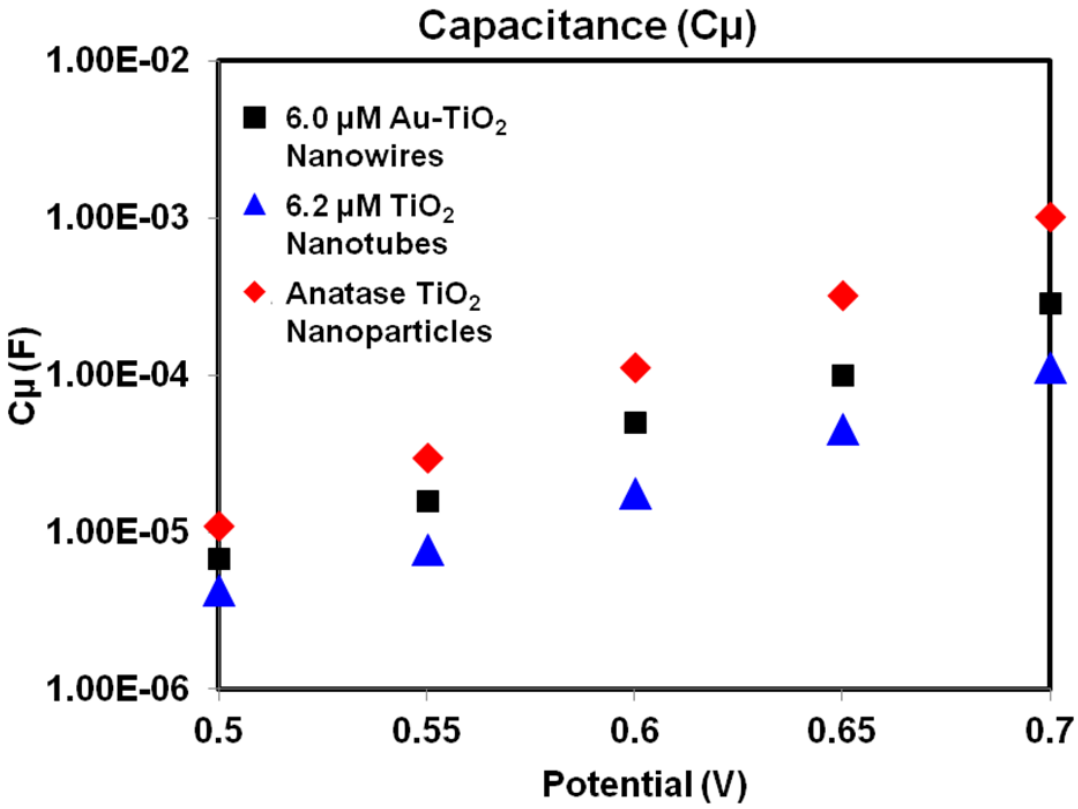

Fig 5.6 Chemical capacitance (Cμ) extracted from EIS measurements for DSSCs with Au-TiO_2 core-shell nanowire (black squares), TiO_2 nanotube (blue triangles), and TiO_2 nanoparticle (red diamonds) photoanodes.

5.6.3. e^- lifetime (τ_n) data

The e^- lifetime data in Figure 5.7 below reveals that the Au-TiO_2 nanowire electrode with a large R_{ct} value exhibits a relatively longer e^- lifetime, as compared with those in nanoparticle or nanotube cells. One possible explanation for the longer electron lifetime in the Au-TiO_2 core-shell nanowire structures is the high work function (5.1 eV) of gold. The gold nanowires may be drawing electrons from the oxide and acting as large trap states which are supported by the higher capacitance values obtained for Au-TiO_2 core-shell nanowire cell than the TiO_2 nanotube device.

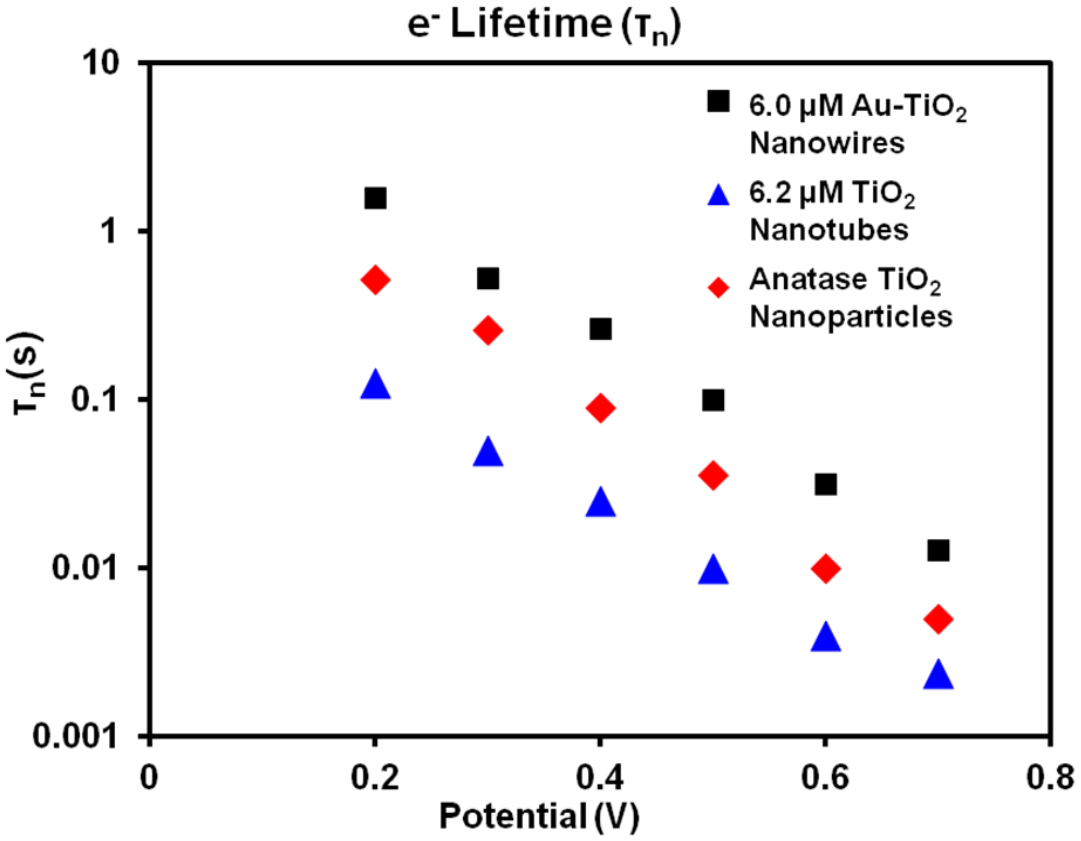

Fig 5.7 Electron lifetime (τ_n) extracted from EIS measurements for DSSCs with Au-TiO_2 core-shell nanowire (black squares), TiO_2 nanotube (blue triangles), and TiO_2 nanoparticle (red diamonds) photoanodes.

5.6.4. e^- conductivity (σ_n) data

The data presented in Figure 5.8 suggests that, compared to the TiO_2 nanoparticle cell and the TiO_2 nanotube array device, the Au-TiO_2 nanowire cell shows enhanced conductivity at equal applied potential, with respect to I^-/I_3^-. This is an important result with respect to photovoltaic performance as it provides support for the nanowire cell's tolerance to much faster electron recombination kinetics (e.g. with a faster redox couple).

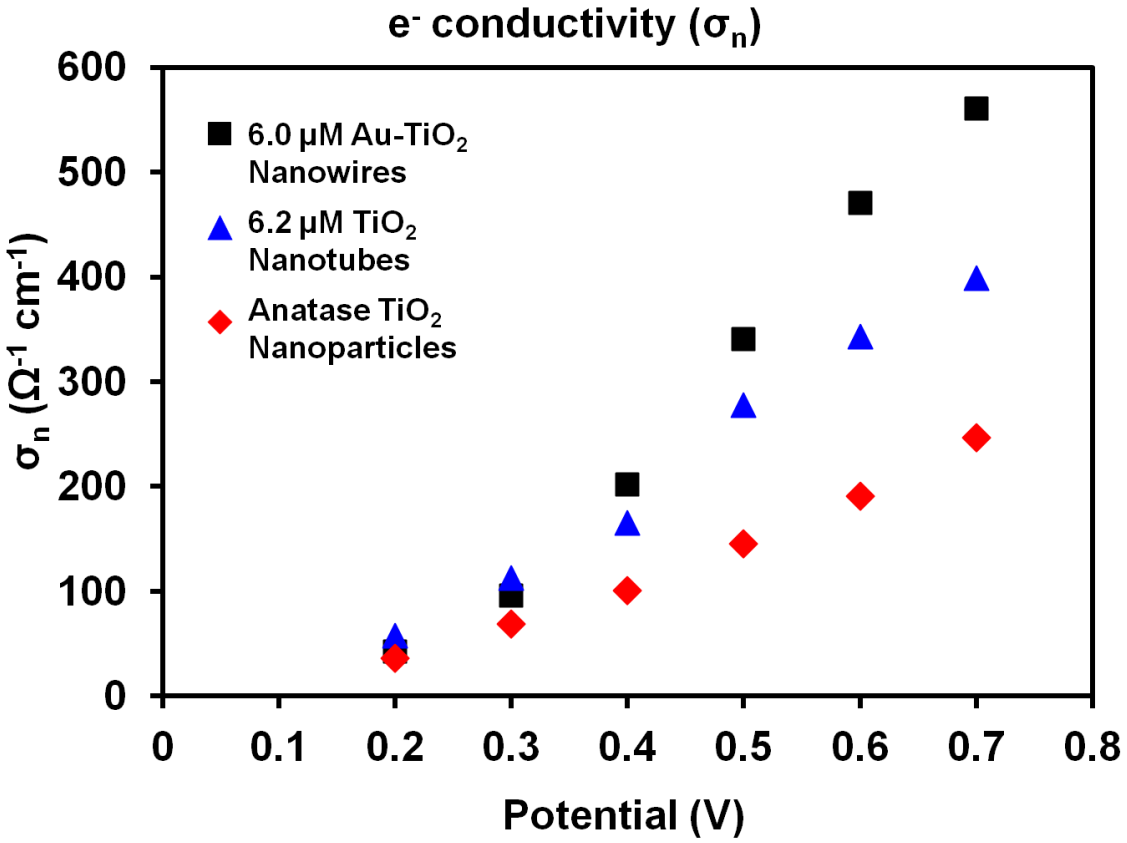

Fig 5.8 Electron conductivity (σ_n) extracted from EIS measurements for DSSCs with Au-TiO_2 core-shell nanowire (black squares), TiO_2 nanotube (blue triangles), and TiO_2 nanoparticle (red diamonds) photoanodes.

5.6.5. Electron diffusion length (L_n) data

The electron diffusion length, L_n, of three different electrodes is calculated and a comparative analysis has been given in Table 5.2 below. The increased conductivity of the Au-TiO_2 nanowire anode should attribute to a higher mobility of electrons in the Au-TiO_2 nanowire based device. As a consequence of this increased conductivity, the calculated diffusion length, L_n, of electrons for the Au-TiO_2 nanowire based DSSC was found to be excellent as compared to the TiO_2 nanotube and TiO_2 nanoparticle based cells.

Table 5.2 Diffusion length L_n calculated for various electrodes

Type of Photoanode	Length/Thickness of Photoanode (μm)	L_n (μm)
TiO_2 nanoparticle	3.0	2.7
TiO_2 nanotube	4.0	4.2
Au-TiO_2 nanowire	4.5	5.4

5.7. Summary

TiO_2 nanoparticles, TiO_2 nanotubes and Au-TiO_2 nanowire arrays exhibit different semiconductor electrochemical behaviors when they are employed in dye-sensitized solar cells. In this photo electrochemical system, charge separation, transport, and recombination strongly depend on the nanostructure geometry in the photo electrode. For the cell containing Au-TiO_2 nanowire arrays, decreasing the series resistance at the bottom of the electrode effectively promotes the separation of photogenerated charge carriers and prevents recombination of the electron with the holes. The uninterrupted metal pathway with fewer boundaries and fast band conduction is beneficial for transport of electron toward the conducting substrate. Simultaneously, the decrease of trap sites in the band gap and the surface state effectively enhances the electron diffusion mechanism and suppression of the interfacial charge transfer. Due to the good charge-

transport properties and higher recombination resistance, cells consisting of Au-TiO_2 core-shell nanowire structures exhibit longer electron lifetime, larger electron diffusion length, and higher conductivity. This study has given clear evidence on the improvement of charge transport properties in dye-sensitized solar cells based on 3D Au-TiO_2 core-shell nanowire anodes.

5.8. References

(1) *http://www.gamry.com/application-notes/*.
(2) Kern, R.; Sastrawan, R.; Ferber, J.; Stangl, R.; Luther, J. *Electrochimica Acta* **2002**, *47*, 4213.
(3) Hauch, A.; A. Georg *Electrochim. Acta* **2001**, *46*, 3457.
(4) van de Lagemaat, J.; Park, N. G.; Frank, A. J. *Journal of Physical Chemistry B* **2000**, *104*, 2044.
(5) Fabregat-Santiago, F.; Garcia-Belmonte, G.; Bisquert, J.; Zaban, A.; Salvador, P. *Journal of Physical Chemistry B* **2002**, *106*, 334.
(6) Fabregat-Santiago, F.; Bisquert, J.; Garcia-Belmonte, G.; Boschloo, G.; Hagfeldt, A. *Sol. Energy Mater. Sol. Cells* **2005**, *87*, 117.
(7) Han, L. Y.; Koide, N.; Chiba, Y.; Islam, A.; Mitate, T. *Comptes Rendus Chimie* **2006**, *9*, 645.
(8) Bisquert, J. *Phys. Chem. Chem. Phys.* **2000**, *2*, 4185.
(9) Bisquert, J. *Journal of Physical Chemistry B* **2002**, *106*, 325.
(10) Fabregat-Santiago, F.; Bisquert, J.; Palomares, E.; Otero, L.; Kuang, D. B.; Zakeeruddin, S. M.; Gratzel, M. *Journal of Physical Chemistry C* **2007**, *111*, 6550.
(11) Wang, Q.; Moser, J. E.; Gratzel, M. *Journal of Physical Chemistry B* **2005**, *109*, 14945.
(12) Martinson, A. B. F.; Elam, J. W.; Hupp, J. T.; Pellin, M. J. *Nano Letters* **2007**, *7*, 2183.
(13) Bisquert, J.; Cahen, D.; Hodes, G.; Ruhle, S.; Zaban, A. *Journal of Physical Chemistry B* **2004**, *108*, 8106.
(14) Bisquert, J. *J. Phys. Chem. Chem. Phys.* **2008**, *10*, 3175.
(15) He, C.; Zhao, L.; Zheng, Z.; Lu, F. *Journal of Physical Chemistry C* **2008**, *112*, 18730.
(16) Bisquert, J. *Journal of Physical Chemistry C* **2007**, *111*, 17163.
(17) Bisquert, J.; Vikhrenko, V. S. *Journal of Physical Chemistry B* **2004**, *108*, 2313.
(18) Martinson, A. B. F.; Goes, M. S.; Fabregat-Santiago, F.; Bisquert, J.; Pellin, M. J.; Hupp, J. T. *Journal of Physical Chemistry A* **2009**, *113*, 4015.
(19) Bisquert, J. *Phys. Chem. Chem. Phys.* **2003**, *5*, 5360.

Chapter 6

Conclusions

Today, solar cells are too expensive to be seriously considered as primary sources for energy production. The high cost prevents solar from competing with the existing fossil fuel driven electricity generation. However, due to the increased attention being paid to global warming and the limited supply of fossil fuels, solar cells have a promising future. To decrease the cost, efforts have been taken to commercialize cheaper solar cells, known as the second generation thin-film technology based solar cells such as CIGS and CdTe. These devices have recently shown promising efficiency and stability. However, the future for these solar cells as a long term solution is uncertain since their manufacture needs a clean production environment and some rare earth elements are used which cannot be considered for mass production. An interesting alternative to these cells are advanced third generation excitonic dye-sensitized solar cells (DSSCs).

Even though DSSCs had an experimental breakthrough in the early 1990s, major improvements, in terms of efficiency, have been limited. This is not because effort has not been made but because the complexity of the device far exceeds that of traditional solar cell technologies. The electron transport and recombination in the so called state-of-the-art mesoporous film are still subjects of debate. The basic objective of this work was to understand and gain in-depth knowledge of the practical problems associated with DSSCs efficiency. To increase our understanding of the limitations of electron transport and for the purposes of comparison with conventional nanoparticle based DSSCs, various experiments have been carried out. The advanced 3D core-shell Au-TiO_2 nanowire architectures were fabricated using three different techniques such as 1) template based sol-gel followed by electrodeposition, 2) electrodeposition followed by pulsed laser deposition (PLD), and 3) E-beam nanolithographically patterned nanopillar arrays on FTO. The achieved nanostructures were applied as photoanodes in dye sensitized solar cells for studying the influence of the morphology and geometry of photoanodes on the electron transport properties and the influence of electron-ion interactions on electron transport mechanism.

In detail, DSSCs have attained considerable attention during the last decade because of the potential of becoming a low cost alternative to silicon based solar cells. Although efficiencies

exceeding 10% in full sunlight have been reported, major improvements of the system are however limited by few factors. Electron transport is one of the prominent processes in the cell and is of major importance for the overall cell performance. It is further a complex process because the transport medium is a mesoporous film, and the gaps in the pores are completely filled by an electrolyte with high ionic strength, resulting in electron-ion interactions. Therefore, the electron transport in these so called state-of-the-art systems has a practical limit in terms of improving the DSSCs efficiency because of the low electron diffusion coefficient (D_n) in this randomly oriented mesoporous film photoanode. This work focuses in particular on the influence of the advanced core-shell nanoarchitecture geometry on electron transport and electron-ion interactions. In order to achieve the proposed goals, dye sensitized solar cells (DSSCs) based on innovative, highly aligned, ordered, three dimensional (3D) radial core-shell hybrid nanowire arrays were fabricated, that integrated gold or nickel nanowire core with anatase titanium dioxide (TiO_2) shell using three different approaches. In the first approach, both short (~2.5 µm) and long (~6.2 µm) crystalline anatase TiO_2 nanotubes were synthesized by a non aqueous sol-gel template synthesis route. Then the hollow channels of the TiO_2 nanotubes were filled with Au or Ni nanorods by galvanostatic constant current electrodeposition. The TiO_2 nanostructures, Au-TiO_2 and Ni-TiO_2 core-shell nanostructures were characterized by various electron microscopy and diffraction techniques. The obtained nanoarchitectures were used as photoanodes in DSSC devices by using N535 dye as the sensitizer, iodide/triiodide (I^-/I_3^-) or Ferrocene/Ferrocenium (Fc/Fc^+) as the redox couple, and Pt coated FTO as cathode. Subsequently the J-V curve parameters and IPCE data were generated. The practical power conversion efficiency calculated from J-V data showed improvements by using core-shell Au-TiO_2 or Ni-TiO_2 core-shell nanowires compared to only TiO_2 nanotubes as photoanode. Furthermore, $TiCl_4$ treatment of the Au-TiO_2 core-shell nanowire structures resulted in additional efficiency improvements due to increased electron transport rate. The highest efficiency obtained by using Au-TiO_2 (6.2 µm) core-shell nanostructures was 5.4 % and fill factor was 65 %. In a second approach, first highly aligned and well separated Au nanowire arrays were synthesized by using templated galvanostatic room temperature constant current electrodeposition, and then a layer of crystalline TiO_2 anatase shell was deposited onto the Au nanowires using an efficient thin film deposition technique known as pulsed laser deposition, (PLD). A neodymium-doped yttrium aluminum garnet (Nd:YAG) laser was used to ablate the TiO_2 disc target in the PLD system. The nanostructures were characterized and both back side (Pt) and front side (Au-TiO_2) illuminated DSSC devices

were fabricated. DSSCs efficiency was realized by using the core-shell Au-TiO_2 nanostructures as photoanode. Subsequently, $TiCl_4$ surface treatment of the novel nano architectures further doubled the power conversion efficiency of the passivated cell as compared to the non-passivated device. The highest efficiency and fill factor obtained by using these nanostructures in a front side illuminated cell were 6.7 % and 67 % respectively. In a third approach, TiO_2 nanopillars and core-shell Au-TiO_2 nanopillars were patterned on FTO by e-beam nanolithography using negative polymer resist (polymethyl methacrylate, PMMA) as the sacrificial template. The obtained nanopillars were characterized by field emission scanning electron microscopy (FESEM) which proved successful patterning of the nanopillar arrays on FTO. Subsequently, the nanopillar patterns were subjected to spectroscopic techniques in order to study the spectral properties. The plasmon-enhanced light absorption, photocurrent, and power conversion efficiency for TiO_2 nanopillar or Au-TiO_2 core-shell nanopillar based DSSCs were demonstrated. Our spectroscopic data indicates that the corrosion-protected gold nanopillar as plasmonic optical elements of the photoelectrode help in plasmon-enhanced photocarrier generation which in turn increases photocurrents of Au-TiO_2 nanopillars system. The efficiency obtained with only TiO_2 nanopillar and plasmon enhanced Au-TiO_2 core-shell nanopillar based DSSCs suggested that there is clear enhancement of the dye extinction when plasmonic gold nanopillar arrays are present in the anode.

Apart from the current density-voltage (J-V) measurements, incident photon to current efficiency (IPCE), and electrochemical impedance spectroscopy (EIS) characteristics were also studied. The efficiency, light scattering and charge transport properties of the core-shell nanowire based devices were compared to TiO_2 nanotube as well as TiO_2 mesoporous film based DSSCs. The Au nanowires inside the crystalline TiO_2 anatase nanoshell provided a direct conduction path from the TiO_2 shell to the transparent conducting oxide (TCO) substrate and improved transport of electrons between the TiO_2 and the transparent conducting substrate. The optical effects were studied by IPCE measurement which demonstrated that Au-TiO_2 nanowires showed an improved light harvesting efficiency, including at longer wavelengths where the sensitizer has weak absorption. The metal nanostructures could enhance the absorption in DSSCs by either scattering light enabling a longer optical path-length, by a dipole-dipole interaction, resonant energy transfer, localized surface plasmon resonance (LSPR) or by near-field coupling between the surface plasmon polariton (SPP) and the dye excited state. Charge transport, charge recombination, electron lifetime and electrical conductivity properties were studied using AC

impedance techniques. Comparisons of these transport times and lifetimes produced estimates of the effective electron dynamics and charge collection properties of the photoanodes. Rapid, radial electron collection is of practical significance because it should allow alternate redox shuttles that show relatively fast electron-interception dynamics to be utilized without significant sacrifice of photocurrent.

In general, for the mesoporous nanoparticle network, the electron diffusion coefficient is very small and the one-dimensional (1D) nanostructures with relatively high electron diffusion coefficient show efficiencies lower than those obtained for the TiO_2 nanoparticle cells. One of the reasons behind this low efficiency is the limit in the surface area of the one-dimensional nanostructures. To increase the surface area, an increase in the length of the one-dimensional nanostructures is necessary. However, this approach faces difficulty in the fabrication technique. For example, it becomes difficult to maintain the integrity of nanotubes when their length is over several tens micron meters.

One solution to the above problems could be the application of 3D Au-TiO_2 core-shell nanowire structures, which possesses high surface area, show the capability of easy, uninterrupted electron transport, and generate light scattering and plasmon resonance. It is understood that light scattering is effective in extending the effective path length of incident light within the photoanode film. Scattering may significantly enhance the light harvesting efficiency of photoanodes. It is therefore rational that, with a use of metal current collector, the photoelectrode film could be optimized with thinner designs than conventional solar cells. The importance of this point is that a thinner photoelectron film means a shortening of the distance for the photogenerated electrons to travel from the site of electron injection to the collecting electrode. As such, the charge recombination rate in a DSSC can be significantly lowered and, therefore, one can expect a breakthrough of the dye-sensitized solar cell efficiency. A combination of improved electron transport and enhanced light harvesting capability make Au-TiO_2 core-shell nanowire arrays a promising photoanode nanoarchitecture for improving photovoltaic efficiency while minimizing costs by allowing thinner devices that use less material in their construction. However, there is a challenge to the synthesis of long Au-TiO_2 core-shell nanowire arrays with suitable length, porosity, and surface chemistry.

6.1 Future directions

The research underlying this thesis has helped to improve our fundamental understanding of electron transport and interpretation of the trap distribution in DSSCs. Various approaches to the application of metal-metal oxide core-shell nanoarchitectures as photoanode in advanced 3D DSSCs have been explored. Each method has its merits and should be regarded as valuable tools in describing metal-metal oxide nanoarchitecture's role in charge transport mechanism. Despite all these advances, considerable effort must be devoted to both experimental and theoretical work. To further develop these devices, Molecular dynamics modeling (MD) simulations of these advanced DSSCs should be performed due to inherent difficulties in accurately and simultaneously describing all the fundamental components and processes underlying the functioning of such complex systems. Some future approaches would be:

1) Other inexpensive metals such as Cu or Al should be used as core in order to test their viability and performance in the 3D DSSCs.
2) Longer nanostructures with high aspect ratio should be synthesized in order to increase the electron diffusion length (L_n) and available surface area for dye adsorption.
3) Highly efficient panchromatic dyes such as Black dye or C101 dye should be applied as sensitizer in order to increase the possibilities of maximum absorption of visible light of all colors.
4) New dyes with sufficiently high redox potential should be synthesized and used so that they can be regenerated rapidly via electron donation from the electrolyte.
5) Other electrolytes with long-term stability, including chemical, thermal, optical, electro-chemical, and interfacial stability should be applied in the 3D DSSCs. The suitable electrolyte should not cause the desorption or degradation of the dye from the oxide surface. Also, the electrolyte should not exhibit a significant absorption in the visible range. One possible electrolyte to incorporate would be Co(II/III)tris(bipyridyl) based redox shuttles which has proven to fulfill most of the desired requirements for an efficient electrolyte in DSSCs.

6.2. General perspective

In the future, further gains in the efficiency of dye-sensitized solar cells are expected. This efficient technology has the potential to be used in real world producing electricity when people will be able to have skylights and windows with a layer of dye-sensitized solar cells, which should actually produce energy at the same time being aesthetically pleasing. At present, they aren't quite as efficient yet, but they are significantly cheaper than their silicon counterparts. Sony's prototype Hana-Akari (flower lamps) made of 8.2% efficient DSSCs glass panels have already achieved the world's top class of energy conversion efficiency. The solar modules generate sufficient electricity that is stored in batteries to power the LEDs. This news is concrete evidence that it is worth having high expectations for this device as the next generation solar cell that will create more innovative applications to be an intimate part of our daily lives. In view of the increased attention being paid to renewable energy, this effort will certainly be forthcoming.

Vita

The author was born in G. Udayagiri, Orissa, India. She obtained her Bachelor's degree and Master's degree in Chemistry from Berhampur University, India in 2002, and 2005 respectively. During her Masters she chose Materials Science as special paper where she studied the synthesis and properties of various forms of conducting polymer, Polyaniline (PANI) and ferrites under the guidance of Dr. R. K. Panda. She joined the University of New Orleans chemistry graduate program to pursue a PhD in Materials Chemistry in spring, 2008 and became a member of Professor Matthew A Tarr's group in May, 2008. On the way to her PhD degree she also earned a second Master's degree in Chemistry from University of New Orleans in fall 2011.